UC Berkeley
UC Berkeley Electronic Theses and Dissertations

Title
Stable Isotope Fractionations in Biogeochemical Reactive Transport

Permalink
https://escholarship.org/uc/item/6467h0h0

Author
Druhan, Jennifer Lea

Publication Date
2012

Peer reviewed|Thesis/dissertation

eScholarship.org Powered by the California Digital Library
University of California

Stable Isotope Fractionations in Biogeochemical Reactive Transport

By

Jennifer Lea Druhan

A dissertation submitted in partial satisfaction of the

Requirements for the degree of

Doctor of Philosophy

in

Earth and Planetary Science

in the

Graduate Division

of the

University of California, Berkeley

Committee in charge:

Professor Donald J. DePaolo, Chair
Professor Bruce Buffett
Professor Garrison Sposito

Spring 2012

Stable Isotope Fractionations in Biogeochemical Reactive Transport

Copyright 2012
by
Jennifer Lea Druhan

Abstract

Stable Isotope Fractionations in Biogeochemical Reactive Transport

by

Jennifer Lea Druhan

Doctor of Philosophy in Earth and Planetary Science

University of California, Berkeley

Professor Donald J. DePaolo, Chair

Characterizing the reactivity and fate of solutes in groundwater presents a formidable challenge in that these environments are inherently isolated from the observer. Samples are commonly limited to sediment cores and fluid collected from discrete well bores, while the measurements from these locations must be used to infer geochemical processes occurring across continuous, dynamic and heterogeneous systems. Stable isotope fractionations are an important tool in the quantitative analysis of reactive transport processes in porous media because they provide information coupled to, but distinct from solute concentrations. Examples of the combined analysis of solute concentrations and stable isotope fractionations abound in the literature, but almost entirely involve analytical models that decouple isotopic fractionation from the full extent of reactive pathways contributing to water-rock interaction in porous media flow.

It is the purpose of this dissertation to apply analysis of stable isotopes to elucidate the processes of biogeochemical reactivity contributing to in situ bioreduction of uranium during electron donor augmentation in the Old Rifle aquifer in western Colorado. Bio-induced stabilization of heavy metals in subsurface systems involves a complex and concurrent series of dissimilatory reduction reactions, each with a unique metabolism and contaminant affinity. In such a complex system, application of simplified fractionation-reactivity relationships is shown to be inadequate to describe the behavior of multiple stable isotope systems. As a result, the methodology is developed to explicitly incorporate the isotopologues of these species into a multi-component reactive transport model of the system. The result is a means of mechanistically analyzing isotopic fractionation within an integrated framework encompassing the complete reactive network associated with electron-donor augmented bioreduction.

The chapters herein are roughly divided into two sections. In the first half, sulfur and calcium isotopes are measured during field scale acetate amendments at Old Rifle. The results of these analyses demonstrate the utility of isotopic fractionation to track the development of terminal electron accepting processes and the formation of secondary mineral precipitates. However, these studies also demonstrate the limitations incurred by restriction to discrete well bores. In the second half, a flow-though column study is designed to overcome these limitations and test the extent to which individual isotopic fractionations are conserved during reactive transport under Old Rifle conditions. The results provide the first carbon budget during electron donor augmentation, and demonstrate that while the $\delta^{34}S$ fractionation induced by biogenic sulfate reduction is conservative, ion exchange effects dampen the $\delta^{44}Ca$ fractionation associated with carbonate precipitation.

To my mom, for believing I could do this so strongly that I believed her;
and to my dad, for the joy of finding things out.

Table of Contents

List of Figures . . . . . **v**

List of Tables . . . . . **ix**

Acknowledgments . . . . . **x**

1 General introduction **1**
1.1 Heavy metal and radionuclide bioremediation 3
1.1.1 Context 3
1.1.2 Stimulated subsurface heavy-metal bioremediaton . . . 4
1.2 Old Rifle 6
1.2.1 Hydrology and groundwater geochemistry 6
1.2.2 Contaminant legacy 7
1.2.3 Remediation strategy 8
1.2.4 The integrated field research challenge (IFRC) . . . 9
1.2.5 Stable isotope signatures of bioremediation 11
1.3 Modeling isotope fractionation 12
1.3.1 Comment on incorporation of isotopes into reactive transport codes. 13

2 Sulfur isotope fractionation in multiple *in situ* uranium bioremediation experiments **17**
2.1 Overview 17
2.2 Introduction 17
2.3 Methods 20
2.4 Results and discussion 22
2.4.1 Aqueous concentrations and $\delta^{34}S$ 22
2.4.2 Timing the onset of sulfate reduction 25
2.4.3 $\delta^{34}S$ constraints on reactive transport parameters . . . 27
2.5 Summary 29

3 Calcium isotope fractionation as a function of solution stoichiometry in groundwater **31**
3.1 Overview 31
3.2 Introduction 31
3.2.1 Calcite precipitation and associated $\delta^{44}Ca$ fractionation . . 31
3.2.2 Secondary carbonate formation during bioremediation . . 33
3.3 Methods 34
3.4 Results and discussion 36

3.4.1 Aqueous concentrations and $\delta^{44}Ca$ 36
3.4.2 First-order, homogeneous Rayleigh fractionation . . . 38
3.4.3 CrunchFlow simulations of well bore geochemistry . . . 40
3.4.4 Calcium isotopes in CrunchFlow 45
3.4.5 Ca^{2+}:CO_3^{2-} ion activity ratio 51
3.5 Summary 56

4 A mesoscale study of isotopic fractionation in biogeochemical reactive transport: I. Experimental design and carbon cycling . . . 57
4.1 Overview 57
4.2 Introduction 57
4.2.1 The e-folding length scale of Old Rifle bioremediation . . 58
4.2.2 Flow-through column studies 59
4.2.3 ^{13}C-labeled acetate 60
4.3 Methods 61
4.3.1 Column design 61
4.3.2 Artificial groundwater. 63
4.3.3 Aqueous sampling methods 64
4.4 Results and discussion 66
4.4.1 Hydrology 66
4.4.2 Fluid chemistry 67
4.4.3 Tracking carbon 71
4.5 Summary 76

5 A mesoscale study of isotopic fractionation in biogeochemical reactive transport: II. Reactive transport modeling and $\delta^{34}S$ . . . 78
5.1 Overview 78
5.2 Introduction 78
5.2.1 Modeling sulfur isotopes 79
5.2.2 Monod kinetics 79
5.3 Methods 82
5.4 Results. 83
5.4.1 Sulfur species concentrations and $\delta^{34}S$ 83
5.4.2 CrunchFlow model of sulfate reduction 86
5.4.3 Modeling $\delta^{34}S$ fractionation 91
5.5 Summary 95

6 A mesoscale study of isotopic fractionation in biogeochemical reactive transport: III. Calcite formation, ion exchange and $\delta^{44}Ca$ . . 96
6.1 Overview 96
6.2 Introduction 96
6.2.1 Cation exchange 97
6.2.2 Influence on isotope fractionation 98

6.3 Methods 100
6.4 Results and discussion 100
6.4.1 Aqueous calcium concentrations and $\delta^{44}Ca$ 100
6.4.2 CrunchFlow model of calcium solute profiles . . . 103
6.4.3 Extension of the model to $\delta^{44}Ca$ 105
6.5 Summary 109

References. **110**

Appendix A. **126**

Appendix B. **156**

List of Figures

1.1 Old Rifle field site in Garfield County, Colorado. Red dashed line indicates site boundary, red circles show locations of recently installed wells as part of the IFRC. 7

1.2 Groundwater uranium concentrations collected in May, 1998. Red circles indicate individual sample locations and solid lines denote associated contours of uranium concentrations in mg/L. Dark blue corresponds to 0.018 mg/L, red corresponds to 0.24 mg/L. 8

1.3 Well gallery design for Old Rifle biostimulation experiments . . . 9

1.4 Reaction schematic representing important pathways in the biogeochemical response to acetate addition at Old Rifle. Black lines show catabolic (energy producing) pathways, green lines show anabolic (microbial growth) pathways and red lines show abiotic pathways. Species in yellow font are electron acceptors, in blue are the resultant reduced species and in purple are secondary minerals. 10

1.5 Kinetic isotope fractionation in a closed, homogeneous system. ε refers to the fractionation factor in delta notation. 14

2.1 Background sulfate concentrations over the period spanning July 2008 to May 2009 in the Old Rifle aquifer. This pronounced background variability leads to substantial error in timing the onset of sulfate reduction during acetate addition 18

2.2 Well gallery schematic for the 2007 – 2009 Rifle IFRC field experiments. Geochemical and stable isotope data reported for those wells marked in blue. . . . 21

2.3 (A) Time series of Fe(II) and sulfate concentrations for well D04, dashed lines denote 2σ standard deviations in background sulfate concentrations measured up-gradient of the injection well gallery during the 2007 amendment; (B) for well D07. (C) Time series of d34S of sulfate and sulfide concentrations for well D04; (D) for well D07. All times are noted as days relative to the start of acetate addition to the injection wells. . . 23

2.4 (A) Sulfate concentrations and $\delta^{34}S$ of sulfate for well D04, dashed lines denote 2σ standard deviation in background sulfate concentrations measured up-gradient of the injection well gallery during the 2008 amendment; (B) for well D07; (C) for well D11. (D) Sulfide concentrations and $\delta^{34}S$ of sulfate for well D04; (E) for well D07; (F) for well D11. All times are noted as days relative to the start of acetate addition to the injection wells. 24

2.5 (A) Sulfate concentrations and $\delta^{34}S$ of sulfate for well D01, dashed lines denote 2σ standard deviation in background sulfate concentrations measured up-gradient of the injection gallery during the 2009 amendment. (B) Sulfide concentrations and $\delta^{34}S$ of sulfate for well D01. All times are noted as days relative to the start of acetate addition to the injection wells. 25

2.6 For wells in the first row down-gradient of the injection gallery (D04 and D01), number of days since the start of each acetate addition taken to measure arrival of acetate and the start of DIRB activity (based on elevated Fe(II) concentrations) and SRB activity (based on (1) systematic drop in sulfate below 2σ standard deviation in background concentrations, (2) systematic increase in sulfide concentrations and (3) systematic

enrichment in $\delta^{34}S$ of sulfate) for each of the three consecutive years of acetate amendment. For the 2007 amendment, sulfate concentrations dropped below 2σ standard deviation on day 35, but failed to continue decreasing in a systematic trend. . 26
2.7 Measured values and CrunchFlow simulation results for the first row of monitoring wells in the 2007 amendment experiment. (A) CrunchFlow modeled Fe(II) and sulfide concentrations, (B) measured Fe(II) and sulfide concentrations in well D04, (C) CrunchFlow modeled acetate and sulfate concentrations, (D) measured acetate and sulfate concentrations in well D04. All times and noted as days relative to the start of acetate addition to the injection wells. 29

3.1 (A) Well gallery schematic for 2007 – 2009 Rifle IFRC field experiments. Geochemical and stable isotope data reported for those wells marked in blue. (B) Change in hydraulic conductivity measured in injection wells. Wells labeled in blue correspond to data reported herein 35
3.2 Acetate, bromide, sulfate, chloride, calcium and strontium concentration profiles from injection wells G51, G52 and G53 during the 2009 acetate amendment. Days are counted from the start of acetate addition and the solid vertical line marks the cessation of injection. 37
3.3 Fluid $\delta^{44}Ca$ in injection wells G51, G52 and G53. Days are counted since the start of acetate addition and the vertical black line denotes the cessation of amendment. At this scale the error in $\delta^{44}Ca$ measurements is contained within the size of the data points. 39
3.4 Distillation (Rayleigh) models and measured $\delta^{44}Ca$ trends in wells G51 and G52. . 40
3.5 Measured data (blue) and associated model results (red) for wells G51 (left column) and G52 (right column). Shown are bromide inert tracer fits (top row), sulfate (middle row) and acetate (bottom row). Days are counted from zero as the last day of acetate injection to the wells. 46
3.6 Calcium concentrations measured (blue) and modeled (red) for wells G51 and G52. Days are counted from zero as the last day of acetate injection into the wells. . . 47
3.7 (A) fluid $\delta^{44}Ca$ data collected in well G51 (blue), CrunchFlow model of $\delta^{44}Ca$ based on a solid solution calculated using aqueous $CaCO_3$ complex (red) and a solid solution calculated using the mineral $CaCO_3$ composition (green). (B) ratio of ^{44}Ca-calcite to ^{40}Ca-calcite for both models shown in (A). Dashed black line represents starting ratio for zero fractionation. 50
3.8 (A) $\delta^{44}Ca$ datasets for well G51 (blue) and G52 (green) and corresponding CrunchFlow simulations of G51 (red) and G52 (black) for a single kinetic fractionation factor ($\varepsilon \approx$ -1.18‰). (B) $\delta^{44}Ca$ dataset for well G52 (green) and a suite of simulation with kinetic fractionation factors of $\varepsilon \approx$ -0.92‰ (purple), $\varepsilon \approx$ -1.18‰ (black) and $\varepsilon \approx$ -1.38‰ (blue). 52
3.9 (A) speciated $Ca^{2+}_{(aq)}$ concentrations as a function of time in wells G51 and G52 from associated CrunchFlow simulations. (B) speciated $CO_3^{2-}{}_{(aq)}$ concentrations and (C) Ca^{2+}:CO_3^{2-} ion activity ratios for G51 and G52. 53
3.10 Measured $\delta^{44}Ca$ profiles of wells G51 (red open circles) and G52 (blue open squares) and associated calculated $\delta^{44}Ca$ profiles from the Nielsen et al., 2012 model for G51 (solid red line) and G52 (solid blue line). 55

4.1 Acetate concentration profiles as a function of distance down-gradient using the model presented in Chapter 2. Injection wells are located at 4 m and days are labeled relative to the start of sulfate reduction. 59
4.2 (A) schematic of column design including influent artificial groundwater chemistry and fluid samples collected. (B) schematic of side port sampler design (courtesy of Soil Moisture Equipment Corporation). (C) picture of packed, flowing column and (D) close up of sample collected from side port. 62
4.3 (A) bromide concentration profiles for all side ports and effluent over the 43 day acetate amendment. (B) deuterium breakthrough curve started on the same day as acetate and bromide addition. (C) $\delta^{18}O$ breakthroughs starting on day 24 and (D) on day 40. Numbers in plots B, C & D indicate the hour since the start of the tracer addition that the corresponding profile was measured. 67
4.4 (A) sulfate concentration profiles as a function of time along the length of the column, (B) calcium and (C) uranium. Sulfate and calcium influent values and the UMTRA compliance limit for uranium are shown as horizontal black lines. . . . 68
4.5 (A) Fe(II) and HS^- measured in column effluent and (B) pictures of the lower 30 cm of the column demonstration color changes associated with FeS precipitation. . 70
4.6 (A) effluent TOC and TIC concentrations and corresponding influent concentrations (horizontal lines). (B) effluent TOC and TIC $\delta^{13}C$ values and corresponding influent $\delta^{13}C$. 72
4.7 (A) measured TOC influent and effluent concentrations and the difference between these values. (B) measured TIC in effluent and the calculated TIC assuming all acetate consumed (as shown in A) is converted to TIC. 73
4.8 Dissolved methane concentrations and corresponding $\delta^{13}C$ values for a time series of column effluent samples. 75
4.9 Measured $\delta^{13}C$ of TIC in effluent and corresponding calculated $\delta^{13}C$ of TIC (eq. 4.5). 75
4.10 Heat map of phylogenetic community structure based on DNA sequences of fluid samples collected from side ports and effluent during acetate addition. Numbers at the base indicate sampling day relative to the start of acetate addition. . . . 77

5.1 Hyperbolic function of the form presented in eq. 5.6 illustrating the relationship between sulfate concentration and reduction rate for a Monod rate law. . . . 81
5.2 Effluent sulfate and acetate (measured at TOC) time series from the mesoscale column experiment for the full 43 days of acetate amendment. 83
5.3 Sulfate concentration profiles across the length of the column for the final 23 days of acetate amendment. 84
5.4 (A) $\delta^{34}S$ of sulfate enrichment profiles across the length of the column for the final 23 days of acetate addition. (B) effluent $\delta^{34}S$ of sulfate and sulfide over the same time period. 85
5.5 $\delta^{34}S$ of sulfate measured in the 30 (left plot, red squares) and 90 cm (right plot, blue crosses) side ports in comparison to Rayleigh models for fractionations of 10‰ (purple line) and 11‰ (black line). x-axis is the fraction of sulfate remaining in solution. . 86
5.6 Measured acetate (open diamonds) and sulfate (crosses) are compared with modeled acetate (red) and sulfate (blue) concentration profiles for the mesoscale column effluent. 89

5.7 Measured sulfate concentrations (open circles) and simulated profiles (red) for (A) 10 cm, (B) 30 cm, (C) 50 cm, (D) 70 cm, (E) 90 cm and (F) effluent as a function of time. 91
5.8 Crunchflow simulated $\delta^{34}S$ fractionation of sulfate (red line) and sulfide (blue line) at 100 cm, compared with measured values of effluent sulfide (x), sulfate in the effluent (diamond), and sulfate in the 90 cm side port (pink cross). 94

6.1 Calcium and TIC concentrations in the effluent solution for the 43 consecutive days of acetate amendment. Horizontal lines indicate respective influent concentrations. . 101
6.2 Calcium concentrations in the side port and effluent samples over the final 18 days of acetate amendment. 101
6.3 Fluid $\delta^{44}Ca$ as a function of time measured in the 10, 30 and 50 cm side ports and the effluent. Error bars show 0.12‰ range based on replicate sample measurements and long term reproducibility of the standard. Influent $\delta^{44}Ca$ is bounded by 0.16‰ range of uncertainty based on 4 replicate measurements collected over time from the influent reservoir. Background $\delta^{44}Ca$ of the Rifle aquifer fluid is shown for reference. . 102
6.4 (A) measured (open circles) and simulated (thick line) effluent sodium concentration; (B) potassium; (C) calcium and (D) magnesium using Fox et al. (in review) CEC and selectivity coefficients. 104
6.5 Simulated TOC (red) and calcium (blue) effluent concentrations compared with measured TOC (crosses) and calcium (open diamonds) 105
6.6 Simulated and measured calcium concentrations at 10 cm (light blue), 30 cm (red), 50 cm (green) and effluent (dark blue) for the last 23 days of acetate addition. . . 106
6.7 Simulated and measured $\delta^{44}Ca$ in the 50 cm side port (green) and the effluent (blue) in the final 23 days of acetate amendment. 107
6.8 Simulated and measured $\delta^{44}Ca$ in the 50 cm side port (green) and the effluent (blue) along with measured values for the 10 cm (light blue) and 30 cm (red) side ports and the range defining the influent solution. Simulated $\delta^{44}Ca$ values differ from those in Fig. 6.6 due to modification of the ion exchange parameters. 108

List of Tables

1.1 Half-reactions of common environmental TEAPs and associated Gibb's standard free energy at pH 7.0, 298.15 K (values calculated from log K given in Sposito, 2008). 5

2.1 Background sulfate and $\delta^{34}S$ values from well U01 for the three consecutive years of acetate amendment. Shown are the mean and 2σ standard deviations for sulfate and $\delta^{34}S$ as well as the number of measurements contributing to each value (n) and the range of dates over which the samples were collected (dates). 22

3.1 Sulfate reduction and acetoclastic methanogenesis TEAP stoichiometry and associated parameters. Maximum utilization rates for methanogenesis differ between wells and are listed as G51/G52. Half saturation constants from Dale et al. (2008) and Fang et al. (2009). 41
3.2 Heterogeneous reactions used to model clogged wells and associated parameters. Individual values for each well are listed as G51/G52 where they differ. . . 42
3.3 Initial conditions of aqueous primary species within the well bore for the start of simulation. Individual values for each well are listed as G51/G52 where they differ. 42
3.4 Initial conditions of mineral volume fraction in the well bore for the start of simulation. Individual values for each well are listed as G51/G52 where they differ. . . 43
3.5 Secondary reactions calculated using associated equilibrium constants as instantaneous products based on primary species values. 43

4.1 Concentration of salts added to DI water to achieve an artificial groundwater representing Old Rifle background conditions. 63
4.2 Charge balance for artificial groundwater solution 63
4.3 Tracer breakthrough curve analysis of pore water velocity and porosity for multiple inert tracers introduced over the course of the acetate amendment experiment. . . 66

5.1 Iron and sulfate reduction TEAP stoichiometry and associated parameters. Iron reduction is calculated using a bioavailable pool of ferrihydrite. Maximum specific utilization rates are in units of log(mol/m^2 cell/s) for iron reduction and mol/g cell/yr for sulfate reduction. Half saturation constants are consistent with the range of values from Dale et al. (2008) and Fang et al. (2009). 87
5.2 Heterogeneous reactions used to model clogged wells and associated parameters. . 88
5.3 Initial conditions of aqueous primary species for the start of the mesoscale column simulation. 88
5.4 Initial conditions of mineral volume fraction for the start of the mesoscale column simulation. 88

6.1 Exchange coefficients for >2 mm size fraction of Old Rifle sediment (Fox et al., in review) 98

Acknowledgments

This thesis is the product of countless hours of guidance and support from my Ph.D. advisers, Don DePaolo and Carl Steefel. I am exceedingly grateful to Don for the generosity and seemingly infinite support that he has provided. Through my five years as his student, Don has never asked me to stop pursuing a research topic that fascinated me, and through this freedom I feel he has helped me learn more than I ever could have otherwise. I must consider Carl my second adviser because his office has always been open to me as a place to discuss questions and ideas with the guarantee of leaving knowing more than when I arrived. Through an immensely generous dedication of time and effort Carl has singly helped me develop my research, my skill set and my confidence as a scientist. For these reasons I am tremendously fortunate to have had the honor to work with my advisers.

The Department of Earth and Planetary Sciences has been a home and a family for the past 5 years. I have benefited from the time spent with all of my former and current officemates, Amanda Thomas, Bill Cassata, Vicky Lee, Chris Huber, Brook Peterson, Laura Nielsen, Daniele Rosa and Jim Watkins. In particular I must thank Jim, who has been both a mentor and a friend to me, somehow simultaneously setting an example of professionalism and helping me laugh off any struggle. I would not have a single data point to report without the help of Shaun Brown, Tom Owens, Markus Bill, Joern Larsen, and Wenbo Yang, who have shown infinite patience in allowing me to learn by their example. Marilyn Saarni has been an equally invaluable resource in fixing any issue that I have managed to come up with. In addition the administrative staff of the department, Margie Winn, Micaelee, Ellswyth, Dawn Geddes and Marion Banks have all been wonderfully supportive.

In addition to my own department on campus, Lawrence Berkeley National Laboratory has been an invaluable resource where I have found the opportunity to collaborate and learn from scientists in a variety of disciplines. The work presented herein reflects collaboration with Ken Williams, Mark Conrad, Susan Hubbard, Eoin Brodie, Peter Nico, Li Yang, Jim Davis, Stefan Finsterle and Eric Sonnenthal for which I am greatly appreciative. Through LBNL I have received the majority of my financial support via the Director, Office of Science, Office of Basic Energy Science, of the U.S. Department of Energy under Contract No., DE-AC02-05CH11231, and through the Office of Biological and Environmental Research, Subsurface Biogeochemical Research Program.

Finally I must thank my friends and family, Marisa Palucis, Dan Berwick Evans and my parents, who I love and without whom I would be lost.

Chapter 1

General introduction

This thesis develops improved conceptual models for the hydrologic, biologic and geochemical processes associated with bioremediation of heavy metals and radionuclides in groundwater. The focus is on analysis and modeling of the partitioning of stable isotopes of sulfur, carbon and calcium that occurs as a consequence of subsurface bioremediation processes. Heavy metal and radionuclide contamination presents a uniquely challenging problem because these species do not degrade in the natural environment in the same manner as organic compounds. For locations in which these contaminants are widely dispersed in the subsurface, remediation techniques are under development with the objective of changing the oxidation state of toxic metals, commonly from oxidized soluble forms to reduced insoluble forms, and to accomplish this reduction "in situ", meaning within the subsurface environment. This technique seeks to avoid the need for costly excavation or pump-and-treat methods in favor of trapping the contaminants as stabilized, insoluble and immobile mineral phases within the aquifer. Bioreduction is a promising means of accomplishing this task; however the approach is still exploratory and there remain many aspects that require development.

The general principle of bioreduction is to leverage naturally occurring microorganisms present in the subsurface environment that are capable of reducing metals as part of their anaerobic respiration to influence the oxidation state of contaminants. Such organisms are ubiquitous in the subsurface, though their populations are commonly limited by the availability of nutrients. Thus supplying an artificial source of nutrients, such as simple organic carbon compounds like acetate, provides the native microbial community with a reducing agent, a means of rapid growth, and ultimately the ability to effect large-scale metal reduction. This process, referred to as "*in situ* stimulated bioremediation" of heavy metals, therefore seeks to utilize native microbial populations to catalyze the reduction of soluble, toxic heavy metals and radionuclides. The principle engineering challenge is to successfully implement this complex stimulation while operating essentially blind: the nutrient is supplied to the aquifer through a limited number of wells, with minimal ability to guide the delivery to metal-contaminated regions or to control the growth of desired metal-reducing microbial populations in proximity to these contaminants. Consequently, monitoring and verification of this type of remediation is difficult and there is a need to develop tracers that can clarify the processes occurring during subsurface stimulated bioremediation.

Variations in the isotopic ratios of major elements like S, O, C and Ca that are active components of microbial redox and associated reactivity can provide a much

needed perspective on the stimulated bioremediation process. However, to date the interpretation of stable isotope effects have been largely limited to simplified mass balance calculations that do not account for important complexities influencing stable isotope fractionations. These complexities stem from the rapidity of redox reactions during bioremediation, associated changes in groundwater chemistry and the inherent heterogeneity in aquifers. To address such effects it is necessary to incorporate relevant isotopologues into multi-component reactive transport codes and thus develop improved conceptual models for the controls on stable isotope fractionation when the chemical processes are kinetically controlled. These issues are the major foci of the research described here.

Chapter 1 reviews the basic aspects of subsurface stimulated heavy metal bioremediation, focusing on a uranium-contaminated field site in western Colorado. This chapter includes a description of isotopic data from field experiments, approaches to the use of kinetic stable isotope fractionation processes, and concludes with a proposed framework for incorporating these data in reactive transport models. Chapters 2 and 3 present field scale studies of stable isotope fractionation during active *in situ* uranium bioremediation. Chapter 2 focuses on the fractionation of sulfur isotopes associated with sulfate reduction as a terminal electron accepting process (TEAP). The results are used to identify a previously undocumented trend towards earlier onset of sulfate reduction when the subsurface has been pretreated with electron donor. In addition a modification to the standard biogeochemical reactive transport model for the field site is developed in which the onset of sulfate reduction is established based on $\delta^{34}S$ enrichment.

Chapter 3 describes a study where secondary mineral formation induced by the bioremediation process leads to substantial permeability reduction around injection wells at the field site. While this example presents an engineering failure in that electron donor was not effectively delivered to the aquifer, the conditions resulted in a dataset documenting significant calcium isotope fractionation associated with carbonate precipitation and showed variation in the magnitude of Ca isotope fractionation as a function of fluid Ca^{2+}:CO_3^{2-} ratio. This study presents some of the first field evidence supporting theoretical predictions of this relationship.

Chapters 4-6 present the results of a large-scale (100 cm length) flow-through column experiment designed to study heavy metal bioreduction processes and accompanying stable isotope effects in a controlled environment. This experimental approach demonstrates that the length scales over which bioreduction takes place in the subsurface are often much smaller than the typical spacing of sampling wells, highlighting what is a significant limitation to field-scale subsurface monitoring. As a result of the column design, isotopic datasets of necessary spatial and temporal resolution were generated and used to validate simulations of stable isotope fractionations implemented in biogeochemical reactive transport models.

Chapter 4 describes the experimental design of this meso-scale column, presents the major ion chemistry and tracer results, and develops a carbon budget for the experiment based on introduction of a $\delta^{13}C$-labeled organic carbon source. Chapter 5 utilizes the results of the meso-scale column study to develop a biogeochemical reactive transport model capturing the changes in major ion chemistry and secondary mineral precipitation using single and dual Monod reactions for individual terminal electron accepting processes (TEAP)s. The model is extended to explicitly incorporate the ^{32}S

and ^{34}S isotopologues of sulfate and associated product sulfur species. Chapter 6 addresses the observation that the enriched calcium isotope signal detected in well bores at the field scale is not preserved in down-gradient monitoring wells. The $\delta^{44}Ca$ reactive transport dataset confirms this observation, showing enrichment within the first 50 cm of flow followed by a return to background values by 100 cm. This trend reflects competing influences of carbonate precipitation (fractionation) and ion exchange (mixing), and demonstrates how calcium isotopes may be used to discern the relative contribution of each process to observed calcium concentrations.

1.1 Heavy metal and radionuclide bioremediation

1.1.1 Contamination

Containment and decontamination of former nuclear weapons production installations is the most expensive environmental remediation effort in the history of the United States (Lloyd and Renshaw 2005a). The extent and complexity of this contamination is largely due to exemption of the nuclear weapons production process from environmental regulations and record keeping during World War II and the Cold War. As a result, in 1995 when the Department of Energy (DOE) was directed to report the waste and associated environmental impacts of each step of nuclear weapons production, the department had to first indentify and then quantify a vast array of contaminated environments (DOE, 1997). Currently, the DOE maintains responsibility for approximately 10,000 contaminated sites within 120 individual installations spanning 30 states (National Research Council, 1999; Lloyd and Renshaw 2005a) at an estimated combined cost of remediation of more than a trillion dollars (Lloyd and Renshaw, 2005b).

An important component contributing to the magnitude of the nuclear contaminant legacy is the persistence of these toxins in the subsurface environment (National Research Council, 1999). Short of radioactive decay, inorganic heavy metals and radionuclides do not naturally decompose or degrade, therefore mitigating the risks associated with elevated concentrations of these contaminants requires manipulations of mobility and toxicity. For example chromium ore is recovered as hexavalent chromium (Cr(VI)) which is an acute toxin, whereas cell walls are impermeable to reduced trivalent chromium (Cr(III)) (National Research Council, 1999). Furthermore, many contaminants are often mobile and soluble in the near-surface environment. For example at neutral pH, uranium occurs in a soluble hexavalent oxidation state with mobility largely governed by adsorption to sediments, however the reduced quadrivalent state is insoluble (Davis et al., 2004). The complexity and cost of remediation therefore stems from the diversity of contaminants as well as the environments in which they are dispersed. Mining and processing of heavy metal and radionuclides was predominantly conducted across the western United States in areas rich in actinide and transition metal-bearing ore, thus

superimposing high volume, low concentration contamination over what are naturally low-recharge, redox sensitive, heterogeneous environments.

Because of the complexity and extent of heavy metal and radionuclide contamination, a suite of technologies are required to adapt to the specific conditions of each site. Where contamination is localized and concentrated, sediments may be extracted or flushed, or the contaminants may be contained in place through either subsurface barriers or vitrification (e.g. Bacon and McGrail, 2005). More often contamination is disperse and mobile in groundwater systems, thus requiring application of permeable reactive barriers, bio- or phyto-remediation (e.g. Adriano et al., 1997) or other forms of redox manipulation. Common to all remediation efforts is the uncertainty stemming from the physical and biogeochemical heterogeneity of the subsurface environment. Therefore, the ability to predict the success of a given strategy is contingent upon the accuracy of models representing our understanding of relevant reactive transport processes.

1.1.2 Stimulated subsurface heavy-metal bioremediation

Perhaps the most familiar form of cellular respiration is aerobic, in which cells derive energy by transferring an electron from a nutrient to oxygen (O_2). This redox reaction transforms the nutrient to a useful form for cellular function (typically adenosine triphosphate) and produces CO_2 as a waste product. All animals and many bacteria and archaea require oxygen in order to accomplish this basic function. However, a wide variety of microbes have also adapted to respire in the absence of oxygen through the use of alternate electron acceptors. These populations, termed chemolithotrophes, can use oxidized compounds such as nitrate and sulfate to respire in environments where oxygen is unavailable. Oxygen depletion is common in saturated subsurface systems in which the groundwater has been segregated from the atmosphere for long timescales, such as in arid climates. In these systems, microbial populations are ubiquitously found surviving off of the energy gained by transferring electrons from available organic carbon sources to alternate electron acceptors (Table 1.1).

Most alternate electron acceptors are soluble (e.g., nitrate and sulfate) and can readily pass through the cell walls of microbes adapted to reduce these species. These microbes avoid toxins by exclusively allowing these specific compounds through their cellular membranes, which are then reduced internally and expelled as waste. A particular class of microbes are unique in that they function by using Fe(III)-(hydr)oxide minerals as electron acceptors. These insoluble minerals cannot be taken into the cell interior to accomplish reduction, and so the microbes have adapted to accomplish electron transfer externally. The ability to transfer electrons externally means these populations are not as selective against contaminants and could potentially reduce high mass metals and radionuclides (Lloyd and Macaskie, 2002).

In 1991, Lovley et al. reported results of a cell culture experiment in which two common anaerobic iron reducing bacteria, *Geobacter sulfurreducens* and *Shewanella putrefaciens*, demonstrated direct reduction of soluble U(VI) as a terminal electron acceptor. The energetically favorable, microbially catalyzed reaction was faster than common abiotic uranium reduction pathways, and suggested a new means of stabilizing

uranium *in situ* as insoluble U(IV). Similar microbially mediated redox reactions were subsequently shown to facilitate the solubilization of plutonium (Rusin et al., 1994), immobilization of technetium (Lloyd et al., 1997) and detoxification of chromium (Turick et al., 1996). Since these pioneering studies a new generation of research into microbe-metal and microbe-radionuclide interactions has developed (e.g. Lovley, 2000; Keith-Roach and Livens, 2002; Lloyd and Renshaw, 2005a,b; Gadd, 2010; Lloyd and Gadd, 2011).

Fe(III)-(hydr)oxide minerals such as goethite and ferrihydrite occur in high abundance in most near-surface environments and correspondingly so do native populations of iron-reducing microbes. This natural prevalence has lead to the development of stimulated *in situ* bioremediation strategies using native iron reducers in heavy-metal contaminated groundwater systems (Lovley, 2000, Jørgensen, 2007). The general strategy for in situ stimulation is to supplement the groundwater system with the naturally limiting nutrient, and thus promote growth of the indigenous population. The inherent difficulty lies in targeting growth of iron reducing microbes within the larger community. In this sense stimulated bioremediation seeks to achieve the biogeochemical conditions that favor a particular TEAP from among a range of potentials (Table 1.1).

TEAP	Half-Reaction	$\Delta G^{0'}$ (kJ/e$^-$ eq)
oxygen	$\frac{1}{4}O_{2(g)} + H^+ + e^- = \frac{1}{2}H_2O_{(l)}$	-78.49
nitrate	$\frac{1}{2}NO_3^- + H^+ + e^- = \frac{1}{2}NO_2^- + \frac{1}{2}H_2O_{(l)}$	-40.81
goethite	$FeOOH_{(s)} + 3H^+ + e^- = Fe^{2+} + 2H_2O_{(l)}$	43.72
sulfate	$\frac{1}{8}SO_4^{2-} + \frac{9}{8}H^+ + e^- = \frac{1}{8}HS^- + \frac{1}{2}H_2O_{(l)}$	20.69
methanogenesis	$\frac{1}{8}CO_{2(g)} + H^+ + e^- = \frac{1}{8}CH_{4(g)} + \frac{1}{4}H_2O_{(l)}$	23.63

Table 1.1: Half-reactions of common environmental TEAPs and associated Gibbs standard free energy at pH 7.0, 298.15 K (values calculated from log K given in Sposito, 2008).

The challenges faced in successfully executing *in situ* heavy metal or radionuclide bioremediation are therefore largely kinetic in nature. How to target the growth of those microbial communities identified as contaminant reducers, how to deliver electron donor to the subsurface system without rapidly reducing local permeability as a result of secondary mineral formations, and how to verify that contaminants are successfully sequestered in immobilized phases. The ability to address these questions is often undermined by the spatial and temporal heterogeneity of the *in situ* environment. Non-uniform delivery of injected electron donor as well as fluctuations in groundwater flow rate and solute composition contribute to a complex geochemical signal that requires a multi-component reactive transport approach to resolve.

1.2 Old Rifle

The Old Rifle site in western Colorado was the former location of a uranium and vanadium ore processing facility that operated for 34 years. During this period a large volume of mill tailings was accumulated on the site, leading to an elevation in the heavy-metal and radionuclide concentration of the sediment and groundwater. The site has since been closed and remediation is currently underway through the DOE Office of Legacy Management. The Old Rifle site is fairly simple when contrasted with many other DOE remediation projects such as the Hanford site in eastern Washington and the Savanna River site in Georgia. Specifically, the number and concentration of contaminants are low, and the aquifer system is small and well described. As a result, the Old Rifle site has been selected by the DOE Office of Science for a pilot scale study of *in situ* bioremediation. The following sections describe the physical system, the origin of contamination and the current progress in developing bioremediation techniques.

1.2.1 Hydrogeology and groundwater geochemistry

The Old Rifle site is located on a small alluvial terrace along the northern bank of the Colorado River roughly 0.3 miles east of the city of Rifle, Colorado (Figure 1.1). The shallow system is bounded from beneath by variegated claystone, siltstone and sandstone of the Tertiary Wasatch formation at a depth from land surface of 6 to 9 m. The northern, eastern and western sides of the crescent shaped alluvium are similarly bounded by the Wasatch, which rises steeply away from the small floodplain. Hydraulic conductivity in the saturated alluvium averages 30 – 38 m/day with a wide range in porosity from 10% – 35%. In contrast the Wasatch formation conductivity is on average 3 orders of magnitude lower and is considered to hydrologically bound the local system (DOE, 1999; 2011).

Groundwater follows a general southwest gradient, discharging to the Colorado River at the western boundary. Typically the lower 3-5 m of sediment is saturated, though the water table may rise several meters during spring snowmelt as a result of both increased local recharge and river stage. Recharge to the system occurs predominantly as inflow of groundwater from the elevated region above the northern boundary of the site through fractures in the Wasatch and as seeps along the terrace. Groundwater in the alluvial aquifer is typically sub-oxic, with dissolved oxygen (DO) concentrations of >0.3 mg/L. Nitrate concentrations are >30 μM, whereas sulfate concentrations are elevated and highly variable, ranging from 5 – 20 mM. Carbonate alkalinity is in the range of 300 – 600 mg/L and pH is generally neutral but can range from 6.8 to 8.5 (DOE, 1999; Anderson et al., 2002; DOE, 2011).

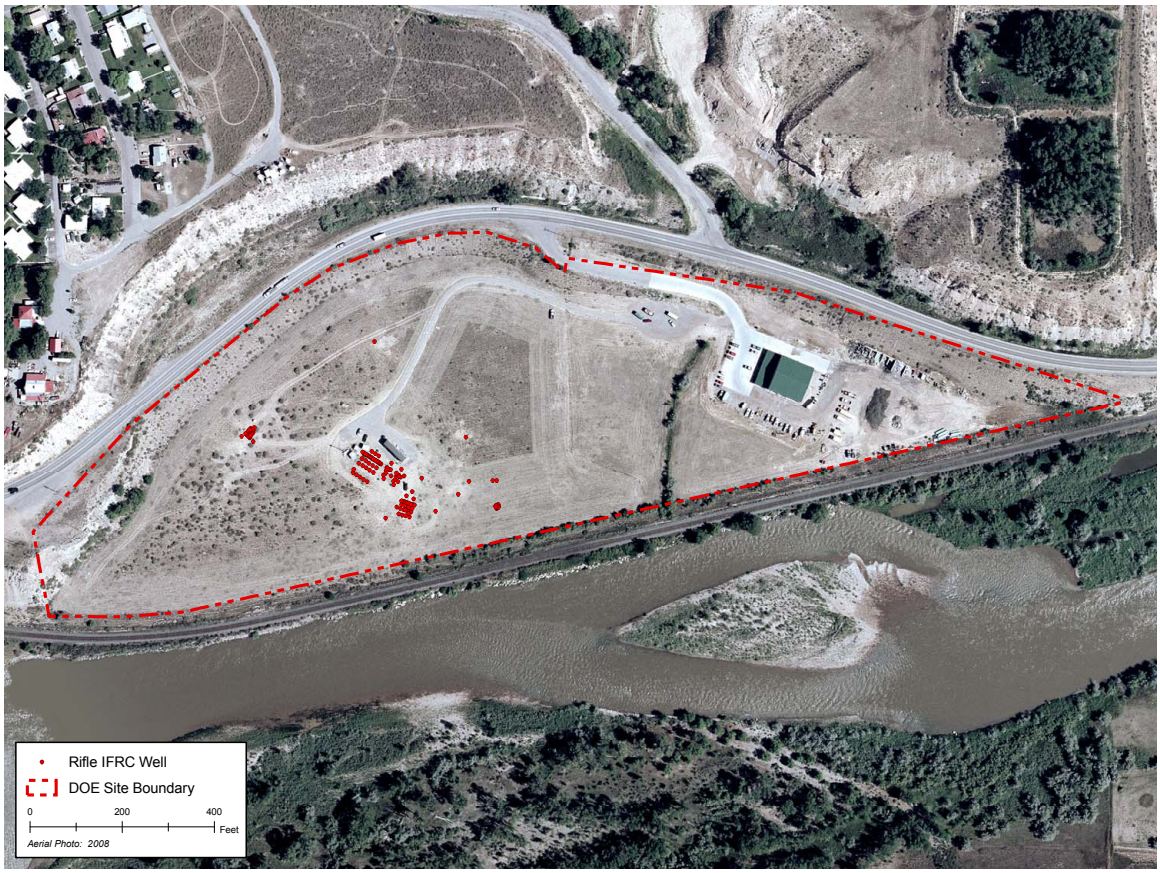


Figure 1.1: Old Rifle field site in Garfield County, Colorado. Red dashed line indicates site boundary, red circles show locations of recently installed wells as part of the IFRC (by permission from DOE, 2011).

1.2.2 Contaminant legacy

The ore processing plant formerly located on the Old Rifle site was originally constructed for vanadium production. The plant operated intermittently from 1924 to 1946 when the facilities were modified to include production of uranium. In 1958 the plant was shut down and ore processing operations moved to a new location. In 1978 the Uranium Mill Tailings Radiation Control Act was passed by congress (Public Law 95-604) and remediation began on the Old Rifle site under the Uranium Mill Tailings Remediation Action (UMTRA) project, which included a maximum groundwater uranium standard of 0.044 mg/L (NRC, 2000). When the DOE became responsible for meeting UMTRA standards at Old Rifle, no buildings remained on the site but the western ~13 acres were still covered by stabilized tailings (DOE, 1999). Surface remediation involved removing and transporting these tailings to a modern storage facility and a 1.5 – 3 m thick cap of fine-grained soil was placed over the remaining alluvium. Four groundwater contaminants of concern following the completion of surface remediation: arsenic, selenium, uranium and vanadium. Concentrations of uranium in recharge waters range from 0.02 – 0.055 mg/L, while concentrations within

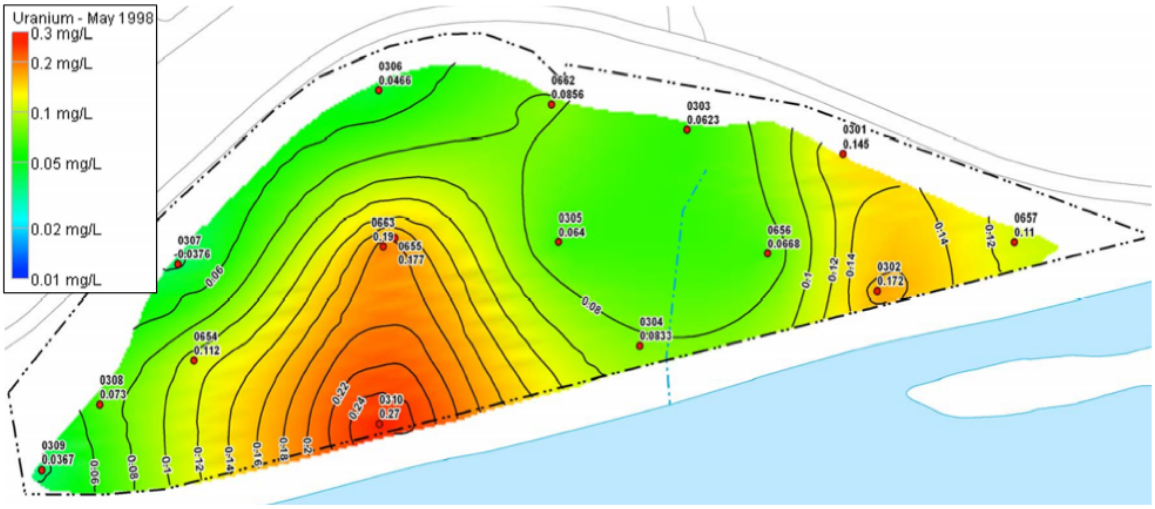


Figure 1.2: Groundwater uranium concentrations collected in May 1998. Red circles indicate individual sample locations and solid lines denote associated contours of uranium concentrations in mg/L (DOE, 2011). Dark blue corresponds to 0.018 mg/L, red corresponds to 0.24 mg/L (by permission from DOE, 2011).

the aquifer approach 0.3 mg/L with substantial temporal fluctuations (Figure 1.2; DOE, 2011).

1.2.3 Remediation strategy

In 1999, following surface remediation, a model of groundwater flow and uranium transport for the Old Rifle site was developed using the USGS codes MODFLOW (McDonald and Harbaugh, 1988) and MT3D (Zheng, 1990). Values of conductivity, dispersivity and partition coefficient for uranium sorption were treated as stochastic parameters in a Monte Carlo framework to predict the time necessary to flush uranium to background concentrations. The simulations unanimously predicted uranium concentrations in the aquifer would return to background conditions within 10 years (DOE, 1999). Based on this analysis, the DOE Office of Legacy Management elected to rely upon natural flushing as the optimal means to reach the 0.044 mg/L UMTRA standard for groundwater uranium concentration (DOE, 2000). Fluid samples collected from monitoring wells between 1996 and 2010 have since shown that uranium concentrations have remained elevated and even increased in some parts of the aquifer. A recent report prepared by the DOE Office of Legacy Management has acknowledged this lack of attenuation and suggests the complex nature of heterogeneous biogeochemistry and permeability, fluctuating water table and recharge sources bearing elevated uranium concentrations all contribute to the persistence of contamination (DOE, 2011). The conclusion is that the ability to predict contaminant mobility is inherently dependant upon the development of more sophisticated modeling capabilities.

1.2.4 The Integrated Field Research Challenge (IFRC)

In 2002 the DOE Office of Science initiated a series of pilot scale uranium bioremediation experiments at the Old Rifle site. The purpose of these initial studies was to demonstrate *in situ* stimulation of native iron reducers to directly reduce uranium as the insoluble mineral uraninite as had been suggested by earlier laboratory experiments (e.g. Lovley et al., 1991). The studies successfully demonstrated decreased U(VI) concentrations through addition of acetate as an electron donor (Anderson et al., 2003). Concurrent with decreased U(VI), acetate addition lead to increased aqueous Fe^{++} and growth of microbial populations predominantly of the iron-reducing family *Geobacteraceae* (Vrionis et al., 2005). However, these conditions were only maintained for the first ~30 days before the system transitioned from iron reduction to sulfate reduction as the dominant TEAP, at which point U(VI) concentrations partially rebounded (Anderson et al., 2003).

In 2006 the Office of Science selected Old Rifle as an Integrated Field Research Challenge (IFRC) site. Under the IFRC, biostimulation experiments at Old Rifle have continued to the present. The general design of the acetate amendment experiments has remained largely unchanged since the initial studies. A series of wells are installed and screened through the saturated zone of the aquifer over an area of roughly 400 m^2 (Figure 1.3). The well gallery consists of several background wells located up-gradient of a row of injection wells oriented perpendicular to the mean flow path. Down-gradient and parallel to the injection wells are several rows of monitoring wells where aqueous samples are collected during acetate amendment. Injectate consists of groundwater pumped into a storage tank, mixed with acetate and bromide salts and held under an N2 headspace. Delivery to injection wells is calibrated to minimize impact to the local hydraulic gradient and to achieve a target acetate concentration specific to each study (Anderson et al., 2003; Williams et al., 2011).

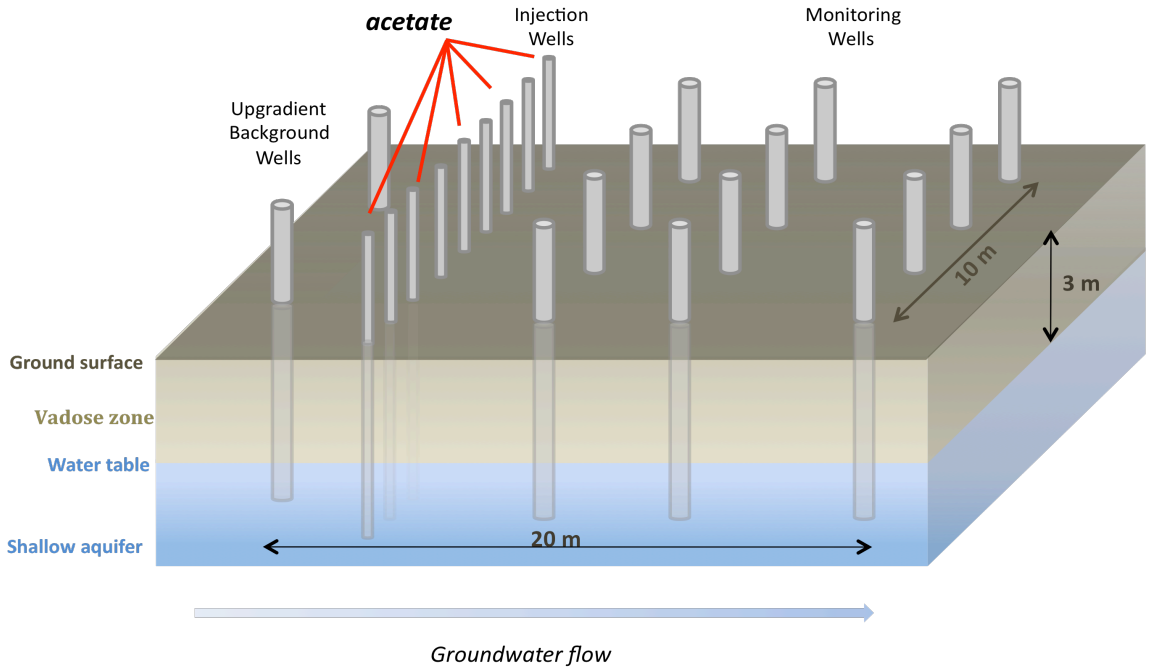


Figure 1.3: Well gallery design for Old Rifle biostimulation experiments

Ten consecutive years of pilot-scale bioremediation studies have resulted in substantial improvements to the conceptual and numerical models of uranium mobility at Old Rifle. It is now recognized that the biostimulation process broadly influences the subsurface system through increase in biomass and production of highly reactive sulfide, Fe^{++} and bicarbonate. These products reduce the permeability of the porous medium (Englert et al., 2009). They also interact with uranium in both beneficial and counterproductive ways. A problematic way involves the generation of bicarbonate ion, which increases alkalinity and causes soluble uranium to become bound in aqueous uranyl-carbonato complexes that are harder for microbes to reduce (Brooks et al., 2003; Dong and Brooks, 2006). An advantageous example is the coupled generation of Fe^{++} and sulfide, which can abiotically reduce uranium (Poulton et al., 2004; Long, 2011). Thus the overall conceptual framework of in situ stimulated uranium bioremediation has developed into an interrelated network of reactivity induced by the addition of acetate (Figure 1.4).

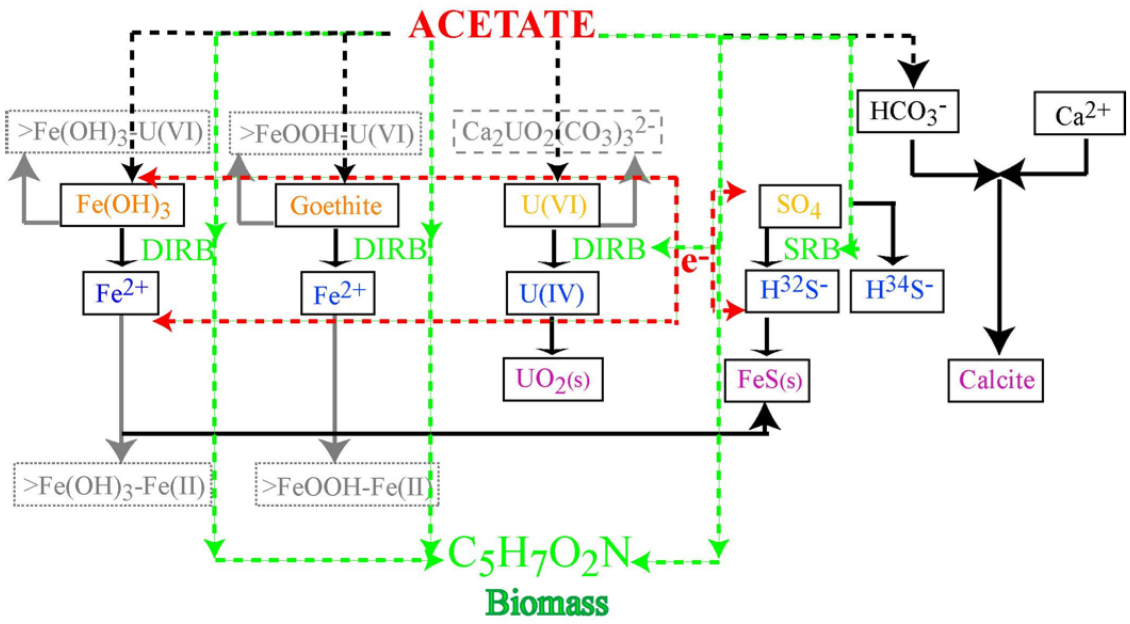


Figure 1.4: Reaction schematic representing important pathways in the biogeochemical response to acetate addition at Old Rifle. Black lines show catabolic (energy producing) pathways, green lines show anabolic (microbial growth) pathways and red lines show abiotic pathways. Species in yellow font are electron acceptors, in blue are the resultant reduced species and in purple are secondary minerals (adapted from the LBNL SFA).

This reaction network (Fig. 1.4) has developed from many years of acetate stimulation studies at Old Rifle and many of the pathways have been identified as a consequence of the inability to simulate observed biogeochemical fluctuations using simpler models. Thus these pathways have been shown to exert non-negligible effects on the in situ bioreduction process and as a result biogeochemical reactive transport models of the system have taken on complexity in order to accurately capture these relationships. For example, Yabusaki et al. (2007) developed a 1D reactive transport model of the original acetate amendment experiment conducted in 2002 using the HYDROGEOCHEM code (Yeh et al. 2004). The 1D model included iron, sulfate and

uranium TEAPS and reproduced most of the trends in dissolved solutes measured in the monitoring gallery, but the authors recognized they had oversimplified the geochemical reaction network. Fang et al. (2009) then extended the Yabusaki et al. (2007) model to include many of the associated abiotic reaction pathways observed during acetate amendment. This updated model did a better job of reproducing variations in pH and solute concentrations and was used for simulations of the 2003 and 2007 field experiments. Based on the Fang et al. (2009) model, Yabusaki et al. (2011) then moved to a 3D domain to capture the effects of physical heterogeneity on the stimulation of iron reducers and corresponding uranium mobility, improving upon the previous simulations of the 2008 experiment. Li et al. (2009) used the CrunchFlow code (Steefel, 2007) and a reaction network similar to Fang et al. (2009) to consider the effect of decreasing permeability and porosity in the aquifer during bioremediation. The model incorporated growth of a solid phase biomass and suggested the majority of permeability change would occur in close proximity to the acetate injection wells. In 2010 Li et al. extended their model to a 2D domain and incorporated a heterogeneous conductivity field, which was further revised (Li et al., 2011) to a systems based approach, quantifying the effects of heterogeneity at a variety of scales on the calculation of uranium reduction rate. This work utilized both forward and inverse modeling components to quantify heterogeneity, including stochastic modeling of inert tracer data (Kowalsky et al., 2011). Despite these substantial developments in multi-component modeling of the bioreduction, to date no published models for the site have incorporated isotopes.

1.2.5 Stable isotope signatures of bioremediation

Kinetic isotope fractionation involves a variation in the abundance of stable, non-radiogenic isotopes accompanying chemical processes that are fast, incomplete or unidirectional. Examples range from diffusive transport to phase changes to metabolic processes, but all originate from the difference in mass between the isotopes of an element. For example, when a microbe reduces a compound, the rate of reduction of the compound containing the lighter isotope is typically slightly faster than that for the heavy isotope because the chemical bonds are slightly easier to break when the mass is smaller. As a result, the heavy isotope is enriched in the residual pool of unreduced compound. Similarly, as a mineral phase precipitates from a solution, the heavy isotope is typically enriched in the solid phase relative to equilibrium partitioning because the bonds are slightly stronger and more favorable in this lower energy state. This partitioning, in combination with the mass balance requirement preserving the total number of each isotope in the system, results in a quantitative relationship between chemical reactivity and isotopic fractionation that can be used to gain further insight into the processes occurring in a kinetically controlled system. In particular this relationship is useful in systems where the concentration of reactive species are highly variable, so that the measured solute chemistry is the product of multiple competing processes, such as the reaction network of acetate addition at Old Rifle. The utility of isotopic signatures to improve mechanistic understanding of bioremediation processes can be broken into four categories: the electron donor source, dominant TEAPs, secondary mineral formations and contaminants. Examples of each of these categories pertinent to Old Rifle are:

1) **Carbon**: electron donor is supplied as an organic carbon (acetate) source. The ability to track the distribution, metabolism and ultimate fate of carbon supplied to the system governs the success of the bioremediation strategy. Chapter 4 presents a carbon budget for amendment at Old Rifle through introduction of a ^{13}C-labeled acetate.
2) **Sulfur**: Fe(III) and sulfate reduction are the dominant TEAPs facilitating acetate metabolism at Old Rifle. The transition from iron reduction to sulfate reduction marks a critical shift in the bioremediation process. However, the variability in background sulfate concentrations and the reactivity of sulfide produced during biogenic reduction compromises our capacity to precisely detect this transition. Chapter 2 presents $\delta^{34}S$ analysis over three years of consecutive acetate amendment at Old Rifle, and chapter 5 presents a mechanistic incorporation of sulfur isotopes into a reactive transport model for the system.
3) **Calcium**: Carbonate precipitation due to increased alkalinity is one of the primary contributors to permeability reduction during bioremediation (Li et al., 2010). Recent developments in conceptual and analytical modeling of calcium isotopes presents a unique means of quantifying this process in a complex and variable system (e.g. DePaolo, 2011; Turchyn and DePaolo, 2011). Chapter 3 describes incorporation of calcium isotope fractionation into a reactive transport model. Chapter 6 presents extension of the reactive transport model to identify the relative contributions of precipitation and ion exchange to measured fluid $\delta^{44}Ca$.
4) **Uranium**: Recent improvements in analytical precision have lead to exploration of isotopic variations in heavy metals as a result of biogenic activity. At the Old Rifle site a pilot study of uranium fractionation demonstrated a roughly 1‰ shift in the $^{238}U/^{235}U$ ratio concurrent with decreasing concentration during iron reduction (Bopp et al., 2010). While direct biogenic fractionations of contaminant species are beyond the scope of the current thesis, the computational methods for modeling stable isotope fractionation generated here have direct application to analysis of U-isotope datasets.

The individual isotope systems in this list provide examples of fractionations associated with electron donors, TEAPs, secondary mineralization and contaminants chosen specifically for their relevance to the Old Rifle system. It is important to note that there are multiple isotope systems in addition to those described above relevant to each of the four categories. For example, fractionation of iron isotopes may be applied to the study of TEAPs in systems where the oxidized and reduced Fe species occur in separate phases and magnesium isotopes may provide additional constraints on the precipitation of carbonate.

1.3 Modeling Isotope Fractionation

Analytical models incorporating isotopes have been utilized for a variety of conditions to identify sources, transport and reactivity in near-surface environments. Examples include characterization of flow paths (Johnson and DePaolo, 1994; Johnson et

al., 2000; DePaolo, 2006), vadose zone recharge (Maher et al., 2003; DePaolo et al., 2004; Singleton et al., 2006), fluid-mineral exchange rates (Richter and DePaolo, 1987; DePaolo and Getty, 1996; Johnson and DePaolo, 1997a,b), sediment transport rates (DePaolo et al., 2006); and groundwater residence time (Johnson and DePaolo, 1996). While these models accurately reproduce the measured trends in isotope ratios of natural systems, simplifying assumptions limiting flow and reactivity to a few basic components are required. As computing power has grown, treatment of complex hydrogeochemical systems such as stimulated subsurface heavy-metal bioremediaton has developed into reactive transport models coupling hydrology, chemistry and biology as a means of improved integration and analysis (Steefel et al., 2005). Multi-component reactive transport models such as HYDROGEOCHEM (Yeh et al. 2004), TOUGHREACT (Xu, et al., 2004) and CrunchFlow (Steefel, 2007) integrate hydrologic transport, aqueous and surface complexation, dissolution/precipitation and microbially mediated redox reactions into a comprehensive network of kinetic and equilibrium pathways. Incorporation of isotopic ratios into such multi-component models has been demonstrated in analysis of vadose zone infiltration rates from temperature dependent equilibrium fractionation of water isotopes (Singleton et al., 2004), plagioclase dissolution from uranium-series isotopes (Maher et al., 2006) and recently the influence of hydrologic transport on measured isotope fractionation in compound-specific stable isotope analysis (Rolle et al., 2010).

Thus far, examples of kinetic stable isotope fractionations directly calculated in multi-component reactive transport models are scarce. van Breukelen et al. (2004) modeled a landfill leachate plume using PHREEQC-2 (Parkhurst and Appelo, 1999) including explicit ^{12}C and ^{13}C species. The simulation included fixed fractionation factors for first-order anaerobic methane oxidation, precipitation of carbonate minerals (tracking fluid phase only) and CO_2 degassing, but did not include isotopic variation due to microbial degredation of organic carbon. Carbon isotope fractionation due to biodegredation was addressed by van Breukelen and Prommer (2008) in a system restricted to first order behavior. A recent study modeled the individual isotopologues of sulfur during microbial sulfate reduction within the MIN3P code (Gibson et al., 2011) but the model was again restricted to first-order behavior despite the use of a Monod rate law.

1.3.1 Comment on incorporation of isotopes into reactive transport codes

For a reaction involving two isotopologues of a given species, a simple first order kinetic reaction may be written for each isotope such that the reactions are uncoupled:

$$N \xrightarrow{k} P \tag{1.1a}$$

$$N^* \xrightarrow{k^*} P^* \tag{1.1b}$$

where N (N*) is the number of atoms or moles of the common (rare) reactant isotopologue, P (P*) is the number of atoms or moles of the common (rare) product isotopologue and k (k*) is the reaction rate constant of the common (rare) isotopologue. The rate of these reactions may be written as a change in concentration per unit time

$$R = \frac{dN}{dt} = -\frac{dP}{dt} = -kN \tag{1.2a}$$

and

$$R^* = \frac{dN^*}{dt} = -\frac{dP^*}{dt} = -k^* N^* \tag{1.2b}$$

where R (R*) is the rate of reaction for the common (rare) isotope. The ratio of N*/N at any given time in the progress of the reaction is the cumulative isotope ratio of the reactant (Fig. 1.5). Similarly the ratio P*/P is the cumulative isotopic ratio of the product. As the reaction progresses, the cumulative isotope ratio of the residual reactant becomes exponentially enriched, and thus the instantaneous isotopic ratio of the product, dP*/dP, tracks this exponential enrichment. As a result, in the limit where all reactant is consumed, mass balance is achieved as the cumulative product isotopic ratio reaches the starting value of the reactant.

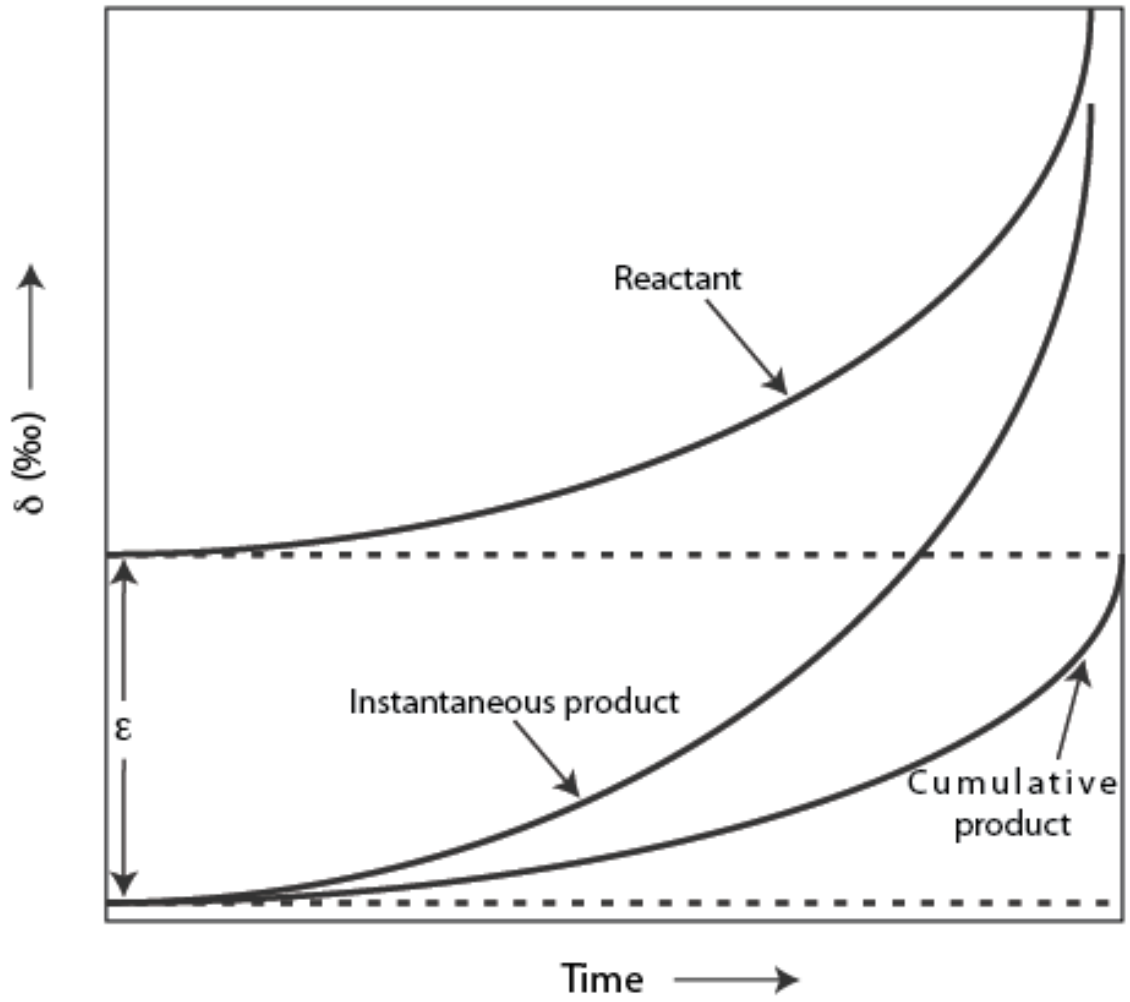


Figure 1.5: Kinetic isotope fractionation in a closed, homogeneous system. ε refers to the fractionation factor in delta notation.

The kinetic fractionation factor (α) is defined at the ratio of the instantaneous product species over the ratio of the cumulative reactant species (Mariotti et al., 1981):

$$\alpha = \frac{dP^* / dP}{N^* / N} = \frac{-k^* N^* / -kN}{N^* / N} = k^* / k \tag{1.3}$$

Typically eq. 1.1 and 1.2 are related through the fractionation factor and then integrated to obtain the Rayleigh equation for first order, homogeneous fractionation (Criss, 1999).

$$\frac{N^*}{N} = \left(\frac{N^*}{N}\right)_0 f^{(\alpha-1)} \tag{1.4}$$

Here $(N^*/N)_0$ is the initial isotopic ratio at the start of the reaction and f is the fraction of reactant remaining.

There are many common examples of fractionating reactions that do not accommodate the simplifying assumptions necessary to apply the Rayleigh equation (e.g. Brandes and Devol, 1997; Clark and Johnson, 2008; van Breukelen, 2007; Berna et al., 2010). The limitations of such a distillation model may be circumvented by directly incorporating the individual rates of reaction for the isotopologues as unique 'species' in a multi-component reactive transport framework. Such a mechanistic treatment of isotope fractionation is desired because it allows any process of transport or reactivity influencing a given species to inherently influence its isotopic ratio. Isotopic fractionation is then no longer removed from the reactive transport framework as a secondary calculation, but fully integrated within the dynamic system. However, the relationship between the individual isotopic 'species' and the reactivity of the bulk species must be carefully considered. The amount of the individual isotopologues must sum to the total amount of the species, where the subscript T indicates the total species.

$$N_T = N + N^* \tag{1.5}$$

Similarly the rate of reaction (i.e. moles per unit time) of each isotopologue must sum to the rate of the total species.

$$R_T = R + R^* \tag{1.6}$$

Following the example above of a first order rate law, the total reaction rate of the species is then the sum of the product of each rate constant and each isotope.

$$R_T = -k_T N_T = -kN + -k^* N^* \tag{1.7}$$

and the ratio of the net rates is then equivalent to the product of the fractionation factor (eq. 1.3) and the ratio of the concentrations of the individual isotopes.

$$\frac{R^*}{R} = \frac{k^* N^*}{kN} = \alpha \frac{N^*}{N} \tag{1.8}$$

Based on this formula, when α is unity (i.e. no fractionation), the ratio of the net rates is equivalent to the ratio of the concentrations, thus preserving the initial isotopic composition throughout the reaction. Combining equations 1.5 and 1.7 results in the following relationship of rate constants for a first order reaction:

$$k_T = \frac{kN + k^* N^*}{N + N^*} \tag{1.9}$$

It is worthwhile to note here that neither of the values of k for the individual isotopes can equal the total rate constant (k_T) without the relationship reducing to $\alpha = 1$. The total rate constant of the bulk species is then closely bounded by the individual isotopic rate constants and is calculated as their concentration-weighted average. Within a multi-component reactive transport framework, problems arise when the nature of the reaction rate laws impose differences in the rates of the individual isotopologue 'species' in addition to this relationship. For example, a heterogeneous reaction in which a species

precipitates out of solution requires a reactive surface area that has to be specified for each isotope and related through a solid solution. Demonstration of a variety of such issues and methods of addressing them will be presented in the following chapters. In this sense there are two primary purposes of the present work (1) to utilize stable isotope fractionations as a means of analyzing carbon delivery, biogenic redox and secondary mineral precipitation during subsurface uranium bioremediaton and (2) to demonstrate the techniques and utility of incorporating kinetic isotope fractionation as a mechanistic component of a biogeochemical reactive transport model.

Chapter 2

Sulfur isotope fractionation in multiple *in situ* uranium bioremediation experiments

2.1 Overview

This chapter presents an example of how biogenic sulfur isotope fractionation can be used to infer subsurface processes. Analysis of $\delta^{34}S$ in biogeochemistry is a well-established method. Here the technique is applied to analysis of sulfate reduction over three consecutive years of acetate amendment in a single well gallery at the Old Rifle field site. Results indicate previously undocumented hysteretic effects in the spatial and temporal dynamics of microbially-mediated sulfate reduction.

2.2 Introduction

At the Rifle Integrated Field Research Challenge (IFRC) site in western Colorado, USA, biogenic reduction of soluble uranium U(VI) in groundwater as insoluble U(IV) has been successfully achieved through injection of acetate as an organic carbon electron donor (Anderson et al., 2003; Holmes et al., 2005; Vrionis et al., 2005; Williams et al., 2011). Addition of acetate at a target concentration of 5-15 mM rapidly induces reduction of bioavailable iron oxides (eq. 2.1). This Fe(III) reduction phase is associated with a substantial decline in aqueous U(VI) concentrations attributed to dissimilatory iron reducing bacteria (DIRB), predominantly by members of the *Geobacteraceae* (Lovley et al., 1991; Lovley, 1995; Wilkins et al., 2006). This period of Fe(III) reduction has been observed for up to roughly 30 days before sulfate reducing bacteria (SRB) become active (eq. 2.2) with sulfate reduction overtaking Fe(III) reduction as the dominant terminal electron accepting process (TEAP).

$$\frac{1}{8}CH_3COO^- + Fe(OH)_3 \rightarrow \frac{1}{4}HCO_3^- + Fe^{2+} \quad (2.1)$$

$$CH_3COO^- + SO_4^{2-} \rightarrow 2HCO_3^- + HS^- \quad (2.2)$$

The onset of sulfate reduction marks a critical juncture in the bioremediation process because this transition is associated with a partial rebound in aqueous uranium concentration. As shown in eq. 2.2, SRB require a 1:1 molar ratio of acetate oxidation to sulfate reduction, resulting in rapid depletion of the electron donor source. As a result the activity of SRB restricts the availability of acetate for DIRB capable of U(VI) reduction (eq. 2.1) and simultaneously generates a large rise in bicarbonate alkalinity (eq. 2.2). This combination of effects is thought to give rise to the observed partial rebound in aqueous U(VI) concentrations associated with the onset of SRB activity (Williams et al., 2011; Davis et al., 2004). Therefore optimizing the electron donor strategy to maximize the amount of uranium removed from solution requires a precise understanding of the timing of sulfate reduction and the mechanisms governing this transition.

The term metabolic lag is used to describe an observed delay between the time when nutrients become available and the associated microbial activity begins. While the onset of SRB metabolism is of principal importance to the uranium bioremediation strategy, the factors governing this metabolic lag between electron donor addition and SRB activity are still speculative. This lag was originally believed to derive from suppression of SRB activity due to competition for the electron donor until exhaustion of a pool of high surface area and/or poorly crystalline Fe(III) oxides resulted in decreased DIRB activity (Anderson et al., 2003; Holmes et al., 2005). However as advances in proteomics, compound specific stable isotope analysis, and gene expression have developed in application to the Rifle experiments, a growing body of evidence suggests that Fe(III) minerals remain abundant throughout the acetate amendment, and DIRB continue to metabolize acetate during SRB activity provided excess electron donor is available (Williams et al., 2011; Kerkhof et al., 2011; Callister et al., 2010) . Thus while depletion of a bioavailable pool of Fe(III) may still contribute to the dynamic relationship between DIRB and SRB, it is equally likely that initial SRB growth rates at Rifle are intrinsically slower than those for *Geobacter*. The relative contribution of these factors requires further laboratory investigation.

Despite the aforementioned developments in our conceptual understanding of TEAP succession at Rifle, field scale biogeochemical models of the site have predominantly relied upon inhibition of SRB activity using a bioavailable Fe(III) mineral phase (Yabusaki et al., 2007; Fang et al., 2009; Li et al., 2009; 2010). While some of these models do allow for simultaneous DIRB and SRB metabolism once this threshold-inhibiting mineral has been consumed, they still impose what may be an unsubstantiated relationship between Fe(III) mineral bioavailability and the onset of SRB metabolism. The most recent biogeochemical reactive transport model of field scale acetate amendment at Rifle improves upon the inhibition technique by incorporating a small, active population of SRB from the start of acetate addition in conjunction with a microbial decay term serving to slow initial growth rates (Yabusaki et al., 2011). The incorporation of active SRB throughout the acetate amendment marks an important development in the conceptual model of biogeochemistry during Rifle U(VI) reduction, however this approach has only been presented as a model for field experiments in which previous biostimulation has already occurred. In order to contribute to the development of this novel technique in modeling field scale SRB activity, we present stable isotope fractionation of sulfur as a means to further constrain the in situ balance between initial population, growth and decay factoring into the overall rate of SRB growth, and we put

forth a similarly revised approach to modeling SRB populations over multiple years of acetate amendment.

Timing the onset of sulfate reduction at the field site is difficult, due to the background variability and non-conservative behavior of the reactant and product species. Between the spring of 2002 and fall of 2003, background sulfate concentrations at Rifle averaged 9.7 mM with large spatial and temporal variations (Figure 2.1; Appendix A, Table A1). The combined result of these variations yields a 2σ standard deviation of 2.0 mM for background aqueous sulfate concentrations. Quantitative detection of the onset of SRB activity therefore requires a ca. 20% drop from the average background sulfate concentration, resulting in an overestimation of the delay between acetate addition and sulfate reduction. Pinpointing the onset of SRB activity by detecting the production of aqueous sulfide is equally problematic because of multiple reactive pathways. Sulfide readily precipitates with aqueous Fe^{++} generated from iron reduction (eq. 2.3) and also directly reduces iron oxides, forming elemental sulfur and Fe^{++} (eq. 2.4).

$$Fe(II) + HS^- \rightarrow FeS_{(am)} + H^+ \tag{2.3}$$

$$2FeOOH + HS^- + 5H^+ \rightarrow 2Fe^{2+} + S_0 + 4H_2O \tag{2.4}$$

The combination of reactant variability and product titration effects can cause a substantial delay in the detection of SRB activity in down gradient monitoring wells.

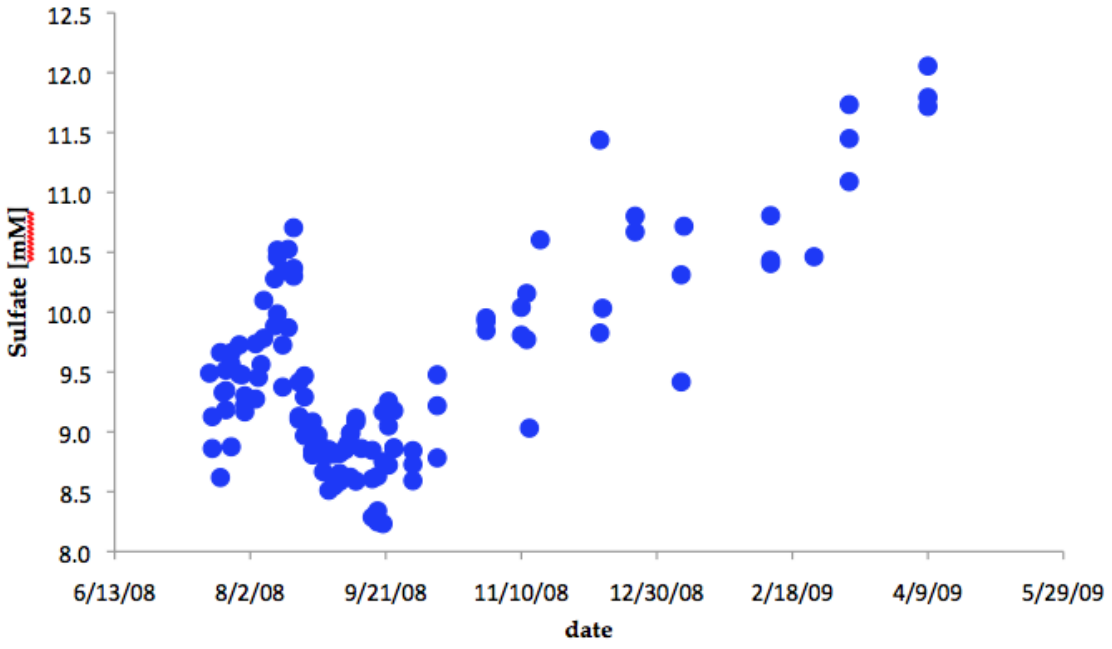


Figure 2.1: Background sulfate concentrations over the period spanning July 2008 to May 2009 in the Old Rifle aquifer. This pronounced background variability leads to substantial error in timing the onset of sulfate reduction during acetate addition.

Here we test the use of shifts in stable isotope compositions of sulfur as a means of circumventing the variability in concentration data to achieve a more precise estimate of the metabolic lag associated with the onset of SRB metabolism. Bacterially-mediated

sulfate reduction strongly favors sulfate molecules containing the lighter isotope of sulfur (^{32}S) causing the residual sulfate pool to become enriched in the heavier isotope (^{34}S) (Canfield, 2001). The characteristic enrichment in $\delta^{34}S$ of sulfate is commonly used to detect SRB activity in subsurface systems (e.g. Massmann et al., 2003; Knoller et al., 2008). During acetate amendment at the Old Rifle site, enrichment of 10-20‰ in $\delta^{34}S$ has previously been measured in association with SRB activity (Druhan et al., 2008). The referenced study reported a background $\delta^{34}S$ sulfate value of -8.1‰ with a 2σ standard deviation of 0.2‰ for 35 consecutive days of sample collection and suggested the sensitivity of the $\delta^{34}S$ sulfate shift associated with SRB could provide a more precise method of detecting the onset of sulfate reduction. Here we present application of this method to 3 years of consecutive bioremediation experiments within a discrete portion of the aquifer at the Rifle site. With these data we can quantify variations in the metabolic lag period over the course of multiple amendments. The ability to precisely measure this delay leads to the development of a new biogeochemical reactive transport model where the timing of SRB is directly controlled by a lag time parameter based on $\delta^{34}S$ sulfate data.

2.3 Methods

Samples were collected for sulfur stable isotope analysis during three consecutive acetate biostimulation experiments in a single well gallery at the Rifle site (Figure 2.2). The experiments took place during the summers of 2007, 2008 and 2009. Experimental design and results for the 2007 and 2008 field experiments are detailed in Williams et al. (2011). Briefly, acetate addition was made through a row of injection wells installed perpendicular to mean hydraulic gradient. Three rows of monitoring wells were installed parallel to the injection gallery at distances of 2.5, 5 and 9 m down gradient. Groundwater was pumped from the aquifer into a storage tank where it was mixed with sodium acetate and sodium bromide and kept under an N_2 headspace. This solution was delivered through the injection wells at a calibrated rate to minimize alteration of the local hydraulic gradients. In 2007 acetate was delivered at a target aquifer concentration of 5 mM for 31 days with a pause at days 12-18 to refill the tank. A target of 5 mM acetate was delivered for the first 15 consecutive days of the 2008 experiment, and for 36 consecutive days in the 2009 experiment.

Sampling and measurement methods for sulfate, sulfide, acetate and Fe^{++} concentrations are described in Williams et al. (2011). Samples for sulfur isotopes were pumped from one background well and at least one downgradient monitoring well for each of the three consecutive years of acetate amendment. Groundwater was immediately filtered through a 0.2 mm Stericup® vacuum filtration system (Millipore Co.) into vials containing a $BaCl_2$ solution in excess of background sulfate to precipitate $BaSO_4$. Samples were then shipped to the Lawrence Berkeley National Laboratory where they were filtered, rinsed and dried in preparation for isotopic analysis. The $\delta^{34}S$ measurements were performed following established methods (Giesemann et al., 1994) using a Eurovector model 3028 elemental analyzer in helium continuous flow mode interfaced with a GV Isoprime isotope ratio mass spectrometer at the University of

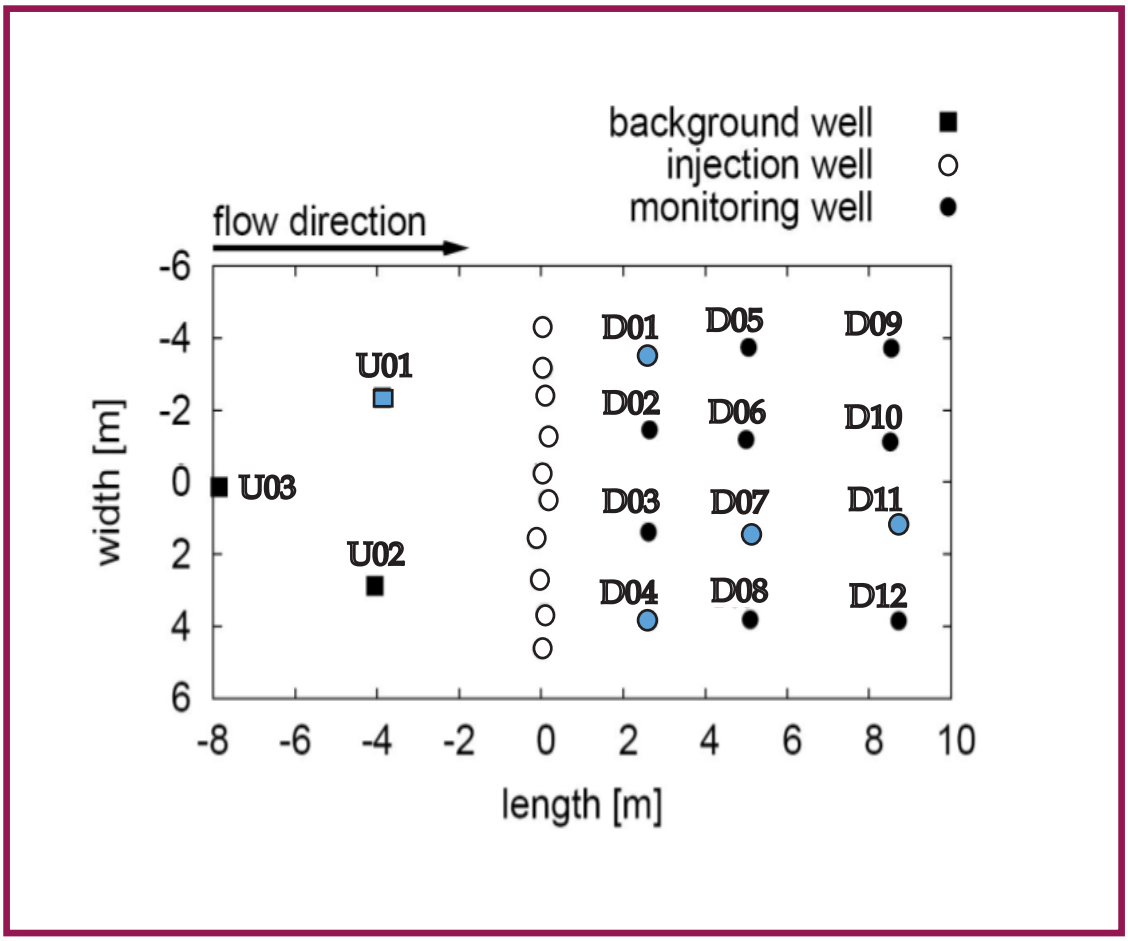


Figure 2.2: Well gallery schematic for 2007 – 2009 Rifle IFRC field experiments. Geochemical and stable isotope data reported for those wells marked in blue.

California Berkeley, Laboratory for Environmental and Sedimentary Isotope Geochemistry. Long-term internal precision for the instrument is ±0.15‰. V_2O_5 was added to the $BaSO_4$ samples during loading as a combustion aid, yielding improvements on the reported precision. Sulfur isotope ratios are reported in standard delta notation (eq. 2.5)

$$\delta^{34}S = \left(\left(\frac{R_{sample}}{R_{std}}\right) - 1\right) \times 1000 \qquad (2.5)$$

where $R = {}^{34}S/{}^{32}S$ and the value is reported in per mil (‰) units relative to the Canyon Diablo Troilite standard ($R_{std} = 0.0441216$).

2.4 Results and discussion

2.4.1 Aqueous concentrations and $\delta^{34}S$

Table 2.1 lists the mean and 2σ standard deviation of sulfate concentration and $\delta^{34}S$ of sulfate in background well U01 for the range of dates covering each annual acetate amendment experiment. Sulfate concentrations vary about each mean by a 2σ standard deviation of roughly 1.0mM for all three years, while $\delta^{34}S$ values vary from the precision limit of the measurement to as much as 0.42. Of note are large shifts in the value of the mean between years for both sulfate and $\delta^{34}S$, well beyond the range of 2σ standard deviations. This inter-annual variation suggests multiple sulfate sources

year	SO_4 (mM)	2σ SD	n	dates	$\delta^{34}S$ (‰)	2σ SD	n	dates
2007	10.9	1.0	11	Aug 10 – Sep 18	-8.56	0.14	3	Aug 10 – Sep 14
2008	9.2	1.1	31	Jul 19 – Sep 24	-8.78	0.21	5	Jul 31 – Oct 1
2009	9.2	1.0	22	Jul 8 – Sep 28	-7.69	0.42	11	Jul 22 – Sep 29

Table 2.1: Background sulfate and $\delta^{34}S$ values from well U01 for the three consecutive years of acetate amendment. Shown are the mean and 2σ standard deviations for sulfate and $\delta^{34}S$ as well as the number of measurements contributing to each value (n) and the range of dates over which the samples were collected (dates).

contributing to the groundwater composition of the aquifer and highlights the necessity of monitoring background conditions during each amendment experiment. While beyond the scope of the current study, this finding suggests that expanding sulfur concentration and stable isotope analysis to samples across the regional aquifer system could yield valuable insight into the origin of groundwater and solutes governing the bioremediation process. The values reported in Table 2.1 define the range considered background in analyzing all subsequent data.

For the 2007 amendment, time series of Fe^{++}, sulfate, sulfide and $\delta^{34}S$ of sulfate are shown for well D04 in the first row and D07 in the second row of monitoring wells, 2.5 and 5 meters down gradient of the injection wells, respectively (Figure 2.3). Fe^{++} increased from a starting value of roughly 20-30 mM to a peak of 57 mM in well D04 18 days after the start of acetate injection, and 136 mM in well D07 21 days after the start of acetate addition (Figure 2.3A-B). These data indicate the onset of Fe^{++} reduction, detectable as an increase in Fe^{++} 2 days after the start of acetate addition at 2.5 meters down gradient, and 4 days later at 5 meters down gradient. The increased magnitude and time to peak concentration between rows is attributed to increased travel time and reaction progress with distance from the input source. Sulfate concentrations were first measured to be below the 2σ standard deviation background range in both wells on day 35, however in D04 the concentration quickly returned to background range, while in

D07 it continued to drop to a minimum of 6.1 mM on day 42. Sulfide is highly reactive in the system and easily oxidized during sampling, leading to the potential for error in measured sulfide concentrations relative to that of the $\delta^{34}S$ of sulfate. Despite this distinction, the trends in increasing sulfide and enriched $\delta^{34}S$ of sulfate in both wells track closely throughout the amendment experiment (Figure 2.3C-D) and indicate the onset of SRB metabolism by day 20 of acetate addition.

The 2008 acetate injection scheme was more complex than that of 2007, involving an increase in target acetate concentration from 5 to 15 mM during the course of the experiment (Williams et al., 2011). For the first 15 days, acetate was delivered at a target of 5 mM, thus allowing direct comparison to the 2007 experiment at early time. From days 15–24, acetate delivery ceased, before resuming at 5 mM from days 24-38 and finally increasing to 15 mM from days 38-110. Concentrations of sulfate and sulfide as well as $\delta^{34}S$ of sulfate are shown for the 2008 injection in well D04 at 2.5 m down gradient, D07 at 5 meters down gradient and D11 at 9 m down gradient (Figure 2.4).

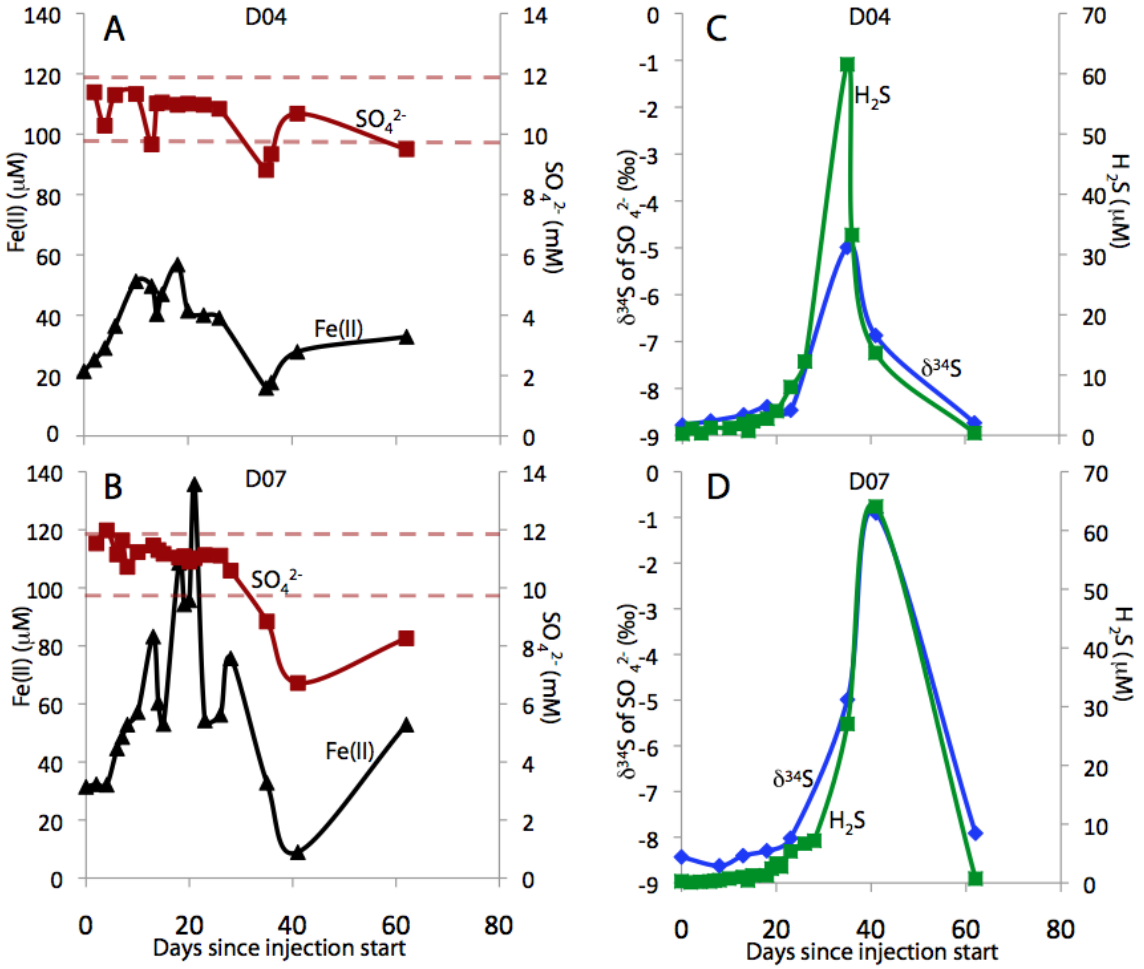


Figure 2.3: (A) Time series of Fe(II) and sulfate concentrations for well D04, dashed lines denote 2σ standard deviations in background sulfate concentrations measured up-gradient of the injection well gallery during the 2007 amendment; (B) for well D07. (C) Time series of $\delta^{34}S$ of sulfate and sulfide concentrations for well D04; (D) for well D07. All times are noted as days relative to the start of acetate addition to the injection wells.

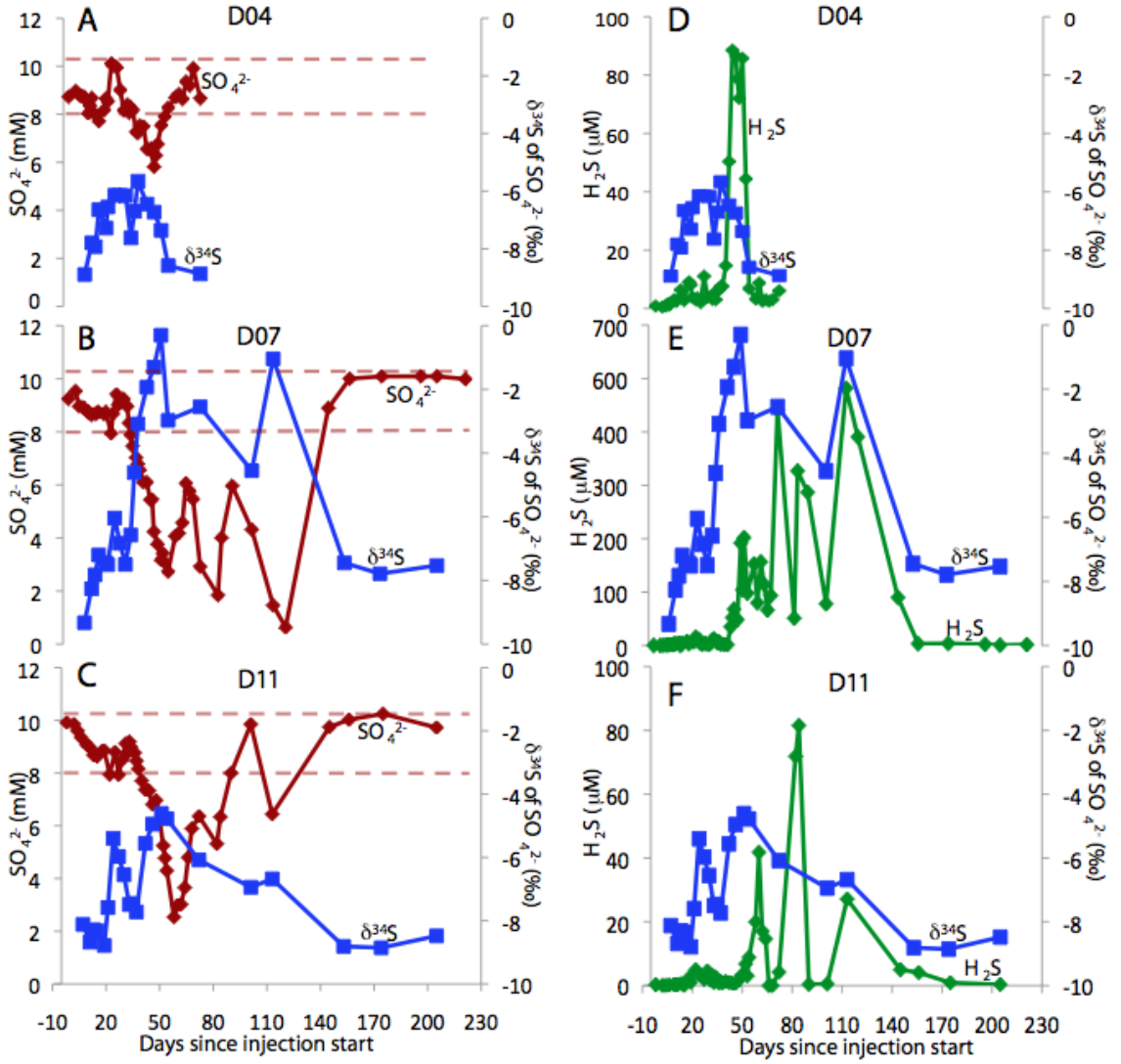


Figure 2.4: (A) Sulfate concentrations and $\delta^{34}S$ of sulfate for well D04, dashed lines denote 2σ standard deviation in background sulfate concentrations measured up-gradient of the injection well gallery during the 2008 amendment; (B) for well D07; (C) for well D11. (D) Sulfide concentrations and $\delta^{34}S$ of sulfate for well D04; (E) for well D07; (F) for well D11. All times are noted as days relative to the start of acetate addition to the injection wells.

Sulfate concentrations in well D04 fell slightly below 2σ background variation on day 15, but rebounded until day 29, when they dropped systematically to a minimum of 5.8 mM (Figure 2.4A). Sulfate concentrations dropped below background range on day 33 in D07 (Figure 2.4B) and day 40 in D11 (Figure 2.4C). Elevated sulfide concentrations were delayed compared to the 2007 injection, showing a systematic increase beginning on day 36 in D04 (Figure 2.4D), day 44 in D07 (Figure 2.4E) and day 48 in D11 (Figure 2.4F). In contrast, sulfate $\delta^{34}S$ enrichment occurred substantially earlier than variations in both sulfate and sulfide, indicating the onset of SRB activity by day 11 in the first and second row of injection wells, and by day 21 in the third.

The 2009 injection was conducted at a target acetate concentration of 5 mM, making the chemical dataset directly comparable to 2007 and the start of 2008. Shown are the sulfate and sulfide concentrations and $\delta^{34}S$ of sulfate for well D01 in the first row (2.5 m) down gradient of the injection gallery (Figure 2.5). A lower sampling frequency resulted in a coarser time series for this experiment, however in well D01, the sulfate data show a drop below the 2σ standard deviation by day 10 (Figure 2.5A) and an increase in sulfide by day 20 (Figure 2.5B). Again the enrichment in $\delta^{34}S$ of sulfate provided the earliest indication of the onset of SRB, showing an increase of 1.3‰ by day 4.

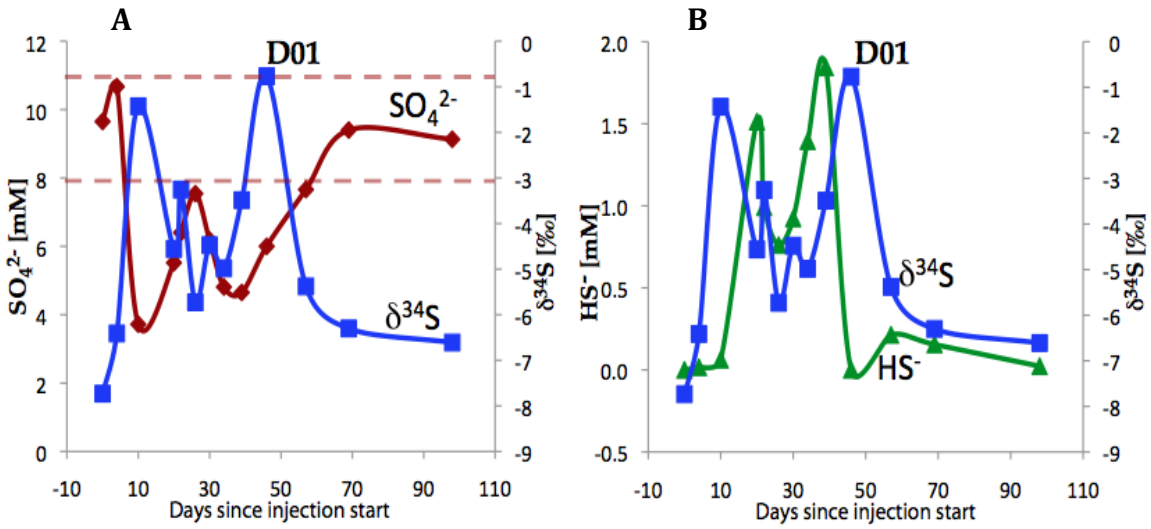


Figure 2.5: (A) Sulfate concentrations and $\delta^{34}S$ of sulfate for well D01, dashed lines denote 2σ standard deviation in background sulfate concentrations measured up-gradient of the injection gallery during the 2009 amendment. (B) Sulfide concentrations and $\delta^{34}S$ of sulfate for well D01. All times are noted as days relative to the start of acetate addition to the injection wells.

2.4.2 Timing the onset of sulfate reduction

To quantify the timing of acetate arrival and the start of DIRB and SRB activity we focus on data collected from the first row of monitoring wells (2.5 m down gradient) where the earliest indication of these transitions are observed. For acetate arrival, the time is determined by the first non-zero measurement reported. For DIRB activity, the time is based on the first measurement of Fe^{++} concentration recorded in a systematically increasing trend. For the start of SRB activity, three methods of timing are considered: (1) the first measured value of sulfate below the 2σ standard deviation of background values in a systematic trend of decreasing concentrations, (2) the first elevated sulfide value measured above non-detect in a systematically increasing trend, and (3) the first $\delta^{34}S$ of sulfate value enriched above the background value in a systematically increasing trend. Based on these criteria, timing for the three consecutive years of acetate addition in the common well gallery is shown (Figure 2.6) and all data used to determine these times are provided (Appendix A, Table A2).

There are two important results. First, in all three years a decrease in sulfate concentration is either undetected or delayed relative to enriched $\delta^{34}S$ sulfate, likely as a

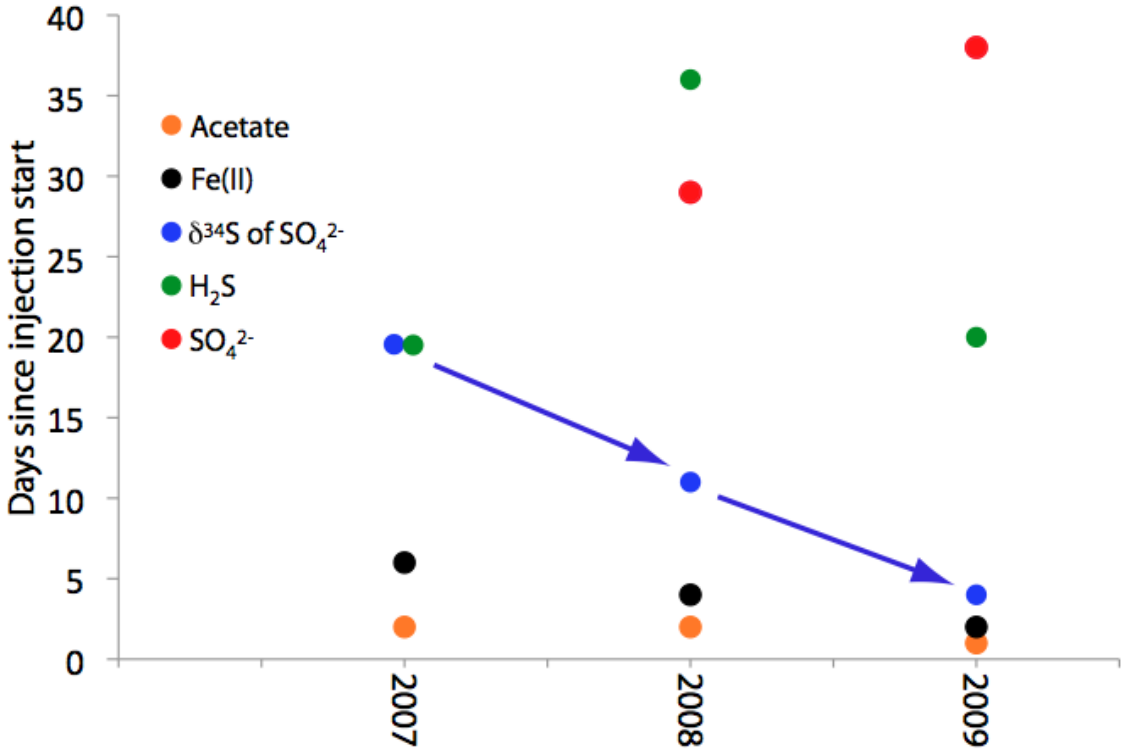


Figure 2.6: For wells in the first row down-gradient of the injection gallery (D04 and D01), number of days since the start of each acetate addition taken to measure arrival of acetate and the start of DIRB activity (based on elevated Fe^{++} concentrations) and SRB activity (based on (1) systematic drop in sulfate below 2σ standard deviation in background concentrations, (2) systematic increase in sulfide concentrations and (3) systematic enrichment in $\delta^{34}S$ of sulfate) for each of the three consecutive years of acetate amendment. For the 2007 amendment, sulfate concentrations dropped below 2σ standard deviation on day 35, but failed to continue decreasing in a systematic trend.

combined result of large background variability and periodic pauses in acetate delivery. In contrast, addition of electron donor to a previously unamended aquifer results in simultaneous detection of increased sulfide and enriched $\delta^{34}S$ sulfate in down gradient monitoring wells, while in subsequent years the sulfide signal is substantially retarded relative to isotopic enrichment. If the SRB activity generating sulfide and fractionating $\delta^{34}S$ were located up gradient, close to the injection well, we would anticipate retardation of the increased sulfide concentration relative to the enrichment of $\delta^{34}S$ sulfate due to the pathways described in eq. 3 and 4. The lack of such retardation then suggests that either (1) there are insufficient available Fe phases capable of reacting with aqueous sulfide along the flow path between the injection and monitoring wells or (2) the distribution of initial SRB activity is not spatially biased in the first year of augmentation. The former argument is contradicted by evidence for ample Fe(III) oxide phases present even after multiple acetate augmentations (Williams et al., 2011). Furthermore, arrival of acetate in the first row of down gradient monitoring wells occurred within 3 days of injection in all three experiments (Figure 2.6), and thus in the first year 17 days passed during which time acetate was available across the entire distance between the injection and monitoring

wells before SRB activity began. Under such conditions in a formerly unamended aquifer there is no *a priori* expectation that SRB should initially predominate near the injection wells. Therefore it is likely that the latter explanation holds for the 2007 experiment and SRB activity first detected in the monitoring wells originated from populations proximal to those wells. In contrast, during subsequent electron donor experiments the onset of increased sulfide concentrations becomes retarded relative to the observed enrichment in sulfate $\delta^{34}S$. This observation indicates that over multiple amendments and longer time periods the SRB populations closest to the point of electron donor injection are first to become active, resulting in retardation of elevated sulfide concentrations as a result of reactive transport over the distance between the injection and monitoring well.

Second, enrichment in residual sulfate $\delta^{34}S$ illustrates a previously undocumented trend towards earlier onset of SRB activity over subsequent electron donor amendments. In 2007, $\delta^{34}S$ enrichment was first noted on day 20, while in 2008 it was observed by day 11 and in 2009 by day 4. Although variability in sulfate and reactivity of sulfide have previously obscured the trend toward earlier SRB activity, our observation agrees with a similar trend in Fe^{++} concentrations over multiple years of acetate addition and suggests that both iron and sulfate reducers are being primed as a result of prior amendments. The nature of this priming requires further investigation, particularly in terms of its effect on uranium mobility and sequestration. Here we show the utility of $\delta^{34}S$ sulfate shifts as a novel means of quantifying low-level SRB activity, particularly in conjunction with newly developed proteomics methods (Callister et al., 2010). Furthermore, the observation of SRB activity as early as 11 days after the start of acetate addition in the 2008 experiment agrees with gene expression studies indicating active *Geobacter* strains during SRB activity (Williams et al., 2011) and supports both the current biogeochemical reactive transport model of the 2008 experiment (Yabusaki et al., 2011) and the overall conceptual model of multiple TEAPs operating concurrently during acetate augmentation.

2.4.3 $\delta^{34}S$ constraints on reactive transport parameters

Enrichment of $\delta^{34}S$ sulfate provides a new parameter with which to constrain the onset of SRB activity in previously unamended sediment that does not depend upon inhibition by Fe(III) mineral phases. This presents the opportunity to develop a biogeochemical reactive transport model in which the onset of SRB activity is prescribed by a metabolic lag term independent of any inhibiting species. The formulation for such a lag was derived by Wood et al. (1995) as a parameter (λ) allowing for a period of zero activity (lag) followed by a linear increase (ramp) to the final reaction rate (eq. 2.6):

$$\lambda_{lag} = 0 \qquad \text{if } t_0 < t < a \qquad (2.6)$$

$$\lambda_{lag} = \frac{t-(t_0+a)}{b-a} \qquad \text{if } a < t < b$$

$$\lambda_{lag} = 1 \qquad \text{if } t > b$$

where t_0 is the starting time of the reaction without inhibition, a is the lag time from t_0 to the beginning of the ramp period and b is the time taken to ramp up to the full reaction

starting from time *a*. Here we modify the dual Monod rate expression for SRB activity used by Li et al. (2009, 2010) in biogeochemical models of field scale acetate amendment at Rifle using the CrunchFlow code (Steefel, 2007) to incorporate this parameter λ_{lag} (eq. 2.7):

$$r_{SRB}^{Ac} = \lambda_{lag}\mu_{SRB}^{Ac}B_{SRB}\left(\frac{\left[SO_4^{2-}\right]}{K_{S-SRB}^{SO_4^{2-}}+\left[SO_4^{2-}\right]}\right)\left(\frac{\left[Ac\right]}{K_{S-SRB}^{Ac}+\left[Ac\right]}\right) \quad (2.7)$$

As stated the overall reaction rate (r) is calculated using the metabolic lag term (defined above), the maximum acetate utilization rate (μ), the biomass of SRB (B), the activities of sulfate ([SO_4]) and acetate ([Ac]), and the half-saturation coefficients for sulfate and acetate (K). The fundamental distinction between the dual Monod rate expression presented above and that used previously is the replacement of all inhibition terms with the metabolic lag parameter. The lag time is taken directly from the first indication of SRB activity using enrichment in $\delta^{34}S$ of sulfate. The ramp time is included for completeness but is found to be largely redundant in the case where a yield factor for biomass growth from a low background starting population is incorporated into the dual Monod rate expression.

Based on our results, this formulation is appropriately applied to a system in which no prior electron donor amendments have occurred. Fe(II), sulfide, sulfate and acetate concentrations from well D04 during the 2007 experiment are shown with corresponding model fits (Figure 2.7). Other than the changes described above, the CrunchFlow geochemical model is identical to that described previously by Li et al. (2009) with input concentrations adjusted where necessary to 2007 measured values. A lag time of 20 days was assigned to SRB activity based on $\delta^{34}S$ data with zero ramp time. Model results match the magnitude of variations for all species and reproduce the correct temporal trends. While the fit of the model output to the measured data is not substantially improved relative to prior results, the technique no longer relies on adjustment of an unsubstantiated inhibition term to fit the measured data. Furthermore, no retardation in sulfide concentrations relative to $\delta^{34}S$ sulfate is captured because the lag term simply sets the start of uniform SRB activity across the domain. Our data indicate that in subsequent years this uniformity is no longer valid, but rather requires the active population to be preferentially located near the injection wells to provide sufficient transport-based retardation of sulfide relative to $\delta^{34}S$ sulfate. The origin of this spatial shift in population may be associated with either microbial decay or chemotaxis as acetate becomes limited as a function of distance away from the injection well (Ginn et al., 2002). While beyond the scope of the current study, these results support the starting active SRB biomass and microbial decay methods used in Yabusaki et al. (2011) and suggest further consideration of the locality and origin of this active population. Finally it is noted that sulfate concentrations are subject to a wide range of background variability that has yet to be incorporated into reactive transport models of bioremediation over spatially-extensive scales, despite the importance of sulfate to acetate ratios in maintaining DIRB activity during concurrent sulfate and Fe(III) reduction.

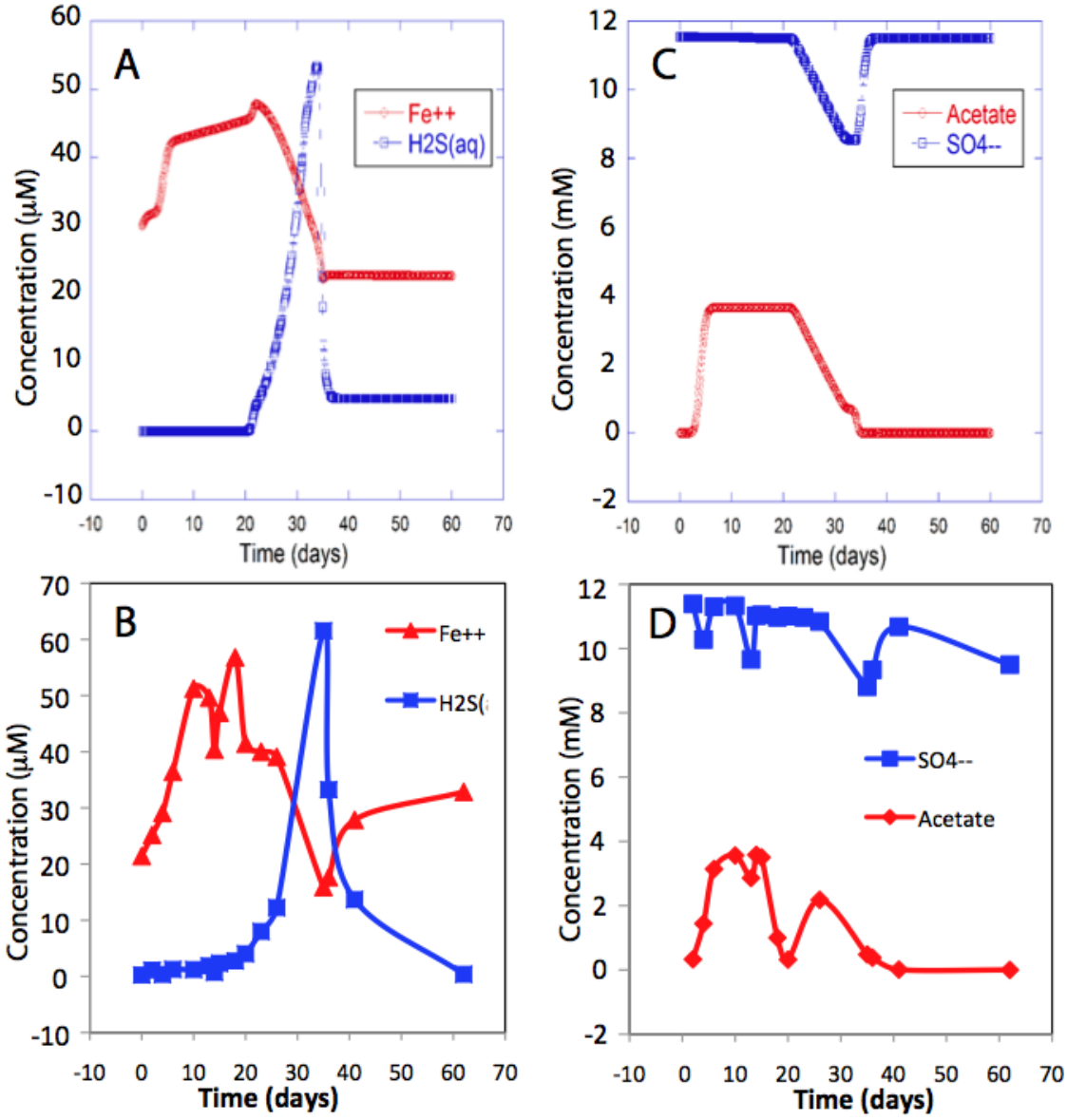


Figure 2.7: Measured values and CrunchFlow simulation results for the first row of monitoring wells in the 2007 amendment experiment. (A) CrunchFlow modeled Fe(II) and sulfide concentrations, (B) measured Fe(II) and sulfide concentrations in well D04, (C) CrunchFlow modeled acetate and sulfate concentrations, (D) measured acetate and sulfate concentrations in well D04. All times and noted as days relative to the start of acetate addition to the injection wells.

2.5 Summary

Our observations indicate that supplementing an aquifer with an exogenous electron donor alters the biogeochemical conditions of the system over periods of time much greater than the length of the amendment. We demonstrate that the use of $\delta^{34}S$ of SO_4 fractionation provides a more sensitive indication of the onset of SRB activity than

SO_4 concentration (due to background variability) and sulfide concentration (due to secondary reactivity). Using shifts in the stable isotope ratios of sulfur, we have shown evidence for early onset of sulfate reduction in a well field where multiple electron donor additions have occurred. This early onset motivates further investigation into the population and activity of the *in situ* microbial community between acetate additions and suggests a potential priming effect that may substantially influence long-term sequestration efforts.

Chapter 3

Calcium isotope fractionation as a function of solution stoichiometry in groundwater

3.1 Overview

This chapter demonstrates the utility of calcium isotope fractionation as a means of analyzing the geochemical conditions associated with carbonate precipitation in groundwater. A reactive transport model is developed to include isotopologues of calcium and used to reproduce observed fractionation where the calcium to carbonate ion activity ratio remains high. Where this ratio approaches unity, a newly developed analytical model (Nielsen et al., 2012) is required to account for the influence of solution stoichiometry on $\delta^{44}Ca$ fractionation. These results present some of the first field evidence for the influence of solution stoichiometry, in addition to reaction rate, on observed calcium fractionation.

3.2 Introduction

3.2.1 Calcite precipitation and associated $\delta^{44}Ca$ fractionation

As noted in Chapter 1, one of the results of DIRB and SRB activity is the production of alkalinity, which should lead to the precipitation of carbonate minerals (usually calcite). This precipitation step is important because it is confirmation of the reaction that is consuming acetate, and also because the precipitates can cause permeability reduction if they occur in sufficient volume. Recent research has shown that calcite precipitated in the laboratory at rates that are nominally comparable to those observed during bioremediation, is fractionated in calcium isotopes relative to dissolved Ca^{2+} (e.g. Tang et al., 2008; Reynard et al., 2011). This effect suggests that measurements of calcium isotopes in dissolved Ca^{2+} during bioremediation could be used to verify and estimate the amount of calcite precipitation occurring, much like sulfur isotopes are used to detect sulfate reduction. However, as in the case of sulfur isotopes,

there are some complications that arise in estimating the fractionation factor for calcium isotopes during calcite precipitation.

Calcium isotope fractionation has been shown to be rate-dependent, and available data can be described with a relatively simple model if the precipitation rate is known (DePaolo, 2011). However, it has also been shown that the fractionation factor and its dependence on precipitation rate is a function of the calcium to carbonate (Ca^{2+}:CO_3^{2-}) ion activity ratio of the solution from which calcite precipitates. In a bioremediation context, where CO_3^{2-} is being generated while calcite is precipitating, it is inevitable that the Ca^{2+}:CO_3^{2-} ratio will change with time. Therefore, in order to apply the fractionation of calcium isotopes to analysis of carbonate formation, we require an understanding of both the rate-dependence of calcium isotope fractionation under Old Rifle conditions, and the Ca^{2+}:CO_3^{2-} ratios where fractionation varies in addition to this relationship.

The effects of variable calcium to carbonate (Ca^{2+}:CO_3^{2-}) ion activity ratio for a fixed oversaturation state are now recognized as a factor influencing both growth rate and trace element partitioning in calcite (Nehrke et al., 2007; Perdikouri et al., 2009; Larsen et al., 2010; Stack and Grantham, 2010; Gebrehiwet et al. 2012) however the values of activity ratio corresponding to maximal growth rate vary about unity and the degree of asymmetry about each maxima vary substantially between studies. Recent work has sought to develop linear and higher order growth rates into macroscopic parallel rate laws as a means of upscaling molecular behavior to simulations of reactive transport in porous media (Noiriel et al., 2012). In a recent study of the influence of ion activity ratio at a fixed oversaturation on precipitation rate and strontium partitioning, Gebrehiwet et al. (2012) discussed the conceptual basis of incorporating attachment rates of individual ions with the standard affinity-based rate law for calcite growth, but to date no such macroscopic model has been developed.

Stable isotope fractionation of calcium associated with inorganic calcite precipitation has been demonstrated experimentally (Tang et al., 2008; Reynard et al., 2011) and biogenic calcium fractionation has been documented extensively in the field (e.g. Nielsen et al., 2011). Influences of environmental factors in addition to growth rate on the fractionation factor of calcium during carbonate precipitation have only recently begun to be addressed. Tang et al. (2012) showed insensitivity of both strontium partitioning and calcium isotope fractionation to variations in ionic strength of solution, while Neilsen et al. (2012) developed a molecular model of calcite growth rate as a function of solution stoichiometry of the form presented by Wolthers et al. (2012) to predict an isotopic fractionation due to variable Ca^{2+}:CO_3^{2-} ion activity ratio in addition to overall growth rate. The model suggested a maximum calcium fractionation factor should be achieved at a Ca^{2+}:CO_3^{2-} ion activity ratio close to unity, however to date the datasets appropriate to observe such an isotopic effect are lacking.

Applications of calcium isotope fractionation to analysis of secondary carbonate mineral formation in heterogeneous porous media are appealing because the factors influencing isotopic variability of the cation are in many ways simplified relative to that of carbon and oxygen (Zeebe and Wold-Gladrow, 2001). Incorporation of calcium isotopologues as explicit species in a multi-component reactive transport model necessarily begins by utilizing the standard affinity-based rate law for surface-controlled calcite growth (eq. 3.1) where k_i is the rate constant for the individual isotopologue, A_i is

$$R_i = k_i A_i \left[\left(\frac{a_{Ca^{2+}} a_{CO_3^{2-}}}{K_{sp}} \right)^m - 1 \right]^n = k_i A_i \left(\Omega^m - 1 \right)^n \quad (3.1)$$

the specific reactive surface area of calcite, $a_{Ca2+}a_{CO32-}$ the ion activity product of calcium and carbonate in solution, K_{sp} the equilibrium solubility product for calcite, Ω the saturation index, and m and n semi-empirical constants fit to produce the kinetic behavior of the reaction (Lasaga and Kirkpatrick, 1981). The rate law described above is inherently based on the overall saturation state, rather than ion activity ratio, and cannot accommodate transitions from spiral growth to 2D nucleation without adjustment in the exponential parameters. However, there are two potentially beneficial considerations in applying this approach to explicitly model calcium isotope fractionation during subsurface carbonate precipitation: (1) the vast majority of groundwater systems exist at circumneutral pH where bicarbonate is the prevalent form of dissolved carbon (Appelo and Postma, 2005) and thus the Ca^{2+}:CO_3^{2-} ion activity ratio should typically be far greater than unity; (2) the fractionation model developed by Nielsen et al. (2012) suggests insensitivity of isotopic behavior to the transition between 2D nucleation and dislocation driven growth mechanisms. Therefore provided that the affinity-based rate law can accurately reproduce species variability, the model should be able to adequately predict calcium isotope fractionation for the majority of relevant conditions.

Within this context it is the purpose of the present chapter to present some of the first field evidence of abiotic calcium isotope fractionation occurring as a function of both precipitation rate and Ca^{2+}:CO_3^{2-} ion activity ratio in groundwater. The study incorporates the DePaolo (2011) model for calcium isotope fractionation as a function of relative attachment and detachment fluxes into the CrunchFlow (Steefel, 2007) multi-component reactive transport model by explicitly treating both the Ca-40 and Ca-44 isotopologues as independent species. By analyzing data collected from clogged well bores during an in situ biostimulation experiment, we are able to document the circumstances of transition from high to low Ca^{2+}:CO_3^{2-} ion activity ratio and demonstrate the point at which the affinity-based model fails to reproduce the observed fractionation effect. The influence of Ca^{2+}:CO_3^{2-} ion activity ratio is verified by accurately reproducing fractionation at low ion activity ratio using the Nielsen et al. (2012) analytical model.

3.2.2 Secondary carbonate formation during bioremediation

Bioremediation of heavy metals in groundwater commonly relies upon microbially catalyzed redox transitions to sequester contaminants as reduced, nominally insoluble compounds. This process requires augmentation of the system's naturally limiting nutrient, typically in the form of an organic carbon electron donor (Lloyd and Macaskie, 2002). Addition of large organic carbon concentrations and subsequent microbial metabolism produces a substantial increase in dissolved inorganic carbon (DIC). This rise in alkalinity results in two important consequences, first permeability reduction due to carbonate precipitation, and second increased dissolved metal complexation, causing a more recalcitrant contaminant plume (Li et al., 2009, 2010; Davis et al., 2004). Careful monitoring of the transitions between redox states during

augmentation is therefore required in order to mediate DIC production and optimize the bioremediation strategy.

At the Rifle Integrated Field Research Challenge (IFRC) site in western Colorado, USA, groundwater bioremediation of aqueous uranium has been successfully demonstrated through the injection of acetate (Anderson et al., 2003; Williams et al., 2011). The Rifle aquifer is naturally suboxic, with a very low nitrate concentration. As a result, addition of acetate quickly induces iron-hydroxide and -oxyhydroxide reduction that subsequently gives way to the onset of sulfate reduction on the order of tens of days later. The catabolic components of both iron and sulfate reduction generate bicarbonate. The substantial increase in alkalinity and corresponding secondary carbonate precipitation resulting from this metabolism are thought to contribute, along with biomass growth, FeS precipitation and methane generation, to permeability reduction observed during acetate augmentation.

Between 2007 and 2009, three annual acetate amendment experiments were conducted in a single well gallery at the Old Rifle site (Fig. 3.1A). Following the 2008 injection the influences of permeability reduction associated with acetate augmentation were directly observed in decreased hydraulic conductivity of multiple injection wells (Fig. 3.1B). Slug test data indicated that while some wells showed no significant change in conductivity (e.g. G53) others decreased by over four orders of magnitude (e.g. G51; Williams et al., 2011). A third and final acetate biostimulation experiment was conducted in this well gallery in 2009, during which substantial increases in water level were observed in multiple injection wells during amendment as a result of decreased permeability. The geochemical and isotopic datasets collected from these wells, in comparison to wells that remained hydraulically connected to the aquifer, present comparisons of open and closed system behavior.

3.3 Methods

Experimental design and sampling procedure for the 2009 Old Rifle acetate amendment are described in detail for previous amendment experiments (Williams et al., 2011). Briefly, acetate was added to a series of injection wells (G51 – G60, Fig. 3.1A) installed perpendicular to the mean hydraulic gradient. Acetate and bromide salts were mixed with groundwater recovered from the aquifer in a storage tank to yield concentrations of 150 mM and 13 mM, respectively. Delivery to the injection wells was calibrated to achieve a 10:1 dilution for a final delivery concentration of 15 mM acetate and 1.3 mM bromide. Unlike previous years, cross-well mixing pumps were not utilized for the 2009 injection, resulting in discrete geochemical evolution of individual injection wells. Injection was started on July 22, 2009 and continued for 36 consecutive days. Fluid samples were collected throughout the 36-day injection period and for an additional 100 days thereafter.

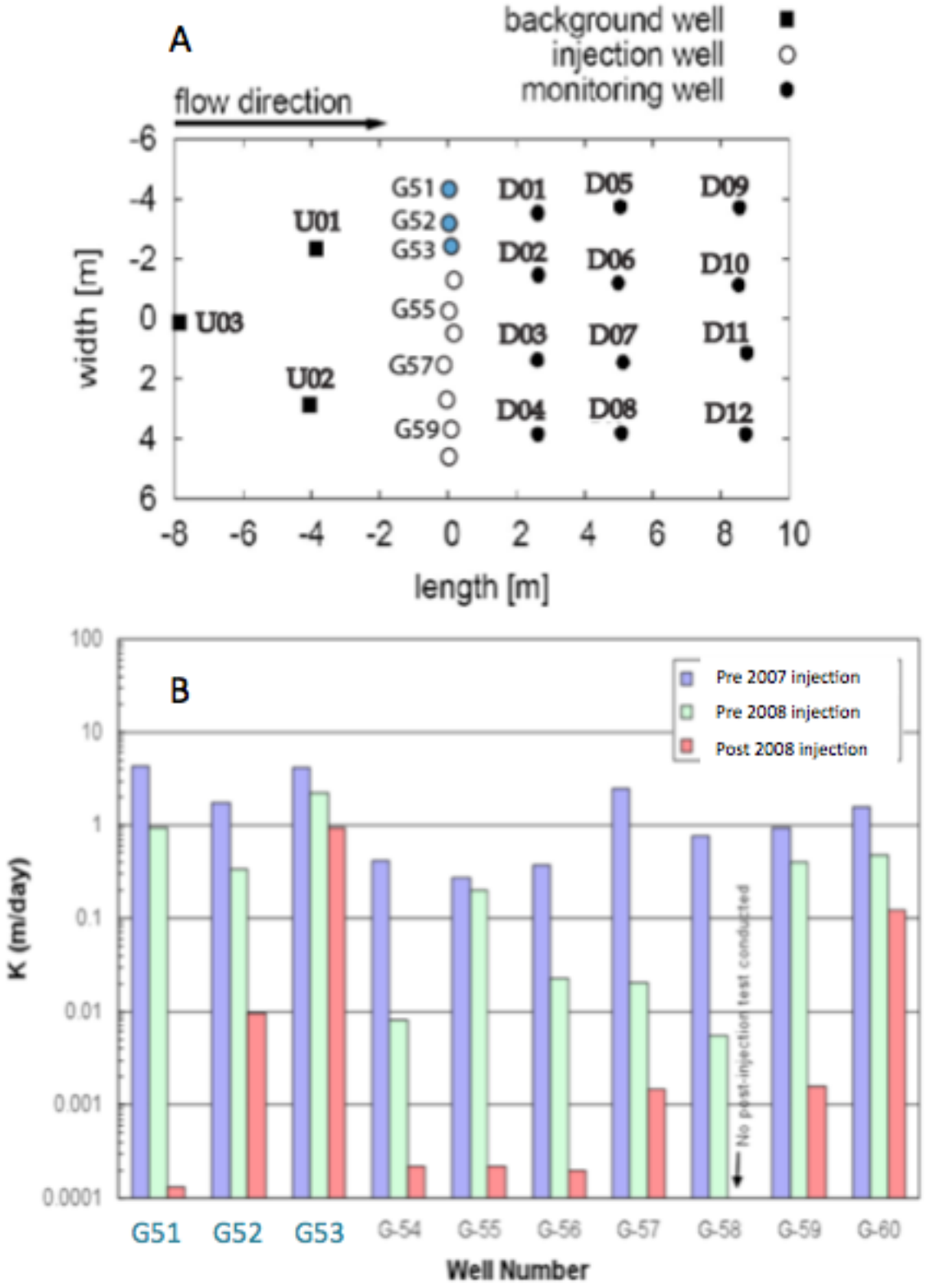


Figure 3.1: (A) Well gallery schematic for 2007 – 2009 Rifle IFRC field experiments. Geochemical and stable isotope data reported for those wells marked in blue. (B) Change in hydraulic conductivity measured in injection wells. Wells labeled in blue correspond to data reported herein (3.1B adapted from Williams et al., 2011).

Fluid samples collected from injection wells G51, G52 and G53 were pumped from the wells and immediately filtered through 0.2 μM PTFE syringe filter. Anions were measured on site using a Dionex ICS-1000 ion chromatograph with an AS-22 column. Cation samples were preserved by acidification with trace metal grade 12 N HNO_3 and shipped to the Lawrence Berkeley National Laboratory, Berkeley, CA. Analysis was made on a Perkin Elmer SCIEX Elan DRC II quadrupole ICP-MS with a dynamic reaction cell (DRC) using ammonia NH_3 as a reaction gas to remove polyatomic interferences. Calcium isotope analysis was conducted using aliquots of the samples preserved for cation analysis at the University of California, Berkeley Center for Isotope Geochemistry. Measurements were made using thermal ionization mass spectrometry (TIMS) on a Thermo-Finnigan Triton TI with nine mobile Faraday collectors. Each sample was spiked and measured in duplicate, collecting 200 individual ratios for each filament loaded, and yielding in-run uncertainties of roughly ±0.04‰ and external reproducibility of 0.1 – 0.2‰ (DePaolo, 2004). Isotope ratios are reported relative to bulk silicate earth (BSE) standard in delta notation (eq. 3.2; Skulan et al., 1997).

$$\delta^{44}Ca = \left[\frac{(^{44}Ca/^{40}Ca)_{sample}}{(^{44}Ca/^{40}Ca)_{std}} - 1 \right] \times 1000 \qquad (3.2)$$

3.4 Results and discussion

3.4.1 Aqueous concentrations and δ^{44}Ca

Injection well G53 showed little variation in hydraulic conductivity across pump tests (Fig. 3.1B) and geochemical behavior similarly reflected an open system. Acetate concentrations in this well increased up to 300 mM during amendment, but rapidly returned to baseline (zero detectable concentration) when injection stopped (Fig. 3.2). In contrast, injection wells G51 and G52 demonstrated substantial conductivity reduction, and both elevated acetate and bromide concentrations persisted in these wells for over 100 days after the stop of amendment. Of particular note are the bromide concentrations in G51, which gradually return to near-baseline values, and G52, which remain elevated for the duration of sample collection. Unlike the slug test data, these results suggest G51 was more hydraulically connected to the surrounding aquifer than G52. Despite this variation the removal rate of acetate in these wells following the cessation of injection are remarkably similar. The complete dataset is provided in Appendix A, Table A3.

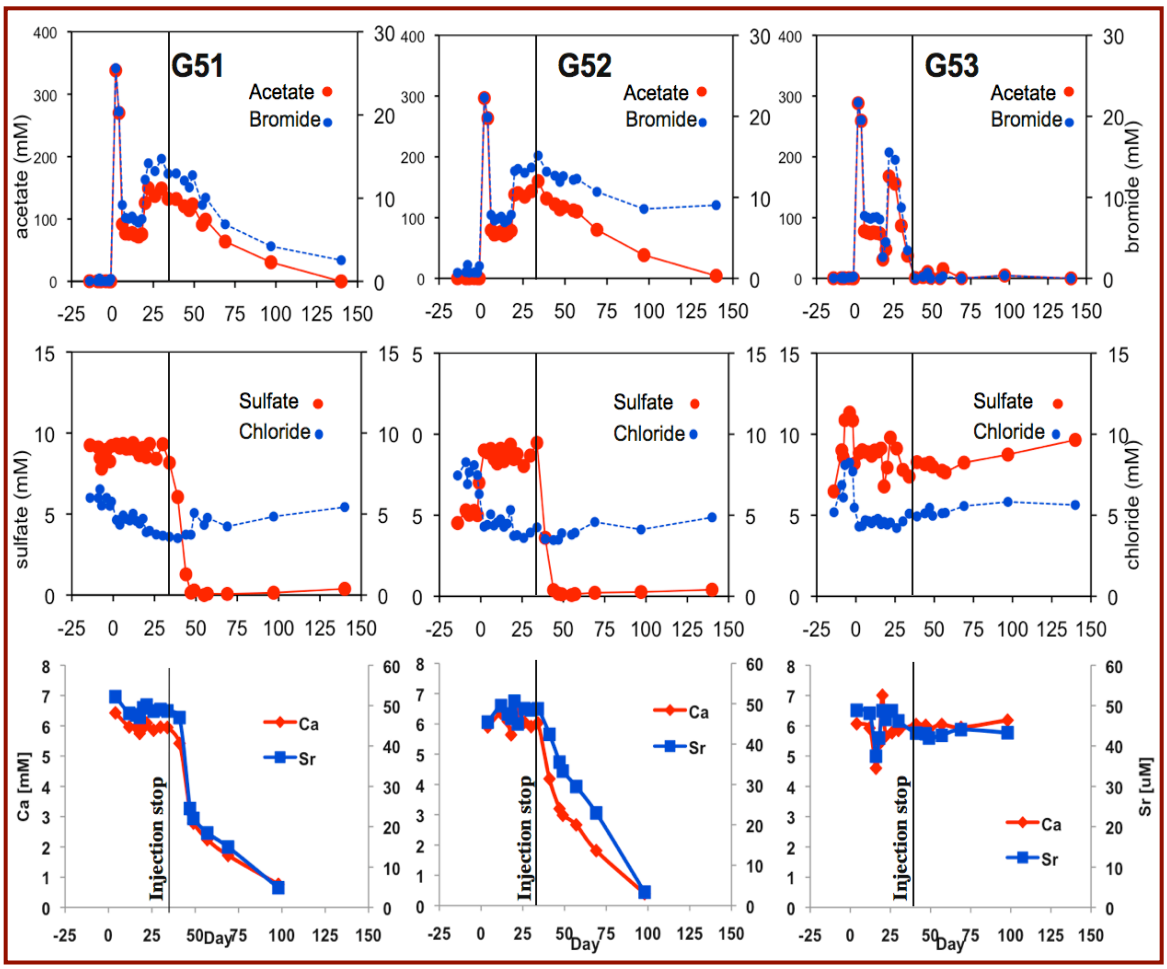


Figure 3.2: Acetate, bromide, sulfate, chloride, calcium and strontium concentration profiles from injection wells G51, G52 and G53 during the 2009 acetate amendment. Days are counted from the start of acetate addition and the solid vertical line marks the cessation of injection.

Evidence for microbial metabolism of acetate is shown in the sulfate profiles of the three wells. While sulfate concentrations in G53 never substantially deviated from background concentrations, those in G51 and G52 dropped precipitously upon termination of the injection. This trend indicates sulfate concentrations were being maintained at background range despite substantial SRB activity as a result of the injection of acetate amended groundwater, however once this source was removed, the TEAP was readily depleted. The subsequent slow decline in acetate concentrations despite depleted sulfate suggests an additional TEAP was active in the injection wells. Within the well casing the lack of available iron (hydr)oxides negates substantial contribution via this pathway, therefore the only remaining plausible metabolic process is acetoclastic methanogenesis (Goevert and Conrad, 2009). While beyond the scope of the current work, it is important to note that this evidence for microbial methane generation supports current investigations into the role of gas phases in permeability reduction.

Calcium and strontium in well G53 similarly remain near baseline concentrations for the duration during and after acetate amendment. In contrast the concentration of calcium in G51 and G52 dropped from a background of roughly 6 mM to >1 mM in the period following the end of the injection. The concurrent decline in both calcium and

strontium in association with metabolism of acetate strongly suggest secondary carbonate formation in both well bores. Based on this concentration dataset, aliquots of the samples for cation analysis were used to measure $\delta^{44}Ca$ in the fluid as a function of time for the three well bores shown (Fig. 3.3). Again the value of $\delta^{44}Ca$ in well G53 remained at a baseline of -0.5‰, however substantial fractionation was observed in both G51 and G52. The G51 isotopic trend closely followed the inverse of calcium concentration with time, moving from baseline to an enrichment of ~1‰ within the first 10 days following cessation of acetate amendment. For the remaining time thereafter the value of $\delta^{44}Ca$ persisted at roughly +1.3‰. In well G52, the decrease in calcium concentration was similar to that in G51, however the final value reached a minimum of 0.39 mM, in comparison to a final value of 0.74 in G51. The $\delta^{44}Ca$ profile of G52 is markedly more pronounced that that of G51, with enrichment continuing throughout the duration of measurements following the end of acetate addition, reaching a final value of +2.3‰.

The evolution of both concentration and $\delta^{44}Ca$ with time following the end of acetate amendment in these injection wells gives rise to the following question: what is the difference in the geochemical conditions of wells G51 and G52 that produces such unique calcium isotope fractionation profiles? The remainder of the chapter will seek to employ a series of models to address the underlying mechanisms of this discrepancy.

3.4.2 First-order, homogeneous Rayleigh fractionation

The simplest description of fractionation in a closed system is a first-order distillation (Rayleigh) model. This approach assumes the reaction progresses in a well mixed, homogenous system based on a first-order (linear) reaction rate (eq. 3.3). Here r is the instantaneous ratio of the isotopes, r_0 is the initial isotopic ratio, f is the fraction of the reactant remaining in the system and α is the fractionation factor. Application of this

$$r = r_0 f^{(\alpha - 1)} \tag{3.3}$$

model in the present context may fail to account for variations in the reaction rate of carbonate precipitation as the system approaches equilibrium as well as any heterogeneity in the rate of reaction or fractionation factor both spatially and temporally within a given well bore. Calcium isotope data and corresponding distillation models are shown for wells G51 and G52 (Fig. 3.4). An effective fractionation factor of 0.9991 provides a fairly good representation of the isotopic trend observed in well G52. However, the behavior observed in well G51 clearly cannot be addressed with a single effective fractionation factor distillation model. Both the isotopic trends in G51 and G52 appear to indicate a larger fractionation at early time, which subsequently decreases as calcium is removed from the aqueous phase.

The inability to adequately reproduce this data with such a simplified model leads us to treat the data with a more complete multi-component reactive transport simulation of the well bores that explicitly incorporates the isotopologues of all relevant calcium species. Within this framework hydraulic communication between the well bores and surrounding aquifer evidenced by the bromide datasets can be incorporated, as well as variations in the calcite precipitation rate as a function of oversaturation.

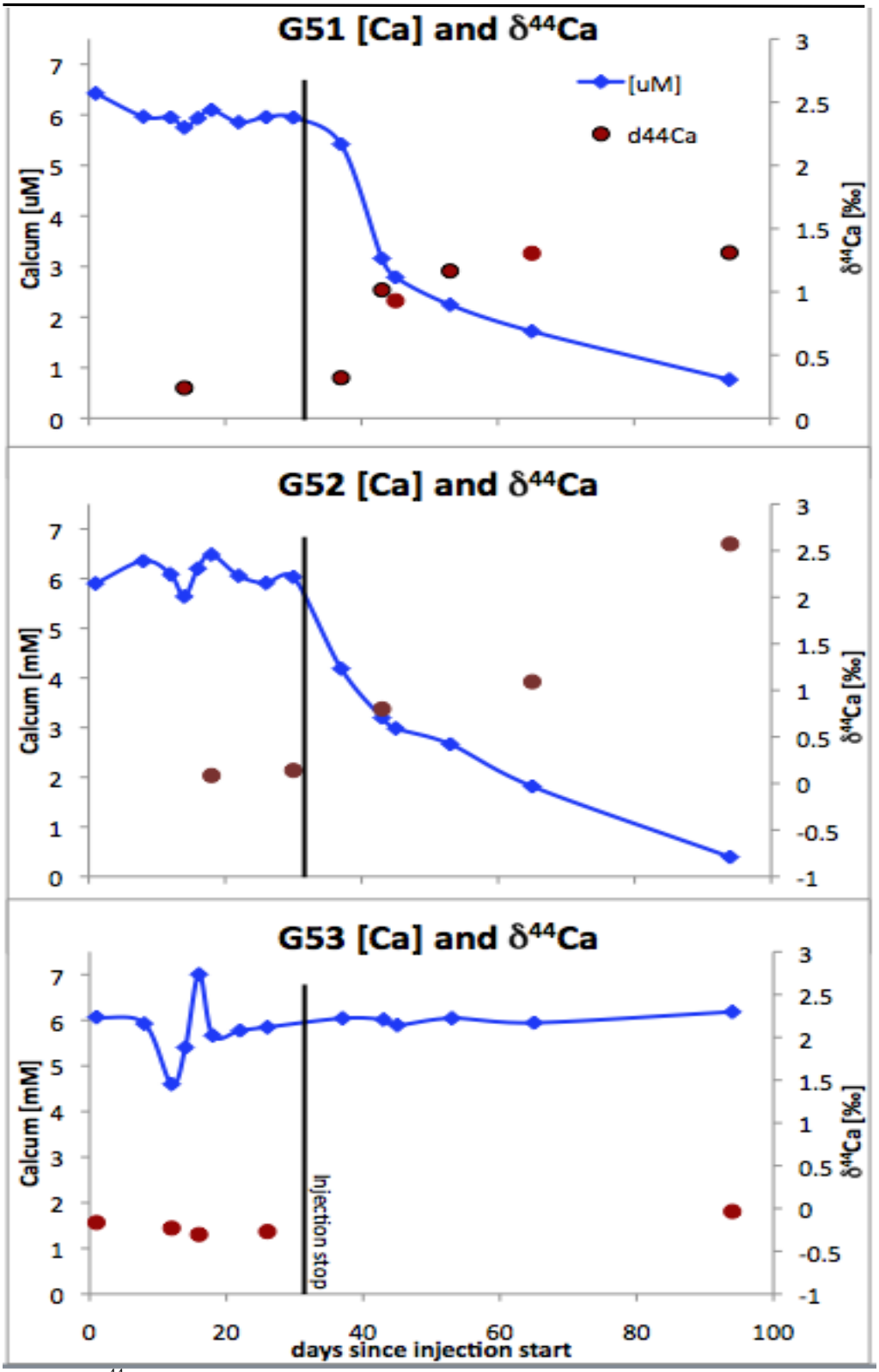


Figure 3.3: Fluid $\delta^{44}Ca$ in injection wells G51, G52 and G53. Days are counted since the start of acetate addition and the vertical black line denotes the cessation of amendment. At this scale the error in $\delta^{44}Ca$ measurements is contained within the size of the data points.

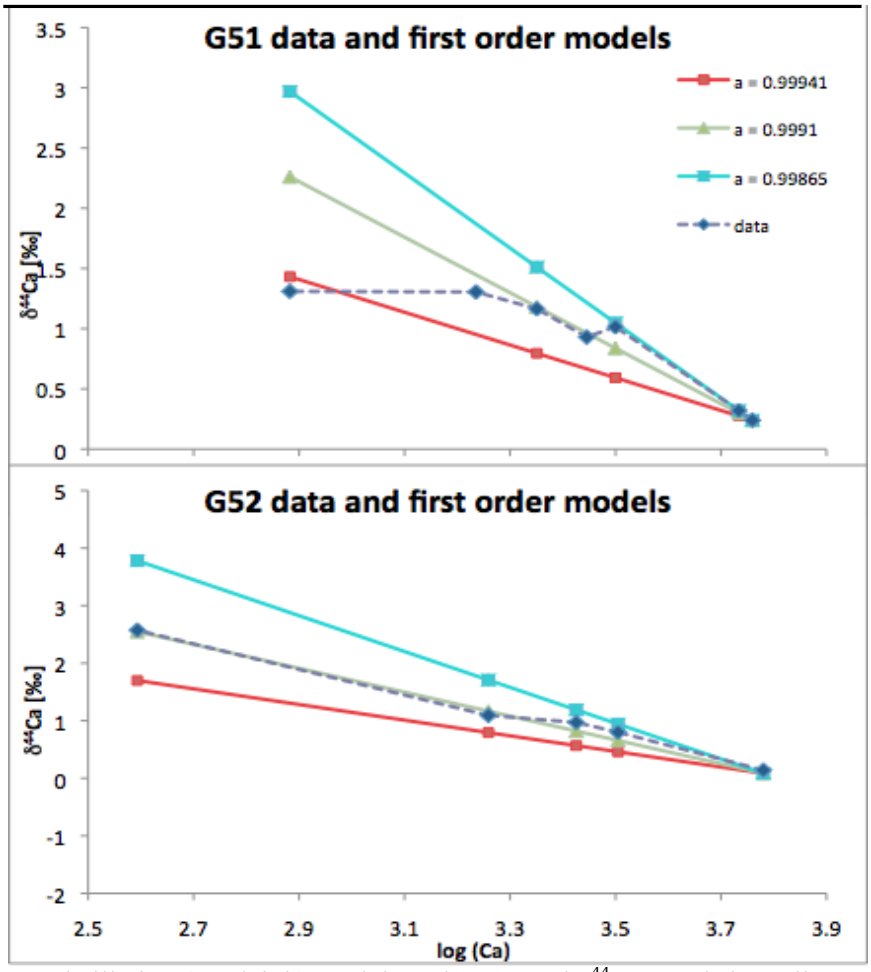


Figure 3.4: Distillation (Rayleigh) models and measured $\delta^{44}Ca$ trends in wells G51 and G52.

3.4.3 CrunchFlow simulations of well bore geochemistry

CrunchFlow is a multi-component, biogeochemical reactive transport code developed to solve the coupled equations for conservation of mass, energy and momentum for conditions pertinent to saturated subsurface systems (Steefel, 2007). The code has been applied to simulate a variety of complex biogeochemical systems (e.g. Li et al., 2008; Maher et al., 2006) and has been utilized extensively to model Old Rifle bioremediation experiments (Li et al., 2009, 2010, 2011). Conservation of mass for a solute (i) is given in equation 3.4 as (Li et al., 2009):

$$\frac{\partial(\phi C_i)}{\partial t} = \nabla(\phi D_i \nabla C_i) - \nabla(\phi u C_i) - \sum_{r-1}^{N_r} v_{ir} R_r - \sum_{m=1}^{N_m} v_{im} R_m \qquad (3.4)$$

where ϕ is the porosity of the media, C_i is the concentration of the solute (mol/kg H_2O), D_i is the combined dispersion-diffusion coefficient, and u is the darcy flux (length/time). The reaction portion of eq. 3.4 is divided into two summations, the first for homogeneous (aqueous) kinetics and the second for heterogeneous kinetics. The first reaction term is

summed over the total number of kinetic aqueous reactions (N_r) which influence species i, v_{ir} is the stoichiometric coefficient for this species in reaction r, and R_r is the rate of the aqueous reaction (moles/kg H_2O/time), which is determined in separate calculations for each time step. In the final term, dealing with heterogeneous reactions, the summation is made over the total number of mineral reactions influencing species i, v_{im} is the stoichiometric coefficient for this species in reaction m, and R_m is the rate of the heterogeneous (e.g. dissolution or precipitation) reaction (moles/volume solid/time) determined in separate calculations (Steefel, 2007; Li et al., 2009). The total number of aqueous species in the system is divided into two groups: those that are independently solved for, termed primary, and those that are calculated assuming instantaneous chemical equilibrium based on total primary species concentration, termed secondary.

The driving reactions for microbial metabolism and carbonate production governing the clogged well bore systems are modeled using a homogeneous (aqueous) dual-Monod rate law as described in Chapter 2 (Monod, 1942; 1949). A dual-Monod rate for coupled microbial sulfate reduction and acetate oxidation was given in chapter 2 (eq. 2.7), here a generalized form of the dual-Monod law is presented without the lag parameter developed in chapter 2 (eq. 3.5). The reaction rate R_S (mol/m^3/time) is written

$$R_S = -k_{\max} X_S \frac{C_S}{K_{s-half} + C_S} \frac{C_{teap}}{K_{s-half} + C_{teap}} \tag{3.5}$$

for the electron donor (acetate) and is equal to the maximum utilization rate, k_{max} (mol/kg H_2O/time), the volume fraction of bacterial cells in the specific TEAP, X_s (m^3 cells/m^3), the concentration of the electron donor (acetate), C_s (mol/kg H_2O) and the electron acceptor, C_{teap}, and the half-saturation constants for the electron donor and acceptor, K_{s-half} and $K_{teap-half}$, respectively. The relationship of half-saturation constants to total reaction rate will be discussed in detail in chapter 5. Here it is sufficient to note that the magnitude of the electron donor and acceptor concentrations relative to their individual half saturation constants governs the proximity of the overall rate (r_s) to the maximum utilization rate (k_{max}). The principle difference between the dual-Monod rate law presented here (eq. 3.5) and that shown by Li et al. (2009, 2010) is the lack of an inhibition term. Two TEAPs are used to model the microbial metabolism of acetate in the clogged well bores, sulfate reduction and acetoclastic methanogenesis (Table 3.1). The two TEAPs shown include both catabolic and anabolic components, meaning that for

stoichiometry	k_{max} (mol/kgw/yr)	K_{s-half} (mol/kgw)	$K_{teap-half}$ (mol/kgw)
$SO_4^{2-} + 1.082CH_3COO^- + 3.05H^+ + 0.035NH_4^+ \rightarrow$ $0.033C_5H_7O_2N_{SRB} + 2.1H_2O + 2CO_{2(aq)} + H_2S_{(aq)}$	9000	5.0×10^{-3}	1.0×10^{-3}
$CH_3COO^- + 0.985H^+ + 0.015NH_4^+ \rightarrow$ $0.015C_5H_7O_2N_{meth} + 0.046H_2O +$ $0.962CO_{2(aq)} + 0.962CH_{4(aq)}$	1500/9000	1.5×10^{-5}	

Table 3.1: Sulfate reduction and acetoclastic methanogenesis TEAP stoichiometry and associated parameters. Maximum utilization rates for methanogenesis differ between wells and are listed as G51/G52. Half saturation constants from Dale et al. (2008) and Fang et al. (2009).

each mole of substrate consumed, the majority goes to energy production and a minor amount goes to growth of more biomass. The percentage of substrate diverted to the anabolic pathway, termed the yield factor, is unique for each population. For the present model a yield factor of 8.2% was used for sulfate reduction, and 3.8% for methanogenesis (Rittmann and McCarty, 2000). For each time step the volume fraction of biomass (represented as $C_5H_7O_2N$) for each TEAP is calculated (eq. 3.6) based on the volume fraction from the previous time

$$X_S^{t+\Delta t} = X_S^t + R_S M \Delta t \tag{3.6}$$

step, the reaction rate (eq. 3.5) and the molecular volume of the cells (m^3 cells/mol).

In addition to the aqueous reactions, a series of heterogeneous reactions are employed to account for mineral dissolution and precipitation. These reactions are calculated using a standard transition state theory (TST) rate law (Lasaga, 1981) described in section 3.2.1 (eq. 3.1). Table 3.2 provides the reaction stoichiometry and relevant parameters for those heterogeneous reactions utilized in modeling the clogged

stoichiometry	log k (mol/m^2/s)	log K_{sp}
$CaCO_{3(s)} \leftrightarrow Ca^{2+} + CO_3^{2-}$	-4.1/-4.6	-8.4801
$MgCO_{3(s)} + H^+ \leftrightarrow Mg^{2+} + HCO_3^-$	-5.0	2.9734
$Fe^{2+} + H_2S_{(aq)} \leftrightarrow FeS_{(am)} + 2H^+$	-8.0	3.5
$C_5H_7O_2N_{SRB} \leftrightarrow C_5H_7O_2N_{SRB(aq)}$	-2.0	-15.0
$C_5H_7O_2N_{meth} \leftrightarrow C_5H_7O_2N_{meth(aq)}$	-2.0	-15.0

Table 3.2: Heterogeneous reactions used to model clogged wells and associated parameters. Individual values for each well are listed as G51/G52 where they differ.

wells. The last two reactions listed in Table 3.2 represent the near-instantaneous conversion of aqueous biomass growth through the anabolic component of the TEAPs to the solid phase.

Because the simulation is based on a system in which a column of water is contained within a well bore and almost completely disconnected from the aquifer sediments, no surface complexation or ion exchange reactions and no solid phase iron reduction are included in the model. In addition the simulation is started for conditions reflecting the final day of acetate amendment to the well bore. This removes the complexity of the injection input function and variable water levels during acetate amendment and focuses the model on the period of interest following cessation of artificial delivery. Primary aqueous species used for initial conditions within the well bore were taken from measured values on the final day of acetate amendment (Table 3.3).

primary species	concentration (mol/ kg H_2O)
pH	7.05
Fe^{2+}	1.0E-08
Fe^{3+}	in equilibrium with iron hydroxide
$SiO_{2(aq)}$	0.35
Na^+	charge balanced

primary species	concentration (mol/ kg H_2O)
K^+	1.0
Ca^{2+}	6.0/5.6
Mg^{2+}	5.6
SO_4^{2-}	9.0
Cl^-	3.9
$CO_{2(aq)}$	15.0
Acetate	150.0
$H_2S_{(aq)}$	1.0E-15
$O_{2(aq)}$	15.6E-03
NH_4^+	1.0
Br^-	15.0
$Methane_{(aq)}$	1.0E-15
$C_5H_7O_2N_{SRB(aq)}$	1.0E-10
$C_5H_7O_2N_{meth(aq)}$	1.0E-12

Table 3.3: Initial conditions of aqueous primary species within the well bore for the start of simulation. Individual values for each well are listed as G51/G52 where they differ.

In addition, non-zero initial calcite and biomass minerals were included within the well bores (Table 3.4). This was done to account for both mineral and biomass growth prior to the last day of acetate injection.

mineral	volume fraction (m^3/m^3)
calcite	1.0E-03
$C_5H_7O_2N_{SRB}$	4.7E-04 / 5.7E-04
$C_5H_7O_2N_{meth}$	1.0E-05 / 5.0E-04

Table 3.4: Initial conditions of mineral volume fraction in the well bore for the start of simulation. Individual values for each well are listed as G51/G52 where they differ.

Boundary conditions for the model are established to represent groundwater solute and mineral composition measured at the time of the 2009 bioremediation experiment (Williams et al., 2011; Li et al., 2010). Primary aqueous species are identical to those listed in table 3.3, however Ca^{2+} concentration is consistently 6.0 mol/kgw and both acetate and bromide concentrations are zero. Similarly the mineral volume fraction for the boundary conditions is the same as that listed in table 3.4, however both biomass components are zero. A series of secondary reactions are calculated in the model assuming instantaneous aqueous speciation from the primary species (Table 3.5).

speciation reaction	$logK_{eq}$
$H_2O \leftrightarrow H^+ + OH^-$	-14.0
$HCO_3^- + H^+ \leftrightarrow CO_{2(aq)} + H_2O$	6.34
$CO_3^{2-} + 2H^+ \leftrightarrow CO_{2(aq)} + H_2O$	16.7
$FeOH^+ + H^+ \leftrightarrow Fe^{2+} + H_2O$	9.5
$Fe(OH)_{2(aq)} + 2H^+ \leftrightarrow Fe^{2+} + 2H_2O$	20.6
$Fe(OH)_3^- + 3H^+ \leftrightarrow Fe^{2+} + 3H_2O$	31.0

speciation reaction	$\log K_{eq}$
$FeOH^{2+} + H^+ \leftrightarrow Fe^{3+} + H_2O$	2.19
$FeCl^+ \leftrightarrow Fe^{2+} + Cl^-$	0.165
$FeCl^{2+} \leftrightarrow Fe^{3+} + Cl^-$	0.815
$Fe(OH)_2 + 2H^+ \leftrightarrow Fe^{3+} + 2H_2O$	5.67
$Fe(OH)_{3(aq)} + 3H^+ \leftrightarrow Fe^{3+} + 3H_2O$	12.0
$FeS_{(aq)} + 2H^+ \leftrightarrow Fe^{2+} + H_2S_{(aq)}$	9.2
$FeCO_{3(aq)} + 2H^+ \leftrightarrow Fe^{2+}CO_{2(aq)} + H_2O$	11.9
$Fe(CH_3COO)_{2(aq)} \leftrightarrow Fe^{2+} + 2CH_3COO^-$	-2.48
$FeCH_3COO^- \leftrightarrow Fe^{2+} + 2CH_3COO^-$	-1.29
$CaOH^- + H^+ \leftrightarrow Ca^{2+} + H_2O$	12.9
$CaCO_{3(aq)} + 2H^+ \leftrightarrow Ca^{2+} + H_2O + CO_{2(aq)}$	13.4
$CaSO_{4(aq)} \leftrightarrow Ca^{2+} + SO_4^{2-}$	-2.1
$CaCl^- \leftrightarrow Ca^{2+} + Cl^-$	0.7
$CaHCO_3^+ + H^+ \leftrightarrow Ca^{2+} + H_2O + CO_{2(aq)}$	5.3
$Ca(CH_3COO)_{2(aq)} \leftrightarrow Ca^{2+} + CH_3COO^-$	-2.13
$CaCH_3COO^+ \leftrightarrow Ca^{2+} + CH_3COO^-$	-0.928
$MgCO_{3(aq)} + 2H^+ \leftrightarrow Mg^{2+} + H_2O + CO_{2(aq)}$	13.7
$MgCl^+ \leftrightarrow Mg^{2+} + Cl^-$	0.139
$MgSO_{4(aq)} \leftrightarrow Mg^{2+} + SO_4^{2-}$	-2.41
$CH_3COOH_{(aq)} \leftrightarrow H^+ + CH_3COO^-$	-4.75
$HS^- + H^+ \leftrightarrow H_2S_{(aq)}$	6.98
$S^{2-} + 2H^+ \leftrightarrow H_2S_{(aq)}$	19.9
$NH_{3(aq)} + H^+ \leftrightarrow NH_4^+$	9.24

Table 3.5: Secondary reactions calculated using associated equilibrium constants as instantaneous products based on primary species values.

The domain of the model simulation is 1D homogeneous, comprised of 7 evenly spaced nodes at a resolution of 10 cm, resulting in a total domain length of 70 cm. The central node (node 4) is treated as the well bore, with a fixed porosity of 0.98. The surrounding 6 nodes are treated as the Rifle aquifer and the simulation is run for 75 days for each well bore. Flow rate across the domain represents the hydraulic communication between the clogged well bores and the aquifer and is unknown prior to modeling the inert bromide tracer. Measured aqueous data and corresponding model fits for wells G51 and G52 are shown (Fig. 3.5) using flow rates of 1.98 and 0.85 mm/day, respectively. The resulting flow velocity in G52 is only 43% that of G51 and, for the given domain, leads to total displacement of the fluid in center node for G51 and only partial displacement of the fluid in G52. As a result the well bore chemistry in G51 is more influenced by exchange with the surrounding aquifer, while that in G52 is more representative of a closed system.

Despite this substantial difference in flow it is noted that the concentration profiles for both sulfate reduction and acetate metabolism are remarkably similar between wells. Sulfate reduction occurred so rapidly in both wells that a single, large rate constant (9000 mol/kgw/cell/yr) adequately reproduced the trends in both simulations. However, because well G51 was being flushed with aquifer water bearing a zero acetate concentration, the remaining acetate removal due to acetoclastic methanogenesis was much lower in this well relative to G52. The difference in these rates (1500 vs. 9000 mol/kgw/yr) marks a fundamental difference in the chemistry of these well bores. In G51, acetate is partially removed by methanogens and partially flushed by background water, whereas in G52 acetate is almost entirely removed by microbial metabolism.

Calcium concentration profiles in wells G51 and G52 also showed fairly similar trends despite the difference in flow (Fig. 3.6). In contrast to acetate, influx of aquifer water represents a replenishment of calcium at background (6 mM) concentrations. Therefore the rate constant for calcite precipitation necessary to reproduced the observed aqueous chemical evolution in G51 is larger than that for G52 (-4.1 vs. -4.4 log[mol/m^3/sec]). Multiple rate laws were tested, including linear, second order and a pseudo-linear function developed to describe multi-sourced spiral growth (Teng et al., 2000; Noriel et al., 2012). While each rate law required a unique rate constant in order to simulate the observed trend, no appreciable improvement was noted in the overall fit to the data. This, in conjunction with a paucity of information as to the growth dynamics of calcite in such a complex system, supports the assumption of a linear rate law as shown (Fig. 3.6).

3.4.4 Calcium isotopes in CrunchFlow

As described in chapter 1, section 1.3.1, rigorous incorporation of isotopologues into a TST-type model requires careful tracking of the parameters influencing the individual rate laws. While the model treats these parameters as independent, in reality their combined behavior must reproduce the behavior of the bulk solute. Toward the objective of incorporating ^{40}Ca and ^{44}Ca isotopes as unique "species" within the CrunchFlow framework, we begin by developing the TST-type rate law appropriate to describe calcite precipitation for the individual isotopes of calcium. DePaolo (2011) describes the net rate of calcite precipitation for the ^{40}Ca and ^{44}Ca isotopologues (eq. 3.7a) as a combination of the irreversible forward (precipitation; eq. 3.7b) and backward (dissolution; eq. 3.7c) reactions. Here the superscript i represents the individual isotope

$$ {}^{i}R_N = {}^{i}R_f - {}^{i}R_b \tag{3.7a} $$

$$ {}^{i}R_f = {}^{i}k_f a_{{}^{i}Ca} a_{CO_3} \tag{3.7b} $$

$$ {}^{i}R_b = {}^{i}k_b a_{{}^{i}CaCO_3} \tag{3.7c} $$

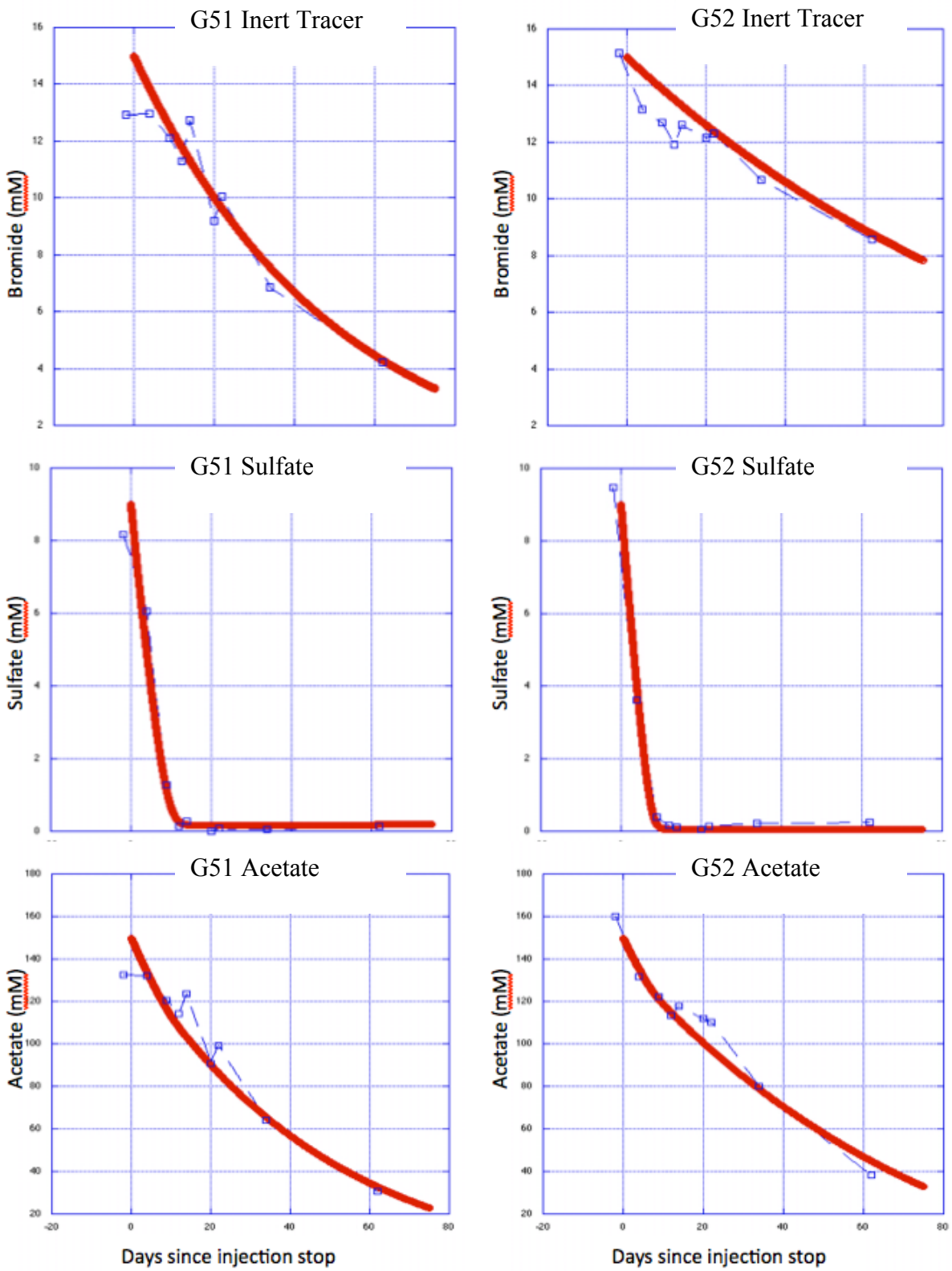


Figure 3.5: Measured data (blue) and associated model results (red) for wells G51 (left column) and G52 (right column). Shown are bromide inert tracer fits (top row), sulfate (middle row) and acetate (bottom row). Days are counted from zero as the last day of acetate injection to the wells.

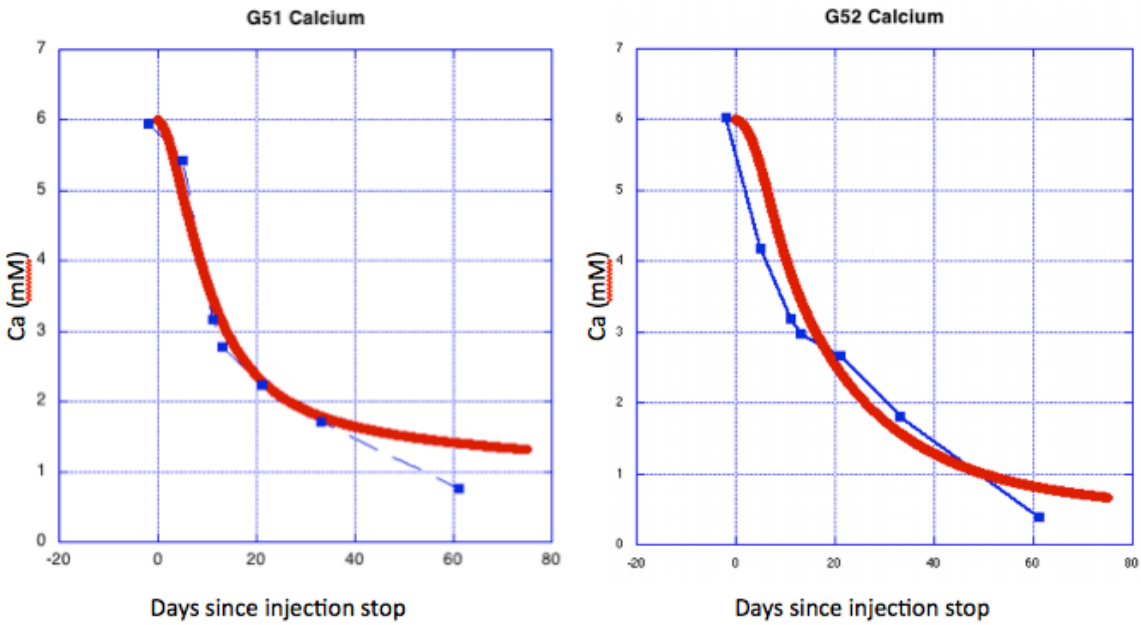


Figure 3.6: Calcium concentrations measured (blue) and modeled (red) for wells G51 and G52. Days are counted from zero as the last day of acetate injection into the wells.

of calcium, R_N is the net reaction rate, R_f is the forward rate, R_b is the backward rate, *k* terms are the corresponding rate constants and *a* terms are the activities of the labeled species. Combining and rearranging eq. 3.7a-c results in an expression for the net rate (eq. 3.8). This rate is strictly the result of competition between two irreversible reactions

$$ {}^{i}R_N = {}^{i}k_b a_{i_{CaCO_3}} \left[\frac{{}^{i}k_f}{{}^{i}k_b} \frac{a_{i_{Ca}} a_{CO_3}}{a_{i_{CaCO_3}}} - 1 \right] \tag{3.8} $$

and is not yet tied to any specific equilibrium conditions. Defining equilibrium as the point at which the forward (eq. 3.7b) and backward (3.7c) rates equal one another generates a formula for K_{sp} (eq. 3.9), which is set equal to a known solubility product

$$ K_{sp} = \frac{{}^{i}k_b}{{}^{i}k_f} = \frac{a_{i_{Ca}} a_{CO_3}}{a_{i_{CaCO_3}}} = 10^{-8.4801} \tag{3.9} $$

(Table 3.2). It is important to note that if the forward (precipitation) rate constants for ^{40}Ca and ^{44}Ca differ such that a fractionation occurs during calcite precipitation, then eq. 3.9 shows that either (1) the backward rates must also differ in order to accommodate a common equilibrium constant, or (2) the equilibrium constants must differ in order to maintain a common backward rate. Here a single equilibrium constant is used for both isotopologues in eq. 3.9 in order to generate zero equilibrium fractionation of calcium isotopes between solutes and carbonate (Fantle and DePaolo, 2007). Other isotope systems in which a non-zero equilibrium fractionation is desired would necessarily require unique solubility products. Combining eq. 3.8 and 3.9 yields a net rate expression

for each isotopologue (eq. 3.10). Here the specific reactive surface area of the mineral (A) has been split from the rate constant (*k*) as in the CrunchFlow code.

$$ {}^{i}R_N = A^{i}k a_{{}^{i}CaCO_3}\left[\frac{a_{{}^{i}Ca}a_{CO_3}}{K_{sp}a_{{}^{i}CaCO_3}}-1\right] = A^{i}k a_{{}^{i}CaCO_3}\left[\frac{{}^{i}Q}{K_{sp}}-1\right] \tag{3.10} $$

Both the activity coefficient and the concentration of the solid phase are commonly treated as unity, thus simplifying eq. 3.10 to eq. 3.1, however this is not necessarily valid when applied to the individual isotopologues of a single species. This issue derives from the fact that the extent of oversaturation of a fluid phase with respect to a particular mineral is calculated based on the composition of that solid (Benning and Waychunas, 2008). Thus if calcite is precipitated using a fixed isotopic composition, as $^{40}Ca_{(1-X)}{}^{44}Ca_XCO_3$ where X is a constant, then the oversaturation of the solution will not reflect the time-dependant variation in removal rates (i.e. the fractionation) of the isotopologues of calcium. Such a problem is faced in any situation where the composition of the mineral phase changes with time as a result of the evolution of the fluid, and is treated using a solid solution wherein the solid phase is not held to a specific ordering, but allowed to vary between two or more end-member compositions (Langmuir, 1997).

Isotopic substitution of a single element within a crystal structure represents one of the closest real approximations to an ideal solid solution (Anderson and Crerar, 1993). The assumption of ideality allows equivalency of activity and concentration or molar volume, allowing the use of mole fractions to represent the isotopic end members of the solid phase (eq. 3.11).

$$ {}^{i}X = \frac{{}^{i}Ca}{Ca_T} \tag{3.11} $$

Here the superscript i denotes the individual isotope and the subscript T denotes total calcium. The mole fraction of each isotopologue in calcite replaces the single activity coefficient for calcite in eq. 3.10 to yield a final formulation for the precipitation rates of each isotopic end member (eq. 3.12). The ratio of the net rates of the rare ^{44}Ca and

$$ {}^{i}R_N = A^{i}k^{i}X\left[\frac{a_{{}^{i}Ca}a_{CO_3}}{K_{sp}{}^{i}X}-1\right] = A^{i}k^{i}X\left[\frac{{}^{i}Q}{K_{sp}{}^{i}X}-1\right] \tag{3.12} $$

common ^{40}Ca isotopes during calcite precipitation (eq. 3.13) then becomes a function of

$$ \frac{{}^{44}R}{{}^{40}R} = \alpha_f\left(\frac{a_{{}^{44}Ca}a_{CO_3}-{}^{44}XK_{sp}}{a_{{}^{40}Ca}a_{CO_3}-{}^{40}XK_{sp}}\right) \tag{3.13} $$

the kinetic fractionation factor, α_f, defined in chapter 1 (eq 1.3), the activities of the species in solution, the equilibrium constant and the mole fraction.

The primary issue in applying eq. 3.12 within the CrunchFlow model is the choice of definition for the mole fractions ${}^{i}X$. DePaolo (2011) and Nielsen et al. (2012) describe exchange between the aqueous solution and the surface of the mineral, leading to a

formula for the observed fractionation factor (α_p) that is a function of the ratio of the forward (precipitation) and backward (dissolution) reaction rates, i.e. the saturation state of the system. However, some fluid calcium isotope compositions of deep sea sediments have been shown to maintain distinct fluid and solid isotopic compositions deep into the sediment layer, suggesting that in the presence of high clay and organic compound content the backward reaction is suppressed (Turchyn and DePaolo, 2012). In this context the influence of the saturation state on the observed fractionation factor would deviate from the DePaolo (2011) model though a lack of dependence on the backward rate.

Within the CrunchFlow framework, the DePaolo (2011) formulation is most closely represented by a mole fraction calculated using the bulk calcite mineral. In contrast, the influence of the backward rate may be suppressed by utilizing the fluid calcium concentrations to calculate the mole fraction, in which case the ratio of a_{44Ca} to a_{40Ca} (i.e. the ratio of the Q terms) is equivalent to the ratio of ^{44}X to ^{40}X and eq. 3.13 reduces to:

$$\frac{^{44}R}{^{40}R} = \alpha_f r = \frac{^{44}k\,^{44}Ca}{^{40}k\,^{44}Ca} \tag{3.14}$$

Here we demonstrate application of a mole fraction calculated from the fluid vs. from the bulk mineral in modeling the observed fractionation in the clogged wells. The two primary differences between the clogged well system and the more controlled calcite precipitation experiments the DePaolo (2011) model has been previously applied to are (1) the system does not begin at a steady state precipitation regime in which the $\delta^{44}Ca$ of the solid is offset from the fluid by the observed fractionation factor, α_p, and (2) the presence of clays in the borehole and organics in the fluid is highly likely.

The influence of the fluid vs. the bulk mineral in calculating the calcite solid solution is illustrated (Fig. 3.7a) for simulations of fluid $\delta^{44}Ca$ fractionation in well G51. Calcite precipitation is modeled using the parameters listed in section 3.4.3. The calcite precipitation rate constant for ^{40}Ca is -4.1 (Table 3.2), and that for ^{44}Ca is -4.10051, resulting in a fit to the measured data using a kinetic fractionation factor (α_f) of 0.9988 ($\varepsilon \approx 1.18‰$). The model utilizing the fluid concentrations as the basis for the solid solution provides a much closer approximation of the measured $\delta^{44}Ca$ trend than the bulk-mineral-based solid solution. The corresponding observed fractionation factors (α_p) for the fluid- and bulk solid - based mole fractions (Fig. 3.7b) illustrate the differences between eq. 3.13 and 3.14. When the fluid – based mole fraction is used, the observed fractionation factor (α_p) remains a constant value, slightly higher than the kinetic fractionation factor, throughout the simulation. In contrast, when the bulk solid is used, the fractionation factor is closer to unity and time-variant as a result of the influence of the changing composition of the fluid calcium composition relative to the aggregate mineral. Based on the trends shown (Fig. 3.7a,b) it becomes clear that for the clogged well system α_p does not depend upon the difference in isotopic composition of the fluid and solid (i.e. the backward flux) but is best approximated by a constant value that is near the kinetic fractionation factor end member. This result agrees with the findings of Turchyn and DePaolo (2012) and supports the hypothesis that the presence of either clays or organics may suppress the dissolution rate. As a consequence this outcome cannot be considered

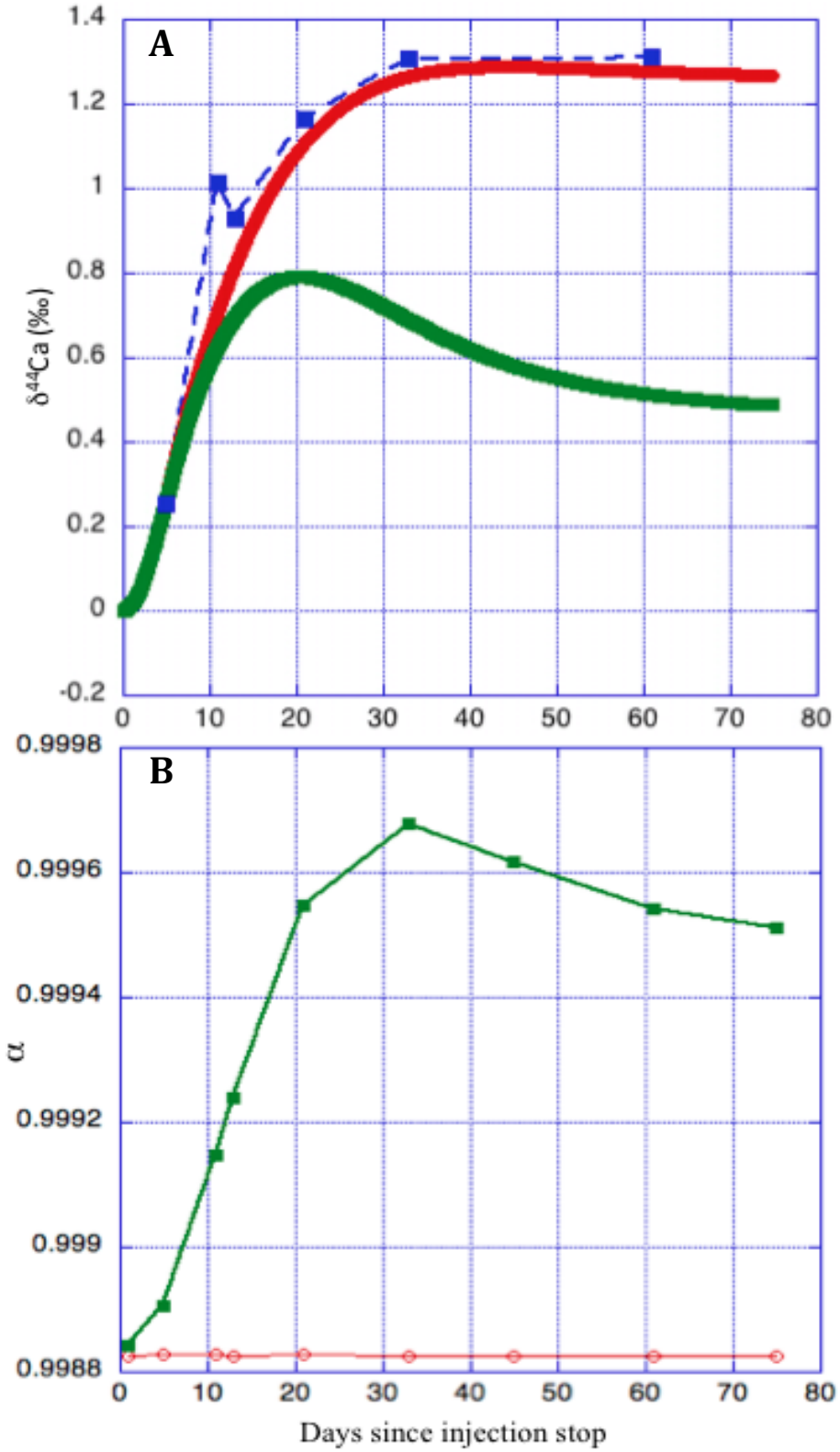


Figure 3.7: (A) fluid $\delta^{44}Ca$ data collected in well G51 (blue), CrunchFlow model of $\delta^{44}Ca$ based on a solid solution calculated using aqueous $CaCO_3$ complex (red) and a solid solution calculated using the mineral $CaCO_3$ composition (green). (B) fractionation factors from both models shown in (A).

a general solution, and it is likely that different systems such as the Fantle and DePaolo (2007) would be better approximated by a solid solution based on the bulk mineral, or even the instantaneous mineral surface composition. Extension of the current model to these systems will be the focus of future research.

Using the fluid – based solid solution model, the $\delta^{44}Ca$ profile for well G52 was simulated for the same kinetic fractionation factor ($\alpha = 0.9988$, $\varepsilon \approx 1.18‰$) as G51 (Fig. 3.8a). The resulting comparison between models and measured data clearly demonstrate that while the $\delta^{44}Ca$ trend of well G51 is accurately reproduced, the simulation of well G52 does not calculate enough enrichment in $\delta^{44}Ca$. The bulk calcite precipitation rate in G52 is lower than in G51 (Table 3.2), however the influx of background water is also substantially less, so there is no clear reason to expect the simulation to succeed in reproducing the G51 trend and yet fail to reproduce the G52 trend. To test for variations in the kinetic fractionation factor between the two wells, a variety of α values were simulated (Fig. 3.8b), including the value calculated from the Rayleigh fractionation model (Fig. 3.4, $\varepsilon \approx -0.92‰$) and a larger fractionation ($\varepsilon \approx -1.38‰$). While the larger kinetic fractionation comes closer to reproducing the range of $\delta^{44}Ca$ in G52, the profile does not reproduce the observed trend and the maximum fractionation is still substantially underestimated. These results suggest that as the fluid reaches equilibrium with the solid at late time in G52, an additional process influencing the fractionation of calcium causes enrichment in fluid $\delta^{44}Ca$ not observed in G51 and not currently accounted for in the CrunchFlow model. The following section will address Ca^{2+}:CO_3^{2-} ion activity ratio as potential cause of this additional enrichment.

3.4.5 Ca^{2+}:CO_3^{2-} ion activity ratio

As demonstrated in the previous section, the TST-style reaction rate law generally utilized in multi-component reactive transport models such as CrunchFlow relies upon the product of ion activities (Q) to determine the overall saturation state (Q/K_{sp}) of the fluid with respect to a given mineral. This means that for a fixed saturation state the model is insensitive to variations in the ratio of ion activities. However, as described in section 3.2.1, the ratio of these activities is now thought to influence both the bulk reaction rate and the fractionation of calcium isotopes. The potential of this influence readdresses the fundamental difference in biogeochemical behavior between the two clogged well bores. In well G51, the influx of groundwater was more than 2x greater than that in G52, however the decline in acetate, sulfate and calcium were remarkably similar. This behavior required changes to the simulation parameters between wells, to account for a larger bulk microbial acetate metabolism in well G52 and a larger flushing of unamended groundwater in G51. This difference suggests that a higher carbonate generation rate should be achieved in well G52 relative to G51 as a result of elevated microbial metabolism. To observe this behavior, the speciated concentrations (after both primary and secondary reactions are calculated) of calcium (Fig. 3.9a), carbonate (Fig. 3.9b) and the ratio of speciated calcium to carbonate (Fig. 3.9c) as a function of time for both wells are calculated. While the simulated calcium profiles of G51 (red line) and G52 (blue line) are not substantially different, there is a clear difference in the carbonate

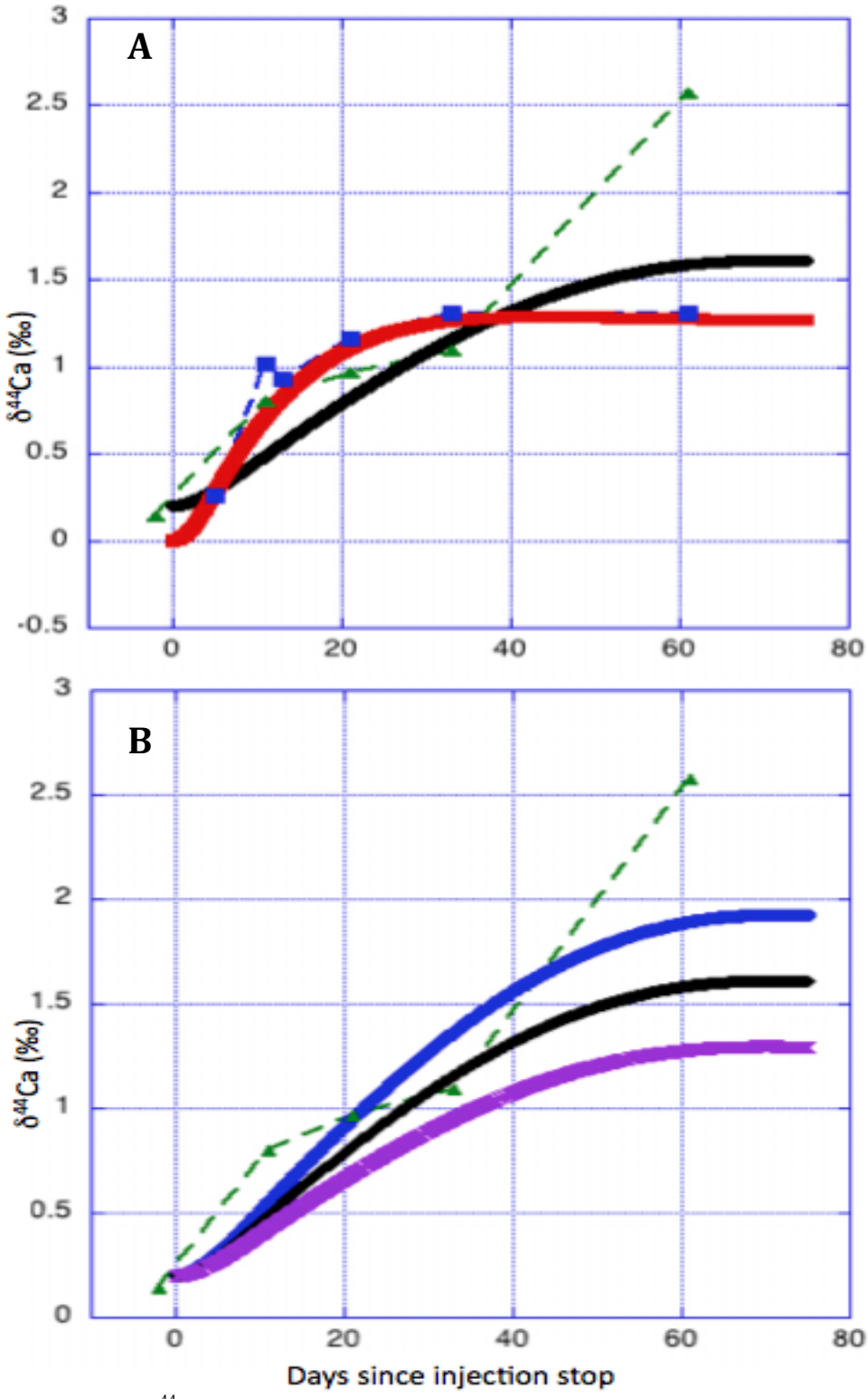


Figure 3.8: (A) $\delta^{44}Ca$ datasets for well G51 (blue) and G52 (green) and corresponding CrunchFlow simulations of G51 (red) and G52 (black) for a single kinetic fractionation factor ($\varepsilon \approx -1.18‰$). (B) $\delta^{44}Ca$ dataset for well G52 (green) and a suite of simulation with kinetic fractionation factors of $\varepsilon \approx -0.92‰$ (purple), $\varepsilon \approx -1.18‰$ (black) and $\varepsilon \approx -1.38‰$ (blue).

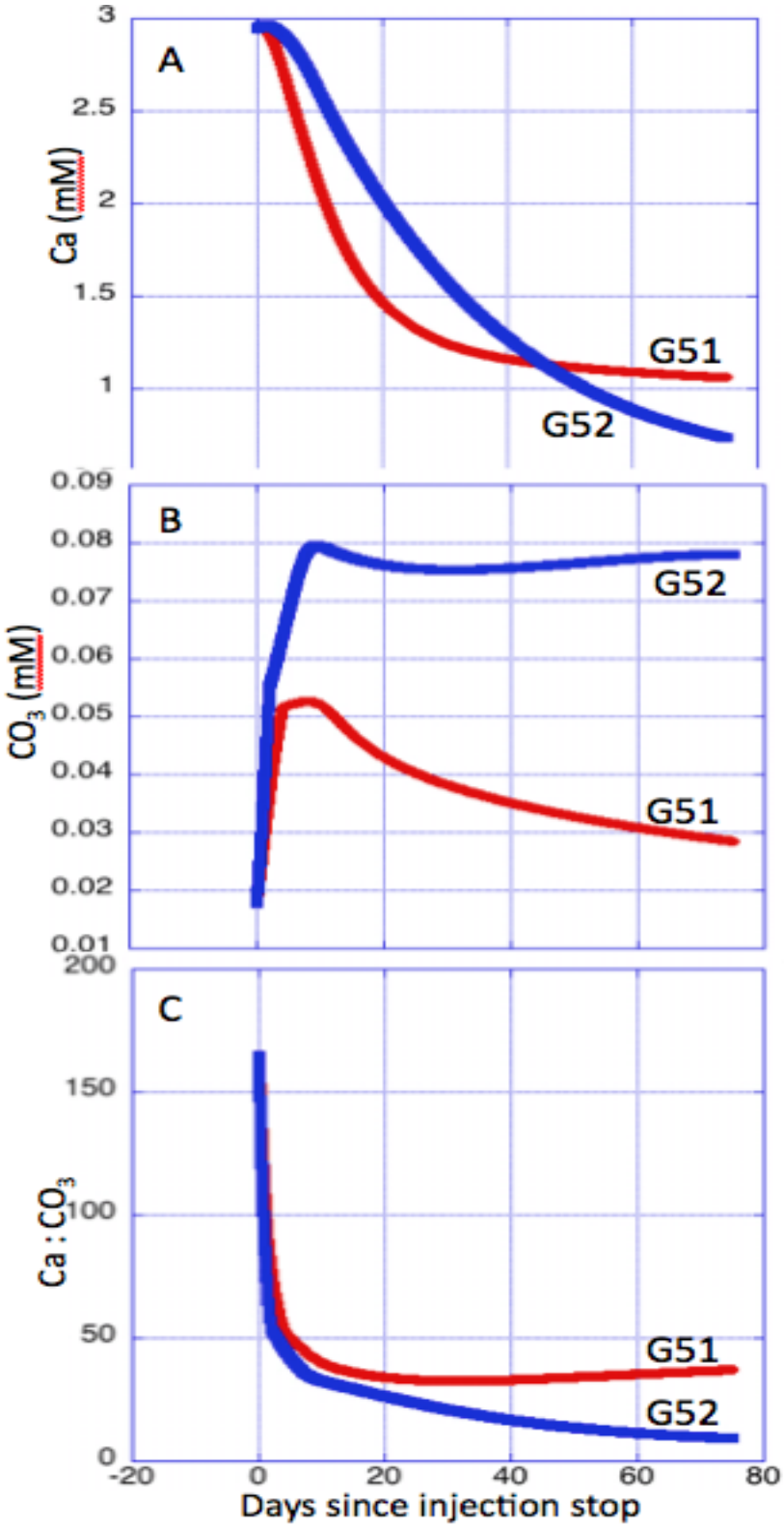


Figure 3.9: (A) speciated $Ca^{2+}_{(aq)}$ concentrations as a function of time in wells G51 and G52 from associated CrunchFlow simulations. (B) speciated $CO_3^{2-}{}_{(aq)}$ concentrations and (C) Ca^{2+}:CO_3^{2-} ion activity ratios for G51 and G52.

concentrations between wells. As suggested, the carbonate in G52 is higher than in G51, and maintains an elevated concentration of ~80 μM for most of the simulation. In contrast carbonate production in G51 peaks at ~50 μM by day 10 and then declines thereafter. The resulting Ca^{2+}:CO_3^{2-} ratio reaches a minimum of ~37 in well G51 before returning to higher values, whereas G52 continues to decrease to ~9.5 by the end of the simulation.

To account for the effects of variable Ca^{2+}:CO_3^{2-} ion activity ratio on the $\delta^{44}Ca$ trends measured in these wells, the speciated concentrations from the CrunchFlow simulations are used in an analytical model of calcium isotope fractionation (Nielsen et al., 2012). The analytical model is designed to simulate the fractionation of calcium between the fluid and mineral phases based on the addition (precipitation) and removal (dissolution) of individual ions at available kink sites on the mineral surface. Calcium fractionation in the fluid phase is calculated using a single formula for both spiral growth and 2D nucleation regimes as:

$$\alpha = \frac{\alpha_k k_A [A] P_B}{k_A [A] P_B + \nu_A P_A \left(\frac{\alpha_k}{\alpha_{eq}} - 1 \right)} \tag{3.16}$$

where α is the observed fractionation factor, α_k is the kinetic fractionation factor ($^{44}k/^{40}k$), α_{eq} is the equilibrium fractionation factor (here equal to one for calcite precipitation), k_A the rate constant of attachment of ^{40}Ca to a CO_3^{2-} kink site, [A] the concentration of speciated ^{40}Ca, P_A the probability of a given kink site being appropriate for ^{40}Ca, P_B the probability of a given kink site being appropriate for CO_3^{2-} and ν_A the rate constant of detachment of ^{40}Ca from the mineral (Nielsen et al., 2012). For lack of specific information on the composition and attachment / detachment rates of the carbonate formed in the well bores, parameters were used from the Nielsen et al. (2012) study for pure calcite. These values were 1.05E-8 (s^{-1} m^{-1}) for the attachment rate constants of Ca-40 and CO_3^{2-} (k_A and k_B) and 5.64E-3 (s^{-1}) for the rate constant of ^{40}Ca detachment (ν_A). The probabilities of a given kink site being suitable for ^{40}Ca or CO_3^{2-} were calculated as:

$$P_A = \frac{k_A [A] + \nu_B}{k_A [A] + k_B [B] + \nu_A + \nu_b} \tag{3.17a}$$

$$P_B = \frac{k_B [B] + \nu_A}{k_A [A] + k_B [B] + \nu_A + \nu_b} \tag{3.17b}$$

where ν_B, the probability of a given kink site being suitable to CO_3^{2-}, is considered equal to ν_A (Zhang & Nancollas, 1998; Wolthers et al., 2012; Nielsen et al., 2012). For all calculations the speciated concentrations of ^{40}Ca (A) and CO_3^{2-} (B) were taken from the CrunchFlow simulations of wells G51 and G52 (Fig. 3.9). Given the fitted attachment and detachment parameters from Nielsen et al. (2012), the only variation in the model between the two well bores is the speciated ^{40}Ca and CO_3^{2-} from the CrunchFlow simulation, and the kinetic fractionation factor. Results of the analytically calculated $\delta^{44}Ca$ for both wells is shown (Fig. 3.10) for a single kinetic fractionation factor of

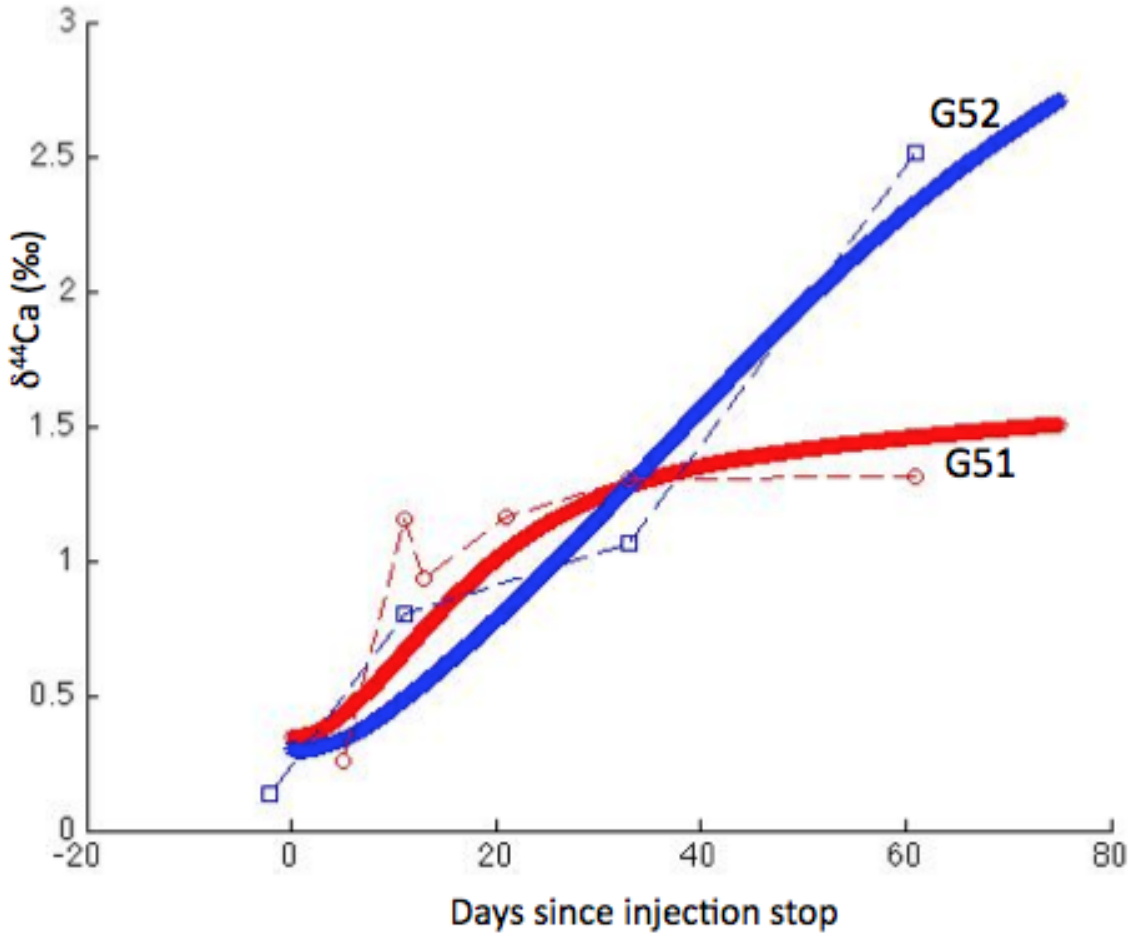


Figure 3.10: Measured $\delta^{44}Ca$ profiles of wells G51 (red open circles) and G52 (blue open squares) and associated calculated $\delta^{44}Ca$ profiles from the Nielsen et al., 2012 model for G51 (solid red line) and G52 (solid blue line).

0.9997 ($\varepsilon \approx 0.3‰$). The resulting correspondence between modeled and measured values in both wells is remarkably good considering that the parameters used in the analytical model were intended for pure calcite in a simplified precipitation environment. In the clogged well bores it is almost certainly true that the carbonate formed during acetate metabolism was not a pure calcite. Furthermore the presence of organics in solution has been implicated as an additional influence on fractionation and the rate of precipitation (DeYoreo, unpublished data). Despite these complications the input of the simulated CrunchFlow ^{40}Ca and CO_3^{2-} speciated values as a function of time was able to account for the variety of reactive transport processes influencing the well bore concentrations and the analytical model proved remarkably robust at predicting the $\delta^{44}Ca$ evolution given these inputs.

The extremely low kinetic fractionation factor used to fit both profiles is likely a result of the choice of rate coefficients in the analytical model. Nielsen et al. (2012) found that the kinetic fractionation factor needed to fit the Tang et al. (2008) data varied from 0.9920 to 0.9962 depending on the parameters used. Without further information as to the parameters appropriate for the solid phase forming in the well bores it is impossible

to consider this particular kinetic fractionation factor a unique solution and therefore it is not considered in disagreement with the 0.9988 value used for well G51 in the CrunchFlow model.

3.5 Summary

Results of this study indicate that the TST-type rate law utilized by most reactive transport codes can be adjusted, with careful treatment of the reactive surface area and solid solution, to simulate the $\delta^{44}Ca$ fractionation associated with carbonate precipitation for the majority of geochemical environments anticipated in subsurface hydrology. However, the solubility product fails to account for the influence of variable Ca^{2+}:CO_3^{2-} ion activity ratios on calcium isotope fractionation. For the conditions modeled in this study, it was found that the TST-type rate law accurately simulated fractionation at a Ca^{2+}:CO_3^{2-} ion activity ratio $\geq$37, but failed to do so at ratios lower than this value. Where the Ca^{2+}:CO_3^{2-} ion activity ratio become low, $\delta^{44}Ca$ is accurately modeled by combining the multi-component capabilities of the TST-based reactive transport code with an analytical model for calcium fractionation as a function of attachment and detachment probabilities of individual ions at the mineral surface developed by Nielsen et al. (2012). The accuracy of combining these approaches motivates future work towards integrating such Ca^{2+}:CO_3^{2-} ion activity ratio influences into the CrunchFlow framework.

Chapter 4

A mesoscale study of isotopic fractionation in biogeochemical reactive transport: I. Experimental design and carbon cycling

4.1 Overview

This chapter describes the design and results of a meso-scale flow-through column study developed to reproduce acetate addition at Old Rifle and generate reactive transport datasets of stable isotope fractionation pertinent to subsurface bioremediation. The scale of the column allows for sample collection volumes necessary to analyze stable isotopes in a variety of reactant – product pairs, generating a uniquely coherent reactive transport dataset of fractionation associated with biogeochemical processes. In this chapter, the control afforded by the column design is employed to execute the first ^{13}C-labeled acetate amendment under Old Rifle conditions. The results of this label study are used to generate a carbon budget for the system, demonstrating the first evidence for a secondary cycling of organic carbon during bioreduction.

4.2 Introduction

One of the primary purposes of this thesis is to apply analysis of stable isotope fractionations to elucidate the processes governing carbon metabolism, terminal electron acceptors and secondary mineral formation during stimulated *in situ* uranium bioremediation. Chapter 2 has shown sulfur isotope fractionation provides a more sensitive indication of the onset of sulfate reduction, thus exposing a previously unobserved trend towards earlier onset of SRB metabolism over subsequent years of acetate amendment. However, the study was restricted to samples from monitoring wells located several meters down gradient of the amended carbon source. As a result the precise location and reactive-transport processes influencing the $\delta^{34}S$ signal detected in the monitoring wells could only be speculated upon. Chapter 3 demonstrated a clear

$\delta^{44}Ca$ enrichment signal associated with secondary carbonate precipitation and developed a reactive transport modeling approach to simulate this fractionation under Old Rifle conditions. However, the study was once again restricted to the samples obtained within well bores and lacked the datasets necessary to validate extension of the calcium fractionation model to porous media flow. It is the purpose of the remaining three chapters to describe the method, results and modeling of a laboratory based large-scale column experiment designed to generate a comprehensive reactive transport dataset of stable isotope fractionations associated with Old Rifle uranium bioremediation.

4.2.1 The e-folding length scale of Old Rifle bioreduction

Field scale models of the Old Rifle uranium bioremediation studies were restricted to calibration and simulation of data obtained from the well bores. The typical well gallery occupies a footprint of 200 m^2, consisting of three rows of down-gradient monitoring wells at distances of 2.5, 5 and 8.5 m from the injection wells (Williams et al., 2011). Dispersivity is then calculated based on inert tracer data collected over these distances, resulting in values of 0.4 – 0.95 m (Fang et al., 2009; Yabusaki et al., 2011). Recent field modeling studies incorporate physical and chemical heterogeneities of the porous media within the flow field domain. These studies used inverse modeling techniques to obtain permeability distributions from the bromide tracer data (Li et al., 2010), and distributions of bioavailable Fe(III) within this heterogeneous structure (Li et al., 2011). While these studies ubiquitously show that the region in close proximity to the injection wells plays a dominant role in the biogeochemical reactivity and U reduction of the system (Fang et al., 2009; Li et al., 2009; 2010; 2011; Yabusaki et al., 2011), there remains little direct evidence of the ability of these models to capture the processes occurring in this highly reactive zone.

The simplified 1D homogeneous reactive transport code presented in chapter 2 for the 2007 field amendment uses a sulfate reduction rate of $2.5x10^5$ mol/kgw/yr calibrated to fit the measured concentration profile in the first row of monitoring wells (Fig. 2.7). At this rate, the modeled spatial profiles between the injection well and down-gradient monitoring wells demonstrate clear exponential decreases as a function of the first order rate laws governing their reactivity. For example acetate injected at a concentration of 3.6 mM is consumed rapidly as a result of this sulfate reduction (Fig. 4.1). As the time since the start of sulfate reduction increases, the distance over which the acetate is oxidized down gradient of the injection wells declines, reaching a value 1/e of the starting concentration at 1.37 m on day 11. Thus the longer electron donor is added to the system, the smaller the e-folding length of the reactant gets relative to the injection point and the sharper the reactive fronts become. Modeling such rapid biogeochemical processes presents a formidable challenge in numerical simulations. Furthermore, as the distance over which a reactive species is consumed decreases, the travel time between this reactive front and the down-gradient monitoring wells increases. As a result, more distance (time) becomes available in which this bioreduction signal may be complicated by secondary reactions and mixed with background water. Therefore, as electron donor is continually supplied to the system, the variations in solute chemistry observed in the down-gradient monitoring wells become a less reliable indication of the processes

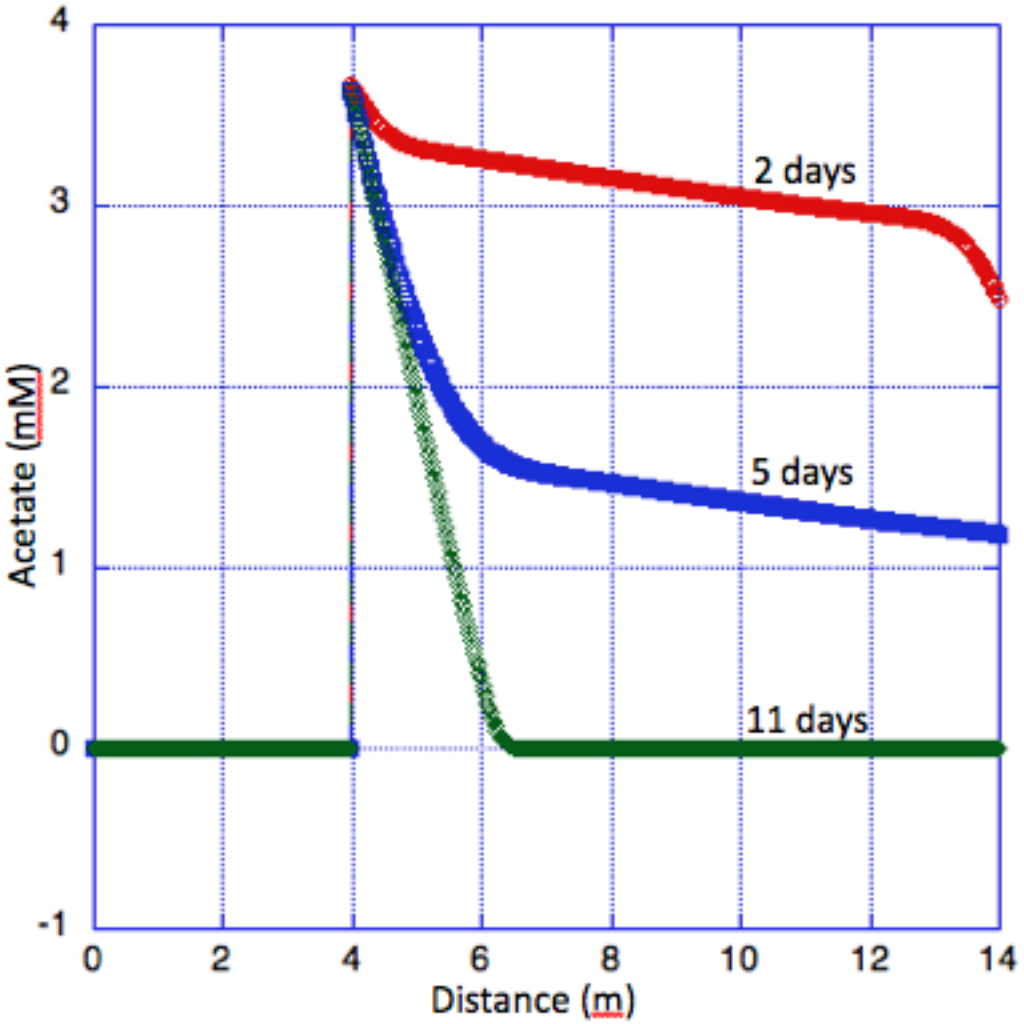


Figure 4.1: Acetate concentration profiles as a function of distance down-gradient using the model presented in Chapter 2. Injection wells are located at 4 m and days are labeled relative to the start of sulfate reduction.

occurring at the zone of reactivity because this front effectively moves away from the point of sampling. Our ability to explain and predict the relative contributions of primary reactivity and secondary processes influencing the concentrations of reactive solutes and their isotopes over this key zone adjacent to the point of injection has never been systematically addressed.

4.2.2 Flow-through column studies

Through-flowing columns packed with porous media to represent subsurface systems have been extensively used in a variety of hydrogeochemical applications (e.g. White et al., 1999; Steefel et al., 2003; Buris et al., 1996). The advantages of these systems as proxies to field scale studies include improved control over physical and chemical parameters, ability to vary these parameters and observe system response in

ways that would be impractical at the field scale, improved ability to monitor and sample the system and correspondingly better constraints on the initial and boundary conditions necessary to model the data. The primary disadvantage is that a column can never precisely reproduce the suite of factors contributing to field scale behavior, and is at best only an *ex situ* representation of a small section of the natural system. Therefore the results obtained from column studies are not necessarily expected to directly extrapolate to field scale behavior, but provide an analog in which to identify primary controls and test the response to variations in boundary conditions.

Column-scale studies using sediment recovered from the Old Rifle aquifer have been applied to address reoxidation of uranium following the end of electron donor supplementation (Moon et al., 2007; Moon et al., 2009), effects of iron vs. sulfate reducing conditions on uranium sequestration (Komlos et al., 2008), and tracking of Fe(III) reduction using ^{57}Fe-labeled goethite (Moon et al., 2010). These studies have made important contributions to our understanding of uranium mobility during bioremediation and utilized column designs appropriate to address the purposes of the intended work. However, as a result the 15 cm long glass columns employed in these experiments could only be sampled for fluid chemistry at the effluent and thus did not capture mobility of the reactive fronts of bioactive species. A column experiment using Old Rifle sediment and groundwater was conducted to identify the reaction network applicable to modeling field-scale bioremediation as part of the Li et al. (2009) study. These columns were 30 cm in length and designed to reproduce field scale flow rates without the need for scaling relationships. While the CrunchFlow model accurately reproduced observed solute profiles in the columns as a precursor to application at the field scale, the dataset was again restricted to a single effluent sampling point and thus could not verify simulation of reactive fronts developing across the system.

Fractionations due to kinetically driven reactivity represent one of several processes that commonly influence stable isotope ratios during reactive transport. Often the stable isotope ratios of a species are more sensitive to mixing processes and re-equilibration than are bulk concentrations (e.g. DePaolo, 2006; Singleton et al., 2004). Therefore in order to accurately address the variations in stable isotope ratios observed during Old Rifle uranium bioremediation we present a meso-scale flow-through column study designed to provide high spatial resolution datasets of solute concentration and isotopic variation during acetate amendment. The study employs multi-port samplers (e.g. Williams et al., 2005) to generate multiple datasets of temporal variation at <20 cm resolution across a 100 cm flow path of porous media recovered from the Old Rifle aquifer. The large size of the system is intended to allow for direct reproduction of field scale flow rates and to generate volumes of fluid sample sufficient to measure stable isotope ratios of a variety of reactant – product pairs. This chapter reports the design of the experiment, the resultant solute chemistry datasets and presents an analysis of carbon mobility and utilization based on introduction of a labeled δ^{13}C tracer.

4.2.3 ^{13}C-labeled acetate

Compound-specific stable isotope analysis (CSIA) is becoming a common means of tracking the sources and degradation processes of organic contaminants through

analysis of the stable isotope fractionations characteristic of microbial metabolism (e.g. Schmidt et al., 2004). While the majority of these studies investigated the fractionation of compounds bearing natural isotopic abundances, a growing subset of research has used labeled isotopic compounds to track the fate of hydrogen, oxygen and carbon originating from organic contaminant sources (Hunkeler, 2002; Meckenstock and Richnow, 2002; Meckenstock et al., 2004). Similarly, isotopically labeled compounds may be applied to heavy metal and radionuclide bioremediation to track the utilization and cycling of organic carbon electron donor added to the subsurface system. ^{13}C-labeled acetate has been used in conjunction with Old Rifle amendments to supplement microbially active samples removed from the aquifer in order to conduct gene expression studies (Chang et al., 2005; Williams et al., 2011), however labeled acetate has never been delivered to the subsurface system.

As part of the mesoscale column study we present the first application of ^{13}C-labeled acetate as a means of tracking carbon through the uranium bioremediation process. The design of the column avoids many complexities encountered at the field scale such as the effect of dilution with background water bearing organic carbon of natural isotopic abundance. This allows a highly enriched ^{13}C label to be introduced to the system, relegating the carbon isotope fractionations associated with carbonate precipitation and microbial metabolism to second order effects, and resulting in an essentially conservative carbon tracer. The tracer dataset is used to generate the first carbon budget for acetate amendment in Old Rifle sediment.

4.3 Methods

4.3.1 Column design

The column flow rate was specified so as to match the average pore water velocity of v = 50 cm/day at the Old Rifle field site (Williams et al., 2011). With direct proportionality to the field scale flow rate, the 100 cm long column served as an analog to the first meter down gradient of the injection wells (Fig. 4.2a). A diameter of 10 cm (cross-sectional area 78.5 cm^2) was selected to (1) provide a ratio of column diameter (D) to mean sediment grain diameter (d) larger than 40 so as to negate the effects of preferential flow along the walls on the mean radial flow distribution (Fand et al., 1990) and (2) to provide adequate sample volume for δ^{34}S analysis of sulfide. Given an average porosity (ϕ) of 0.3 for Old Rifle sediments exhumed, sieved and repacked in columns (Li et al., 2009), the pore volume is then ~2350 cm^3 and the Darcy flux of the column system is calculated as:

$$q = v\phi \tag{4.1}$$

yielding a value of q = 15 cm/day. For the specified cross sectional area the volumetric flux of the column is then 1.178 cm^3/day. A calibrated peristaltic pump operating between the influent reservoir and inlet of the column maintained this volumetric flux. At this volume, assuming 100% recovery, effluent collected for a full 24 hours may be used to analyze δ^{34}S of sulfide in triplicate down to a concentration of 5 μM.

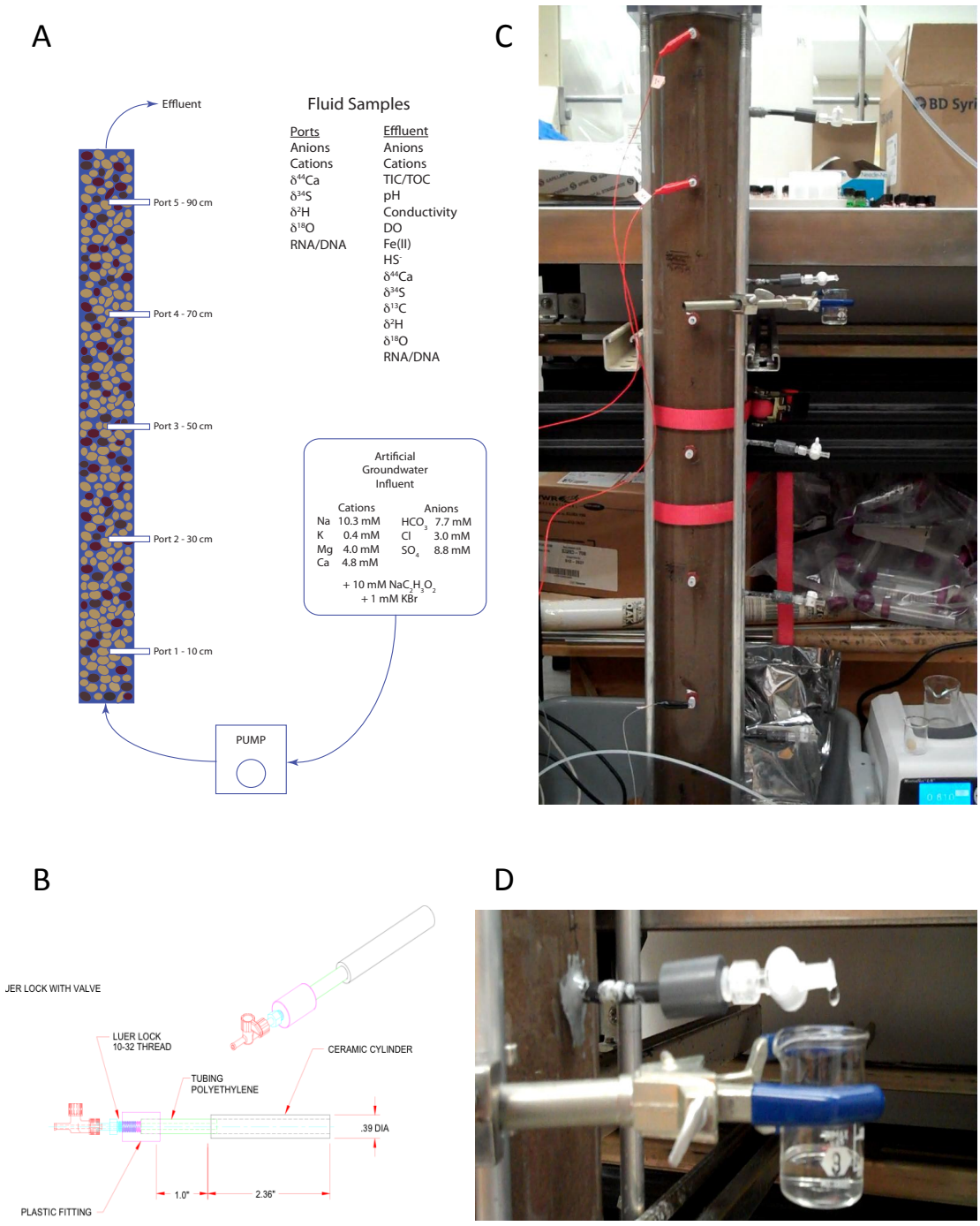


Figure 4.2: (A) schematic of column design including influent artificial groundwater chemistry and fluid samples collected. (B) schematic of side port sampler design (courtesy of Soil Moisture Equipment Corporation). (C) picture of packed, flowing column and (D) close up of sample collected from side port.

Central to the column design is the use of side port samplers to obtain solute chemistry at a high spatial resolution. Consideration was given to the design of these samplers such that a flux-weighted average of the solution could be obtained at each location, rather than simply the fluid adjacent to the wall of the column. In order to

accomplish this requirement, custom designed ports were fabricated in collaboration with Soil Moisture Equipment Corporation (www.soilmoisture.com) consisting of 6 cm long, 1 cm diameter inert porous ceramic tubes connected to plastic leur-lock fittings (Fig. 4.2b). This ceramic is commonly used in lycimeters and combines both high porosity and permeability with a chemically inert composition. Bores were drilled into the side of the acrylic column wall at distances of 10, 30, 50, 70 and 90 cm from the base and the side ports were installed and secured with inert epoxy such that the ceramic tubing extended 5 cm across the diameter of the column at each port (Fig. 4.2a).

Sediments from a previously unamended section of the Old Rifle aquifer were trenched and extracted from beneath the water table at a depth of ~4 m. The sediments were sieved to <38 mm, sealed in opaque, gas-impermeable mylar bags and shipped to the University of California, Berkeley for storage at 4 ºC (Li et al., 2009). These sediments were subsequently wet packed into the column by adding small sections of solids along with artificial groundwater solution to keep the sediment entirely saturated without allowing the solids to settle through a substantial height of water and thus sort during packing. A total of 19.05 kg of sediment were used to fill the column (Fig. 4.2c).

4.3.2 Artificial groundwater

An artificial groundwater recipe was calculated using the speciation code visual MINTEQ (http://www2.lwr.kth.se/English/OurSoftware/vminteq/) to match background well data from the Old Rifle aquifer (Williams et al., 2011). The solution (Table 4.1) was specified to saturation with calcite and ordered dolomite at equilibrium with a 3.5:96.5

Species	Concentration (mol/L)
$NaHCO_3$	7.70E-03
KCl	4.00E-04
$MgSO_4 \bullet 7H_2O$	4.00E-03
$CaSO_4$	4.80E-03
NaCl	2.60E-03

Table 4.1: Concentration of salts added to DI water to achieve an artificial groundwater representing Old Rifle background conditions.

CO_2:N_2 gas headspace. The resulting charge balanced solution (Table 4.2) was mixed in 20 L batches and sparged with the 3.5:96.5 CO_2:N_2 gas (Praxair Co.) for 30 minutes per

Cations	(mol /L)	Anions (mol/L)	
Na	1.03E-02	HCO_3	7.70E-03
K	4.00E-04	Cl	3.00E-03
Mg	4.00E-03	SO_4	8.80E-03
Ca	4.80E-03		
sum:	2.83E-02	sum:	2.83E-02

Table 4.2: Charge balance for artificial groundwater solution

liter to achieve a final dissolved oxygen of >2 mg/L and a pH of 7.0. The solution was transferred without exposure to air to a sterile, 20 L gas-impermeable bag connected with Norprene tubing (Tygon Co.) to the bottom of the column via a peristaltic pump. Influent of this composition was driven continuously up the column for 116 days prior to the start of acetate amendment while flow rate, dissolved oxygen, pH, conductivity, anions and cations were monitored to verify stabilization of effluent values. Following this stabilization period, 50 L of the artificial groundwater solution was mixed and sparged with an additional 41 g of sodium acetate, 0.475 g of 1,2-^{13}C2 labeled sodium acetate, and 5.95 g of potassium bromide. This solution resulted in a final concentration of 9.75 mol/L acetate with a $\delta^{13}C$ of 970‰ and 1.32 mol/L bromide. The total volume was stored in a 50 L inert, gas impermeable bag with a 3.5:96.5 CO_2:N_2 headspace and subsequently transferred in 10 – 20 L aliquots to smaller bags for delivery to the column. This process allowed introduction of multiple inert tracers in addition to the continuous bromide addition in order to track flow field evolution during the electron donor amendment. Over the total 43 days acetate was supplied to the influent of the column, tracer breakthroughs were obtained on days 1, 24 and 40.

4.3.3 Aqueous sampling methods

Samples were collected daily from the five side ports and the effluent for anions, cations, and stable isotopes of hydrogen, oxygen, sulfur and calcium. Weekly samples were also collected for planktonic phase DNA. Additional effluent samples were collected daily for total inorganic carbon and organic carbon (TIC/TOC), pH, conductivity, DO, Fe(II), sulfide concentration and $\delta^{34}S$ and carbon isotopes, and weekly for dissolved methane. The decision to limit atmospherically reactive samples such as inorganic carbon and sulfide to the effluent was done in order to accommodate a passive method of side port sampling that minimized disruption to the flow field. Fluid from side port samplers was obtained by clamping the column effluent tubing closed while keeping the influent peristaltic pump operating and opening a leur lock™ fitting on a chosen side port. As a result fluid was driven from the base of the column to the height of the side port and discharged passively into a collection vial (Fig. 4.2d) while the saturated section of column fluid above this height was held static by the back pressure of the closed effluent tubing. This method negated the need to apply suction to the side ports in order to obtain sample and thus provided a more representative measure of flux-weighted fluid chemistry at each location. Side port fluid was purged for 10 mL before sample was collected and preserved for individual analyses.

Effluent samples sensitive to atmospheric exchange were collected by connecting the end of the effluent tubing to a degassed 50 mL glass syringe with a low-friction plunger. Once fluid had filled the syringe at the flow rate of the column, a needle containing a 0.2 μM PTFE filter was fitted to the syringe and sample was pushed into degassed containers with septa caps. This method was used to collect samples for TIC/TOC, $\delta^{13}C$ of organic and inorganic carbon and dissolved methane. TIC/TOC measurements were made on a Shimadzu Total Organic Carbon Analyzer (TOC-VLSH) where the organic fraction was obtained as the difference between total carbon and inorganic carbon. Samples for Fe(II), sulfide and dissolved oxygen were collected in the

glass syringe and immediately analyzed using a HACH DR2500 spectrophotometer with a photoilluminator using methods 8146, 8131 and 8316, respectively (HACH, 2003). Anion samples were collected and filtered directly into 0.5 mL auto sampler vials for analysis on a Dionex DX120 ion chromatograph. Cations were filtered and acidified with trace metal grade 12 N HNO_3 for later analysis on a Perkin Elmer SCIEX Elan DRC II quadrupole ICP-MS with a dynamic reaction cell (DRC) using ammonia as a reaction gas to remove polyatomic interferences. Hydrogen and oxygen isotopes were filtered into 5 mL glass vials with septa caps and analyzed at the Laboratory for Environmental and Sedimentary Isotope Geochemistry at the University of California, Berkeley using a GV Isoprime isotope ratio mass spectrometer. Hydrogen measurements are made by coupling the Isoprime to a Eurovector Elemental Analyzer (EuroEA3028-HT) and oxygen measurements are made using a Liquid Autosampler (EuroAS300). Carbon isotopes were measured in the inorganic carbon fraction by reaction with H_3PO_4 in a degassed headspace prior to measurement in a Micromass JA Series Isoprime mass spectrometer fitted with a trace gas pre-concentration system and a Gilson auto-sampler (Torn et al., 2003). Organic carbon $\delta^{13}C$ was prepared by calibrated acidification with HCl in 500 μL tin capsules to bring pH down to a range in which inorganic carbon was driven off without volatilizing acetate. These solutions were dried, folded and loaded into a Costech ECS 4010 elemental analyzer coupled to a Thermo Delta V Plus mass spectrometer. Methane samples were collected in the glass syringe and transferred directly to 300 mL evacuated glass vials with septa caps via filter tipped syringes such that no headspace remained in the vials. Dissolved methane concentrations were obtained by replacing a known volume of sample with helium gas, and subsequently measuring the methane concentration of the helium for conversion back to dissolved concentration using an appropriate Henry's Law constant (Conrad et al., 2010). Carbon isotopes of methane were analyzed on the same helium gas sample using a Micromass Trace Gas system to convert the gas phase CH_4 to CO_2 before introducing it into the Micromass JA Series Isoprime isotope ratio mass spectrometer.

Fluid and solid phase $\delta^{13}C$ is reported using standard delta notation as the per mil (‰) disparity from the Vienna Pee Dee Belemnite (V-PDB) reference standard:

$$\delta^{13}C = \left(\frac{R_{sample}}{R_{std}} - 1 \right) \times 1000 \qquad (4.2)$$

where $R = {}^{13}C/{}^{12}C$. Internal standards and replicate samples yielded reproducibility of ±0.25‰ for both aqueous and solid phase $\delta^{13}C$ of DIC and ±0.7‰ for $\delta^{13}C$ of methane. While the organic carbon Montana soil standards reproduced solid phase $\delta^{13}C$ at ±0.3‰, the fluid phase reproducibility increased to ±4‰ as a result of the large ^{13}C label on the acetate, however this increase proved insignificant in comparison to measured values.

DNA samples were directly added from column effluent and side ports to vials containing RNAlater (Qiagen, Valencia, CA.) to stabilize tissues for subsequent analysis. Effluent samples consisted of 150 mL added to 300 mL of RNAlater and side port samples consisted of 5 mL added to 10 mL of RNAlater. Samples were filtered (0.2 μM Sterivex) and divided such that half of the filtrate was processes for analysis and half stored at -80 C for future analyses. Total nucleic acid was extracted according to the protocol described in Ivanov et al., (2009). Extraction, bar-coded pyrosequencing, data processing and statistical analysis are provided in Appendix B.

4.4 Results and discussion

4.4.1 Hydrology

Bromide tracer data indicated continuous delivery of artificial groundwater solution throughout the column for the 43 days of amendment (Fig. 4.3a). Bromide, δ^2H and $\delta^{18}O$ tracers (Appendix A, Table A4) were introduced on days 1 (Fig. 4.3a & b), 24 (Fig. 4.3c) and 40 (Fig. 4.3d). For each day of the experiment, a Darcy flux was obtained by weighing a quantity of effluent fluid collected over a known period of time and dividing by the cross-sectional area of the column, assuming a fluid density of 1 g/cm^3. Based on these data, porosity was calculated (eq. 4.1) using pore water velocities corresponding to $C/C_0 = 0.5$ for each of the breakthrough curves shown. The 24-hour profile was chosen for each analysis based on the distribution of tracer concentration across the column at this sampling time. Results (Table 4.3) show that the deuterium

day	tracer	Darcy flux (cm/min)	pore water velocity at 24 hrs (cm/min)	porosity
1	δ^2H	1.0E-02	3.00E-02	0.33
24	$\delta^{18}O$	8.5E-03	3.07E-02	0.28
40	$\delta^{18}O$	8.4E-03	3.10E-02	0.27

Table 4.3: tracer breakthrough curve analysis of pore water velocity and porosity for multiple inert tracers introduced over the course of the acetate amendment experiment.

tracer introduced on day 1 yielded a porosity of 0.33, which is consistent with previous estimates of Old Rifle sediments recovered and packed into columns (Moon et al., 2007; Li et al., 2009). Subsequent tracers introduced later in the acetate amendment show a slight increase in the pore water velocity in correspondence with a drop in the Darcy flux rate despite a constant pressure applied by the pump to the inlet section of the column. The resulting calculated porosity indicates a decline of about 19% relative to the starting value in association with acetate augmentation. A single falling head measurement conducted prior to the start of acetate addition yielded a permeability value of 1.08×10^{-8} cm^2, however additional falling head measurements were omitted in order to preserve anaerobic conditions in the system.

The tracer data were also used to determine a longitudinal dispersion coefficient for the system, using the pore water velocities and breakthrough times obtained from the 24-hour tracer profiles (eq. 4.3). Here the dispersion coefficient is calculated as a

$$\frac{C}{C_0} = \frac{1}{2}\left[erfc\left(\frac{l - vt}{2\sqrt{Dt}}\right) + \exp\left(\frac{v}{D}\right) erfc\left(\frac{l + vt}{2\sqrt{Dt}}\right)\right] \quad (4.3)$$

function of the average pore water velocity (v), the distance along the flow path (l), and the time (t) at which the chosen C/C_0 occurs (Freeze and Cherry, 1979). The resulting dispersion coefficient of 0.2 cm^2/min yields a dispersivity of roughly 7 cm for the given

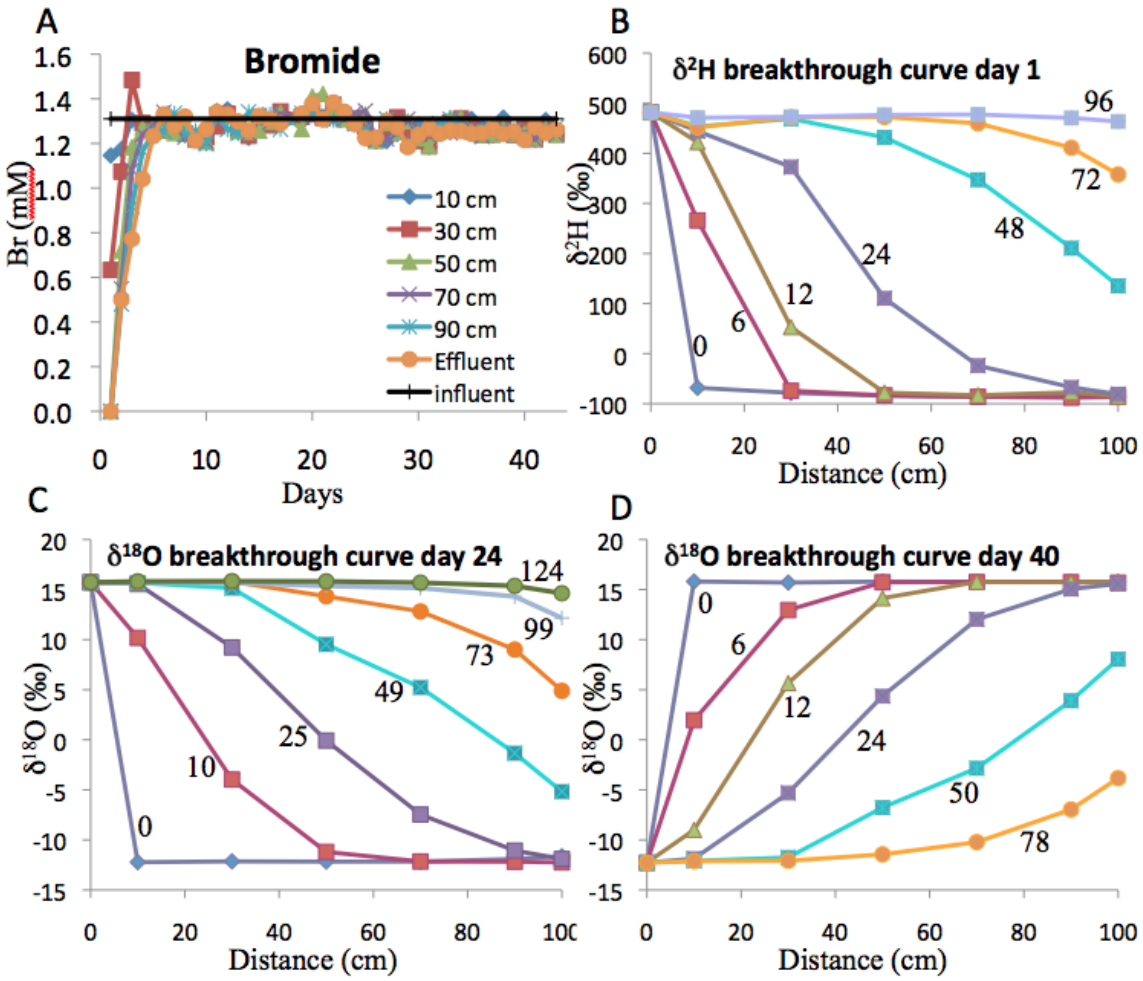


Figure 4.3: (A) bromide concentration profiles for all side ports and effluent over the 43-day acetate amendment. (B) deuterium breakthrough curve starting on day 1 of acetate addition, numbers correspond to hour since start of tracer addition. (C) $\delta^{18}O$ breakthroughs starting on day 24 and (D) on day 40.

average pore water velocity. This dispersivity is substantially lower than the 0.4 – 0.95 m value obtained from field scale tracers and is attributed to decreased grain size distribution and removal of hierarchical heterogeneity effects in the sieved and repacked sediments (Gelhar et al., 1992).

4.4.2 Fluid chemistry

Sulfate concentrations across the length of the column matched the influent value of 8.9 mM for approximately the first 25 days of acetate amendment (Fig. 4.4a; Appendix A, Table A5). Following this period the measured values decreased as a function of distance down the column, reaching a minimum of 0.5 mM by day 41. Time series of sulfate concentration obtained from the side ports indicates that the vast majority of

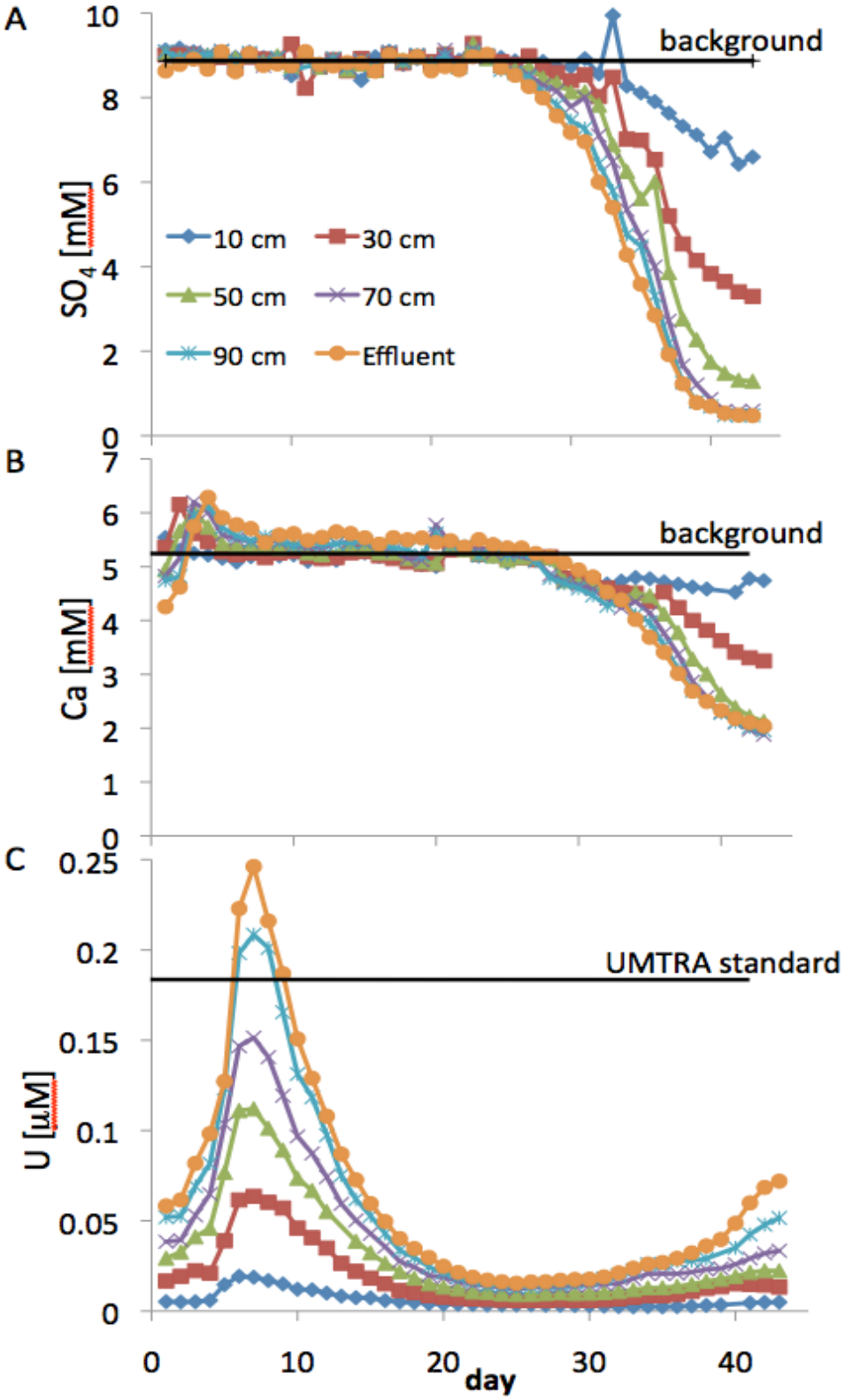


Figure 4.4: (A) sulfate concentration profiles as a function of time along the length of the column, (B) calcium and (C) uranium. Sulfate and calcium influent values and the UMTRA compliance limit for uranium are shown as horizontal black lines.

sulfate reduction occurred over the first 50 cm of the column. On day 43, 27% of the total sulfate reduction occurred over the first 10 cm, 39% occurred between the 10 and 30 cm ports, and 24% between the 30 and 50 cm ports, resulting in 90% of the total sulfate reduction from solution in the first 50 cm of flow. Consequently the reduction of sulfate as a result of SRB activity was completed by 70 cm and preserved in the 90 cm and effluent samples within the column system. The extent to which this reduction signal is preserved at the field scale over the 2.5 m path length between the injection and monitoring wells in unclear.

Calcium (Fig. 4.4b), magnesium and strontium concentration profiles (Appendix A; Table A6) were similar to sulfate in that they remained near the influent value until roughly day 25 before decreasing with distance along the column. This decrease in coordination with sulfate reduction is attributed to carbonate precipitation in conjunction with increased alkalinity as a result of the SRB metabolism as described in chapter 2. A small increase in concentration was noted in the first 5 days of the acetate amendment (Fig. 4.4b). This increase has been observed previously at the field scale (Anderson et al., 2003; Williams et al., 2011) and is attributed to the addition of elevated sodium and potassium concentrations as a result of the acetate and bromide salts, leading to ion exchange and mobilization of the larger divalent cations. In fact, over the first 20 days of amendment, a small increase in calcium concentration is observed at any one time as a function of distance down the column, likely as a result of this exchange effect. Late in the experiment, when carbonate precipitation is occurring in conjunction with SRB metabolism, calcium is removed from solution with distance down the column, from an inlet concentration of 5.2 mM to a minimum of 2.0 by day 43. This removal occurs over the first 50 cm of flow, with no appreciable change in the calcium concentration thereafter.

Uranium was not added to the influent as part of the artificial groundwater recipe because the presence of this solute in μM concentrations is not anticipated to influence the overall system behavior and because omitting this constituent eased restrictions on sample handling and storage procedures. As a result, uranium concentration profiles in the side ports and effluent are entirely the result of exchange between the fluid and Old Rifle sediments (Fig. 4.4c). This effect is reflected in an observed systematic increase in concentration with distance down the column at any given point in time, from a non-detect influent value to a maximum effluent value of 0.25 μM on day 7, which is substantially larger than the UMTRA compliance limit of 0.18 μM (NRC, 2000). It is interesting to note that the highest levels of uranium are observed in the first 12 days of the experiment when iron reduction, and nominally uranium reduction, should be taking place. Uranium concentrations subsequently decline to near-influent values between days 12-32, and then partially rebound, likely as a result of increased alkalinity during SRB metabolism (Davis et al., 2004). The pronounced rise in concentration at early time may be the combined result of introduction of undersaturated influent fluid and ion exchange effects similar to the calcium profiles at early time. The effects of the later have never been observed at the field scale due to the high uranium concentration of influent groundwater. The datasets shown (Fig. 4) and corresponding stable isotope ratios of sulfur and calcium will be discussed further in subsequent chapters.

The primary TEAP product species, Fe(II) and HS^-, were detected in effluent samples (Fig. 4.5a; Appendix A, Table A7), demonstrating an initial period of iron reduction giving way to a subsequent period of sulfate reduction. The slow transition

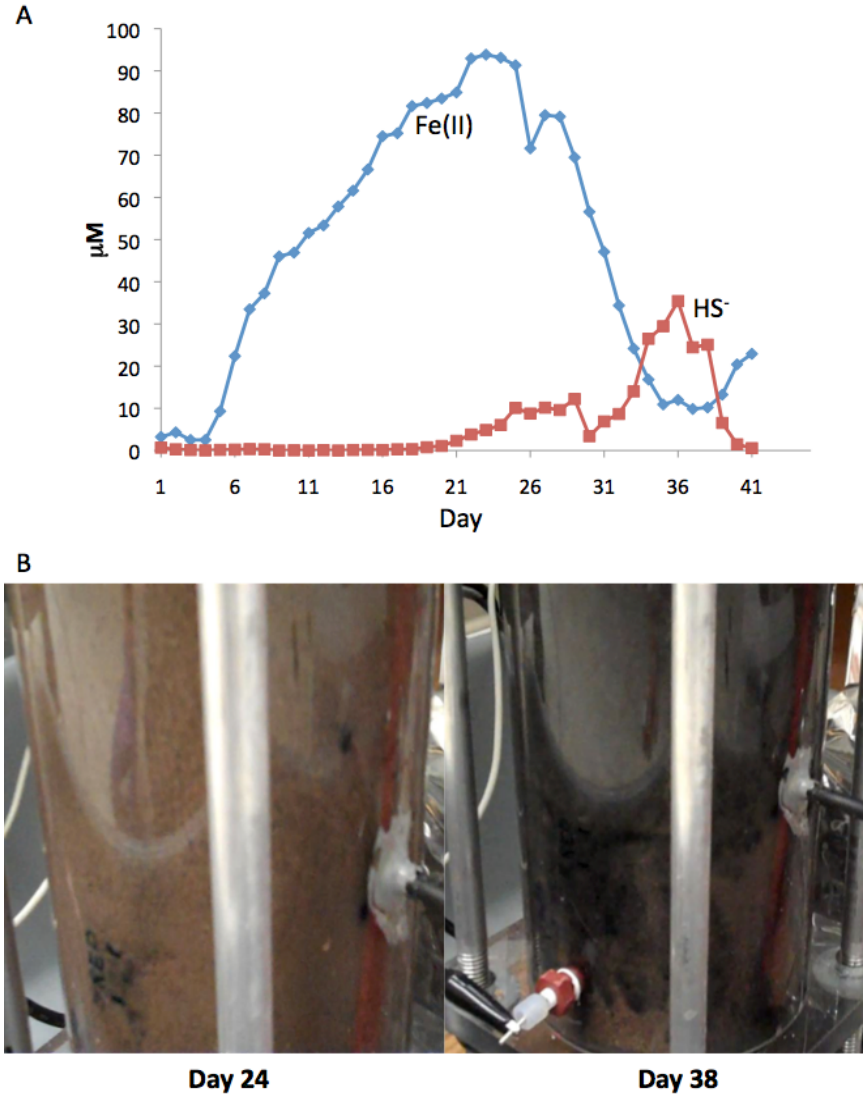


Figure 4.5: (A) Fe(II) and HS^- measured in column effluent and (B) pictures of the lower 30 cm of the column demonstration color changes associated with FeS precipitation.

from elevated Fe(II) to HS^- between days 20 – 34 substantiates the current conceptual model of multiple TEAPs operating in tandem during acetate augmentation (Yabusaki et al., 2011; Williams et al., 2011). Sulfide concentrations are on the order of 40 µM on day 36, whereas sulfate concentrations on the same date decrease by roughly 8 mM over the length of the column, thus requiring a substantial amount of available iron to facilitate secondary sulfide depletion. In addition, a minimum Fe(II) concentration of 10 µM in the presence of excess sulfide could only be achieved by active iron reduction. The presence of secondary FeS precipitates was visually evident in the lower 30 cm of the column (Fig. 4.5b), which turned a characteristic dark color as acetate amendment continued. This evidence supports the contribution of secondary mineral formation to the

observed porosity reduction (Table 4.3). Between days 36 – 43, sulfide concentration declined and Fe(II) concentrations rebounded despite a constant removal rate of sulfate. This reversal corresponds with the approximate time at which 90% of sulfate reduction is accomplished over the first 50 cm of the column. Therefore the trend is considered a reflection of the abiotic sulfide oxidation – iron reduction pathway (Chapter 2; eq. 2.4), oxidizing sulfide and generating excess Fe(II) in the latter 30 cm of the column where sulfide is no longer locally produced. If this pathway is actively influencing the measured effluent values, the data demonstrate an example of a secondary influence on the measured sulfide concentrations between the point of sulfate reduction and the down-gradient measurement as described in the introduction (Fig. 4.1). While the field scale acetate amendment studies are rarely allowed to continue far enough into sulfate reduction to observe such an effect, some evidence is shown by declining sulfide concentrations prior to cessation of acetate in the 2006 field experiment (Druhan et al., 2008).

4.4.3 Tracking carbon

Effluent total organic carbon (TOC) concentrations prior to acetate addition were below detection. Influent TOC was raised to 19.5 mM carbon (9.75 mM acetate) for the 43 days of consecutive amendment (Fig. 4.6a) with a carbon isotope composition of 970‰ $\delta^{13}C$ (Appendix A, Table A8). Total inorganic carbon (TIC) was 9 mM prior to acetate addition with a $\delta^{13}C$ value of -10‰. TIC of the influent solution was maintained at 9 mM throughout the acetate amendment. The increase in effluent TIC during the amendment is therefore attributed to bacterial oxidation of acetate. This pathway is further evidenced by a substantial increase in $\delta^{13}C$ of TIC reflecting addition of the +970‰ TOC label (Fig. 4.6b). However, the conversion of TOC to TIC is clearly influenced by additional processes, as illustrated by the imbalance in effluent concentrations. In the last three days of acetate addition, while the 19.5 mM of influent carbon were completely consumed over the 100 cm column, effluent TIC concentrations were roughly 25 mM, reflecting 9 mM of influent TIC and only 14 mM of TIC from TOC metabolism. In addition an increase in both TIC concentration and $\delta^{13}C$ value between days 5 – 23 is observed despite the fact that TOC effluent concentrations match the influent value. The following section addresses these imbalances by evaluating the possible pathways of TOC consumption and TIC removal from solution.

TOC is added to the column through the influent solution at a constant concentration. The solute then either travels the length of the column and exits in the effluent solution or it is consumed or retained within the column. Retention through sorption to column sediments is considered minimal due to the negative charge of the TOC anion, therefore what TOC is not measured in the effluent solution is assumed to be metabolized within the column (Fig. 4.7a). The majority of microbially oxidized TOC goes to TIC, adding to the influent TIC concentration and either (1) discharging in the effluent solution or (2) precipitating as carbonate minerals. In addition a minor component of metabolized TOC goes to the anabolic pathway to generate more microbial biomass. Finally if the system reaches acetoclastic methanogenesis as observed at the field scale in the clogged well bores (chapter 3), then some TOC may be converted to

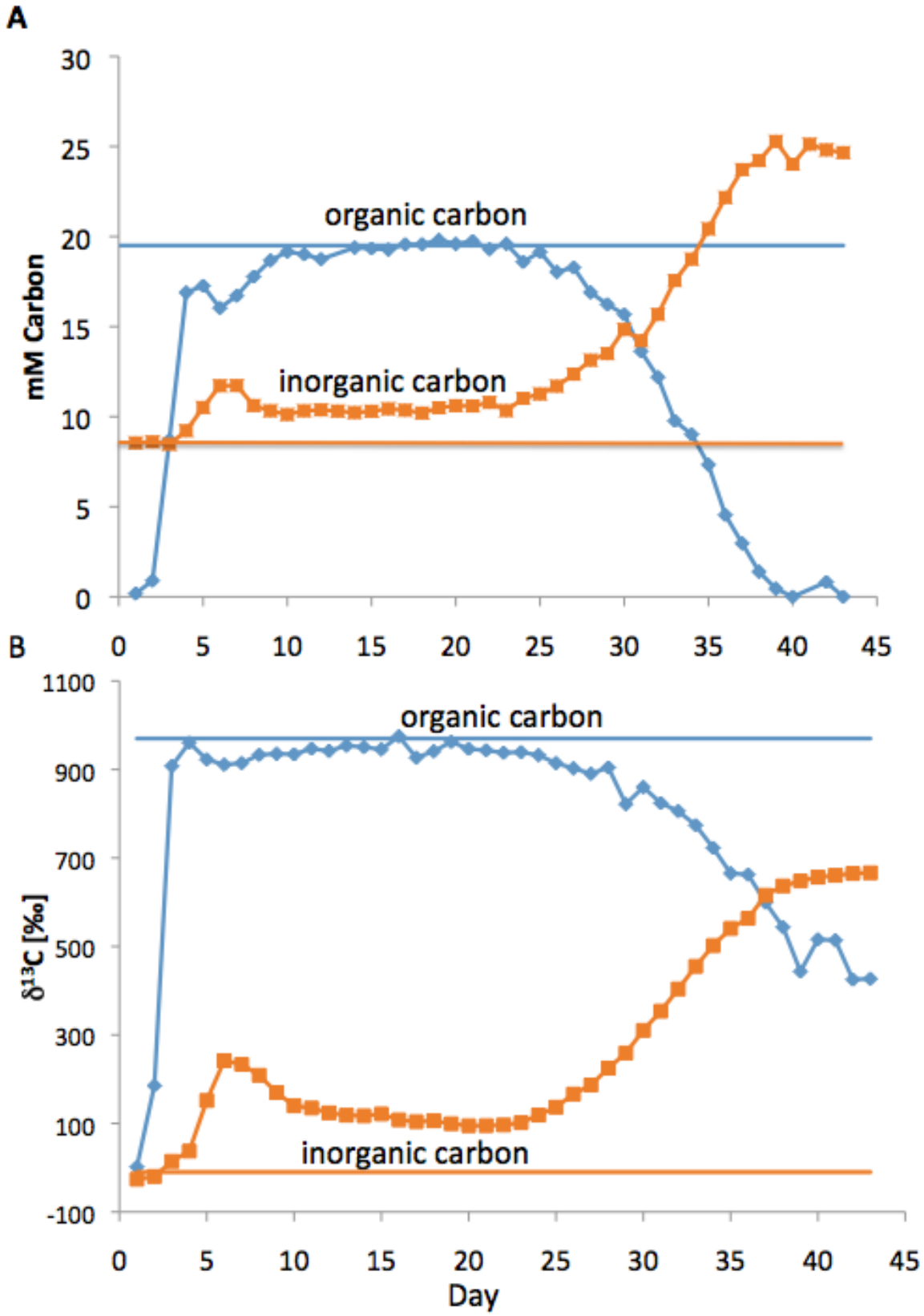


Figure 4.6: (A) effluent TOC and TIC concentrations and corresponding influent concentrations (horizontal lines). (B) effluent TOC and TIC $\delta^{13}C$ values and corresponding influent $\delta^{13}C$.

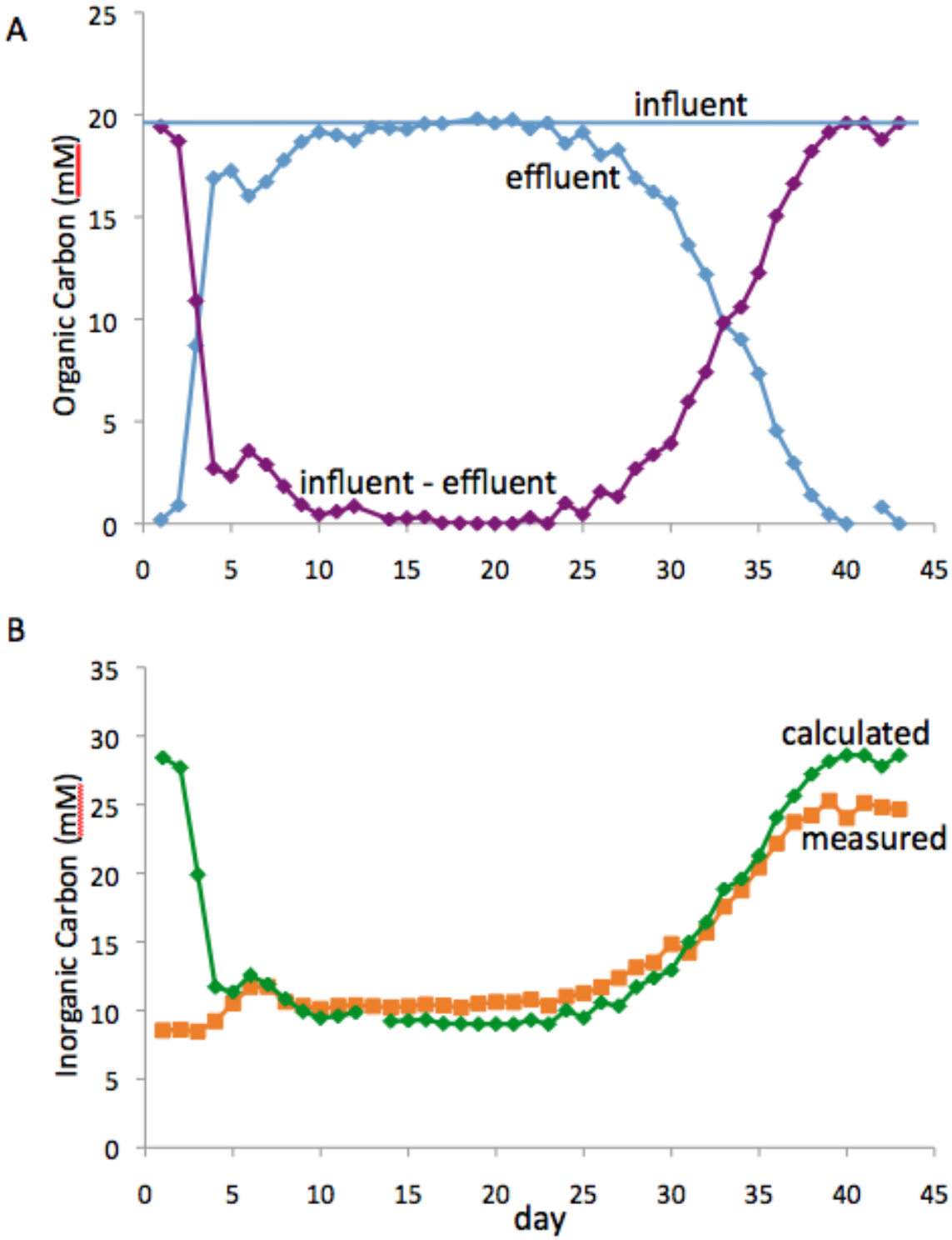


Figure 4.7: (A) measured TOC influent and effluent concentrations and the difference between these values. (B) measured TIC in effluent and the calculated TIC assuming all acetate consumed (as shown in A) is converted to TIC.

methane. In current field scale models of Old Rifle acetate amendment these pathways are considered to describe all important sources and sinks of carbon in the system (Li et

al., 2011; Yabusaki et al., 2011). Since the carbonate, biomass and methane pathways all serve to reduce the amount of TOC consumed during acetate metabolism that is converted to effluent TIC, an upper bound on the TIC concentration should be provided by assuming all TOC consumed in the column was converted to bicarbonate alkalinity such that:

$$TIC_{calc} = \left(TOC_{\inf} - TOC_{eff}\right) + TIC_{\inf} \tag{4.4}$$

where inf and eff represent the influent and effluent concentrations of the corresponding species, respectively. This calculated TIC value is shown (Fig. 4.7b) in comparison to the measured effluent TIC. Disparities between the two values in which the measured TIC is lower than the calculated TIC are attributed to the potential effects of carbonate precipitation, anabolic metabolism and methane production. In addition the large disparity in measured and calculated concentrations in the first few days is largely attributed to the turnover time of the column fluid when acetate was being introduced, however acetate breakthrough was retarded relative to inert tracers. Measured TIC concentrations are slightly higher than calculated values between days 12 – 30. While this disparity is minor, it may indicate the influence of an additional carbon pathway that has yet to be accounted for.

To address the differences in calculated and measured effluent TIC, we consider the additional information provided by the carbon isotope mass balance. The carbon isotopic value of methane measured in the effluent showed a clear $\delta^{13}C$ enrichment reflecting production by acetoclastic methanogenesis of the isotopically labeled acetate (Fig. 4.8). However, the corresponding fluid concentrations of methane were on the order of 0.1 μM, with a maximum value of 0.5 μM on the final day of acetate addition. This minimal amount of methane generation is therefore considered negligible in the carbon concentration and isotopic mass balance of the system. As a result the remaining carbon pathways consist of acetate metabolism generating biomass and bicarbonate, of which the later may precipitate out as carbonate minerals. The effect of carbonate precipitation on the concentration of TIC is already accounted for in the assumption that all TOC removed from solution goes to aqueous TIC (eq. 4.4). Therefore using this calculated value for TIC the carbon pathway is reduced to combined catabolic and anabolic microbial metabolism and the corresponding $\delta^{13}C$ of TIC is calculated as:

$$\delta^{13}C_{calc} = \left(\delta^{13}C\right)_{TOC-\inf}\left(\frac{TOC_{\inf} - TOC_{eff}}{TIC_{calc}}\right) + \left(\delta^{13}C\right)_{TIC-\inf}\left(1 - \frac{TOC_{\inf} - TOC_{eff}}{TIC_{calc}}\right) \tag{4.5}$$

were $(\delta^{13}C)_{TOC\text{-}inf}$ is the 970‰ carbon-labeled acetate, $(\delta^{13}C)_{TIC\text{-}inf}$ is the -10‰ influent TIC value and the concentrations are calculated as in eq. 4.4. The resulting calculated $\delta^{13}C$ of TIC is compared with the measured value of $\delta^{13}C$ in TIC (Fig. 4.9), illustrating excellent correspondence between measured and calculated values during the later, SRB-active portion of the experiment and clear disparities at earlier times. Again the large imbalance at the start of acetate addition is partially attributed to the breakthrough time necessary for acetate to reach the effluent, however this cannot account for the entire disparity. Furthermore the measured $\delta^{13}C$ is substantially enriched relative to the calculated value between days 7 – 28. Various fractionating processes were considered in order to explain this observation. Fractionation factors of up to ε = 10‰ were assigned to carbonate precipitation, iron and SRB metabolism but given the large $\delta^{13}C$

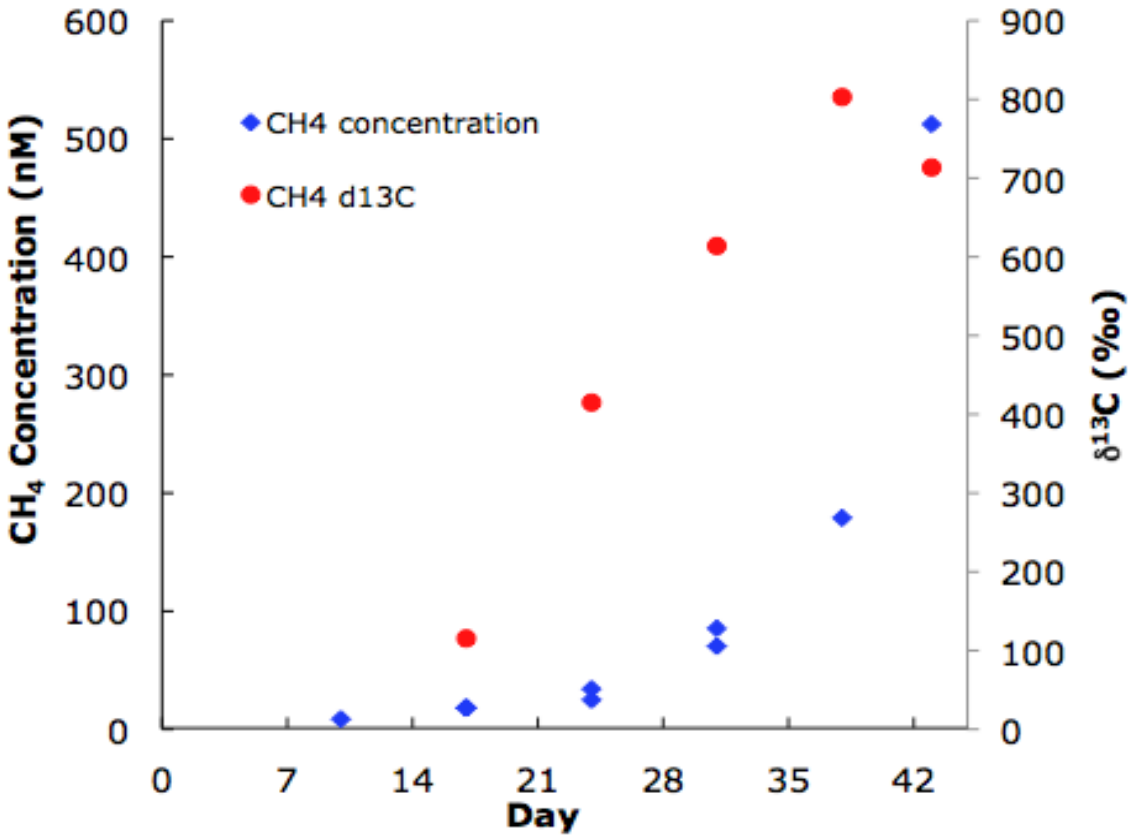


Figure 4.8: Dissolved methane concentrations and corresponding $\delta^{13}C$ values for a time series of column effluent samples.

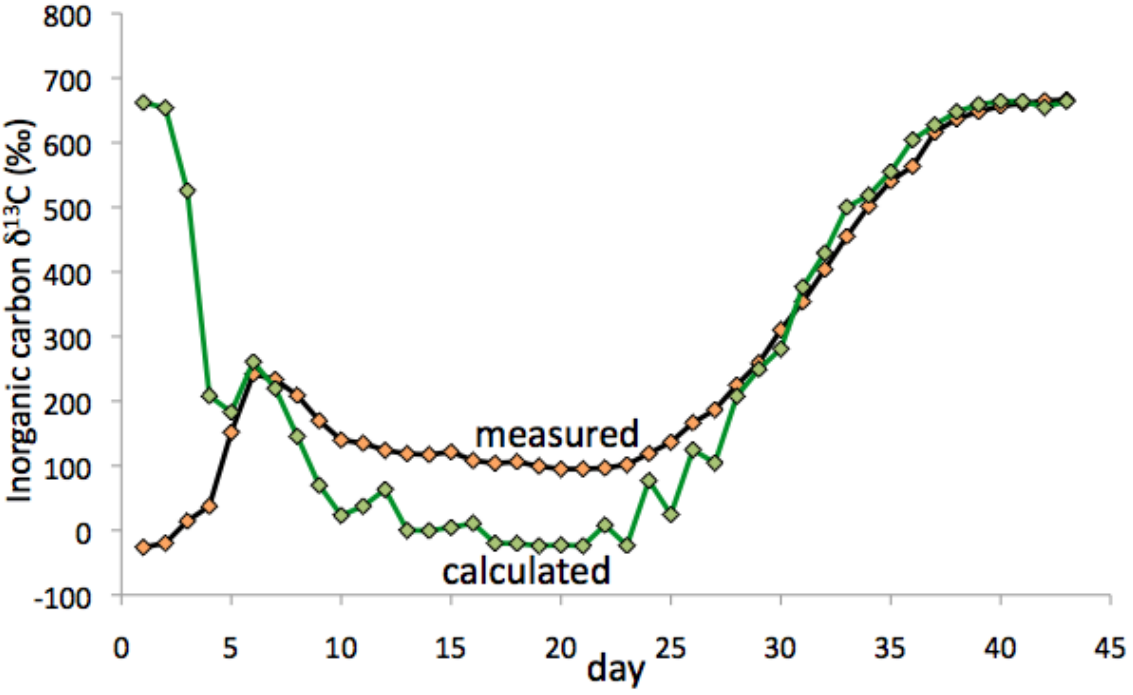


Figure 4.9: measured $\delta^{13}C$ of TIC in effluent and corresponding calculated $\delta^{13}C$ of TIC (eq. 4.5).

TOC label these processes shifted the calculated $\delta^{13}C$ of TIC by a maximum of 0.4‰ and could not support an explanation of the disparity. The difference in measured and calculated $\delta^{13}C$ of TIC is therefore a result of the fact that the model value is contingent upon the difference between influent and effluent TOC (eq. 4.4), which was essentially negligible during this time period (Fig. 4.6a). It is therefore necessary to supply an isotopically enriched TOC source in addition to the influent acetate being pumped into the column over this period of time in order to explain the measured data.

Because this TOC source bears an enriched $\delta^{13}C$ signal, it must be a secondary cycling of the primary carbon delivered as acetate to the column system. Weekly fluid phase DNA analysis yielded the most comprehensive spatial and temporal dataset to date of bacterial populations during an acetate amendment to Old Rifle sediment (Fig. 4.10). Results indicate initial growth of *Azoarcus*, a population typically associated with nitrate reduction, in the first few days of acetate supplementation (Fries et al., 1994). The activity of this population during the early period of amendment may contribute to the observed lag in acetate breakthrough relative to inert tracer data. By day eight members of the family *Geobacteraceae* replaced this population. The iron reducers peaked at roughly 75% of the total community on day 15, before subsequently declining. The cause of this decline is unclear, as SRB populations do not become dominant until much later in the study. A possible explanation for this observation in conjunction with the anomalous enriched $\delta^{13}C$ of TIC is metabolism of lyced bacterial cells. This could be the result of a bacteriophage infection of the *Geobacter* population leading to cryptic growth, however elevated phage cycling is typically observed when the population is stressed (Williams et al., 2005). An alternate mechanism may be activity of Protozoa, eukaryotes capable of feeding on bacterial communities. Protozoa adept at feeding on Geobacter have been documented (Shi et al., 1999), though this process has never been shown during amended bacterial growth at Old Rifle. The DNA samples collected from the column are currently being analyzed for protozoa sequences.

A secondary cycling of organic carbon has never been considered in the design and analysis of Old Rifle bioremediation. Iron reduction requires only 1/8 mole of acetate for each mole of iron reduced (chapter 2, eq. 2.1). As a result previous column studies have been modeled with no substantial decrease in acetate concentrations during iron reduction (Li et al., 2009). In addition, field-scale experiments involve non-uniform dilution of acetate between the injection and monitoring well galleries, further obscuring evidence of organic carbon cycling. Thus the potential influence of a viral or predatory control on the growth of iron reducers presents a substantial update to the current reaction network (chapter 1, Fig. 1.4) utilized to model acetate amended uranium bioremediation.

4.5 Summary

A mesoscale flow-through column was carried out as an analog to the first 100 cm down-gradient of acetate injection wells at the Old Rifle field site. This approach produced high-resolution datasets of solute concentration and stable isotope fractionation over this critical zone of reactivity that will be used to test a multi-component reactive transport model mechanistically incorporating isotopic fractionation of sulfur and calcium species in subsequent chapters. The design of the column facilitated the first

carbon isotope labeled acetate amendment under Old Rifle conditions, and demonstrated evidence for a previously undocumented secondary organic carbon cycling process in conjunction with iron reduction. On going research into the mechanisms of this process is currently focused on the possibility of viral or predatory population controls influencing the *Geobacter* community.

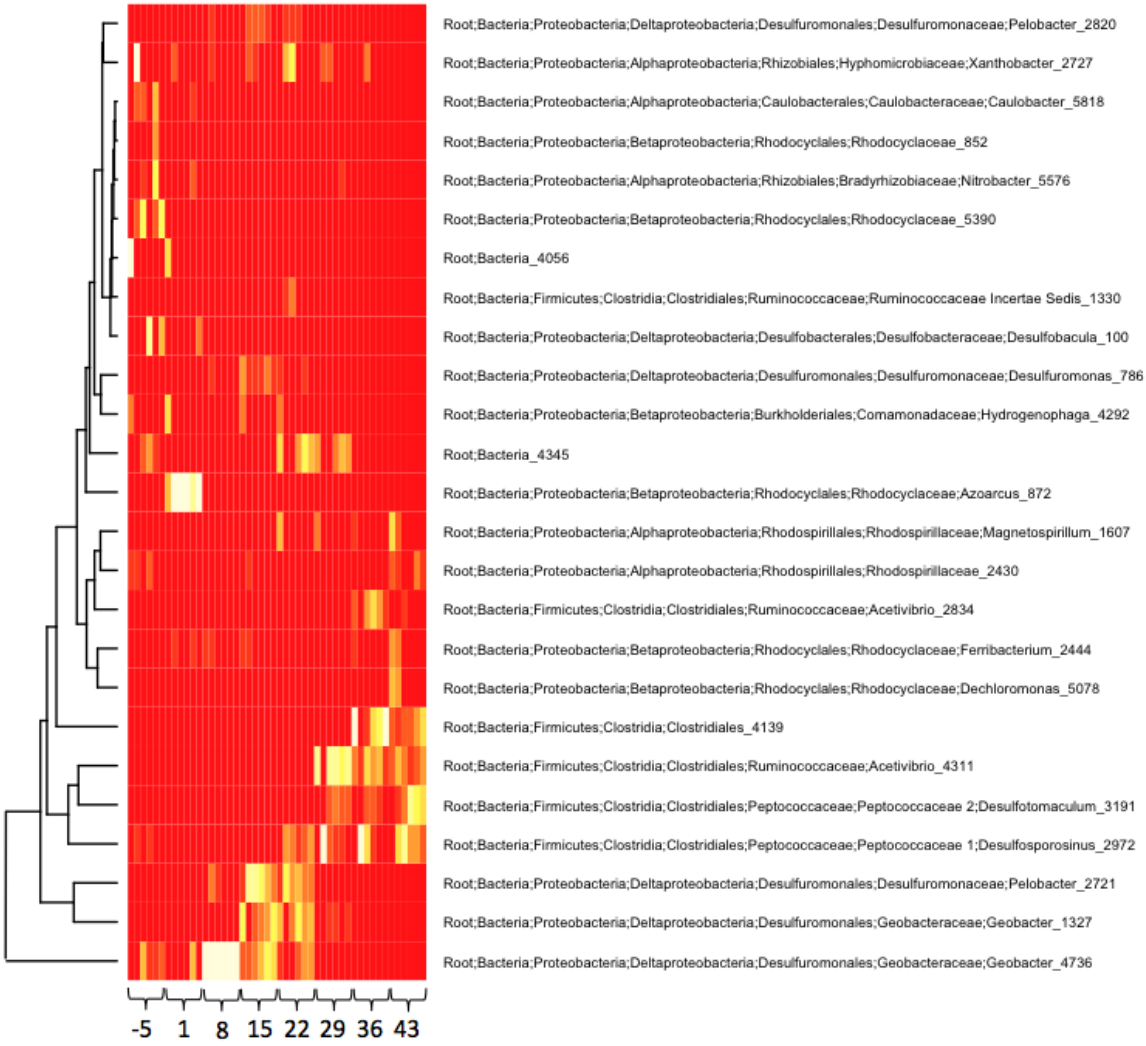


Figure 4.10: heat map of phylogenetic community structure based on DNA sequences of fluid samples collected from side ports and effluent during acetate addition. Numbers at the base indicate sampling day relative to the start of acetate addition.

Chapter 5

A mesoscale study of isotopic fractionation in biogeochemical reactive transport: II. Reactive transport modeling and $\delta^{34}S$

5.1 Overview

This chapter presents a multi-component biogeochemical reactive transport model of the mesoscale column study described in chapter 4. Particular emphasis is placed on the ability to simulate the sulfate TEAP given the high-resolution datasets afforded by the column design. The model is extended to explicitly treat the ^{32}S and ^{34}S isotopes of sulfur in both the reactant and product species of the reduction reaction, resulting in accurate simulation of the $\delta^{34}S$ enrichment of sulfate and sulfide using a single fractionation factor.

5.2 Introduction

The previous chapter detailed the design and results of a mesoscale flow-through column experiment constructed to reproduce conditions of stimulated subsurface uranium bioremediation at the Old Rifle field site in western Colorado (Williams et al., 2011). One of the primary purposes of the column study was to generate high spatial and temporal sampling resolution in the zone immediately adjacent to the injection well gallery in order to discern the influences of primary reactivity and secondary reactive transport processes on measured solute concentrations and stable isotope fractionations. As a result the datasets generated from the column study present a novel opportunity to test the ability of the reactive transport model techniques developed for Old Rifle to simulate the sharp gradients and mobile reactive fronts anticipated in this section of the aquifer, and by extension our ability to predict electron donor delivery, uranium sequestration, and permeability reduction during biostimulation. In addition the mesoscale column provides the datasets necessary to analyze the factors effecting stable

isotope fractionation associated with the bioremediation experiment, and thus support rigorous development of these fractionations as predictive components of the reactive transport model.

5.2.1 Modeling sulfur isotopes

The characteristic fractionation of sulfur isotopes associated with bacterial sulfate reduction is commonly used to identify and even quantify bioactivity in the subsurface environment (e.g. Habicht and Canfield, 2001; Massmann et al., 2003). As shown in chapter 2, the $\delta^{34}S$ fractionation signal provides an excellent indicator of SRB activity under Old Rifle conditions. However, quantifying reduction rates based on measured $\delta^{34}S$, and similarly extending experimentally determined fractionation – rate relationships to field studies is complicated by additional influences (e.g. Stam et al.; 2011). For example the type and availability of organic substrates (Habicht et al., 2005) and the temperature of the system (Canfield et al., 2006) have been shown to influence fractionation of sulfur isotopes during sulfate reduction. In addition the distillation (Rayleigh) equation commonly used to express the relationship between reaction rate and fractionation factor assumes a first order reduction rate (Criss, 1999). This assumption is invalid when describing fractionation due to microbially catalyzed redox transitions such as sulfate and nitrate reduction as these reactions are observed to follow Monod-type rate expressions (Rittmann and McCarty, 2001).

The microbially mediated relationship between fractionation and reduction rate, as well as the suite of complicating factors such as substrate bioavailability, temperature and co-metabolic processes support quantitative treatment of sulfur stable isotope fractionation within a multi-component reactive transport structure. It is the purpose of the current chapter to demonstrate mechanistic incorporation of the stable isotopes of sulfur in a biogeochemical reactive transport code as a means of progressing towards rigorous treatment of such fractionation processes in a multi-component framework.

5.2.2 Monod kinetics

Artificially elevating the concentration of the limiting nutrient in a subsurface environment pushes the system away from steady state by providing a new source of bio-available energy. This energy is utilized by suitable microorganisms through production of enzymatic catalysts for electron transfer. The relationship between the metabolically active, enzyme producing biomass and the electron donor and acceptor substrates is commonly described by a Michaelis-Menton or Monod rate expression (Michaelis and Menton, 1913; Monod, 1942; 1949). The expressions differ only in that the Michaelis-Menton formula describes the reaction mechanism in terms of a free enzyme, whereas the Monod formula uses active cell biomass as the catalyst. A general form of the Monod rate law for microbial reduction of sulfate is derived by assuming an intermediary biomass-substrate complex as (adapted from Roden, 2008):

$$[Bio] + [SO_4] \underset{k_{-1}}{\overset{k_1}{\leftrightarrow}} [BioSO_4] \overset{k_2}{\rightarrow} [Bio] + [HS^-] \tag{5.1}$$

where [Bio] is the cell biomass, [SO_4] is the sulfate electron acceptor, [$BioSO_4$] is the intermediary cell-substrate complex, [HS] is the sulfide product species, and the k terms denote the individual rate constants of the reversible complexation and irreversible reduction reactions. The rate of accumulation of the sulfide product species is then:

$$\frac{d[HS^-]}{dt} = k_2[BioSO_4] \tag{5.2}$$

The classic Monod rate expression makes two assumptions regarding metabolically active biomass. First, it is assumed that the concentration of cell-substrate complex is constant over time, resulting in an expression for biomass concentration as a function of the substrate, cell-substrate complex and rate constants:

$$[Bio] = \frac{k_{-1} + k_2}{k_1[SO_4]}[BioSO_4] \tag{5.3}$$

Second, it is assumed that the total biomass $[Bio]_T$ is also constant, where:

$$[Bio]_T = [Bio] + [BioSO_4] \tag{5.4}$$

Substituting eq. 5.4 into eq. 5.3 and rearranging yields an expression for the cell-substrate complex as:

$$[BioSO_4] = \frac{[Bio]_T[SO_4]}{[SO_4] + \frac{k_{-1} + k_2}{k_1}} \tag{5.5}$$

Subsisting eq. 5.5 into the expression for the rate of product accumulation (eq. 5.2) yields the general Monod rate law for sulfate reduction:

$$r = \frac{d[HS^-]}{dt} = \mu[Bio]_T \frac{[SO_4]}{K_S + [SO_4]} \tag{5.6}$$

where $\mu = k_2$ is the maximum specific growth rate and K_s is the half-saturation constant, calculated as (Koch, 1998; Roden, 2008):

$$K_S = \frac{k_{-1} + k_2}{k_1} \tag{5.7}$$

The rate law described above can be extended to treat systems in which more than one substrate is limiting (Rittmann and McCarty, 2001). Such a situation is described by sulfate reduction during Old Rifle biostimulation in that the system is initially constrained by a deficit of labile organic carbon, but ultimately becomes limited by a depletion of available sulfate as acetate is artificially supplied in excess. This dual limitation is treated as a multiplicative rate law including individual species concentrations and half-saturation constants for acetate and sulfate as shown in chapter 2 (eq. 2.7).

The single and dual Monod rate laws presented here are hyperbolic functions of the general form X/(X+1) (Fig. 5.1). When substrate concentration is high, the value of [SO_4] is far greater than that of K_S and the corresponding microbial reduction rate is close to the maximum (μ). In this high-concentration regime, where $r \approx \mu$, the net rate is essentially zero order. However, as the concentration approaches and falls below the value of K_S, the rate law shifts to first-order behavior. As a result, the half-saturation constant governs the extent of substrate utilization at which this transition point occurs.

Such a variable rate expression requires careful treatment to accommodate the individual isotopologues of relevant sulfur species. The concentration of $^{34}SO_4$ will always be substantially lower than that of $^{32}SO_4$. As a result, if the rate law were applied

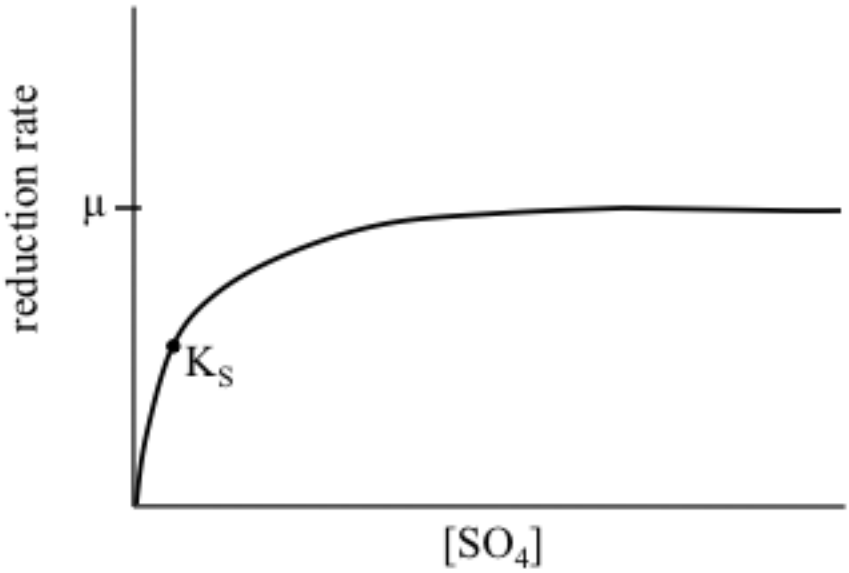


Figure 5.1: Hyperbolic function of the form presented in eq. 5.6 illustrating the relationship between sulfate concentration and reduction rate for a Monod rate law.

literally to these isotopic species, it would lead to a nonsensical fractionation. We address this issue by making appropriate modifications to the Monod formulation that allow it to describe such fractionating processes. Returning to the relationship between isotopic rate laws presented in chapter 1 (section 1.3.1), the zero order rate laws for the individual isotopologues becomes:

$$R = \frac{dN}{dt} = -k \tag{5.8}$$

and

$$R^* = \frac{dN^*}{dt} = -k^* \tag{5.9}$$

where R (R*) is the rate of reaction for the common (rare) isotope and N (N*) is the number of atoms or moles of the common (rare) isotope, here assuming a zero order rate law. As a result the fractionation factor (defined in eq. 1.3) becomes

$$\alpha = \frac{k^*}{k}\frac{N}{N^*} \tag{5.10}$$

which differs from the fractionation factor of the first order reaction by N*/N. Similarly the net rate constant in the zero order regime becomes:

$$k_T = k + k^* \tag{5.11}$$

and as a result the individual isotopic rate constants necessary for a zero order reaction are vastly different than those for first order. In a first order system (chapter 1, section 1.3.1), the rate constants differ by a minor amount, serving to bound the net rate constant and define a kinetic fractionation factor for the system. In contrast the zero order rate requires that the rate constant of the rare isotope (k*) be on the order of N^*/N_T smaller than the common rate constant (k). Thus a rate law such as the Monod expression, which

transitions between zero and first order behavior, presents a substantial complication to direct implementation of explicit rates for individual isotopologues.

A single study has reported results of sulfur isotope fractionation during microbial sulfate reduction within a reactive transport code (Gibson et al., 2011), however the authors erroneously assumed sulfate reduction and $\delta^{34}S$ fractionation obeyed a first order rate law despite utilizing a Monod expression, while simultaneously requiring the net rate constant to equal the sum of the individual isotopic rate constants as in eq. 5.11, which only holds true for the zero order regime. As a result their model misrepresented the relationship between reduction rates and isotopic fractionation. In contrast Maggi and Riley (2009; 2010) rigorously developed a Monod rate law expression for stable isotope fractionation during nitrate reduction, however their model was never extended to a multi-component reactive transport simulation. Here we adapt the Maggi and Riley (2009; 2010) model to sulfate reduction and integrate the expressions for reduction of the explicit isotopologues into the CrunchFlow (Steefel, 2007) framework to present the first rigorous treatment of sulfur isotope fractionation in a multi-component reactive transport code. The simulation capacity afforded by the code allows extension of the fractionation model to treat isotopic ratios of both the reactant and product sulfur species, providing a unique constraint on the associated reduction rate constant.

5.3 Methods

The design and sampling methods of the mesoscale column study are described in chapter 4 (sec. 4.3) including analysis of sulfate and sulfide concentrations. Sulfate $\delta^{34}S$ samples were collected daily from each of the five side ports and effluent of the column. Fluid samples were immediately pushed through 0.2 μM PTFE filters into vials containing $BaCl_2$ in 3x excess of influent sulfate concentrations to precipitate all aqueous sulfate as $BaSO_4$. Sulfide samples were collected overnight by allowing column effluent to discharge directly into a 1L vial containing excess zinc acetate to precipitate ZnS (Carmody et al., 1998). Preserved ZnS precipitate was subsequently separated from solution and reprecipitated as Ag_2S for analysis. Sulfur isotopes were measured at the University of California, Berkeley, Laboratory for Environmental and Sedimentary Isotope Geochemistry using a Eurovector model 3028 elemental analyzer in helium continuous flow mode interfaced with a GV Isoprime isotope ratio mass spectrometer. Long-term internal precision for the instrument is ±0.15‰. V_2O_5 was added to the $BaSO_4$ samples during loading as a combustion aid, yielding improvements on the reported precision. Sulfur isotope ratios are reported in standard delta notation relative to the Canyon Diablo Troilite standard as shown in chapter 2 (eq. 2.5).

5.4 Results and discussion

5.4.1 Sulfur species concentrations and $\delta^{34}S$

The concentrations of acetate and sulfate in the effluent of the column closely track one another as a result of the 1:1 molar ratio of electron donor and acceptor species required to facilitate sulfate reduction (Fig. 5.2). Acetate was added in excess of influent sulfate concentration with the intent of promoting complete reduction of the bioavailable sulfate pool, however, the effluent solute composition clearly demonstrates that acetate became the limiting nutrient at late time. By day 40, effluent acetate concentration (measured as TOC) was not detectable, while effluent sulfate correspondingly stabilized at roughly 0.5 mM. This result illustrates multiple influences on the utilization of acetate in addition to the primary catabolic sulfate reduction pathway. Such processes may include Fe(III) reduction by microbial metabolism and anabolic pathways supporting growth of the active microbial populations. These influences will be tested by incorporation in a multi-component reactive transport model of the column system.

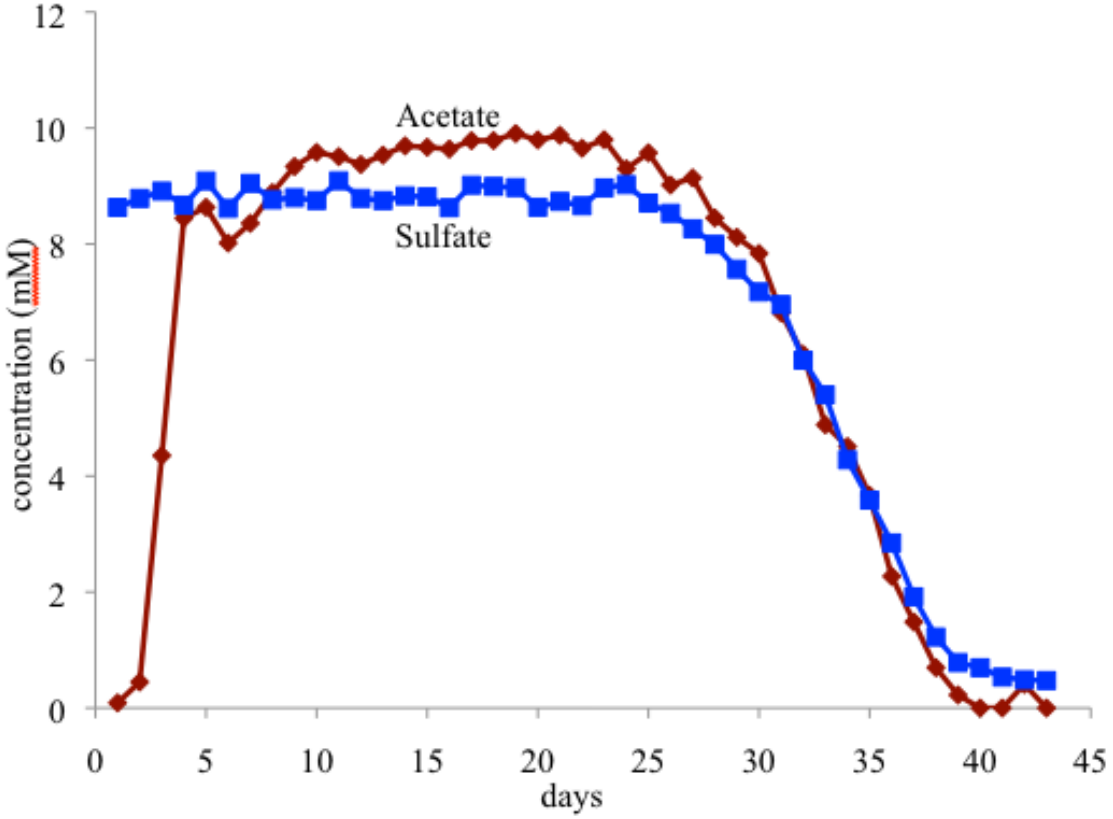


Figure 5.2: Effluent sulfate and acetate (measured at TOC) time series from the mesoscale column experiment for the full 43 days of acetate amendment.

Fluid samples obtained from side ports provided 10 – 20 cm sampling resolution illustrating the development of sulfate reduction gradients across the length of the column (Fig. 5.3). Unlike the sulfate concentration profiles presented in chapter 4 (Fig. 4.4a),

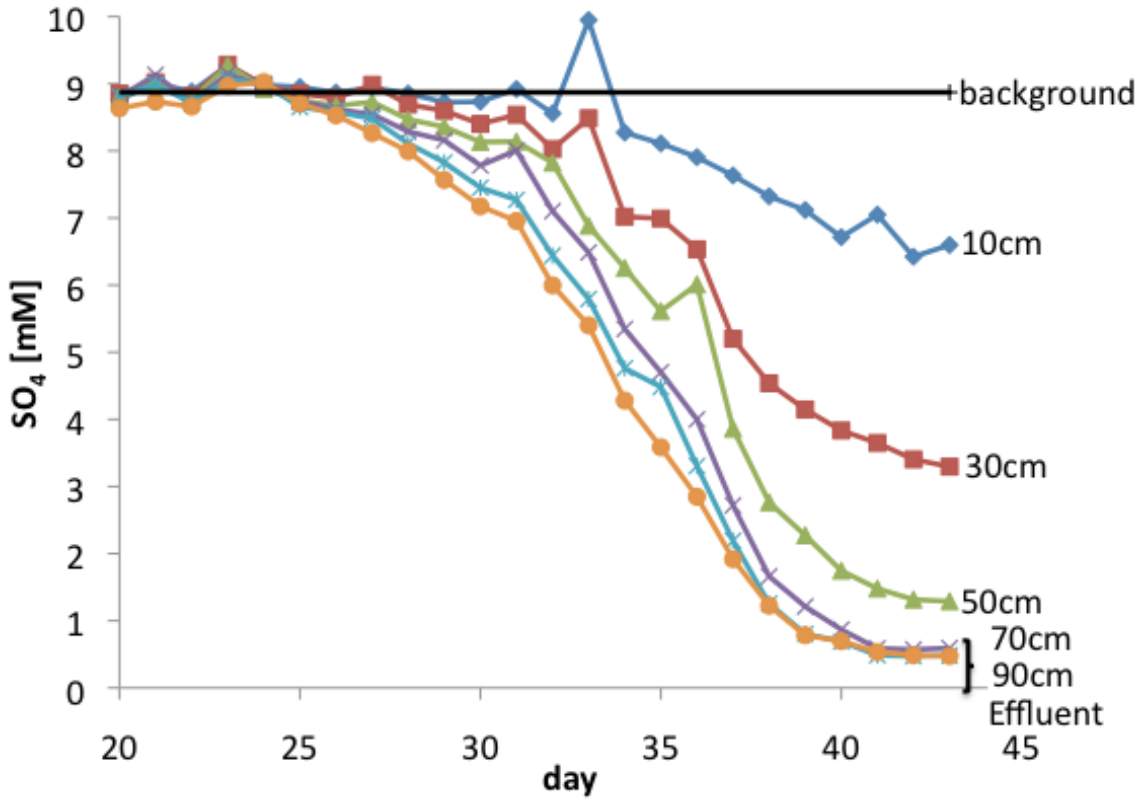


Figure 5.3: Sulfate concentration profiles across the length of the column for the final 23 days of acetate amendment.

here the first 20 days of acetate amendment have been removed to highlight the period of time in which sulfate reduction occurred. Between days 25 – 30 the removal of sulfate from solution appears to occur uniformly across the length of the column, as would be anticipated by a fixed (zero order) reduction rate. However, after day 30 the majority of total sulfate reduction occurring on any given day takes place predominantly in the first 70 cm of the column, reflecting a higher-order reduction rate. This trend becomes more pronounced with time, resulting in sulfate reduction occurring exclusively within the first 70 cm by day 41, with 90% of that reduction occurring in the first 50 cm. Based on the concentration profiles, it appears that the decline in sulfate concentration is preserved in the final 30 cm of the column, however the system circumvents effects of mixing with background water that may be influential in field scale measurements.

Stable isotope ratios of sulfur in these sulfate samples demonstrated a clear enrichment on the order of 36‰ in association with SRB activity (Fig. 5.4a; Appendix A Table A9). On day 43, 10.5% of the total enrichment occurred within the first 10 cm, 19% occurred between 10 – 30 cm, and 28% occurred between 30 – 50 cm, resulting in a total of 57.5% of enrichment within the first half of the column. In comparison, 90% of the total sulfate reduction on this day occurred in the first 50 cm, illustrating an exponential relationship between the extent of reaction and fractionation characteristic of stable isotope enrichment. The values of $\delta^{34}S$ in the final 30 cm of the column all fall within a close range of one another for the majority of the experiment, suggesting that the $\delta^{34}S$ fractionation of sulfate associated with SRB metabolism is preserved in the fluid

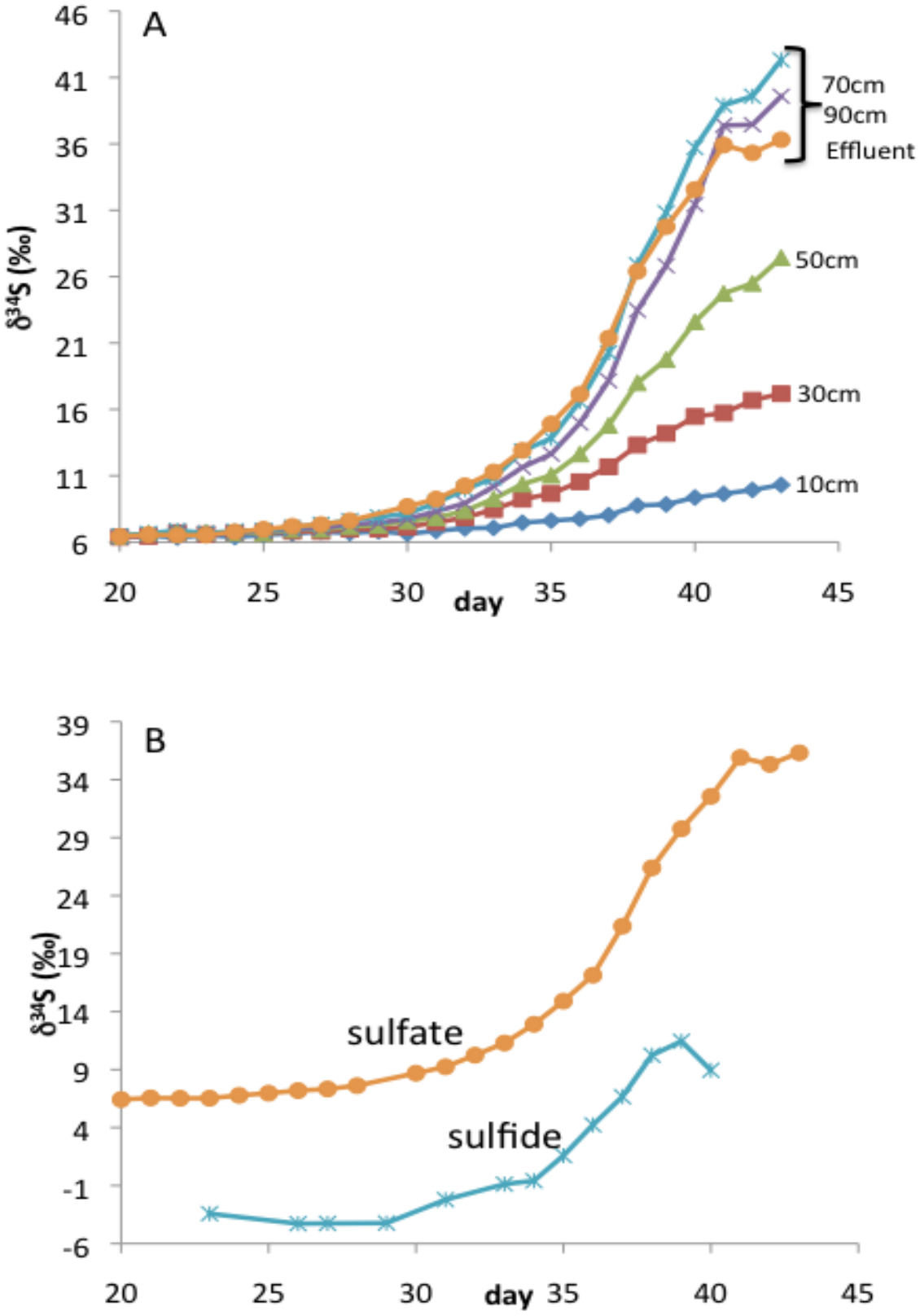


Figure 5.4: (A) $\delta^{34}S$ of sulfate enrichment profiles across the length of the column for the final 23 days of acetate addition. (B) effluent $\delta^{34}S$ of sulfate and sulfide over the same time period.

phase thereafter. However, between days 39 – 43, the $\delta^{34}S$ of the effluent is observed to decrease in comparison to the 70 and 90 cm side port samples. This observation is considered a result of minor amounts of sulfide reoxidation in the effluent tubing, which had to be replaced as a result of clogging. As a consequence, effluent DO concentrations rose from 0.4 to 1.9 mg/L before rapidly returning to low values, likely as a result of aerobically reactive solutes such as sulfide.

The $\delta^{34}S$ of sulfide closely tracked the enrichment observed in effluent sulfate over the period of days 23 – 39 (Fig. 5.4b). Sulfide $\delta^{34}S$ was not collected prior to and after this range of days due to a lack of sufficient concentration for stable isotope analysis (chapter 4, Fig. 4.5a). Fractionation between sulfate and sulfide $\delta^{34}S$ ranged from ε = 11 – 14‰ with a starting value of 11.5‰. Sulfate $\delta^{34}S$ time series collected along the length of the column failed to fit a single Rayleigh fractionation line (Fig. 5.5). Data collected at the 30 cm side port fell between Rayleigh models for ε = 10‰ and 11‰, whereas those collected in the 90 cm side port adhered to a 10‰ value until day 39 before increasing to >11‰ thereafter. This seemingly variable fractionation factor highlights the shortcomings of the Rayleigh distillation model in applications where rate laws are complex and supports incorporation of stable isotope fractionations into a model that can account for these variations.

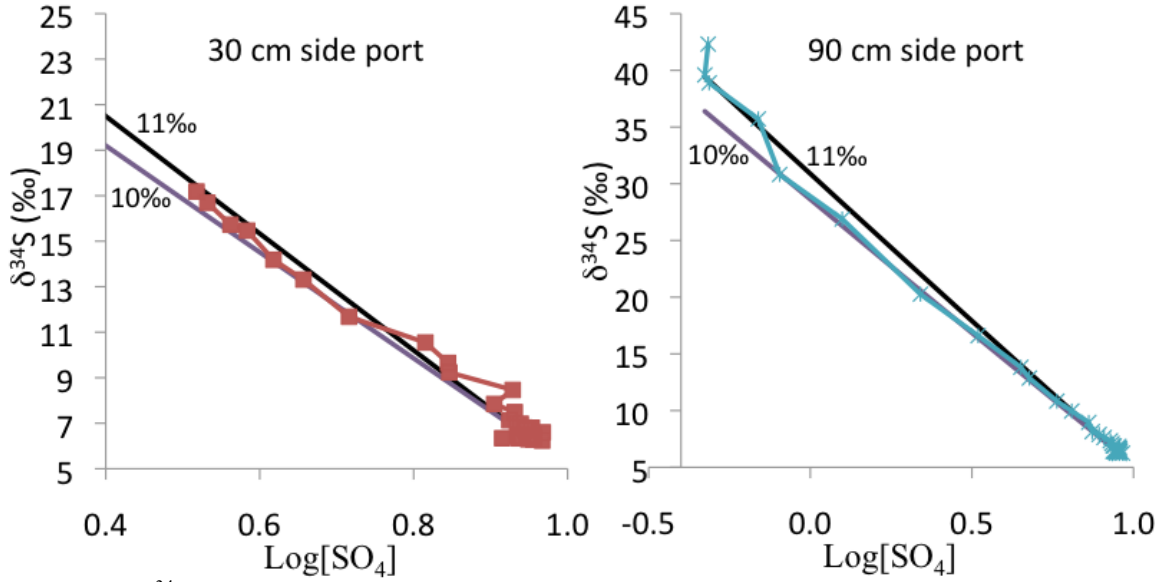


Figure 5.5: $\delta^{34}S$ of sulfate measured in the 30 (left plot, red squares) and 90 cm (right plot, blue crosses) side ports in comparison to Rayleigh models for fractionations of 10‰ (purple line) and 11‰ (black line). x-axis is the fraction of sulfate remaining in solution.

5.4.2 CrunchFlow model of sulfate reduction

The CrunchFlow (Steefel, 2007) model developed to simulate the evolution of fluid chemistry in the clogged well bores (chapter 3, section 3.4.3) was revised to reproduce conditions of the mesoscale column experiment. A new version of the model was utilized, featuring a modification to the dual-Monod rate law driving iron and sulfate

reduction. For an aqueous phase reaction such as sulfate reduction, the rate is calculated as:

$$r = \lambda_{lag}\rho_w \mu B\left(\frac{C_S}{K_{S-half}+C_S}\right)\left(\frac{C_{teap}}{K_{S-teap}+C_{teap}}\right)\left(1-\exp\left(\frac{\Delta G_r + m\Delta G_{ATP}}{\chi RT}\right)\right) \quad (5.12)$$

where r, in units of mol/m^3/yr, is a function of λ_{lag} the microbial metabolic lag term (defined in chapter 2, eq. 2.6), ρ the solution density (1000 kgw/m^3), μ the maximum specific growth rate (mol/g cell/yr), B the volume fraction of cells calculated as $C_5H_7O_2N$ (m^3 cells/m^3), the electron donor and TEAP concentrations and half saturation constants (defined in chapter 3, eq. 3.5), ΔG_r the minimum free energy change of the reaction, ΔG_{min} the minimum free energy change required to drive adenosine tri-phosphate (ATP) synthesis, R the gas constant and T the absolute temperature. The inclusion of the thermodynamic terms honors the free energy change required to drive the reaction and support ATP synthesis by restricting the reduction rate to proceed only above these minima (Jin and Bethke, 2003). The rate law for solid phase TEAPs used for iron reduction differs only in that the density term is replaced by a reactive surface area such that the maximum specific growth rate is entered in units of log(moles/m^2 cell/s). This version of the dual-Monod rate law is utilized in current field-scale models for Old Rifle uranium bioremediation (Fang et al., 2009; Yabusaki et al., 2011).

Both iron and sulfate reduction TEAPs were included in the mesoscale column model (Table 5.1), with yield factors of 8.2%. Iron reduction was modeled as a single Monod rate based on field evidence that Fe(III)-bearing (hydro)oxides remain abundant following multiple electron donor amendments. Iron reduction was allowed to proceed from the start of the simulation, whereas a 20-day lag was imposed on the start of sulfate reduction. In keeping with methods currently utilized for biogeochemical models of field scale acetate amendment at Old Rifle, a zero-order biomass decay term was employed for the SRB population (Yabusaki et al., 2011), at a rate of 0.014 day^{-1}.

stoichiometry	k_{max}	$K_{s\text{-}half}$ (mol/kgw)	$K_{teap\text{-}half}$ (mol/kgw)
$Fe(III) + 0.20833CH_3COO^- + 1.925H^+ + 0.033NH_4^- \rightarrow 0.033C_5H_7O_2N_{FeRB} + 1.6H_2O + 0.25HCO_{(aq)}^- + Fe^{++}$	-7.1	1.0×10^{-5}	
$SO_4^{2-} + 1.082CH_3COO^- + 3.05H^+ + 0.035NH_4^- \rightarrow 0.033C_5H_7O_2N_{SRB} + 2.1H_2O + 2CO_{2(aq)} + H_2S_{(aq)}$	4.80×10^4	1.0×10^{-4}	5.0×10^{-3}

Table 5.1: Iron and sulfate reduction TEAP stoichiometry and associated parameters. Iron reduction is calculated using a bioavailable pool of ferrihydrite. Maximum specific utilization rates are in units of log(mol/m^2 cell/s) for iron reduction and mol/g cell/yr for sulfate reduction. Half saturation constants are consistent with the range of values from Dale et al. (2008) and Fang et al. (2009).

Abiotic heterogeneous reactions and associated rate constants and solubility products are shown in Table 5.2. Initial conditions were established based on the steady state solute concentrations of the influent and effluent solutions prior to the start of acetate addition (Table 5.3). Influent boundary conditions differed from initial conditions only in that acetate increased to 9.7 mmol/kgw, bromide increased to 1.32 mmol/kgw, sodium increased to 22.0 mmol/kgw and potassium increased to 1.58 mmol/kgw. In

stoichiometry	log k (mol/m^2/s)	log K_{sp}
$CaCO_{3(s)} \leftrightarrow Ca^{2+} + CO_3^{2-}$	-4.1	-8.4801
$MgCO_{3(s)} + H^+ \leftrightarrow Mg^{2+} + HCO_3^-$	-8.4	2.9734
$Fe^{2+} + H_2S_{(aq)} \leftrightarrow FeS_{(am)} + 2H^+$	-8.0	3.5
$Fe(OH)_{3(s)} + H_2S_{(aq)} + 2.5H^+ \leftrightarrow Fe^{++} + 0.5S_{(s)} + H_2O + 2OH^-$	-7.5	-19.6
$C_5H_7O_2N_{FeRB} \leftrightarrow C_5H_7O_2N_{FeRB(aq)}$	-2.0	-15.0
$C_5H_7O_2N_{SRB} \leftrightarrow C_5H_7O_2N_{SRB(aq)}$	-2.0	-15.0

Table 5.2: Heterogeneous reactions used to model clogged wells and associated parameters.

primary species	concentration (mmol/ kg H_2O)
pH	7.2
Fe^{2+}	1.0E-08
Fe^{3+}	in equilibrium with iron hydroxide
$SiO_{2(aq)}$	0.35
Na^+	10.6
K^+	0.447
Ca^{2+}	5.30
Mg^{2+}	5.41
SO_4^{2-}	8.8
Cl^-	3.0
$CO_{2(aq)}$	9.0
Acetate	0.0
$H_2S_{(aq)}$	1.0E-15
$O_{2(aq)}$	15.6E-03
NH_4^+	1.0
Br^-	0.0
primary species	concentration (mmol/kg H_2O)
$Methane_{(aq)}$	1.0E-15
$C_5H_7O_2N_{FeRB(aq)}$	1.0E-11
$C_5H_7O_2N_{SRB(aq)}$	1.0E-12

Table 5.3: Initial conditions of aqueous primary species for the start of the mesoscale column simulation.

mineral	volume fraction (m^3/m^3)
ferrihydrite	6.5E-04
goethite	3.6E-04
calcite	4.7E-04
magnesite	1.0E-06
$Fe(OH)_3$	9.4E-04
$C_5H_7O_2N_{FeRB}$	1.0E-06
$C_5H_7O_2N_{SRB}$	1.1E-05
quartz	0.68

Table 5.4: Initial conditions of mineral volume fraction for the start of the mesoscale column simulation.

addition the influent solution contained no biomass. Initial mineral assemblage was based on typical compositions utilized for field-scale models (Table 5.4; Li et al., 2009; 2010). Non-reactive quartz was used to fill the remaining volume fraction to achieve a porosity of 0.32%. Secondary reactions for the model are identical to those used for the clogged well simulation in chapter 3 (Table 3.5).

The model domain is 1D, consisting of 100 grid blocks of 1.0 cm length. Flow is calculated by assigning a permeability of 1.08×10^{-12} m^2 over a pressure gradient of 1.614×10^3 Pa to produce a starting flow rate of 0.15 m/day. The code updates the permeability of the system based on a cubic law relationship with porosity, which decreases as a function of mineral and biomass growth over the course of the simulation.

Simulated effluent acetate and sulfate concentration profiles reproduce the observed trends, including the accelerated consumption of acetate relative to sulfate at late time (Fig. 5.6). Neither the activity of iron reducers or the decay of SRB population influence modeled acetate profile for the given rates. The iron reduction rates are restricted such that effluent acetate concentrations remain near influent values prior to the onset of sulfate reduction. Some evidence based on carbon isotope mass balance (chapter 4) has suggested that a secondary organic carbon cycling process may be supporting a portion of the iron reducing population, though this result is preliminary and has not been included in the simulation. The excess consumption of acetate relative to sulfate is thus

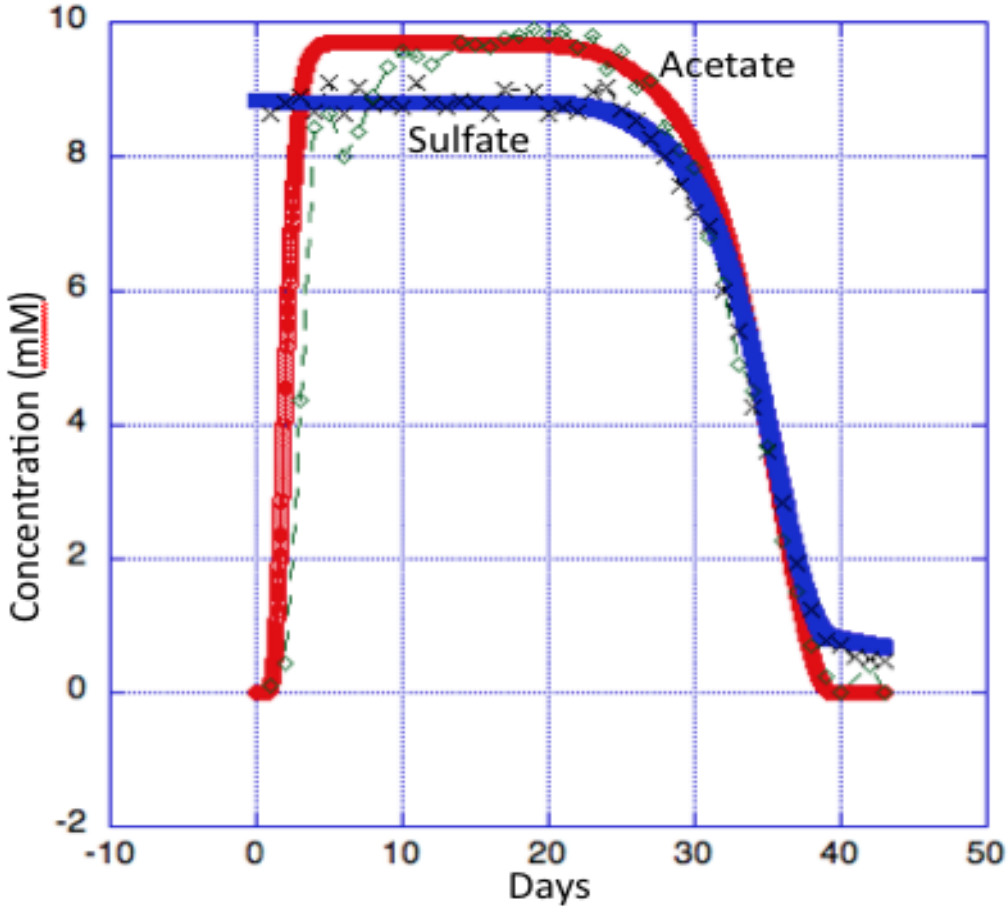


Figure 5.6: measured acetate (open diamonds) and sulfate (crosses) are compared with modeled acetate (red) and sulfate (blue) concentration profiles for the mesoscale column effluent.

entirely due to the anabolic component of SRB metabolism. This anabolism serves to heighten the acetate oxidation rate as well as the overall sulfate reduction rate as a result of increased SRB biomass. The effluent dataset and corresponding model thus provide the first direct evidence to validate the use of an 8.2% yield factor (Rittmann and McCarty, 2001) for SRB growth under Old Rifle conditions.

Proceeding with the sulfate reduction rate established based on the effluent concentration profiles of acetate and sulfate, the simulated sulfate profiles at distances of 10 (Fig. 5.7a), 30 (Fig 5.7b), 50 (Fig. 5.7c), 70 (Fig. 5.7d) and 90 cm (Fig. 5.7e) in the model domain are compared with the concentration profiles of the corresponding side ports. This exercise demonstrates a situation analogous to calibration of field scale reduction rates based on concentration profiles obtained from the monitoring wells, now applied to the zone of primary reactivity immediately adjacent to the injection well gallery. Here, the rate is calibrated based on a concentration timeline obtained 100 cm down gradient of the injection source and the influence of mixing with unamended groundwater is negated. Comparison of the measured and simulated sulfate profiles demonstrates that for the given parameters the model substantially over predicts the extent of sulfate reduction in the first 30 cm of the column and accurately reproduces the measured profiles thereafter. Variation of the half-saturation constants within the range of parameters specified by Dale et al. (2008) and Fang et al. (2009) could not produce an improvement in the 10 and 30 cm simulated solute profiles. Similarly, neglecting the metabolic lag parameter in favor of allowing sulfate reduction to proceed from the start of the simulation using a low starting biomass (as in Yabusaki et al., 2011) produced the same rate distribution. As a result the dampened reduction rate measured in the 10 and 30 cm side ports relative to the simulated profiles are attributed to heterogeneity unaccounted for in the homogeneous model. This heterogeneity may be physical or microbial in nature. Dividing the model domain into sections and assigning unique starting compositions to each, it is possible to improve the fit of the simulated concentration profile by either reducing the initial SRB biomass or increasing permeability in the first 20 cm. At present the data collected from the mesoscale experiment cannot constrain the relative influence of these factors, but ongoing DNA/RNA analysis of the side port samples may provide some insight into the distribution of the microbial populations as a function of distance away from the amendment source.

The overestimate of sulfate reduction in the first 30 cm of the column highlights the limitations of a homogeneous simulation even in a simplified system. The effects of physical and mineralogical heterogeneity have been addressed in recent field scale models (Li et al., 2010; 2011; Yabusaki et al., 2011) however these distributions are largely predicated on inert tracer data obtained from the well bores. Spatial heterogeneity in the microbial distribution has been indirectly modeled as a result of heterogeneous distribution of Fe(III) mineral phases, but such variations have never been directly demonstrated. Given that these models are utilized to predict uranium sequestration and permeability reduction primarily occurring in the zone immediately adjacent to the injection gallery, the use of intermediate scale column studies such as demonstrated here could provide a valuable means of constraining the accuracy of such simulations. The current study was designed specifically to develop the reactive transport datasets necessary to validate incorporation of stable isotope fractionations into a reactive

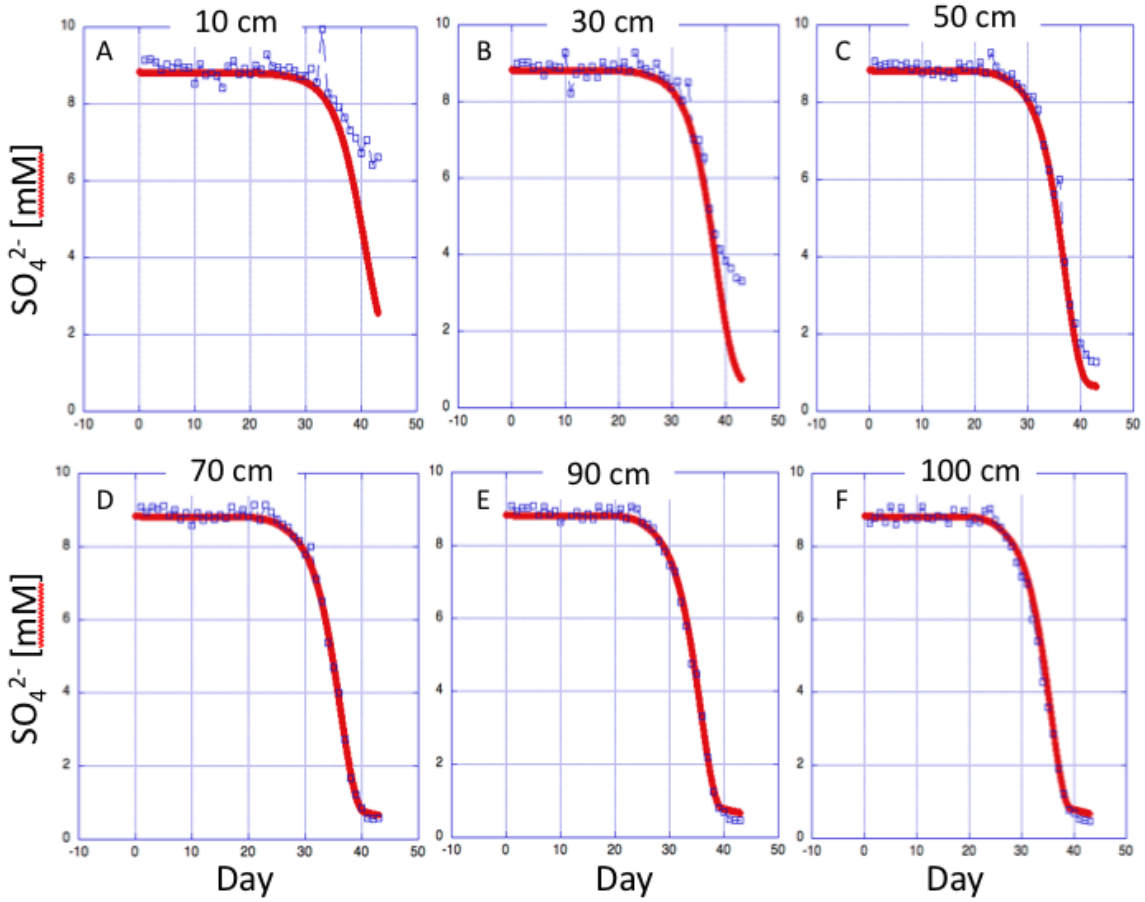


Figure 5.7: measured sulfate concentrations (open circles) and simulated profiles (red) for (A) 10 cm, (B) 30 cm, (C) 50 cm, (D) 70 cm, (E) 90 cm and (F) effluent as a function of time.

transport code, but also describes the methods for implementing similar experiments with the intent of studying relevant physical, mineralogical and microbial heterogeneity.

5.4.3 Modeling $\delta^{34}S$ fractionation

Incorporation of the stable isotopes of sulfur in the CrunchFlow code requires that the reactions affecting each isotopologue are solved explicitly in the model. As a result the dual-Monod rate law for sulfate reduction (eq. 5.12) is solved independently for the $^{32}SO_4$ and $^{34}SO_4$ "species". Similarly the reaction of sulfide with Fe^{++} to precipitate FeS and the oxidation of sulfide by Fe(III) minerals to precipitate elemental sulfur are calculated for the individual isotopologues and related through solid solutions as demonstrated for calcite in chapter 3. An additional complication is presented by the nature of the hyperbolic Monod function as discussed in the introduction (sec. 5.2.2). If the $^{32}SO_4$ and $^{34}SO_4$ reduction rates are calculated independently, then for a common maximum specific growth rate and half-saturation constant the $^{34}SO_4$ rate will be forced to higher order before the $^{32}SO_4$ rate. This is a result of the fact that the relationship between isotopic rate constants for a zero order reaction is vastly different than that for a

first order regime. Thus transitioning from one to the other with a common rate constant value results in an unwarranted fractionating effect.

The most obvious means of circumventing the problems associated with the hyperbolic rate law is to restrict the system to either zero or first order conditions. This may be accomplished by changing the half-saturation constant such that both the $^{32}SO_4$ and $^{34}SO_4$ concentrations are either substantially larger or substantially smaller than K_S throughout the simulation. While such an approach technically works (e.g. Gibson et al., 2011) it requires the use of half-saturation constants that are inconsistent with measured values by several orders of magnitude (Rittmann and McCarty, 2001). In addition the corresponding maximum specific growth rate (i.e. the rate constant) no longer reflects an appropriate value for microbial redox processes.

A modified Monod rate expression for the microbially catalyzed reduction of isotopologues was developed by Maggi and Riley (2009; 2010) in application to nitrate reduction. Using the notation in section 5.2.2, the two step reduction reaction for the isotopologues of sulfate are:

$$[Bio]+[^{32}SO_4]\underset{k_{-1}}{\overset{k_1}{\leftrightarrow}}[Bio^{32}SO_4]\xrightarrow{k_2}[Bio]+[H^{32}S] \tag{5.13a}$$

$$[Bio]+[^{34}SO_4]\underset{k'_{-1}}{\overset{k'_1}{\leftrightarrow}}[Bio^{34}SO_4]\xrightarrow{k'_2}[Bio]+[H^{34}S] \tag{5.13b}$$

$$[Bio]_T=[Bio]+[Bio^{32}SO_4]+[Bio^{34}SO_4] \tag{5.13c}$$

and the total biomass is the sum of the free and complexed components. The total biomass (eq. 5.13c) serves the important purpose of coupling the isotopologues through a common catalyzing microbial population. Under the quasi-steady state assumption for the total complexed biomass the resulting Monod expressions are then:

$$^{32}r=\frac{d[H^{32}S]}{dt}=\mu[Bio]_T\frac{[^{32}SO_4]}{[^{32}SO_4]+K\left(1+\frac{[^{34}SO_4]}{K'}\right)} \tag{5.14a}$$

$$^{34}r=\frac{d[H^{34}S]}{dt}=\mu'[Bio]_T\frac{[^{34}SO_4]}{[^{34}SO_4]+K'\left(1+\frac{[^{32}SO_4]}{K}\right)} \tag{5.14b}$$

where μ (μ') is equal to k_2 (k'_2) and K (K') is equal to $(k_{-1}+k_2)/k_1$ $((k'_{-1}+k'_2)/k'_1)$. As a result the corresponding fractionation factor becomes:

$$\alpha=\frac{\mu' K}{\mu K'}=\frac{k'_2\left(\frac{k_{-1}+k_2}{k_1}\right)}{k_2\left(\frac{k'_{-1}+k'_2}{k'_1}\right)} \tag{5.15}$$

The Monod rate expression is formally derived for the quasi-steady state reaction involving a two-step, intermediary complex catalyzed by a single enzyme. However, it has been shown that the expression describes a variety of more complex, multi-step and multi-catalyst processes and is capable of reproducing the observed rate even when the specific reaction mechanisms are unknown (Van Cappellen and Gaillard, 1996). As a result the Monod expression is ubiquitously used in reactive transport models such as CrunchFlow to describe microbially catalyzed substrate utilization processes. The pathways governing microbial reduction of sulfate are described by Rees (1973) as a

four-step process involving reversible transport of the sulfate compound into the cell interior, reversible reaction with ATP to form adenosine-5'-phosphosulfate, reversible partial reduction to intermediary sulfite and final irreversible reduction and expulsion from the cell interior as sulfide. Each of these intermediary steps represents a fractionating process, which sums to the net fractionation associated with microbial sulfate reduction (Canfield, 2001; Farquhar et al., 2003; Johnston et al., 2005). In the nitrate reduction studies modeled by Maggi and Riley (2009; 2010) the individual rate constants were fit assuming the two-step process shown above. Assuming a four-step process with limited constraints on the relative contributions of each component to the overall fractionation factor under conditions specific to the Old Rifle SRB population presents an underdetermined problem. Therefore, the dual Monod kinetic model for sulfur isotopologues was modified from the Maggi and Riley (2009) derivation to assume a single, common half-saturation constant. As a result the effects of variable half-saturation constants between the isotopologues are folded into the difference in rate constant, such that the rate expressions implemented in CrunchFlow reduce to:

$$^{32}r = \lambda_{lag}\rho_w\mu B\left(\frac{[^{32}SO_4]}{K_{SO_4}+[SO_4]}\right)\left(\frac{[Ac]}{K_{Ac}+[Ac]}\right)\left(1-\exp\left(\frac{\Delta G_r + m\Delta G_{ATP}}{\chi RT}\right)\right) \quad (5.16a)$$

$$^{34}r = \lambda_{lag}\rho_w\mu' B\left(\frac{[^{34}SO_4]}{K_{SO_4}+[SO_4]}\right)\left(\frac{[Ac]}{K_{Ac}+[Ac]}\right)\left(1-\exp\left(\frac{\Delta G_r + m\Delta G_{ATP}}{\chi RT}\right)\right) \quad (5.16b)$$

where parameters are described as in eq. 5.12. Correspondingly the fractionation factor becomes:

$$\alpha = \frac{\mu'}{\mu} = \frac{k'_2}{k_2} \quad (5.17)$$

Simulated $\delta^{34}S$ evolution with time in the effluent sulfate and sulfide reproduce observed trends in the measured data (Fig. 5.8). The sulfate $\delta^{34}S$ reflects a cumulative isotopic ratio of reactant remaining in solution (as described in chapter 1, Fig. 1.5) whereas the highly reactive sulfide is closer to an instantaneous isotopic ratio of the product species. As a result when acetate is completely consumed across the length of the column at late time in the amendment, the $\delta^{34}S$ of sulfate stabilizes while the $\delta^{34}S$ of sulfide continues to increase as more of the sulfide pool is removed from solution. The sulfate $\delta^{34}S$ does not reach the extent of enrichment observed in side ports 70 and 90 as a result of the complete removal of acetate after day 39, suggesting a minor increase in the sulfate reduction rate over the last 4 days that was not captured in the solute chemistry or the model.

The rate constant for the $^{34}SO_4$ reduction reaction (eq. 5.16b) was set to 47482 mol/g cell/yr such that in comparison with the common $^{32}SO_4$ constant (Table 5.1) the simulated fractionation was $\alpha = 0.989$ or $\varepsilon \approx 11‰$. Thus within the CrunchFlow framework a single fractionation factor can account for the observed enrichment in $\delta^{34}S$ of sulfate and sulfide, exhibiting a substantial improvement over the distillation model results and providing a basis for analysis of field-scale isotopic data. The ability to model the fractionation of the reactant and product species simultaneously within a multi-component reactive transport code presents novel opportunities. The model may be used

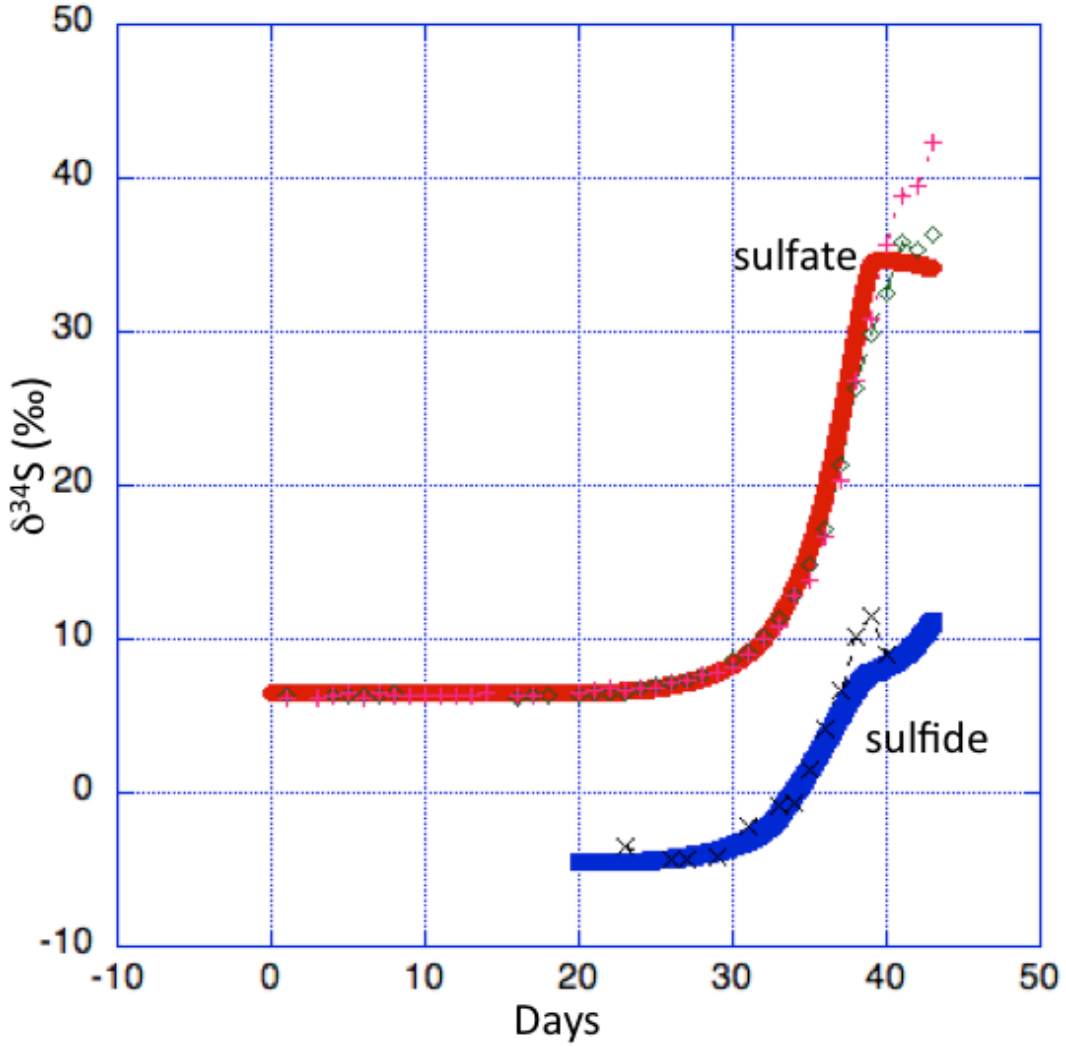


Figure 5.8: Crunchflow simulated $\delta^{34}S$ fractionation of sulfate (red line) and sulfide (blue line) at 100 cm, compared with measured values of effluent sulfide (x), sulfate in the effluent (diamond), and sulfate in the 90 cm side port (pink cross).

to predict the response of the observed stable isotope fractionation to perturbation of a variety of parameters. Results of such analyses demonstrate that for a given reaction rate constant, the fractionation between the reactant sulfate and product sulfide is always fixed, but the extent of enrichment from the starting $\delta^{34}S$ varies in proportion to the rate of reduction. Furthermore the relative magnitudes of the sulfate reduction rate (i.e. the sulfide generation rate) and the secondary sulfide reactions such as FeS precipitation and elemental sulfur formation govern the extent to which the observed $\delta^{34}S$ of sulfide behaves as a cumulative or instantaneous isotopic ratio. Thus the relationship between the $\delta^{34}S$ of the reactant and product species provides information about the relative rates of primary and secondary reactivity in the system. Finally the accumulation of mineral phases such as FeS and S^0 that are isotopically distinct from the background $\delta^{34}S$ composition of sulfate in the aquifer offer the potential to predict the isotopic shifts characteristic of secondary precipitate remobilization following cessation of acetate amendment. Such a method would provide evidence for re-dissolution of solids

specifically generated during the electron donor amendment, and have direct application to the study of long-term contaminant stabilization.

5.5 Summary

Acetate augmentation to a mesoscale column packed with sediment from the Old Rifle aquifer reproduced the microbially mediated TEAPs characteristic of field scale behavior. The high-resolution datasets of sulfate concentration facilitated analysis of simulation capabilities in the zone of primary reactivity immediately adjacent to the injection source, demonstrating that the 1D homogeneous model over predicted sulfate reduction rates within the first 30 cm when the parameters were calibrated to 100 cm solute profiles. The dual-Monod rate law used to simulate sulfate reduction in the CrunchFlow framework was modified to explicitly calculate the reduction rates of the $^{32}SO_4$ and $^{34}SO_4$ isotopologues. The resulting multi-component model mechanistically incorporating isotope fractionation of a dominant TEAP provides the foundation to develop stable isotopes as a more robust monitoring tool for contaminant sequestration.

Chapter 6

A mesoscale study of isotopic fractionation in biogeochemical reactive transport: III. Calcite formation, ion exchange and $\delta^{44}Ca$

6.1 Overview

In this chapter the calcium solute concentration and stable isotope datasets obtained from the mesoscale column study are used to extend the $\delta^{44}Ca$ model developed in chapter 3 to a reactive transport system. In doing so we demonstrate that an ion exchange process within the column sediment dampens the fractionation of $\delta^{44}Ca$ due to calcite precipitation. This result suggests that in porous media of sufficient ion exchange capacity, the $\delta^{44}Ca$ enrichment due to secondary mineral precipitation may be underestimated if such effects are active and unaccounted for.

6.2 Introduction

In Chapter 3, the stable isotopes of calcium were mechanistically incorporated into the CrunchFlow multi-component reactive transport code to simulate the enrichment in $\delta^{44}Ca$ due to calcite precipitation. Results indicated that while the influence of calcium to carbonate ion activity ratio can produce a fractionating effect that the TST rate law cannot accommodate, the conditions under which this effect becomes significant are rarely achieved in the near-surface environment. As a result the treatment of calcium isotope fractionation in CrunchFlow is extend from the semi-static clogged well system to a reactive transport regime based on the datasets collected from the mesoscale column (chapter 4).

As demonstrated in the clogged well model, calcium isotope fractionation is accomplished by precipitating calcite as a solid solution. The observed enrichment was reproduced by a model where the solid solution composition was calculated based on the fluid ^{40}Ca and ^{44}Ca concentrations rather than the bulk mineral phase. This apparent

insensitivity of the fluid phase fractionation to the composition of the bulk mineral is anticipated in a highly oversaturated system where precipitation is rapid compared with dampening effects such as recrystallization rate (Fantle, 2010). As a result the fractionation of aqueous calcium isotopes presents a potentially conservative measure to constraint the rate and extent of secondary carbonate formation in kinetically dynamic systems over the timescales pertinent to subsurface contaminant sequestration. However, a limited subset of fluid samples obtained from the down gradient monitoring wells during field scale acetate amendment at Old Rifle have shown no appreciable enrichment in $\delta^{44}Ca$ even during the sulfate reduction phase. The lack of an obvious enrichment signal may be due to (1) minimal carbonate precipitation associated with the acetate amendment, (2) mixing of the enriched $\delta^{44}Ca$ fluid with background water over the distance between the injection and monitoring wells, or (3) secondary reaction(s) serving to dampen the $\delta^{44}Ca$ signal. Substantial decreases in calcium and magnesium concentrations during the field acetate amendments, in conjunction with permeability reduction and measurable carbonate accumulation in over cored well bores have provided evidence for the production of secondary carbonates (Williams et al., 2011). The design of the mesoscale column study presented here negates the influence of mixing with unamended water. Therefore a dampening of $\delta^{44}Ca$ enrichment over the length of the column would demonstrate an additional reaction pathway influencing fluid $\delta^{44}Ca$.

6.2.1 Cation exchange

The influence of a secondary reaction causing dampening of the $\delta^{44}Ca$ enrichment due to carbonate precipitation would mean that the isotopic signal is not conserved over the path length between the injection and monitoring wells. Such a reaction would therefore have to occur at a rate comparable to carbonate precipitation. A potentially influential process operating at the appropriate timescale is exchange of the free cations in solution with those occupying surface sites of minerals with negative electrostatic surface charge. Cation exchange has been cited as an active mechanism during Old Rifle bioremediation to account for the increase in divalent cation concentrations associated with elevated sodium and potassium during acetate amendment (Li et al., 2009; 2010; Yabusaki et al., 2011). In this sense the introduction of electron donor and inert tracers also leads to salinization of the groundwater system, serving to induce mono-for-divalent exchange (Herczeg and Edmunds, 2000).

There are two independent components describing the exchange of cations in a given soil – solution system. First, the cation exchange capacity (CEC) refers to the to the maximum adsorption of cations that can be readily exchanged (i.e. those held by outer-sphere complexation and in the diffuse-ion swarm) from a given unit of soil mass under specified physical conditions (Sposito, 2008; Sparks, 2003). CEC values for both pure minerals and bulk sediments are measured experimentally by saturation and controlled displacement of an index cation. Second, the affinity of one cationic species to occupy an exchangeable site relative to another is described by the cation selectivity coefficients. For example, the exchange of sodium for calcium on a given exchanger site (X) may be described as:

$$CaX_{(s)} + 2Na^{+}_{(aq)} = Na_2X_{(s)} + Ca^{2+}_{(aq)} \quad (6.1)$$

and a corresponding thermodynamic equilibrium constant can be easily stated. However, no standard definition for the activity of the exchangeable cation adsorbed to the solid phase exists. In addition, it has been shown that the calculated equilibrium constant actually varies as the composition of the solid phase surface changes (Sparks, 2003). As a result the term 'selectivity coefficient' is commonly used and a variety of models exist for the value of the sorbed cation activity based on various assumptions about composition dependence. For example, the Gaines-Thomas convention (Gaines and Thomas, 1953) calculates the activities of the exchangeable cations adsorbed to the solid surface using the charge - equivalent fractions, whereas the Vanselow convention (Vanselow, 1932) uses the mole fractions of individual cations on the exchanger surface.

Li et al. (2009) extrapolated a cation exchange capacity (CEC) for montmorillonite (Charlet and Tournassat, 2005) to obtain a bulk sediment CEC of 8.0×10^{-5} eq/g for a field scale model of Old Rifle, however the accuracy of this parameter was never directly verified in the model. Recently, surface complexation parameters were measured for a <2 mm size fraction of Old Rifle sediment, yielding a value of 5.1×10^{-5} exchange sites / g sediment with exchange coefficients (Table 6.1) measured using Gaines-Thomas convention relative to sodium (Fox et al., in review). It is unclear to what extent these <2 mm size fraction values may be extended to the mesoscale column or the bulk composition of Old Rifle alluvium, and it is noted that the exchange coefficients for calcium and magnesium are higher than the typical range of values for natural sediments (Appelo and Postma, 2005). Nonetheless, these parameters provide a

Species	log K
Na-Na	0.0
Na-Ca	0.9
Na-Mg	0.8
Na-K	1.0
Na-H	4.9

Table 6.1: Exchange coefficients for <2 mm size fraction of Old Rifle sediment (Fox et al., in review)

starting point to incorporate ion exchange effects into the reactive transport model of the mesoscale column.

6.2.2 Influence on isotope fractionation

One of the unique features of a mesoscale column study is that the volume of sediment and fluid involved in the system is large and thus a closer approximation to field scale conditions than conventional batch and flow through reactor studies. As a result the CEC obtained from Fox et al. (in review) translates to a potentially substantial influence on cation solute concentrations. As an upper limit, assuming the entire displaceable capacity was occupied by calcium, and all of this calcium was displaced uniformly at a constant rate for the 43 days of acetate amendment, then 19.05 kg of sediment with a CEC of 5.1×10^{-5} eq/g would result in 0.91 total charge equivalents, or roughly 0.46 total moles of calcium. Over the course of 43 days at a constant flow rate of

1.8 L/day, the expected increase in calcium concentration of the fluid phase is then almost 6mM. In reality the CEC is occupied by a variety of cations forming a multicomponent system, and even under the conditions of elevated sodium and potassium concentrations characteristic of Old Rifle bioremediation the entirety of the pre-amendment cations occupying the CEC should not be displaced. Nonetheless, even a minor fraction of the total CEC can have a pronounced influence on solute concentrations. Evidence for this is shown in both the calcium and uranium concentration profiles (chapter 4, Fig. 4.4b,c), which become elevated above the influent concentration with distance through the column upon introduction of acetate, bromide, and correspondingly sodium and potassium.

The effects of such displacement have been shown to influence a variety of cationic isotope systems. Perhaps the simplest example is mixing induced by displacement of exchangeable ions with an isotopic composition distinct from the fluid phase. Such effects have been employed to quantify the CEC of sediments using isotopic equilibrium exchange with a labeled fluid composition (e.g. Steefel et al., 2003) and are commonly associated with variations in the $^{87}Sr/^{86}Sr$ value in groundwater systems (Miller et al., 1993; Johnson and DePaolo, 1997b; Cartwright et al., 2007). Direct fractionation as a result of sorption processes are easily demonstrated in the extreme conditions of cation exchange chromatography (e.g. Russell and Papanastassiou, 1978). Within environmentally relevant conditions, direct fractionation has been demonstrated or implied in a few cationic isotope systems, but these examples are limited to adsorption from the fluid to the solid surface. Boron isotopes were shown to fractionate as a result of adsorption to humic acid, yielding a fractionation factor of 0.975 in $^{11}B/^{10}B$ between pH 5 – 9 (Lemarchand et al., 2005). These results were extended to analysis of water-rock interaction in the Mackenzie River basin, demonstrating changes in the weathering environment through influences of rapid ion exchange and long-term dissolution of shales (Lemarchand and Gaillardet, 2006). Mg-for-Na exchange was implicated as a cause of $\delta^{26}Mg$ enrichment using a mass balance model for dolomite dissolution in the Madison aquifer, however the study only considered the effects associated with adsorption of Mg, and specifically excluded fractionation due to desorption (Jacobson et al., 2010). A study of calcium isotope fractionation by the same group in the Madison aquifer used a mass balance model to suggest that $\delta^{44}Ca$ fractionation due to Ca-for-Na exchange may be on the order of $\Delta_{ex\text{-}H2O} = -1.0‰$, preferentially retaining the ^{40}Ca in the sorbed pool (Jacobson and Holmden, 2008). However, the authors again only treated the removal of calcium from solution and specifically neglected the effects of desorption because they claimed no evidence for fractionation during weathering processes.

Given the current limited evidence for influences of ion exchange on calcium isotopes, we proceed to extend the CrunchFlow model developed for the mesoscale column (chapter 5, section 5.4.2) to include the effects of ion exchange based on the values obtained by Fox et al. (in review) and the $\delta^{44}Ca$ fractionation associated with carbonate precipitation (chapter 3, section 3.4.3). In doing so we seek to test the relative influences of non-fractionating ion exchange and fractionating precipitation on the observed trend in $\delta^{44}Ca$, and the extent to which these assumptions are valid. This study presents the first evidence for the influence of desorption on measured fluid $\delta^{44}Ca$ composition and demonstrates the methods for addressing this influence in the analysis of calcium isotope ratios in reactive transport under mono-for-divalent exchange conditions.

6.3 Methods

The design and sampling methods of the mesoscale column study are described in chapter 4 (sec. 4.3) including analysis of calcium concentrations. Fluid $\delta^{44}Ca$ samples were collected daily from each of the five side ports and effluent of the column. Fluid samples were immediately pushed through 0.2 μM PTFE filters into vials containing trace metal grade 12 N HNO_3. Calcium isotope analysis was conducted at the University of California, Berkeley Center for Isotope Geochemistry. Measurements were made using thermal ionization mass spectrometry (TIMS) on a Thermo-Finnigan Triton TI with nine mobile Faraday collectors. Each sample was spiked and measured in duplicate, collecting 200 individual ratios for each filament loaded, and yielding in-run uncertainties of roughly ±0.04‰ and external reproducibility of 0.1 – 0.2‰ (DePaolo, 2004). Calcium isotope ratios are reported relative to bulk silicate earth (BSE) in standard delta notation (chapter 3, eq. 3.2).

6.4 Results and discussion

6.4.1 Aqueous calcium concentrations and $\delta^{44}Ca$

Effluent calcium and total inorganic carbon (TIC) concentrations over the 43-day acetate amendment closely mirror one another as a result of carbonate precipitation, particularly at late time during sulfate reduction (Fig. 6.1). Evidence for ion exchange increasing the calcium in solution is demonstrated by the elevated concentration above the influent value. This effect is particularly clear at early time when the sodium- and potassium-enriched influent solution was first delivered, but persists until day 25 when the influence of carbonate precipitation becomes dominant. Calcium concentration profiles along the length of the column collected from the side ports (chapter 4, Fig. 4.4b) show further evidence for desorption as the values increase with distance down the column at any given point in time prior to day 25.

In the final 18 days of the amendment experiment, the measured calcium solute concentrations were primarily influenced by carbonate precipitation as a result of increased alkalinity (Fig. 6.2). Calcium concentration decreased from an influent value of 5.2 mM to 2.0 mM on day 43. The vast majority of this decline occurred over the first 50 cm of flow, and appears to be preserved thereafter. However, a closer inspection of the 70 and 90 cm side ports and the effluent profiles between days 40 – 43 illustrates that the concentration reached a minimum in the 70 cm side port, before beginning to increase over the remaining distance of the column. Such an effect may be the result of ion exchange superimposed on the larger precipitation signal.

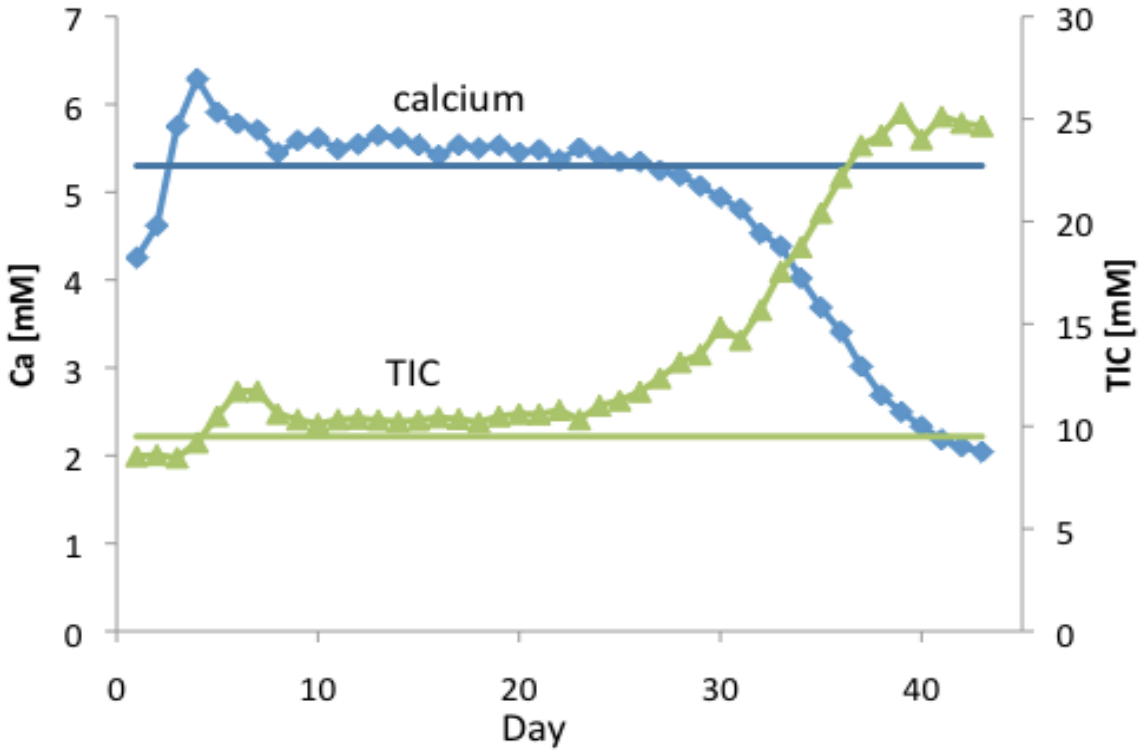


Figure 6.1: Calcium and TIC concentrations in the effluent solution for the 43 consecutive days of acetate amendment. Horizontal lines indicate respective influent concentrations.

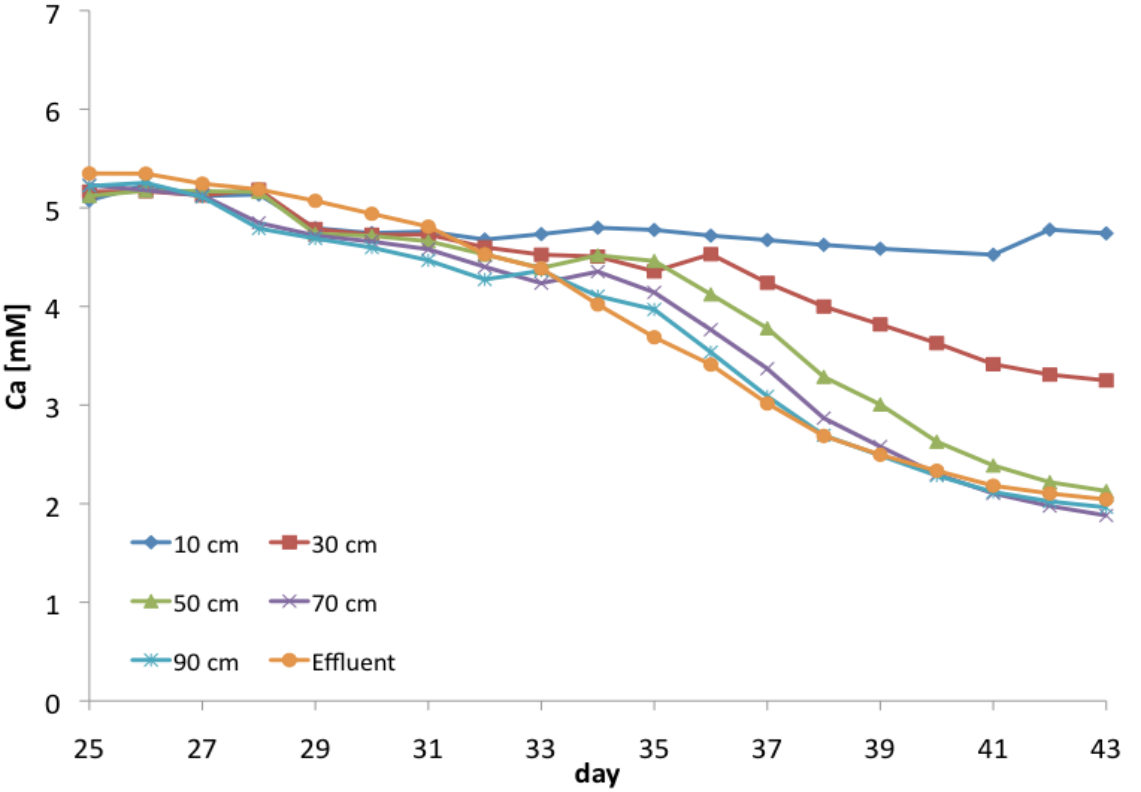


Figure 6.2: Calcium concentrations in the side port and effluent samples over the final 18 days of acetate amendment.

The calcium isotope composition of the gypsum anhydrite used to mix the artificial groundwater solution (chapter 4, Table 4.1) was 0.21‰ ±0.16 (2σ). In comparison, the average background fluid $\delta^{44}Ca$ composition of the Old Rifle aquifer (chapter 3) is -0.05‰ ±0.12 (2σ). The discrepancy in these values was one of the primary reasons that the column was flushed with unamended artificial groundwater for almost 4 months (116 days) prior to the start of acetate amendment. It is assumed that over this extended equilibration period, isotopic exchange between the solute and sorbed calcium pools resulted in a sorbed calcium isotopic composition reflecting the influent solution. Evidence for this equilibration is shown in the $\delta^{44}Ca$ value of the 10 cm and effluent samples collected on day 4 of the acetate amendment, which both plot on the high end of the range for influent $\delta^{44}Ca$ despite substantial Ca-for-Na and Ca-for-K exchange during this period (Fig. 6.3). Calcium isotope values were measured in samples collected on day 4, 21, 28, 33, 37, 40 and 43 relative to the start of acetate addition to focus on analysis of samples collected during sulfate reduction in anticipation of enrichment as a result of carbonate precipitation.

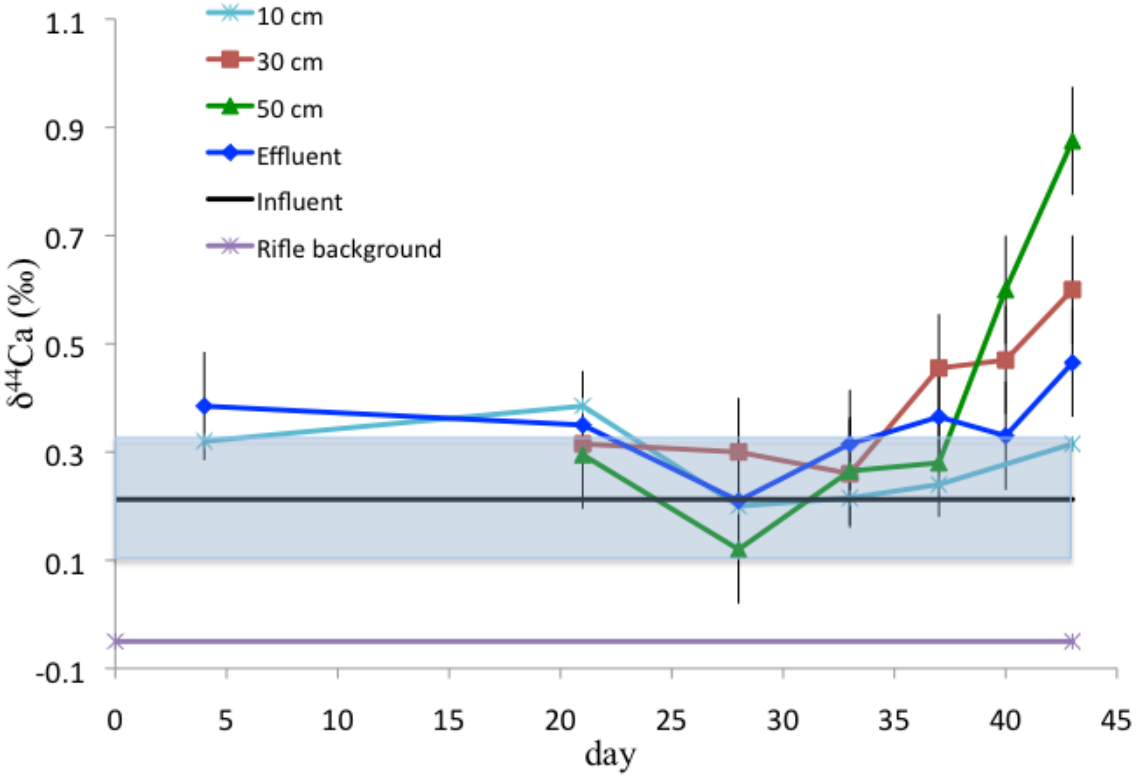


Figure 6.3: Fluid $\delta^{44}Ca$ as a function of time measured in the 10, 30 and 50 cm side ports and the effluent. Error bars show 0.12‰ range based on replicate sample measurements and long term reproducibility of the standard. Influent $\delta^{44}Ca$ is bounded by 0.16‰ range of uncertainty based on 4 replicate measurements collected over time from the influent reservoir. Background $\delta^{44}Ca$ of the Rifle aquifer fluid is shown for reference.

Calcium isotope fractionation in association with carbonate precipitation is evidenced by increasing $\delta^{44}Ca$ values observed in the first half of the column, culminating in a ~0.4‰ enrichment in the 30 cm side port, and a ~0.7‰ enrichment in the 50 cm side port on day 43. However, the elevated $\delta^{44}Ca$ values evident in the first half of the column during this period of time are not preserved down gradient. Effluent $\delta^{44}Ca$ remains within or slightly above the range of influent values for the entirety of the experiment, showing a maximum enrichment of ~0.2‰ on day 43. Given that mixing with unamended water is negated in the flow-through column design, the $\delta^{44}Ca$ profiles are taken as evidence that the fractionation signal is not conserved along the flow path. As a result, the assumption of homogeneous reactivity required in order to apply a distillation (Rayleigh) model is negated, and we proceed directly to modeling the calcium isotopes explicitly in the CrunchFlow framework to test the influence of ion exchange on the observed $\delta^{44}Ca$ trends. In doing so we assume that (1) the exchangeable calcium pool is of the same isotopic composition as the influent, (2) the desorption of calcium from the exchangeable pool into the fluid phase does not represent a fractionating process and (3) the calcite precipitation rate and corresponding fractionation factor are the same as those obtained from fitting the clogged well bores (chapter 3, Table 3.2).

6.4.2 CrunchFlow model of calcium solute profiles

The CrunchFlow model for the mesoscale column experiment developed in chapter 5 (sec. 5.4.2) is extended to include ion exchange based on the values reported by Fox et al. (in review; Table 6.1). CrunchFlow solves multicomponent ion exchange by associating the exchangeable ions with a solid phase exchanger that can either be distributed as a bulk solid or specified in association with a particular mineral. The individual exchange coefficients are specified relative to a reference species (here sodium is used), which is designated by a coefficient of zero. Using the Gaines-Thomas convention (Gaines and Thomas, 1953), the code assigns equivalent fractions for the activities of exchange sites such that the calcium component is populated as:

$$Ca^{2+} + 2X^{-} \leftrightarrow CaX_2 \qquad (6.2)$$

based on the specified Ca equilibrium exchange constant (Table 6.1) where X is the solid exchanger site. In addition to the exchangeable species listed in Table 6.1, Fe^{++} was included with a selectivity coefficient of 0.4 to correspond with previous Old Rifle field scale models (Li et al., 2009; 2010).

The model parameters for the primary TEAPs and corresponding precipitation and speciation reactions are specified in chapter 5, Tables 5.1, 5.2 and 5.4. The calcite precipitation rate constant of 4.1 (log mol/m^3/s) is the same as that fitted for well bore G51 (chapter 3). Simulated effluent sodium, potassium, calcium and magnesium concentrations using the Fox et al. (in review) CEC and selectivity coefficients (Table 6.1) show fairly accurate correspondence with measured concentrations (Fig. 6.4). Sodium (Fig. 6.4a) and magnesium (Fig. 6.4d) are particularly well reproduced by the model. Simulated potassium (Fig. 6.4b) overestimates the observed values, but is still less than the injected concentration of 1.58 mM. Measured calcium concentrations are higher than the simulated values between days 7 – 35 (Fig. 6.4c). This discrepancy corresponds with a slight oversaturation of the fluid phase with respect to calcite. While

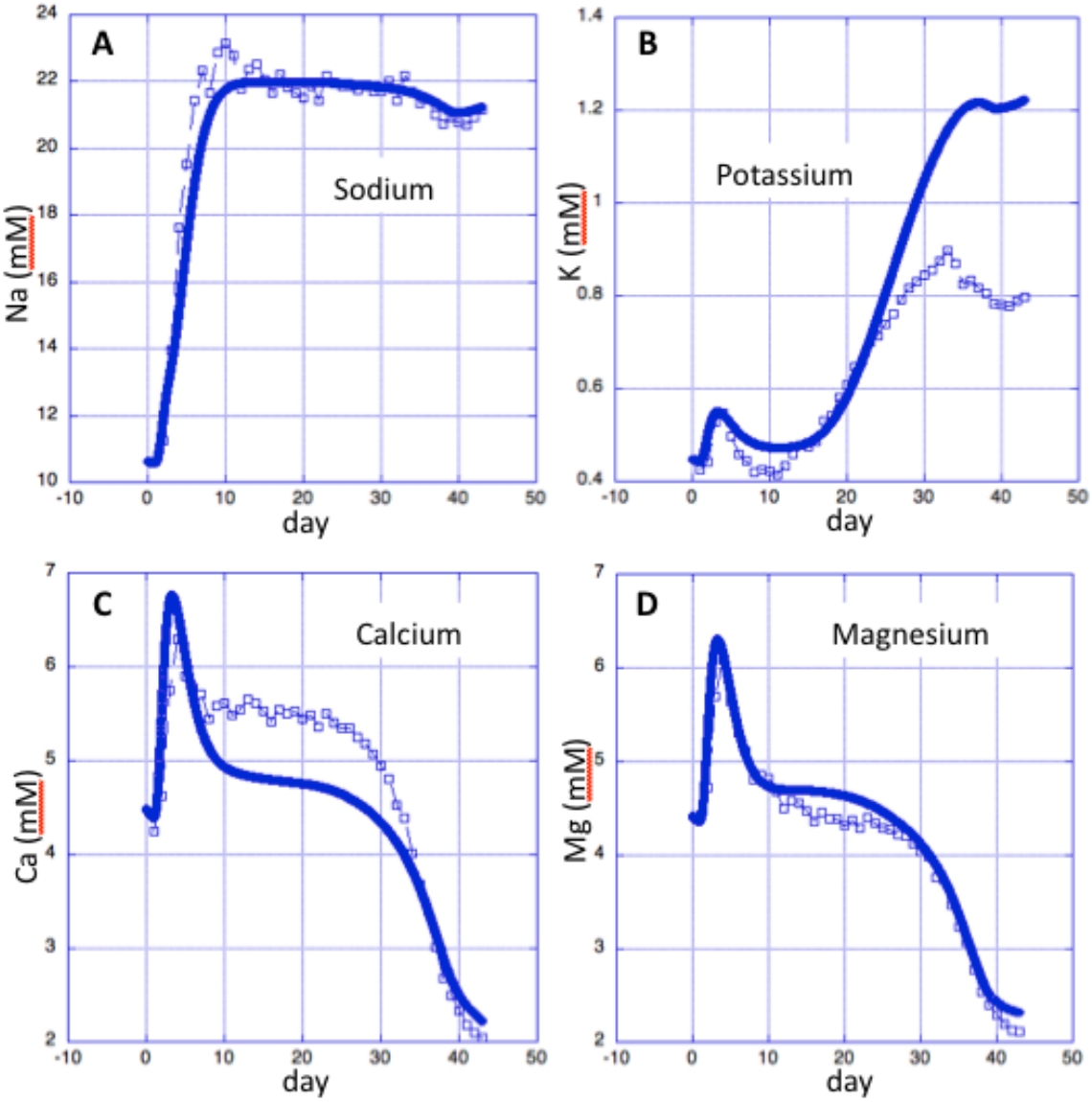


Figure 6.4: (A) measured (open squares) and simulated (thick line) effluent sodium concentration; (B) potassium; (C) calcium and (D) magnesium using Fox et al. (in review) CEC and selectivity coefficients.

the model proceeds to precipitate calcite from solution as a result of this oversaturation, the measured data indicate that this precipitation is inhibited, possibly as a result of the high magnesium concentration. Such minor oversaturation of the fluid phase has also been observed at the field site (Williams et al., 2011) but is not accommodated by the TST rate law implemented in the current simulation.

The simulated effluent calcium and TIC concentrations reasonably reproduce the observed trends (Fig. 6.5), indicating that the precipitation rate constant from the clogged well study is applicable to this through-flowing system. It was found that either decreasing the pH from 7.2 to 7.1, or decreasing the calcite equilibrium constant from 8.48 to 8.28 created a better fit between the simulated and measured calcium

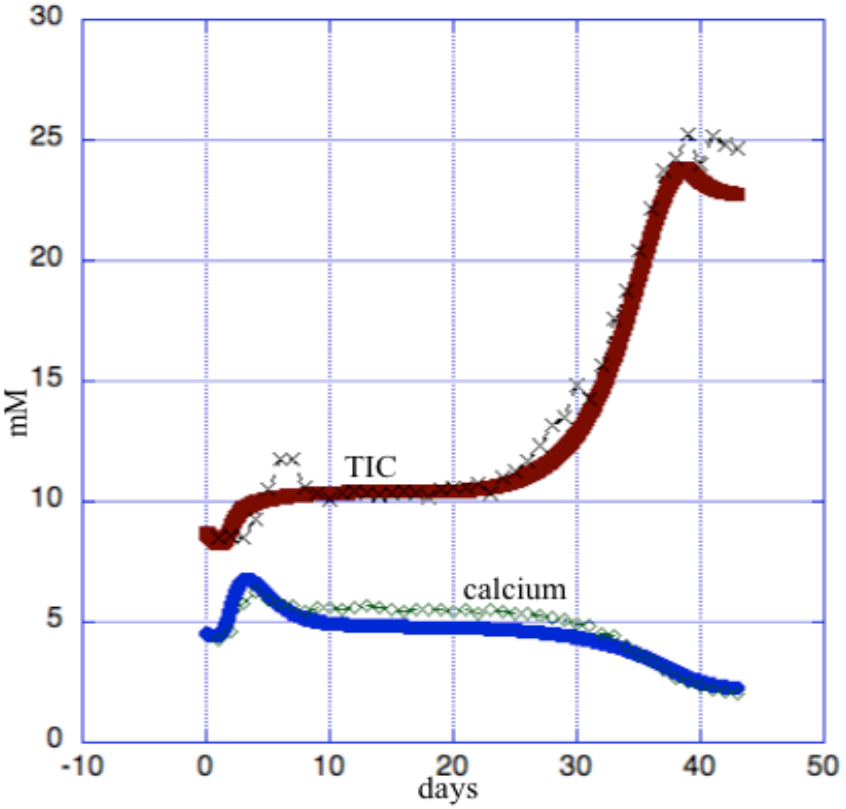


Figure 6.5: Simulated TOC (red) and calcium (blue) effluent concentrations compared with measured TOC (crosses) and calcium (open diamonds).

concentrations, however variations in these parameters lead to substantial differences between measured and modeled TIC. This observation lends further support to the influence of calcite oversaturation on the discrepancy between measured and modeled calcium concentrations. In the last 23 days of acetate addition, the simulated calcium profiles accurately reproduced the calcium removal rate in the 10 and 30 cm side ports as well as the effluent (Fig. 6.6), however the 50 cm sample values were slightly overestimated. The ability to reproduce measured calcium concentrations with distance along the column during calcite precipitation using the rate constant from well G51 supports the simulation of $\delta^{44}Ca$ based on the values obtained from the clogged well study (chapter 3).

6.4.3 Extension of the model to $\delta^{44}Ca$

Calcium isotopes were implemented in the mesoscale column model following the methods described in chapter 3 (section 3.4.3). The TST-type model is considered valid for the current system because the speciated Ca^{2+}:CO_3^{2-} ion activity ratio reached a

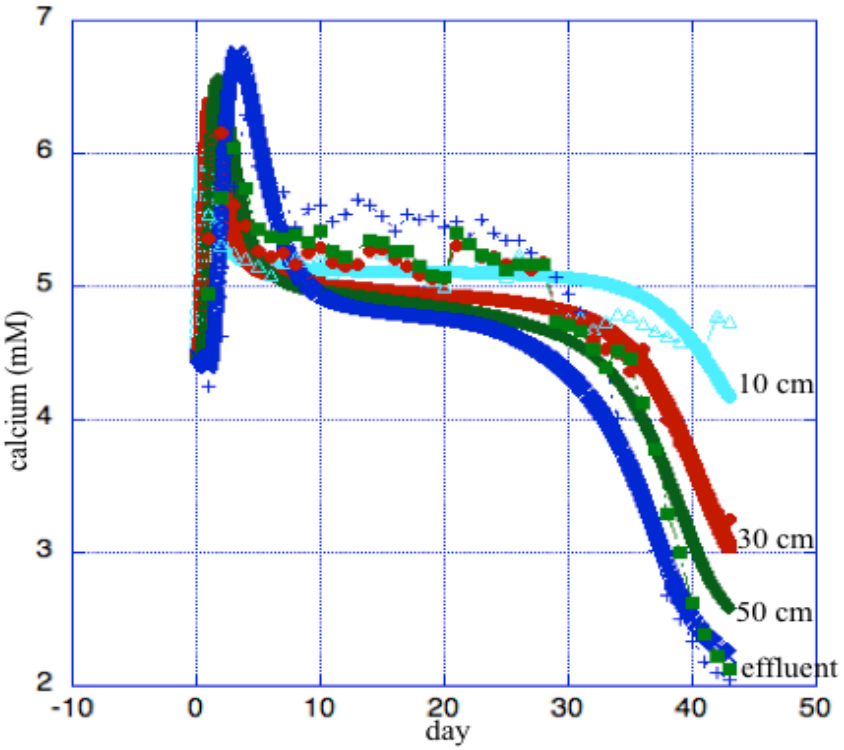


Figure 6.6: simulated and measured calcium concentrations at 10 cm (light blue), 30 cm (red) 50 cm (green) and effluent (dark blue) for the last 23 days of acetate addition.

minimum value of 72.1 during the experiment, well above the minimum value of 37 achieved in well G51 (chapter 3). Both isotopes were precipitated into a common carbonate phase using a solid solution calculated based on the aqueous $CaCO_{(3)}$ complex. The concentration of initial and influent ^{44}Ca was specified relative to the ^{40}Ca concentration (chapter 5, Table 5.3) such that the $\delta^{44}Ca$ was 0.21‰. The selectivity coefficient for ^{44}Ca was the same value as that for ^{40}Ca (Table 6.1), resulting in zero fractionation associated with calcium desorption. The precipitation rate for $^{44}CaCO_3$ was determined for a fractionation factor of $\varepsilon = 1.18$‰ to correspond with the fractionation observed to fit the enrichment in well G51. Utilizing these parameters, the simulated enrichment in $\delta^{44}Ca$ in the last 23 days of acetate amendment underestimates the measured values over the first 50 cm of flow, but the dampening of enriched $\delta^{44}Ca$ values hypothesized to result from ion exchange is illustrated by a decline in $\delta^{44}Ca$ between 50 and 100 cm (Fig. 6.7). It was found that increasing the fractionation factor for calcite precipitation to $\varepsilon = 1.5$‰ yielded the correct enrichment in fluid $\delta^{44}Ca$ at 50 cm, however this adjustment also caused the effluent $\delta^{44}Ca$ value to increase to over 0.7‰.

The relative influences of fractionating calcite precipitation and non-fractionating ion exchange create a combination of transient effects that are difficult to resolve. For a given fractionation factor during calcite precipitation, ion exchange dampens the observed $\delta^{44}Ca$ enrichment as a result of both the size of the pool of sorbed calcium available to exchange with the fluid (the CEC), and the selectivity coefficient of calcium relative to other cations. If the sorbed calcium pool is small, then the exchangeable isotopic composition will quickly equilibrate with the fluid after any change in the $\delta^{44}Ca$.

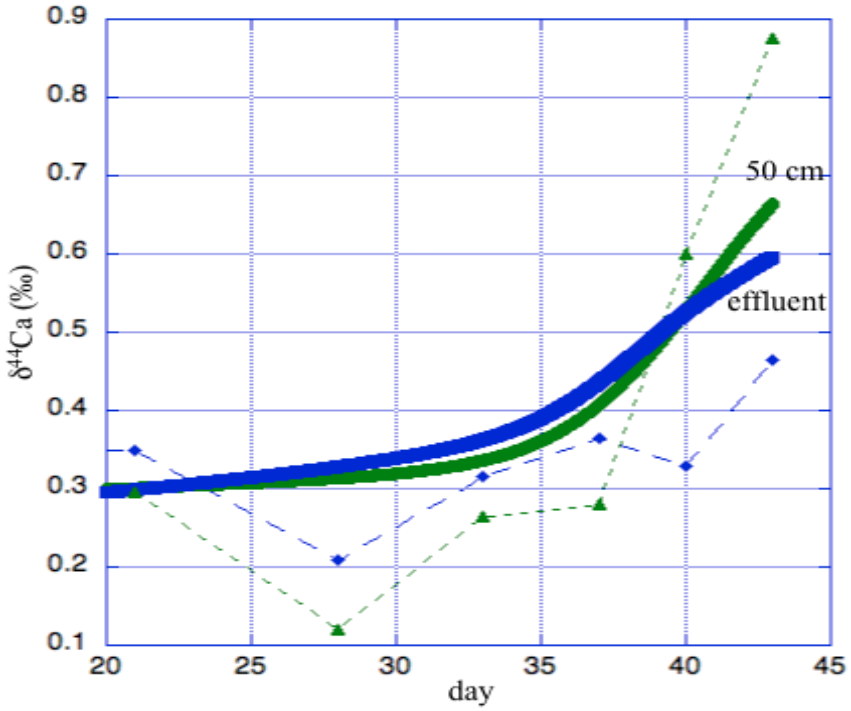


Figure 6.7: Simulated and measured $\delta^{44}Ca$ in 50 cm side port (green) and effluent (blue) in the final 23 days of acetate amendment.

If the sorbed calcium pool is large, then it will have a more pronounced dampening effect on fluid $\delta^{44}Ca$. For example, given the results presented here, we may choose to use the ε = 1.5‰ fractionation factor, and increase the sorbed calcium pool such that the ion exchange effect will cause a larger difference between the 50 cm and effluent $\delta^{44}Ca$ values. Increasing the CEC from the original value of 5.1×10^{-5} eq/g to 9.0×10^{-5} eq/g and decreasing the selectivity coefficients for ^{40}Ca and ^{44}Ca from 0.9 to 0.2 reproduces the observed $\delta^{44}Ca$ profiles (Fig. 6.8). However, such a large increase in the CEC causes significantly more cations to be displaced into the fluid, and thus the simulation no longer accurately reproduces any of the cation concentration profiles shown above (Fig. 6.4). This coupled relationship between the CEC, selectivity coefficients, precipitation rate and fractionation parameters result in a variety of such non-unique results. In particular the inverse relationship between exchange site density and selectivity coefficients is commonly cited as reason to avoid treating both parameters as independently adjustable (e.g. Goldberg, 1991).

Given the underdetermined nature of the problem, the processes contributing to the observed fluid $\delta^{44}Ca$ trends cannot be definitively quantified with the current dataset. However, plausible possibilities can be identified based on several observations. First, fractionation factors determined in non-flowing (batch) systems such as the clogged well bores are typically larger than those observed for the same fractionating reactions during porous media flow. This difference is commonly attributed to the heterogeneity of the porous media, which results in a flux-weighted average of solute chemistry and isotopic fractionation skewed towards the fast flow paths (Steefel and Maher, 2009). As a result

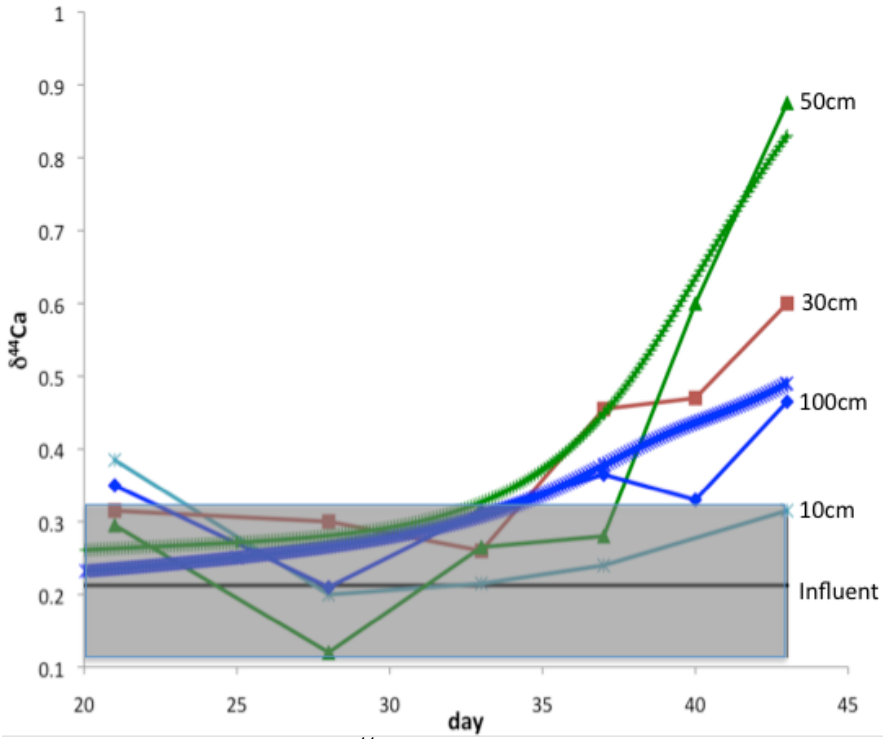


Figure 6.8: Simulated and measured $\delta^{44}Ca$ in the 50 cm side port (green) and the effluent (blue) along with measured values for the 10 cm (light blue) and 30 cm (red) side ports and the range defining the influent solution. Simulated $\delta^{44}Ca$ values differ from those in Fig. 6.6 due to modification of the ion exchange parameters.

the true fractionation factor at the site of reactivity may be observed in the clogged well bores, but the effective fractionation factor measured in the effluent is expected to be somewhat less. Therefore, we do not consider an increase in the fractionation factor from the 1.18‰ value obtained from the well bores a plausible option. Second, the CEC and selectivity parameters obtained from Fox et al. (in review) were measured on a <2 mm sieved size fraction of Old Rifle sediment. Direct application of these values to the >38 mm size fraction packed into the mesoscale column, in conjunction with the calcite precipitation parameters obtained from the clogged well bores, resulted in a remarkably good reproduction of observed fluid cation concentrations. Therefore, any adjustment to these ion exchange parameters is anticipated to be minor and the difference in size fractions would support a decrease, rather than an increase in CEC.

Based on these considerations, increasing CEC and/or the calcite fractionation factor are not considered valid parameter adjustments to simulate the observed fluid $\delta^{44}Ca$. As a result, three potential considerations remain for improving the simulated $\delta^{44}Ca$. First, it may be possible to achieve a better fit to the isotopic data through an improved simulation of the measured calcium concentration, which appears to accommodate a low level of oversaturation that the model cannot reproduce. Second, the assumed isotopic equilibrium between exchangeable calcium and the fluid phase prior to the start of acetate amendment may not be valid, however the fluid $\delta^{44}Ca$ do not support this hypothesis. Finally, the current results cannot rule out the potential for isotopic fractionation associated with the displacement of calcium from the sorbed pool

to the fluid phase. Such a fractionation has been considered negligible for calcium in previous studies (Jacobson and Holmden, 2008) but has never been directly measured.

Further investigations are required in order to test these hypotheses. The multicomponent ion exchange reactions implemented in the CrunchFlow code can be improved through independent analysis of the ion exchange parameters specific to the >38 mm grain size fraction. In addition, the use of a Gaines-Thomas convention to calculate exchange coefficients in a multivalent system incorporates an assumption of equivalent charge fractions rather than true mole fractions which requires independent verification (Sposito and Mattigod, 1979; Sposito, 1981) and a different convention may provide some improvement. Finally, the potential for an isotopic fractionation due to desorption may be explored through a combination of controlled laboratory experiments and molecular dynamics modeling.

While the present study cannot definitively quantify the relative contributions of ion exchange and calcite precipitation influencing observed fluid $\delta^{44}Ca$, the results have yielded important conclusions for the application of calcium stable isotope fractionation as a tracer of secondary mineral formation at Old Rifle. The clogged well bore study presented in chapter 3 demonstrated a clear enrichment of fluid $\delta^{44}Ca$ associated with carbonate precipitation. However, the mesoscale column experiment shows that when this precipitation occurs during porous media flow, interaction with the aquifer sediment results in an ion exchange effect that substantially dampens and retards the fluid $\delta^{44}Ca$ enrichment. Therefore, observation of this enrichment in down gradient monitoring wells during a field scale acetate amendment would occur as a function of the CEC of the sediment over the path length between carbonate precipitation and measurement. This influence complicates the quantitative relationship between observed $\delta^{44}Ca$ enrichment and the amount of carbonate accumulated in the system. However, it also suggests the potential to utilize stable isotope fractionations of cations during acetate amendment as an indication of the bulk ion exchange parameters of the system.

6.5 Summary

The design of the mesoscale column experiment provided >20 cm sampling resolution along a 100 cm reactive flow path scaled to represent the first meter down gradient of injection during a field scale acetate amendment at Old Rifle. Calcium solute profiles and fluid $\delta^{44}Ca$ measured in this system demonstrate that the $\delta^{44}Ca$ enrichment due to carbonate precipitation is not conserved with transport in the fluid phase. The cause of this effect is attributed to a reactive pathway described as an ion exchange process. Mono-for-divalent cation exchange therefore complicates the use of fluid $\delta^{44}Ca$ values as a quantitative indication of secondary carbonate precipitation during acetate amendment.

References

Adriano, D.C.; Bollag, J.M.; Frankenberger, W.T. (eds.), 1999. Bioremediation of Contaminated Soils. American Society of Agronomy, Madison, WI.

Anderson, G.M. and Crerar, D.A., 1993. Thermodynamics in Geochemistry: The Equilibrium Model. Oxford University Press, 609 p.

Anderson, R.T.; Vrionis, H.A.; Ortiz-Bernad, I.; Resch, C.T.; Long, P.E.; Dayvault, R.; Karp, K.; Marutzky, S.; Metzler, D.R.; Peacock, A.; White, D.C.; Lowe, M.; Lovely, D.R., 2003. Stimulating the *in situ* activity of *Geobacter* species to remove uranium from the groundwater of a uranium-contaminated aquifer. Applied and Environmental Microbiology 69, 5884-5891.

Appelo, C.A.J., 1996. Multicomponent ion exchange and chromatography in natural systems *in* Reactive Transport in Porous Media vol. 34 (P.C. Lichtner; C.I. Steefel; E.H. Oelkers, eds.) The Mineralogical Society of America, pp. 193 – 228.

Appelo, C.A.J.; Postma, D. 2005. Geochemistry, groundwater and pollution (2^{nd} ed.). Leiden, New York, 649 p.

Bacon, D.H. and McGrail, B.P., 2005. Waste Form Release Calculations for the 2005 Integrated Disposal Facility Performance Assessment. Pacific Northwest National Laboratory (PNNL-15198) for DOE contract DE-AC05-76L01830, Richland, WA.

Benning, L.G.; Waychunas, G.A., 2008. Nucleation, growth and aggregation of mineral phases: Mechanisms and kinetic controls *in* Kinetics of Water-Rock Interactions (S.L. Brantley; J.D. Kubicki; A.F. White, eds.). Springer, New York, 259-334.

Berna, E.C.; Johnson, T.M.; Makdisi, R.S.; Basu, A., 2010. Cr stable isotopes as indicators of Cr(VI) reduction in groundwater: A detailed time-series study of a point source plume. Environmental Science and Technology 44, 1043-1048.

Bethke, C.M.; Ding, D.; Jin, Q.; Sanford, R.A. 2008. Origin of microbial zoning in groundwater flows. Geology 36, 739-742.

Brandes, J.A.; Devol, A.H., 1997. Isotopic fractionation of oxygen and nitrogen in costal marine sediments. Geochimica et Cosmochimica Acta 61, 1793-1801.

Brooks, S.C.; Fredrickson, J.K.; Carroll, S.L.; Kennedy, D.W.; Zachara, J.M.; Plymale, A.E.; Kelly, S.D.; Kemner, K.M.; Fendorf, S. 2003. Inhibition of bacterial U(VI) reduction by calcium. Environmental Science & Technology 37, 1850-1858.

Bopp, C.J.; Lundstrom, C.C.; Johnson, T.M.; Sanford, R.A.; Long, P.E.; Williams, K.H. 2010. Uranium $^{238}U/^{235}U$ isotope ratios as indicators of reduction: Results from an in situ biostimulation experiment at Rifle, Colorado, USA. Environmental Science & Technology 44, 5927-5933.

Burris, D.R.; Hatfield, K.; Wolfe, N.L., 1996. Laboratory experiments with heterogeneous reactions in mixed porous media. Journal of Environmental Engineering 122, 685-691.

Callister, S.J.; Wilkins, M.J.; Nicora, C.D.; Williams, K.H.; Banfield, J.F.; VerBerkmoes, N.C.; Hettich, R.L.; N'Guessan, L.; Mouser, P.J.; Elifantz, H.; Smith, R.D.; Lovley, D.R.; Lipton, M.S.; Long, P.E. 2010. Analysis of biostimulated microbial communities from two field experiments reveals temporal and spatial differences in proteome profiles. Environmental Science & Technology 44, 8897-8903.

Canfield, D.E.; Olsen, C.A.; Cox, R.P., 2006. Temperature and its control of isotope fractionation by sulfate-reducing bacterium. Geochimica et Cosmochimica Acta 70, 548-561.

Canfield, D.E. 2001. Isotope fractionation by natural populations of sulfate-reducing bacteria. Geochimica et Cosmochimica Acta 65, 1117-1124.

Caporaso, J.G.; Kuczynski, J.; Stombaugh, J.; Bittinger, K.; Bushman, F.D.; Costello, E.K.; Fierer, N.; Pena, A.G.; Goodrich, J.K.; Gordon, J.I.; Huttley, G.A.; Kelley, S.T.; Knights, D.; Koenig, J.E.; Ley, R.E.; Lozupone, C.A.; McDonald, D.; Muegge, B.D.; Pirrung, M.; Reeder, J.; Sevinsky, J.R.; Tumbaugh, P.J.; Walters, W.A.; Wildmann, J.; Yatsunenko, T.; Zaneveld, J.; Knight, R., 2010a. QIIME allows analysis of high-throughput community sequencing data. Nature Methods 7, 335-336.

Caporaso, J.G.; Bittinger, K.; Bushman, F.D.; DeSantis, T.Z.; Andersen, G.L.; Knight, R., 2010b. PyNAST: a flexible tool for aligning sequences to a template alignment. Bioinformatics 26, 266-267.

Carmody, R.W.; Plummer, L.N.; Busenberg, E.; Coplen, T.B., 1998. Methods for collection of dissolved sulfate and sulfide and analysis of their sulfur isotopic composition. USGS Open File Report 97-234.

Cartwright, I.; Weaver, T.; Petrides, B., 2007. Controls on $^{87}Sr/^{86}Sr$ ratios of groundwater in silicate-dominated aquifers: SE Murray Basin, Australia. Chemical Geology 246, 107-123.

Chang, Y.J.; Long, P.E.; Geyer, R.; Peacock, A.D.; Resch, C.T.; Sublette, K.; Pfiffner, S.; Smithgall, A.; Anderson, R.T.; Vrionis, H.A.; Stephen, J.R.; Dayvault, R.; Ortiz-Bernad, I.; Lovley, D.R.; White, D.C. 2005. Microbial incorporation of ^{13}C-

labeled acetate at the field scale: Detection of microbes responsible for reduction of U(VI). Environmental Science & Technology 39, 9039-9048.

Charlet, I.; Tournassat, C., 2005. Fe(II)-Na(I)-Ca(II) cation exchange on montmorillonite in chloride medium: Evidence for preferential clay adsorption of chloride – metal ion pairs in seawater. Aquatic Geochemistry 11, 115-137.

Clark, S.K.; Johnson, T.M. 2008. Effective isotopic fractionation factors for solute removal by reactive sediments: A laboratory microcosm and slurry study. Environmental Science and Technology 42, 7850-7855.

Conrad, M.E.; Brodie, E.L.; Radtke, C.W.; Bill, M.; Delwiche, M.E.; Hope Lee, M.; Swift, D.L.; Colwell, F.S., 2010. Field evidence for co-metabolism of trichloroethene stimulated by addition of electron donor to groundwater. Environmental Science & Technology 44, 4697-4704.

Criss, R.E. 1999. Principles of Stable Isotope Distributions. Oxford University Press, New York, 246 p.

Dale, A.W.; Regnier, P.; Knab, N.J.; Jørgensen, B.B.; Van Cappellen, P., 2008. Anaerobic oxidation of methane (AOM) in marine sediments from the Skagerrak (Denmark): II. Reaction-transport modeling. Geochimica et Cosmochimica Acta 72, 2880-2894.

Davis, J.A.; Meece, D.E.; Kohler, M.; Curtis, G.P. 2004. Approaches to surface complexation modeling of uranium(VI) adsorption on aquifer sediments. Geochimica et Cosmochimica Acta 68, 3621-3641.

DePaolo, D.J. 2011. Surface kinetic model for isotopic and trace element fractionation during precipitation of calcite from aqueous solutions. Geochimica et Cosmochimica Acta 75, 1039-1056.

DePaolo, D.J. 2006. Isotopic effects in fracture-dominated reactive fluid-rock systems. Geochimica et Cosmochimica Acta 70, 1077-1096.

DePaolo, D.J.; Maher, K.; Christensen, J.N.; McManus, J. 2006. Sediment transport time measured with U-series isotopes: Results from ODP North Atlantic drift site 984. Earth and Planetary Science Letters 248, 394-410.

DePaolo, D.J., 2004. Calcium isotopic variations produced by biological, kinetic, radiogenic and nucleosynthetic processes in Reviews *in* Mineralogy and Geochemistry (J. Rosso, ed.) 55, 255-288.

DePaolo, D.J.; Conrad, M.E.; Maher, K.; Gee, G.W. 2004. Evaporation effects on oxygen and hydrogen isotopes in deep vadose zone pore fluids at Hanford, Washington. Vadose Zone Journal 3, 220-232.

DePaolo, D.J.; Getty, S.R. 1996. Models of isotopic exchange in reactive fluid-rock systems: Implications for geochronology in metamorphic rocks. Geochimica et Cosmochimica Acta 60, 3933-3947.

DOE, 2011. Review of the Natural Flushing Groundwater Remedy at the Old Rifle Legacy Management Site, Rifle, Colorado (Draft). DOE/LMS-S07263, Grand Junction Office, Grand Junction, Colorado.

DOE, 2000. Complex Systems Science for Subsurface Fate and Transport, Report from the August 2009 Workshop, DOE/SC-0123, Office of Science.

DOE, 1999. Final Site Observational Work Plan for the UMTRA Project Old Rifle Site, GJO-99-88-TAR, Rev. 1, Grand Junction Office, Grand Junction, Colorado.

DOE, 1997. Linking Legacies: Connecting the Cold War Nuclear Weapons Processes to their Environmental Consequences. DOE/EM-0319. Washington, D.C. DOE.

Dong, W.M.; Brooks, S.C. 2006. Determination of the formation constants of ternary complexes of uranyl and carbonate with alkaline earth metals (Mg2+, Ca2+, Sr2+, and Ba2+) using anion exchange method. Environmental Science & Technology 40, 4689-4695.

Druhan, J.L.; Conrad, M.E.; Williams, K.E.; N'Guessan, L.; Long, P.E.; Hubbard, S.S. Sulfur isotopes as indicators of amended bacterial sulfate reduction processes influencing field scale uranium bioremediaton. Environmental Science & Technology 42, 7842-7849.

Englert, A.; Hubbard, S.S.; Williams, K.W.; Li, L.; Steefel, C.I. 2009. Feedbacks between hydrological heterogeneity and bioremediation induced biogeochemical transformations. Environmental Science & Technology 43, 5197-5204.

Fand, R.M.; Thinakaran, R., 1990. The influence of the wall on flow through pipes packed with spheres. Journal of Fluids Engineering, Transactions of the ASME 112, 84-88.

Fang, Y.L.; Yabusaki, S.B.; Morrison, S.J.; Amonette, J.P.; Long, P.E. 2009. Multicomponent reactive transport modeling of uranium bioremediation field experiments. Geochimica Et Cosmochimica Acta 73, 6029-6051.

Fantle, M.S., 2010. Evaluating the Ca isotope proxy. American Journal of Science 3, 194-230.

Fantle, M.; DePaolo, D.J., 2007. Ca isotopes in carbonate sediment and pore fluid from ODP Site 807A: The Ca2+(aq)-calcite equilibrium fractionation factor and calcite

re-crystallization rates in Pleistocene sediments. Geochimica et Cosmochimica Acta 71, 2524-2546.

Farquhar, J.; Johnston, D.T.; Wing, B.A.; Habicht, K.S.; Canfield, D.E.; Airieau, S.A.; Thiemens, M.H., 2003. Multiple sulfur isotopic interpretations of biosynthetic pathways: Implications for biological signatures in the sulfur isotope record. Geobiology 1, 15-27.

Fox, P.M.; Davis, J.A.; Hay, M.B.; Conrad, M.E.; Campbell, K.M.; Williams, K.H.; Long, P.E.. Rate-limited U(VI) desorption during a small-scale tracer test in a heterogeneous uranium contaminated aquifer. Water Resources Research (in review).

Freeze, A.R.; Cherry, J.A., 1979. Groundwater. Prentice Hall Inc. 604 p.

Fries, M.R.; Zhou, J.H.; Cheesanford, J.; Tiedje, J.M., 1994. Isolation, characterization and distribution of denitrifying toluene degraders from a variety of habitats. Applied and Environmental Microbiology 60, 2802-2810.

Gadd, G.M., 2010. Metals, minerals and microbes: Geomicrobiology and bioremediaton. Microbiology 156, 609-643.

Gaines, G.L.; Thomas, H.C., 1953. Adsorption studies on clay minerals. II. A formulation of the thermodynamics of exchange adsorption. Journal of Chemical Physics 21, 714-718.

Gebrehiwet, T.A.; Redden, G.D.; Fujita, Y.; Beig, M.S.; Smith, R.W. 2012. The effect of the CO_3^{2-} to Ca^{2+} ion activity ratio on calcite precipitation kinetics and Sr^{2+} partitioning. Geochemical Transactions 13 (in press).

Gelhar, L.W.; Welty, C.; Rehfeldt, K.R., 1992. A critical-review of data on field-scale dispersion in aquifers. Water Resources Research 28, 155-1974.

Giesemann, A.; Jager, H.J.; Norman, A.L.; Krouse, H.p.; Brand, W.A. 1994. On-line sulfur-isotope determination using an elemental analyzer coupled to a mass spectrometer. Analytical Chemistry 66, 2816-2819.

Gibson, B.D.; Amos, R.T.; Blowes, D.W. 2011. $^{34}S/^{32}S$ fractionation during sulfate reduction in groundwater treatment systems: Reactive transport modeling. Environmental Science & Technology 45, 2863-2870.

Ginn, T.R.; Wood, B.D.; Nelson, K.E.; Scheibe, T.D.; Murphy, E.M.; Clement, T.P. 2002. Processes in microbial transport in the natural subsurface. Advances in Water Resources 25, 1017-1042.

Goevert, D.; Conrad, R., 2009. Effect of substrate concentration on carbon isotope fractionation during acetoclastic methanogenesis by *Methanosarcina barkeri* and *M. acetivorans* and in rice field soil. Applied and Environmental Microbiology 75, 2605-2612.

Goldberg, S., 1991. Sensitivity of surface complexation modeling to the surface site density parameter. Journal of Colloid and Interface Science, 145, 1-9.

Habicht, K.S.; Salling, L.; Thamdrup, B.; Canfield, D.E., 2005. Applied and Environmental Microbiology 71, 3770-3777.

Habicht, K.S.; Canfield, D.E., 2001. Isotope fractionation by sulfate-reducing natural populations and the isotopic composition of sulfide in marine sediments. Geology 29, 555-558.

Hamady, M.; Walker, J.J.; Harris, J.K.; Gold, N.J.; Knight, R., 2008. Error-correcting barcoded primers for pyrosequencing hundreds of samples in multiplex. Nature Methods 5, 235-237.

Herczeg, A.L.; Edmunds, W.M.. 2000. Inorganic ions as tracers in Environmental tracers in subsurface hydrology (P. Cook; A.L. Herczeg, eds.) Kluwer Academic Publishers, pp. 31-78.

HACH, 2003. DR/2500 Spectrophotometer procedure manual, 4th ed. HACH Company, 790 p.

Holmes, D.E.; Nevin, K.P.; O'Neil, R.A.; Ward, J.E.; Adams, L.A.; Woodard, T.L.; Vrionis, H.A.; Lovley, D.R. 2005. Potential for quantifying expression of the Geobacteraceae citrate synthase gene to assess the activity of Geobacteraceae in the subsurface and on current-harvesting electrodes. Applied Environmental Microbiology 71, 6870-6877.

Hunkeler, D., 2002. Quantification of isotope fractionation in experiments with deuterium labeled substrate. Applied and Environmental Microbiology 68, 5205-5206.

Ivanov, I.I.; Atarashi, K.; Manel, N.; Brodie, E.L.; Shima, T.; Karaoz, U.; Wel, D.G.; Goldfarb, K.C.; Santee, C.A.; Lynch, S.V.; Tonoue, T.; Imaoka, A.; Itoh, K.; Takeda, K.; Umesaki, Y.; Honda, K.; Littman, D.R., 2009. Induction of intestinal Th17 cells by segmented filamentous bacteria. Cell 139, 485-498.

Jacobson, A.D.; Zhang, Z.; Ludstrom, C.; Huang, F., 2010. Behavior of Mg isotopes during dedolomitization in the Madison Aquifer, South Dakota. Earth and Planetary Science Letters 297, 446-452.

Jacobson, A.D.; Holmden, C., 2008. δ^{44}Ca evolution in a carbonate aquifer and its bearing on the equilibrium isotope fractionation factor for calcite. Earth and Planetary Science Letters 270, 349-353.

Jin, Q.; Bethke, C.M., 2003. A new rate law describing microbial respiration. Applied and Environmental Microbiology 69, 2340-2348.

Johnson, T.M.; Roback, R.C.; McLing, T.L.; Bullen, T.D.; DePaolo, D.J.; Doughty, C.; Hunt, R.J.; Smith, R.W.; Cecil, L.D.; Murrell, M.T., 2000. Groundwater "fast paths" in the Snake Rifle Plain aquifer: Radiogenic isotope ratios as natural groundwater tracers. Geology 28, 871-874.

Johnson, T.M.; DePaolo, D.J. 1997a. Rapid exchange effects on isotope ratios in groundwater. 1. Development of a transport-dissolution-exchange model. Water Resources Research 33, 187-195.

Johnson, T.M.; DePaolo, D.J. 1997b. Rapid exchange effects on isotope ratios in groundwater. 2. Flow investigation using Sr isotope ratios. Water Resources Research 33, 197-205.

Johnson, T.M.; DePaolo, D.J. 1996. Reaction-transport models for radiocarbon in groundwater: The effects of longitudinal dispersion and the use of Sr isotope ratios to correct for water-rock interaction. Water Resources Research 32, 2203-2212.

Johnson, T.M.; DePaolo, D.J. 1994. Interpretation of isotopic data in groundwater-rock systems: Model development and application to Sr isotope data from Yucca Mountain. Water Resources Research 30, 1571-1587.

Johnston, D.T.; Farquhar, J.; Wing, B.A.; Kaufman, A.J.; Canfield, D.E.; Habicht, K.S., 2005. Multiple sulfur isotope fractionations in biological systems: A case study with sulfate reducers and sulfur disproportionators. American Journal of Science 305, 645-660.

Jørgensen, K.S. 2007. *In Situ* Bioremediation. Advances in Applied Microbiology 61, 285-305.

Keith-Roach, M.J. and Livens, F.R. (eds.), 2002. Interactions of Microorganisms with Radionuclides in Radioactivity in the Environment Volume 2. Elsevier Science Ltd., Oxford UK.

Kerkhof, L.J.; Williams, K.H.; Long, P.E.; McGuinness, L.R. 2011. Phase preference by active, acetate-utilizing bacteria at the Rifle, CO Integrated Field Research Challenge site. Environmental Science & Technology 45, 1250-1256.

Knoller, K.; Vogt, C.; Feisthauer, S.; Weise, S.M.; Weiss, H.; Richnow, H.H. 2008. Sulfur cycling and biodegredation in contaminated aquifers: Insights from stable isotope investigations. Environmental Science & Technology 42, 7807-7812.

Komlos, J.; Moon, H.S.; Jaffé, P.R., 2008. Effect of sulfate on the simultaneous bioreduction of iron and uranium. Journal of Environmental Quality 37, 2058-2062.

Kowalsky, M.B.; Finsterle, S.; Englert, A.; Williams, K.H.; Steefel, C.I.; Hubbard, S.S. 2011. Inversion of time-lapse tracer data for estimating changes in field-scale flow properties during biostimulation. Journal of Hydrology

Langmuir, D. 1997. Aqueous Environmental Geochemistry. Prentice Hall, 600 p.

Larsen, K.; Bechgaard, K.; Stipp, S.L.S. 2010. Modeling spiral growth at dislocations and determination of critical step lengths from pyramid geometries on calcite {1 0 – 1 4} surfaces. Geochimica et Cosmochimica Acta 74, 558-567.

Lasaga, A.C., 1981. Rate laws of chemical reactions *in* Kinetics of Geochemical Processes (A.C. Lasaga and R. Kirkpatrick, eds.). Reviews in Mineralogy 8, 1-68.

Lemarchand, D.; Gaillardet, J., 2006. Transient features of the erosion of shales in the Mackenzie basin (Canada), evidence from boron isotopes. Earth and Planetary Science Letters 245, 174-189.

Lemarchand, D.; Schott, J.; Gaillardet, J., 2005. Boron isotopic fractionation related to boron sorption on humic acid and the structure of surface complexes formed. Geochimica et Cosmochimica Acta 69, 3519-3533.

Li, L.; Gawande, N.; Kowalsky, M.B.; Steefel, C.I.; Hubbard, S.S. 2011. Physiochemical heterogeneity controls on uranium bioreduction rates at the field scale. Environmental Science & Technology 45, 9959-9966.

Li, L.; Steefel, C.I.; Kowalsky, M.B.; Englert, A.; Hubbard, S.S. 2010. Effects of physical and geochemical heterogeneities on mineral transformation and biomass accumulation during biostimulation experiments at Rifle, Colorado. Journal of Contaminant Hydrology 112, 45-63.

Li, L.; Steefel, C.I.; Williams, K.H.; Wilkins, M.J.; Hubbard, S.S. 2009. Mineral transformation and biomass accumulation associated with uranium bio-remediation at Rifle, Colorado. Environmental Science & Technology 43, 5429-5435.

Lloyd, J.R. and Gadd, G.M., 2011. The geomicrobiology of radionuclides. Geomicrobiology Journal 28, 383-386.

Lloyd, J.R. and Renshaw, J.C., 2005a. Microbial transformations of radionuclides: Fundamental mechanisms and biogeochemical implications *in* "Biogeochemical Cycles", Vol. 43 of Metal Ions in Biological Systems (A. Sigel, H. Sigel and R. K. O. Sigel, eds.). M.Dekker, New York, 205-240.

Lloyd, J.R. and Renshaw, J.C., 2005b. Bioremediation of radioactive waste: radionuclide-microbe interactions in laboratory and field-scale studies. Current Opinion in Biotechnology 16, 254-260.

Lloyd, J.R. and Macaskie, L.E., 2002. Biochemical basis of microbe-radionuclide interactions *in* Interactions of Microorganisms with Radionuclides in Radioactivity in the Environment Volume 2 (Keith-Roach, M.J.; Livens, F.R., eds.). Elsevier Science Ltd., Oxford UK.

Lloyd, J.R.; Cole, J.A.; Macaskie, L.E., 1997. Reduction and removal of heptavalent technetium from solution by *Escherichia coli*. Journal of Bacteriology 179, 2014-2021.

Long, P.E. 2011. Microbiological, geochemical and hydrologic processes controlling uranium mobility: an Integrated Field Scale Subsurface Research Challenge Site at Rifle, Colorado, February 2010 to January 2011. Annual Report to the DOE Office of Science, Subsurface Biogeochemistry Research Program, PNNL-20200, Richland, Washington.

Lovley, D.R. (ed), 2000. Environmental Microbe-Metal Interactions. ASM Press, Washington D.C.

Lovley, D.R. 1995. Bioremediation of organic and metal contaminants with dissimilatory metal reduction. Journal of Industrial Microbiology and Biotechnology 14, 85-93.

Lovley, D.R.; Phillips, E.J.; Gorby, Y.A.; Landa, E.R., 1991. Microbial reduction of uranium. Nature 350, 413-416.

Maggi, F.; Riley, W.J., 2010. Mathematical treatment of isotopologue and isotopomer speciation and fractionation in biochemical kinetics. Geochimica et Cosmochimica Acta 74, 1823-1835.

Maggi, F.; Riley, W.J., 2009. Transient competitive complexation in biological kinetic isotope fractionation explains nonsteady isotopic effects: Theory and application to denitrification of soils. Journal of Geophysical Research - Biogeosciences 114, G04012.

Maher, K.; DePaolo, D.J.; Christensen, J.N. 2006. U-Sr isotopic speedometer: Fluid flow and chemical weathering rates in aquifers. Geochimica et Cosmochimica Acta 70, 4417-4435.

Maher, K.; DePaolo, D.J.; Conrad, M.E.; Serne, R.J. 2003. Vadose zone infiltration rate at Hanford, Washington, inferred from Sr isotope measurements. Water Resources Research 39, 1204-1217.

Massmann, G.; Tichomirowa, M.; Merz, C.; Pekdeger, A. 2003. Sulfide oxidation and sulfate reduction in a shallow groundwater system (Oderbruch aquifer, Germany). Journal of Hydrology 278, 231-243.

Mariotti, A.; Germon, J.C.; Hubert, P.; Kaiser, P.; Letolle, R.; Tardieux, A.; Tardieux, P., 1981. Experimental-determination of nitrogen kinetic isotope fractionation – some principles – illustration for the denitrification and nitrification processes. Plant and Soil 62, 413-430.

McDonald, M.G. and Harbaugh, A.W., 1988. Techniques of Water Resources Investigations of the United States Geological Survey, Chapter A1: A Modular Three-Dimensional Finite-Difference Groundwater Flow Model, Book 6, Modeling Techniques. U.S. Geological Survey Open File Report.

Meckenstock, R.U.; Morasch, B.; Griebler, C.; Richnow, H.H., 2004. Stable isotope fractionation analysis as a tool to monitor biodegradation in contaminated aquifers. Journal of Contaminant Hydrology 75, 215-255.

Meckenstock, R.U.; Richnow, H.H., 2002. Qualifications of isotope fractionation in experiments with deuterium-labeled substrates. Applied and Environmental Microbiology 68, 5206-5207.

Michaelis, L.; Menten, M.M., 1913. Die kinetic der invertigwirkung (The kinetics of invertase activity). Biochemische Zeitschrift 49, 333-369.

Miller, E.K.; Blum, J.D.; Friedland, A.J., 1993. Determination of soil exchangeable – cation loss and weathering rates using Sr isotopes. Nature 362, 438-441.

Monod, J., 1949. The growth of bacterial cultures. Annual Review of Microbiology 3, 371-394.

Monod, J., 1942. Recherches sur las croissance des culture bacteriennes (Research on the growth of bacterial cultures). Hermann et Cie.

Moon, H.S.; McGuinness, L.; Kukkadapu, R.K.; Peacock, A.D.; Komlos, J.; Kerkhof, L.J.; Long, P.E.; Jaffé, P.R. 2010. Microbial reduction of uranium under iron- and sulfate-reducing conditions: Effect of amended goethite on microbial community composition and dynamics. Water Research 44, 4015-4028.

Moon, H.S.; Komlos, J.; Jaffé, P.R. 2009. Biogenic U(IV) oxidation by dissolution oxygen and nitrate in sediment after prolonged U(VI)/Fe(III)/$SO_4^{2=}$ reduction. Journal of Contaminant Hydrology 105, 18-27.

Moon, H.S.; Komlos, J.; Jaffé, P.R., 2007. Uranium reoxidation in previously bioreduced sediment by dissolved oxygen and nitrate. Environmental Science & Technology 41, 4587-4592.

National Research Council, 1999. Groundwater and soil cleanup: Improving management of persistent contaminants. Committee on Technologies for Cleanup of Subsurface Contaminants in the DOE Weapons Complex, National Academies Press, 304 p.

Nehrke, G.; Reichart, G.J.; Van Cappelen, P.; Meile, C.; Bijma, J. 2007. Dependence of calcite growth rate and Sr partitioning on solution stoichiometry: Non-Kossel crystal growth. Geochimica et Cosmochimica Acta 71, 2240-2249.

Nielsen, L.C.; DePaolo, D.J.; DeYoreo, J.J. 2012. Self-consistent model of growth rate and kinetic isotope fractionation during surface controlled calcite growth. Geochimica et Cosmochimica Acta (in press).

Nielsen, L.C.; Druhan, J.L.; Yang, W.; Brown, S.T.; DePaolo, D.J. 2011. Calcium isotopes as tracers of biogeochemical processes in Handbook of Environmental Isotope Geochemistry, Baskaran, M. (ed), Advances in Isotope Geochemistry. Springer-Verlag Berlin Heidelberg, p. 105-124.

Noiriel, C.; Steefel, C.I.; Yang, L.; Ajo-Franklin, J. 2012. Upscaling calcium carbonate precipitation rates from pore to continuum scale. Chemical Geology (in review).

NRC, 2000. Standard Review Plan for the Review of DOE Plans for Achieving Regulatory Compliance at Sites with Contaminated Groundwater under Title I of the Uranium Mill Tailings Radiation Control Act. NUREG-1724.

Parkhurst, D.L.; Appelo, C.A.J. 1999. User's guide to PHREEQC (version 2) – A computer program for speciation, batch-reaction, one dimensional transport and inverse geochemical calculations. Water Resources Investigations Report 99-4259. U.S. Geological Survey.

Perdikouri, C.; Putnis, C.V.; Kasioptas, A.; Putnis, A. 2009. An atomic force microscopy study of the growth of a calcite surface as a function of calcium/carbonate concentration ratio in solution at constant supersaturation. Crystal Growth & Design 9, 4344-4350.

Poulton, S.W.; Krom, M.D.; Raiswell, R. 2004. A revised scheme for the reactivity of iron (oxyhydr)oxide minerals towards dissolved sulfide. Geochimica et Cosmochimica Acta 68, 3703-3715.

Price, M.N.; Dehal, P.S.; Arkin, A.P., 2010. FastTree: Computing large minimum evolution trees with profiles instead of a distance matrix. Molecular Biology and Evolution 26, 1641-1650.

Rees, C.E., 1973. A steady-state model for sulphur isotope fractionation in bacterial reduction processes. Geochimica et Cosmochimica Acta 37, 1141-1162.

Reynard, L.M.; Day, C.C.; Henderson, G.M. 2011. Large fractionation of calcium isotopes during cave-analogue calcium carbonate growth. Geochimica et Cosmochimica Acta 75, 3726-3740.

Richter, F.M.; DePaolo, D.J. 1987. Numerical models of diagenesis and the Neogene Sr isotopic evolution of seawater from DSDP Site 590B. Earth and Planetary Science Letters 83, 27-38.

Rittmann, B.E. and McCarty, P.L. 2001. Environmental Biotechnology: Principles and Applications. McGraw-Hill, New York, NY, 754 p.

Roden, E.E., 2008. Microbiological controls on geochemical kinetics 1: Fundamentals and case study on microbial Fe(III) oxide reduction *in* Kinetics of water-rock interaction (S.L. Brantley; J.D. Kubicki; A.F. White, eds.). Springer, pp. 335-416.

Rolle, M.; Chiogna, G.; Bauer, R.; Griebler, C.; Grathwohl, P.; 2010. Isotopic fractionation by transverse dispersion: Flow-through microcosms and reactive transport modeling study. Environmental Science and Technology 44, 6167-6173.

Rusin, P.; Quintana, L.; Brainard, J.; Streitlemeier, B.; Tait, C.; Ekberg, S.; Palmer, P.; Newton, T.; Clark, D., 1994. Solubilization of plutonium hydrous oxide by iron reducing bacteria. Environmental Science and Technology 28, 1686-1690.

Russell, W.A.; Papanastassiou, D.A., 1978. Calcium isotope fractionation in ion-exchange chromatography. Analytical Chemistry 50, 1151-1154.

Schmidt, T.C.; Zwank, L.; Elsner, M.; Berg, M.; Meckenstock, R.U.; Haderlein, S.B., 2004. Compound-specific stable isotope analysis of organic contaminants in natural environments: A critical review of the state of the art, prospects, and future challenges. Analytical and Bioanalytical Chemistry 378, 283-300.

Shi, Y.; Zwolinski, M.D.; Schreiber, M.E.; Bahr, J.M.; Sewell, G.W.; Hickey, W.J., 1999. Molecular analysis of microbial community structures in pristine and contaminated aquifers: Field and laboratory microcosm experiments. Applied and Environmental Microbiology 65, 2143-2150.

Singleton, M.J.; Maher, K.; DePaolo, D.J.; Conrad, M.E.; Dresel, P.E. 2006. Dissolution rates and vadose zone drainage from strontium isotope measurements of

groundwater in the Pasco Basin, WA unconfined aquifer. Journal of Hydrology 321, 39-58.

Singleton, M.J.; Sonnenthal, E.L.; Conrad, M.E.; DePaolo, D.J.; Gee, G.W. 2004. Multiphase reactive transport modeling of stable isotope fractionation in unsaturated zone pore water and vapor: Application to seasonal infiltration events at the Hanford Site, WA. Vadose Zone Journal 3, 775-785.

Skulan, J.; DePaolo, D.J.; Owens, T.L. 1997. Biological control of calcium isotopic abundances in the global calcium cycle. Geochimica et Cosmochimica Acta 61, 2505-2510.

Sparks, D.L., 2003. Environmental Soil Chemistry (2^{nd} ed.). Academic Press, 352 pp.

Sposito, G., 2008. The Chemistry of Soils (2^{nd} ed.). Oxford University Press, 329 pp.

Sposito, G., 1981. Cation exchange in soils: An historical and theoretical perspective *in* Chemistry in the Soil Environment (D.E. Baker et al., eds.). Soil Science of Society of America, Madison, WI, pp. 13-30.

Sposito, G.; Mattigod, S.V., 1979. Ideal behavior in Na-trace metal cation exchange on Camp Berteau montmorillonite. Clays and Clay Minerals 27, 125-128.

Stam, M.C.; Mason, P.R.D.; Laverman, A.M.; Pallud, C.; Van Cappellen, P., 2011. (34)S/(32)S fractionation by sulfate-reducing microbial communities in estuarine sediments. Geochimica et Cosmochimica Acta 75, 3903-3914.

Stack, A.G.; Gratham, M.C. 2010. Growth rate of calcite steps as a function of aqueous calcium-to-carbonate ratio: Independent attachment and detachment of calcium and carbonate ions. Crystal Growth & Design 10, 1409-1413.

Steefel, C.I.; Maher, K., 2009. Fluid-rock interaction: A reactive transport approach *in* Reviews in Mineralogy & Geochemistry vol. 70, 485-532.

Steefel, C.I. 2007. CrunchFlow User's Manual. Lawrence Berkeley National Laboratory.

Steefel, C.I.; DePaolo, D.J.; Lichtner, P.C. 2005. Reactive transport modeling: An essential tool and a new research approach for the earth sciences. Earth and Planetary Science Letters 240, 539-558.

Steefel, C.I.; Carroll, S.; Zhao, P.H.; Roberts, S. 2003. Cesium migration in Hanford sediment: A multiscale cation exchange model based on laboratory transport experiments. Journal of Contaminant Hydrology 67, 219-246.

Tang, J.; Niedermayr, A.; Köhler, S.J.; Böhm, F.; Kisakürek, B.; Eisenhauer, A.; Dietzel, M. 2012. Sr^{2+}/Ca^{2+} and $^{44}Ca/^{40}Ca$ fractionation during inorganic calcite formation:

III. Impact of salinity/ionic strength. Geochimica et Cosmochimica Acta 77, 432-443.

Tang, J.; Dietzel, M.; Böhm, F.; Köhler, S.J.; Eisenhauer, A. 2008. Sr^{2+}/Ca^{2+} and $^{44}Ca/^{40}Ca$ fractionation during inorganic calcite formation: II. Ca isotopes. Geochimica et Cosmochimica Acta 72, 3733-3745.

Teng, H.H.; Dove, P.M.; DeYoreo, J.J., 2000. Kinetics of calcite growth: Surface processes and relationships to macroscopic rate laws. Geochimica et Cosmochimica Acta 64, 2255-2266.

Torn, M.S.; Davis, S.; Bird, J.A.; Shaw, M.R.; Conrad, M.E., 2003. Automated analysis of C-13/C-12 ratios in CO2 and dissolved inorganic carbon for ecological and environmental applications. Rapid Communications in Mass Spectrometry 17, 2675-2682.

Turchyn, A.V.; DePaolo, D.J. 2011. Calcium isotope evidence for suppression of carbonate dissolution in carbonate-bearing organic-rich sediments. Geochimica et Cosmochimia Acta 75, 7081-7098.

Turick, C.E.; Apel, W.A.; Carmiol, N.S., 1996. Isolation of hexavalent chromium reducing anaerobes from hexavalent chromium-contaminated and noncontaminated environments. Applied Microbiology and Biotechnology 44, 683-688.

van Breukelen, B.M.; Prommer, H. 2008. Beyond the Rayleigh equation: Reactive transport modeling of isotope fractionation effects to improve quantification of biodegredation. Environmental Science & Technology 42, 2457-2463.

van Breukelen, B.M., 2007. Quantifying the degradation and dilution contribution to natural attenuation of contaminants by means of an open system Rayleigh equation. Environmental Science and Technology 41, 4980-4985.

van Breukelen, B.M.; Griffioen, J.; Röling, W.F.M.; van Verseveld, H.W. 2004. Reactive transport modeling of biogeochemical processes and carbon isotope geochemistry inside a landfill leachate plume. Journal of Contaminant Hydrology 70, 249-269.

VanCappellen, P.; Gaillard, J.F., 1996. Biogeochemical dynamics in aquatic sediments *in* Reactive Transport in Porous Media vol. 34 (P.C. Lichtner; C.I. Steefel; E.H. Oelkers, eds.) The Mineralogical Society of America, pp. 335 – 376.

Vrionis, H.A.; Anderson, R.T.; Ortiz-Bernad, I.; O'Neill, K.R.; Resch, C.T.; Peacock, A.D.; Dayvault, R.; White, D.C.; Long, P.E.; Lovley, D.R. 2005. Microbiological and geochemical heterogeneity in an in situ uranium bioremediaton field site. Applied and Environmental Microbiology 71, 6308-6318.

White, A.F.; Bullen, T.D.; Vivit, D.V.; Schulz, M.S.; Clow, D.W. 1999. The role of disseminated calcite in the chemical weathering of granitoid rocks. Geochimica et Cosmochimica Acta 63, 1939-1953.

Wilkins, M.J.; Livens, F.R.; Vaughan, D.J.; Lloyd, J.R. 2006. The impact of Fe(III) reducing bateria on uranium mobility. Biogeochemistry 78, 125-150.

Williams, A.G.B.; Gregory, K.B.; Parkin, G.F.; Scherer, N.M., 2005. Hexahydro-1,3,5-trinitro-1.3.5-triazine transformation by biologically reduced ferrihydrite: Evolution of Fe mineralogy, surface area, and reaction rates. Environmental Science & Technology 39, 5183-5189.

Williams, K.H.; Long, P.E.; Davis, J.A.; Wilkins, M.J.; N'Guessan, A.L.; Steefel, C.I.; Yang, L.; Newcomer, D.; Spane, F.A.; Kerkhof, L.J.; McGuinness, L.; Dayvault, R.; Lovely, D.R. 2011. Acetate availability and its influence on sustainable bioremediation of uranium-contaminated groundwater. Geomicrobiology Journal 28, 519-539.

Wolthers, M.; Nehrke, G.; Gustafsson, J.P.; Van Cappellen, P. 2012. Calcite growth kinetics: Modeling the effect of solution stoichiometry. Geochimica et Cosmochimica Acta 77, 121-134.

Wood, B.D.; Ginn, T.R.; Dawson, C.N. 1995. Effects of microbial metabolic lag in contaminant transport and biodegredation modeling. Water Resources Research 31, 553-563.

Xu, T.; Sonnenthal, E.; Spycher, N.; Pruess, K. 2004. TOUGHREACT user's guide: A simulation program for non-isothermal multiphase reactive geochemical transport in variable saturated geologic media. Lawerence Berkeley National Laboratory Report LBNL-55460, Berkeley, CA, 192 p.

Yabusaki, S.B.; Fang, Y.; Williams, K.H.; Murray, C.J.; Ward, A.L.; Dayvault R.D.; Waichler, S.R.; Newcomer, D.R.; Spane, F.A.; Long, P.E. 2011. Variably saturated flow and multicomponent biogeochemical reactive transport modeling of a uranium bioremediation field experiment. Journal of Contaminant Hydrology 126, 271-290.

Yabusaki, S.B.; Fang, Y.L.; Long, P.E.; Resch, C.T.; Peacock, A.D.; Komlos, J.; Jaffe, P.R.; Morrison, S.J.; Dayvault, R.D.; White, D.C.; Anderson, R.T. 2007. Uranium removal from groundwater via in situ biostimulation: Field-scale modeling of transport and biological processes. Journal of Contaminant Hydrology 93, 216-235.

Yeh, G.T.; Sun, J.; Jardine, P.M.; Burgos, W.D.; Fang, Y.; Li, M.H.; Siegel, M.D. 2004. HYDROGEOCHEM 5.0: A three-dimensional model of coupled fluid flow, thermal transport, and HYDROGEOCHEMical transport through variably

saturated conditions – version 5.0. Prepared by Oak Ridge National Laboratory for the DOE, Oak Ridge, Tennessee.

Zeebe, R.E.; Wolf-Gladrow, D. 2001. CO_2 in seawater: Equilibrium, kinetics, isotopes. Elsevier, 346 p.

Zhang, J.W.; Nancollas, G.H., 1998. Kink density and rate of step movement during growth and dissolution of an AB crystal in a nonstoichiometric solution. Journal of Colloid and Interface Science 200, 131-145.

Zhang, R.S.; Nash, C.P.; Rock, P.A., 1988. Thermodynamics of calcium-isotope-exchange reactions. 1. Exchange between isotopic calcium carbonates and aqueous calcium ions. The Journal of Physical Chemistry 92, 3989-3993.

Zheng, C. 1990. MT3D, A Modular Three-Dimensional Transport Model, Documentation and User's Guide, First Edition, S.S. Papadopulos and Associates, Bethesda, Maryland.

Appendix A

Additional data tables

Table A1: Background sulfate concentrations measured from wells U01, U02 and U03 from August 2007 to December 2009. Used in chapter 2, Fig. 2.1

Date	U01	U02	U03
8/10/07	9.95	10.6266	11.0626
8/12/07	11.13	11.318	11.4178
8/14/07	11.08	11.175	11.4974
8/20/07	10.91	10.5446	
8/21/07	10.75	10.7479	10.758
8/25/07	11.68	11.08	11.6
8/29/07	10.66	10.945	11.205
9/1/07	10.81	10.81	10.81
9/3/07	11.07	11.12	11.17
9/13/07	10.51	10.5378	10.7266
9/18/07	11.73	11.7388	11.9894
7/19/08	8.86	9.1266	9.4899
7/22/08	8.62	9.3281	9.6622
7/24/08	9.52	9.3444	9.1839
7/26/08	8.87	9.5622	9.6612
7/29/08	9.73		9.48145
7/30/08	9.48		
7/31/08	9.23	9.1667	9.3017
8/4/08	9.74		9.2739
8/5/08			9.4546
8/7/08	10.10	9.5623	9.7822
8/11/08	10.28		9.8839
8/12/08	10.46	10.5177	9.9856
8/14/08	9.37	9.7253	10.345
8/16/08	9.87		10.5247
8/18/08	10.37	10.2998	10.7044
8/20/08	9.10	9.4151	9.1291
8/22/08	9.29	9.4675	8.96775
8/23/08	9.07		
8/25/08	8.84	9.0836	8.8064
8/27/08	8.92	8.9749	8.8203
8/29/08	8.79		8.6659
8/31/08	8.81	8.851	8.5115
9/2/08	8.81		8.5486
9/4/08	8.82	8.6528	8.5857
9/6/08	8.86		8.85025
9/7/08	8.90		
9/8/08	8.99	8.62065	8.982525
9/10/08	9.08	8.5885	9.115
9/12/08			8.86085
9/16/08	8.29	8.8453	8.6069
9/18/08	8.63	8.2469	8.3396
9/20/08	8.23	9.1666	8.7514
9/22/08	9.26	9.0482	8.722
9/24/08	8.87	9.1766	8.8604
10/1/08	8.84	8.73	8.592

Date	U01	U02	U03
10/10/08	9.22	9.4764	8.7824
10/28/08	9.84	9.9515	9.9226
11/10/08	9.81		10.0392
11/12/08	9.77	9.0309	10.1558
11/17/08	10.60		
12/9/08	11.44	10.0321	9.826
12/22/08	10.67		10.802
1/9/09	10.72	10.3113	9.4169
2/10/09	10.41	10.8061	10.433
2/26/09	10.46		
3/11/09	11.09	11.7331	11.450
4/9/09	11.72	12.0556	11.793
5/2/09	3.07	10.297	7.997
6/2/09	8.45	10.522	8.866
7/8/09	8.62	9.570	9.500
7/20/09	9.37	10.430	10.570
7/24/09	10.12		
7/26/09	9.80		
7/28/09	9.77	9.975	10.201
7/30/09	9.54		
8/1/09	9.52		
8/3/09	9.35		
8/5/09	8.91	10.054	9.757
8/7/09	9.70		
8/9/09	9.51	10.080	9.658
8/11/09	9.38		
8/13/09	9.77		9.482
8/17/09	9.23	9.819	
8/21/09	8.46		
8/25/09	9.31		8.943
8/30/09	9.06	9.865	8.358
9/3/09	9.0	9.887	8.509
9/6/09	8.88	9.910	8.660
9/9/09	8.5	9.762	9.055
9/15/09	8.22	9.614	9.449
9/17/09	8.82		8.941
9/28/09	9.16	9.118	9.396
10/27/09	10.33	10.191	9.852
12/8/09	9.80		9.388

Table A2: Acetate, Fe(II), sulfate, sulfide and $\delta^{34}S$ of sulfate values used in chapter 2 to generate Fig. 2.5. 2007 and 2008 values reported for well D04, 2009 values reported for well D01. Days are counted from 0 as the first date of acetate addition for the corresponding amendment experiment.

Date	Day	Acetate [mM]	Fe(II) [mM]	SO_4 [mM]	H_2S [mM]	$\delta^{34}S$ of SO_4 [‰]
8/8/07	0		21.43		0.25	-8.78
8/10/07	2	0.33	25.18	11.39	1.13	
8/12/07	4	1.44	29.11	10.28	0.34	
8/14/07	6	3.14	36.43	11.30	1.25	-8.69
8/18/07	10	3.56	51.25	11.33	1.22	
8/21/07	13	2.86	49.64	9.66	1.88	-8.56
8/22/07	14	3.58	40.36	11.02	0.72	
8/23/07	15	3.50	46.96	11.05	2.34	
8/26/07	18	1.00	56.79	10.97	2.75	-8.39
8/28/07	20	0.32	41.43	11.01	4.03	
8/31/07	23		40.00	10.97	8.00	-8.46
9/3/07	26	2.18	39.11	10.84	12.25	
9/12/07	35	0.48	15.89	8.81	61.56	-4.99
9/13/07	36	0.38	17.68	9.34	33.25	
9/18/07	41	0.01	27.86	10.68	13.69	-6.87
10/9/07	62	0.00	32.86	9.50	0.38	-8.74
7/18/08	-2	0.00	0.00	8.73	272.32	
7/22/08	2	0.00	0.00	8.97	279.68	
7/24/08	4	0.72	12.93	8.81	274.81	
7/25/08	5	1.40	24.99	8.76	273.14	
7/26/08	6	1.73	31.01	8.73	272.31	
7/27/08	7	2.07	37.04	8.70	271.47	-8.89
7/29/08	9	3.00	53.72	8.04	250.67	
7/30/08	10	3.03	54.28	8.36	260.64	
7/31/08	11	3.06	54.84	8.68	270.60	-7.80
8/2/08	13	2.44	43.78	7.98	248.83	-7.93
8/4/08	15	1.34	24.04	7.72	240.64	-6.65
8/7/08	18	0.07	1.20	8.19	255.33	
8/8/08	19	0.02	0.43	8.66	270.10	-7.28
8/9/08	20	0.00	0.00	8.54	266.30	-6.55
8/11/08	22	0.00	0.00	10.11	315.42	
8/12/08	23	0.00	0.00	10.03	312.88	-6.14
8/14/08	25	0.00	0.00	9.95	310.34	
8/16/08	27	0.00	0.00	9.01	281.14	-6.15
8/18/08	29	0.01	0.16	8.16	254.57	
8/20/08	31	0.00	0.08	8.40	262.11	-6.15
8/21/08	32	0.00	0.00	8.06	251.51	
8/22/08	33	0.00	0.00	8.28	258.09	-7.62
8/23/08	34	0.00	0.00	8.16	254.58	-6.70
8/25/08	36	0.00	0.00	7.27	226.68	
8/26/08	37	0.00	0.00	7.23	225.52	-5.66
8/27/08	38	0.00	0.00	7.52	234.67	
8/29/08	40	0.01	0.16	7.50	233.81	

Date	Day	Acetate [mM]	Fe(II) [mM]	SO_4 [mM]	H_2S [mM]	$\delta^{34}S$ of SO_4 [‰]
8/31/08	42	0.40	7.18	6.56	204.45	-6.45
9/2/08	44	0.20	3.61	6.57	204.79	
9/4/08	46	0.16	2.81	5.82	181.41	-6.73
9/5/08	47	0.10	1.84	6.29	196.14	
9/6/08	48	0.05	0.86	6.76	210.86	
9/8/08	50	0.00	0.00	7.54	235.27	-7.36
9/10/08	52	0.00	0.00	7.91	246.73	
9/12/08	54	0.00	0.00	8.28	258.20	-8.58
9/16/08	58	0.00	0.00	8.71	271.53	
9/18/08	60	0.00	0.00	8.84	275.63	
9/20/08	62	0.00	0.00	8.64	269.40	
9/22/08	64	0.00	0.00	9.36	291.91	
9/24/08	66	0.00	0.00	9.20	286.77	
9/26/08	68	0.00	0.00	9.92	309.25	
9/30/08	72	0.00	0.00	8.66	270.21	-8.87
10/18/08	90	0.00	0.00	10.37	323.30	
7/22/09	0	0.01	44.23	9.65	0.00	-7.73
7/26/09	4	8.33	71.63	10.67	16.50	-6.41
8/1/09	10	3.72	8.06	3.72	62.37	-1.43
8/11/09	20	0.06	19.34	5.52	1512.55	-4.56
8/13/09	22	0.01	22.38	6.40	991.74	-3.25
8/17/09	26	0.03	35.46	7.54	760.95	-5.73
8/21/09	30	0.01	45.48	6.18	923.12	-4.47
8/25/09	34	0.01	49.60	4.81	1394.04	-4.98
8/30/09	39	0.02	52.47	4.65	1843.91	-3.49
9/6/09	46	0.02	41.54	6.00	0.81	-0.77
9/17/09	57	0.02	68.05	7.66	213.63	-5.38
9/29/09	69	0.00	78.79	9.40	155.15	-6.30
10/28/09	98	0.12	65.54	9.13	22.70	-6.61

Table A3: Anion, cation and $\delta^{44}Ca$ values for the three injection wells discussed in chapter 3. Days are counted since the stop of acetate injection.

Day	Well	Acetate (mM)	Cl (mM)	SO_4 (mM)	Br (mM)	Sr (μM)	Ca (mM)	$\delta^{44}Ca$ (‰)
-14	G51	0.36	6.00	9.25	0.05			
-9	G51	0.27	5.99	9.12	0.03			
-8	G51	0.27	6.53	8.46	0.35			
-7	G51	0.25	5.52	7.80	0.00			
-4	G51	0.31	6.00	8.97	0.00			
-2	G51	0.09	5.51	8.25	0.00			
-1	G51	0.09	5.76	9.21	0.32			
2	G51	338.12	4.63	9.29	25.62			
4	G51	270.01	4.34	9.09	20.42	52.21	6.43	
6	G51	91.56	4.91	9.33	9.19			
8	G51	76.71	4.70	9.03	7.63			
10	G51	76.37	4.61	9.05	7.54			
12	G51	77.66	5.02	9.38	7.79	48.08	5.96	
14	G51	74.08	4.58	8.95	7.33			
16	G51	71.75	4.41	8.63	7.06	47.71	5.95	
18	G51	75.50	4.72	9.08	7.49	47.08	5.75	0.24
20	G51	125.78	3.87	8.52	12.22	49.45	5.93	
22	G51	149.47	3.97	9.33	14.19	50.11	6.10	
26	G51	136.95	3.74	8.41	13.25	48.66	5.85	
30	G51	148.80	3.67	9.31	14.73	49.03	5.96	
34	G51	132.38	3.59	8.16	12.94	48.68	5.95	
39	G51	131.98	3.51	6.05	12.97			
41	G51					47.02	5.42	0.24
44	G51	120.55	3.73	1.28	12.11			
47	G51	114.28	3.73	0.15	11.30	24.51	3.16	1.015
49	G51	123.45	5.07	0.28	12.75	22.06	2.79	0.93
55	G51	90.87	4.33	0.00	9.21			
57	G51	98.91	4.77	0.08	10.06	18.45	2.24	1.165
69	G51	63.83	4.23	0.07	6.86	14.97	1.72	1.305
97	G51	30.65	4.84	0.14	4.22	4.88	0.76	1.31
140	G51	0.02	5.43	0.38	2.54			
-14	G52	0.22	7.45	4.52	0.70			
-9	G52	0.10	8.27	5.30	0.79			
-8	G52	0.28	6.92	5.17	1.67			
-7	G52	0.16	7.65	5.03	0.73			
-4	G52	0.34	8.09	5.27	0.75			
-2	G52	0.13	7.47	5.01	0.72			
-1	G52	0.11	6.30	7.00	1.52			
2	G52	296.71	4.30	9.00	22.32			
4	G52	263.48	4.41	8.87	19.87	45.44	5.90	
6	G52	79.31	5.06	9.09	7.83			
8	G52	72.12	4.36	8.47	7.15			
10	G52	74.17	4.56	8.19	7.37			
12	G52	76.71	4.75	9.10	7.62	49.51	6.35	
14	G52	70.52	4.28	8.34	6.93			

Day	Well	Acetate (mM)	Cl (mM)	SO_4 (mM)	Br (mM)	Sr (μM)	Ca (mM)	$\delta^{44}Ca$ (‰)
16	G52	73.50	4.47	8.58	7.21	47.47	6.09	
18	G52	78.37	5.32	9.36	7.86	46.37	5.64	
20	G52	138.05	3.72	8.46	13.25	50.60	6.20	
22	G52	140.35	3.77	8.76	13.51	45.00	6.48	0.085
26	G52	134.64	3.60	8.03	13.02	48.78	6.06	
30	G52	143.56	3.92	8.68	13.67	48.48	5.91	
34	G52	160.09	4.25	9.47	15.16	48.76	6.03	0.14
39	G52	131.40	3.53	3.60	13.18	42.43	4.19	
44	G52	122.06	3.47	0.38	12.68			
47	G52	113.56	3.48	0.16	11.92	35.54	3.20	0.8
49	G52	117.61	3.89	0.12	12.62	33.29	2.98	
55	G52	112.09	3.80	0.07	12.16			
57	G52	110.07	3.91	0.14	12.29	29.47	2.66	0.97
69	G52	79.93	4.58	0.21	10.69	22.95	1.82	1.0925
97	G52	38.29	4.11	0.26	8.58	3.32	0.39	2.5725
140	G52	4.24	4.87	0.40	9.04			
-14	G53	0.27	5.18	6.47	0.04			
-9	G53	0.32	6.86	9.01	0.06			
-8	G53	0.27	6.09	8.57	0.19			
-7	G53	0.37	8.09	10.87	0.00			
-4	G53	0.37	8.24	11.33	0.12			
-2	G53	0.18	7.70	10.84	0.14			
-1	G53	0.09	5.47	8.18	0.24			
2	G53	288.18	4.30	8.83	21.72			
4	G53	259.26	4.34	9.01	19.53	48.83	6.07	-0.165
6	G53	77.82	4.69	8.91	7.72			
8	G53	75.74	4.63	8.88	7.51			
10	G53	74.24	4.50	8.67	7.36			
12	G53	76.08	4.68	8.99	7.52	48.11	5.92	
14	G53	74.82	4.78	8.93	7.57			
16	G53	73.76	4.45	9.12	7.29	37.47	4.60	-0.23
18	G53	31.12	4.58	6.78	2.65	41.97	5.40	
20	G53	47.70	4.41	7.94	4.47	48.73	7.01	-0.305
22	G53	167.88	4.55	9.79	15.56	46.59	5.67	
26	G53	155.77	4.21	9.12	14.63	48.72	5.77	
30	G53	86.71	4.62	7.80	8.75	46.20	5.85	-0.27
34	G53	37.34	5.10	7.39	3.46			
39	G53	0.62	4.93	8.27	0.00	43.19	6.04	
44	G53	2.06	5.12	8.14	0.22			
47	G53	10.69	5.46	8.23	0.72	43.02	6.01	
49	G53	1.09	4.97	8.00	0.00	41.98	5.89	
55	G53	0.38	5.12	7.74	0.00			
57	G53	15.32	5.15	7.64	0.26	42.65	6.04	
69	G53	0.32	5.57	8.24	0.00	44.06	5.95	
97	G53	4.83	5.82	8.74	0.35	43.30	6.18	-0.035
140	G53	0.02	5.63	9.65	0.00			

Table A4: Deuterium and ^{18}O tracer breakthrough curves for mesoscale column experiment, discussed in chapter 4.

Starting day	Hour	Location	δ^2H (‰)	$\delta^{18}O$ (‰)
1	0	10 cm	-68.22	-14.17
1	0	30 cm	-78.40	-11.63
1	0	50 cm	-84.21	-12.18
1	0	70 cm	-86.29	-12.21
1	0	90 cm	-85.20	-12.11
1	0	effluent	-86.50	-12.22
1	6	10 cm	266.07	-11.37
1	6	30 cm	-74.19	-12.12
1	6	50 cm	-83.35	-12.14
1	6	70 cm	-86.25	-12.14
1	6	90 cm	-87.98	-12.12
1	6	effluent		
1	12	10 cm	422.33	-12.14
1	12	30 cm	53.02	-12.18
1	12	50 cm	-78.00	-12.11
1	12	70 cm	-83.15	-12.06
1	12	90 cm	-77.24	-9.53
1	12	effluent	-85.51	-12.14
1	24	10 cm	444.36	-12.03
1	24	30 cm	372.76	-12.16
1	24	50 cm	110.49	-12.09
1	24	70 cm	-23.99	-12.11
1	24	90 cm	-67.30	-9.85
1	24	effluent	-80.90	-12.18
1	48	10 cm	453.73	-12.12
1	48	30 cm	468.98	-12.16
1	48	50 cm	431.81	-12.08
1	48	70 cm	347.17	-12.10
1	48	90 cm	210.69	-12.16
1	48	effluent	135.40	-12.22
1	72	10 cm	451.71	-9.75
1	72	30 cm	471.85	-12.18
1	72	50 cm	472.75	-11.84
1	72	70 cm	459.97	-11.96
1	72	90 cm	411.17	-12.17
1	72	effluent	357.76	-12.15
1	96	10 cm	471.23	-12.08
1	96	30 cm	472.85	-12.12
1	96	50 cm	476.71	-12.10
1	96	70 cm	477.62	-12.10
1	96	90 cm	470.69	-12.09
1	96	effluent	463.61	-12.16
24	0	10 cm	478.99	-12.23
24	0	30 cm	479.78	-12.14
24	0	50 cm	480.26	-12.17
24	0	70 cm	478.62	-12.17

Starting day	Hour	Location	δ^2H (‰)	$\delta^{18}O$ (‰)
24	0	90 cm	475.18	-11.90
24	0	effluent	474.48	-11.63
24	9.5	10 cm	481.31	10.18
24	9.5	30 cm	479.12	-3.97
24	9.5	50 cm	474.22	-11.20
24	9.5	70 cm	470.71	-12.15
24	9.5	90 cm	478.63	-12.18
24	9.5	effluent	481.00	-12.24
24	25	10 cm	477.49	15.56
24	25	30 cm	476.75	9.23
24	25	50 cm	478.13	-0.08
24	25	70 cm	481.37	-7.47
24	25	90 cm	477.64	-11.07
24	25	effluent	476.18	-11.90
24	49	10 cm	480.88	15.66
24	49	30 cm	481.26	15.15
24	49	50 cm	480.44	9.53
24	49	70 cm	476.69	5.23
24	49	90 cm	476.92	-1.34
24	49	effluent	478.18	-5.18
24	73	10 cm	480.43	15.74
24	73	30 cm	479.87	15.79
24	73	50 cm	477.73	14.33
24	73	70 cm	472.52	12.82
24	73	90 cm	477.67	9.01
24	73	effluent	481.25	4.89
24	99	10 cm	444.51	15.69
24	99	30 cm	468.07	15.68
24	99	50 cm	472.16	15.36
24	99	70 cm	444.89	15.16
24	99	90 cm	466.01	14.31
24	99	effluent	475.13	12.16
24	124	10 cm	475.49	15.82
24	124	30 cm	477.58	15.84
24	124	50 cm	477.19	15.82
24	124	70 cm	477.31	15.69
24	124	90 cm	476.27	15.37
24	124	effluent	476.06	14.63
40	0	10 cm	475.67	15.81
40	0	30 cm	474.20	15.70
40	0	50 cm	475.80	15.80
40	0	70 cm	475.92	15.78
40	0	90 cm	474.98	15.77
40	0	effluent	478.15	15.76
40	6	10 cm	473.15	1.95
40	6	30 cm	476.66	12.95
40	6	50 cm	474.81	15.73
40	6	70 cm	476.86	15.75

Starting day	Hour	Location	δ^2H (‰)	$\delta^{18}O$ (‰)
40	6	90 cm	476.63	15.74
40	6	effluent	474.33	15.68
40	12	10 cm	478.07	-9.00
40	12	30 cm	475.22	5.66
40	12	50 cm	477.63	14.14
40	12	70 cm	474.69	15.76
40	12	90 cm	475.70	15.76
40	12	effluent	476.31	15.73
40	24	10 cm	473.52	-11.87
40	24	30 cm	478.44	-5.31
40	24	50 cm	474.19	4.36
40	24	70 cm	477.71	12.02
40	24	90 cm	476.41	15.05
40	24	effluent	476.57	15.57
40	50	10 cm	477.53	-12.09
40	50	30 cm	474.26	-11.75
40	50	50 cm	478.13	-6.77
40	50	70 cm	475.14	-2.84
40	50	90 cm	477.70	3.90
40	50	effluent	476.01	8.05
40	78	10 cm	475.84	-12.12
40	78	30 cm	477.83	-12.08
40	78	50 cm	474.04	-11.44
40	78	70 cm	478.52	-10.22
40	78	90 cm	475.11	-6.96
40	78	effluent	478.22	-3.83

Table A5: Anion concentrations from the mesoscale column study for all side ports and effluent as described in chapter 4 & 5.

Day	Location	Acetate (mM)	Cl (mM)	Br (mM)	SO_4 (mM)
1	10 cm	6.66	2.90	1.15	9.13
2	10 cm	7.29	2.92	1.17	9.17
3	10 cm	7.12	2.85	1.31	9.08
4	10 cm	6.78	2.79	1.29	8.90
5	10 cm	7.80	2.96	1.27	9.03
6	10 cm	7.67	2.94	1.27	8.95
7	10 cm	7.78	2.94	1.27	9.07
8	10 cm	7.57	2.87	1.24	8.95
9	10 cm	6.24	2.66	1.24	8.94
10	10 cm	6.06	2.63	1.21	8.52
11	10 cm	8.63	3.06	1.34	9.03
12	10 cm	8.24	2.99	1.35	8.74
13	10 cm	7.57	2.84	1.25	8.82
14	10 cm	7.45	2.78	1.23	8.72
15	10 cm	7.05	3.64	1.26	8.41
16	10 cm	8.40	2.97	1.29	8.97
17	10 cm	7.07	2.78	1.29	9.10
18	10 cm	8.22	2.96	1.30	8.79
19	10 cm	9.60	3.27	1.37	8.92
20	10 cm	8.03	2.99	1.31	8.77
21	10 cm	7.90	2.97	1.32	9.01
22	10 cm	7.80	2.94	1.32	8.88
23	10 cm	7.52	2.88	1.29	9.27
24	10 cm	7.27	2.81	1.31	8.98
25	10 cm	7.27	2.81	1.21	8.95
26	10 cm	7.05	2.77	1.21	8.87
27	10 cm	6.97	2.79	1.24	8.94
28	10 cm	6.76	2.75	1.26	8.85
29	10 cm	7.98	2.91	1.28	8.72
30	10 cm	6.46	2.69	1.18	8.73
31	10 cm	6.88	2.86	1.25	8.92
32	10 cm	6.48	2.78	1.25	8.56
33	10 cm	8.29	3.00	1.28	9.95
34	10 cm	7.83	2.95	1.31	8.27
35	10 cm	7.29	2.88	1.28	8.11
36	10 cm	8.03	2.89	1.24	7.91
37	10 cm	7.70	3.08	1.32	7.63
38	10 cm	6.26	2.85	1.24	7.32
39	10 cm	5.72	2.90	1.27	7.12
40	10 cm	5.45	2.97	1.22	6.71
41	10 cm	6.21	3.04	1.30	7.05
42	10 cm	5.31	2.95	1.24	6.42
43	10 cm	5.55	3.03	1.30	6.60
1	30 cm	0.00	2.95	0.63	9.01
2	30 cm	5.58	2.90	1.07	9.02

Day	Location	Acetate (mM)	Cl (mM)	Br (mM)	SO_4 (mM)
3	30 cm	8.49	3.14	1.48	9.02
4	30 cm	6.60	2.80	1.29	8.89
5	30 cm	7.14	2.94	1.27	8.95
6	30 cm	7.07	2.90	1.26	8.70
7	30 cm	8.81	3.18	1.30	8.96
8	30 cm	7.31	2.90	1.24	8.91
9	30 cm	6.27	2.68	1.22	8.90
10	30 cm	6.39	2.69	1.23	9.27
11	30 cm	7.48	2.85	1.28	8.22
12	30 cm	8.18	3.02	1.33	8.73
13	30 cm	7.55	2.89	1.27	8.90
14	30 cm	7.28	2.76	1.23	8.63
15	30 cm	8.31	3.02	1.30	8.93
16	30 cm	7.97	2.96	1.28	8.65
17	30 cm	8.30	3.03	1.34	9.04
18	30 cm	8.11	3.00	1.32	8.82
19	30 cm	8.13	3.23	1.33	8.97
20	30 cm	8.06	3.05	1.31	8.85
21	30 cm	9.24	3.23	1.37	9.02
22	30 cm	7.72	2.94	1.31	8.82
23	30 cm	7.49	2.89	1.30	9.28
24	30 cm	7.16	2.83	1.27	8.97
25	30 cm	7.05	2.80	1.22	8.85
26	30 cm	8.27	3.04	1.27	8.78
27	30 cm	7.26	2.98	1.32	8.99
28	30 cm	6.34	2.76	1.26	8.69
29	30 cm	5.97	2.67	1.21	8.60
30	30 cm	5.98	2.69	1.19	8.40
31	30 cm	6.16	2.83	1.26	8.54
32	30 cm	5.60	2.78	1.30	8.03
33	30 cm	7.45	2.99	1.31	8.49
34	30 cm	6.37	3.01	1.27	7.02
35	30 cm	5.37	2.93	1.24	6.99
36	30 cm	5.73	2.89	1.24	6.53
37	30 cm	4.92	3.00	1.27	5.20
38	30 cm	4.03	2.88	1.24	4.54
39	30 cm	2.14	2.95	1.26	4.15
40	30 cm	2.87	2.81	1.22	3.83
41	30 cm	3.09	3.04	1.28	3.65
42	30 cm	2.36	2.99	1.24	3.40
43	30 cm	2.48	3.05	1.29	3.30
1	50 cm	0.00	3.00	0.00	9.05
2	50 cm	0.00	2.92	0.72	8.94
3	50 cm	6.12	2.88	1.18	8.97
4	50 cm	6.63	2.85	1.27	9.01
5	50 cm	6.93	2.97	1.28	9.01
6	50 cm	6.71	2.97	1.26	8.94

Day	Location	Acetate (mM)	Cl (mM)	Br (mM)	SO_4 (mM)
7	50 cm	6.77	2.93	1.25	9.00
8	50 cm	8.24	3.14	1.28	8.85
9	50 cm	6.10	2.72	1.22	8.99
10	50 cm	5.94	2.63	1.21	8.74
11	50 cm	8.17	3.06	1.35	8.97
12	50 cm	7.93	3.00	1.32	8.72
13	50 cm	7.33	2.88	1.26	8.84
14	50 cm	7.13	2.78	1.25	8.66
15	50 cm	6.62	2.76	1.26	8.79
16	50 cm	7.56	2.97	1.30	8.64
17	50 cm	8.14	3.03	1.34	9.01
18	50 cm	6.47	2.72	1.27	8.89
19	50 cm	8.05	3.05	1.41	8.97
20	50 cm	9.33	3.25	1.42	8.80
21	50 cm	7.83	3.00	1.33	9.04
22	50 cm	7.59	2.93	1.31	8.76
23	50 cm	7.25	2.89	1.30	9.27
24	50 cm	8.25	3.07	1.33	8.92
25	50 cm	6.85	2.81	1.21	8.75
26	50 cm	7.98	3.02	1.29	8.67
27	50 cm	6.30	2.80	1.25	8.73
28	50 cm	7.48	3.02	1.30	8.47
29	50 cm	5.65	2.68	1.22	8.36
30	50 cm	5.43	2.69	1.19	8.13
31	50 cm	5.55	2.95	1.26	8.14
32	50 cm	6.28	3.06	1.31	7.82
33	50 cm	5.70	2.94	1.32	6.88
34	50 cm	5.75	3.05	1.25	6.25
35	50 cm	5.23	2.90	1.24	5.61
36	50 cm	4.07	2.91	1.24	6.01
37	50 cm	3.00	2.92	1.27	3.86
38	50 cm	1.42	2.88	1.24	2.76
39	50 cm	0.37	2.94	1.25	2.27
40	50 cm	0.00	2.85	1.23	1.75
41	50 cm	0.08	3.14	1.27	1.48
42	50 cm	0.00	3.02	1.24	1.32
43	50 cm	0.00	3.13	1.27	1.29
1	70 cm	0.00	2.96	0.00	9.09
2	70 cm	0.00	2.94	0.55	8.94
3	70 cm	4.56	2.92	1.08	9.08
4	70 cm	6.46	2.88	1.24	9.04
5	70 cm	6.55	2.99	1.28	9.11
6	70 cm	7.40	3.19	1.34	8.85
7	70 cm	7.78	3.17	1.29	9.01
8	70 cm	6.39	2.84	1.23	8.75
9	70 cm	5.94	2.70	1.22	8.93
10	70 cm	5.65	2.62	1.21	8.59

Day	Location	Acetate (mM)	Cl (mM)	Br (mM)	SO_4 (mM)
11	70 cm	7.98	3.07	1.33	8.92
12	70 cm	7.83	2.97	1.32	8.71
13	70 cm	8.57	3.10	1.30	8.86
14	70 cm	7.08	2.79	1.24	8.74
15	70 cm	8.00	3.00	1.33	8.86
16	70 cm	7.79	2.98	1.29	8.77
17	70 cm	8.03	3.02	1.33	9.09
18	70 cm	7.81	2.97	1.32	8.87
19	70 cm	7.96	3.06	1.33	9.00
20	70 cm	7.88	3.02	1.32	8.80
21	70 cm	9.14	3.25	1.38	9.13
22	70 cm	7.45	2.94	1.31	8.72
23	70 cm	8.50	3.12	1.34	9.15
24	70 cm	8.37	3.11	1.35	8.95
25	70 cm	6.70	2.83	1.22	8.74
26	70 cm	6.49	2.79	1.22	8.62
27	70 cm	6.05	2.80	1.25	8.54
28	70 cm	5.85	2.78	1.31	8.29
29	70 cm	5.44	2.72	1.24	8.16
30	70 cm	5.05	2.70	1.24	7.78
31	70 cm	5.22	2.95	1.29	8.01
32	70 cm	4.20	2.80	1.25	7.10
33	70 cm	5.41	3.04	1.31	6.49
34	70 cm	4.94	2.94	1.26	5.35
35	70 cm	3.81	2.88	1.23	4.70
36	70 cm	2.74	2.91	1.25	4.00
37	70 cm	1.41	3.00	1.27	2.72
38	70 cm	0.00	2.97	1.24	1.66
39	70 cm	0.00	2.96	1.25	1.21
40	70 cm	0.00	2.93	1.22	0.87
41	70 cm	0.00	3.13	1.27	0.59
42	70 cm	0.00	3.07	1.24	0.57
43	70 cm	0.00	3.17	1.27	0.59
1	90 cm	0.00	2.90	0.00	9.09
2	90 cm	0.00	3.05	0.48	8.94
3	90 cm	2.29	2.94	0.92	9.04
4	90 cm	5.58	2.93	1.17	9.02
5	90 cm	6.30	3.01	1.25	9.09
6	90 cm	5.46	2.94	1.25	8.84
7	90 cm	7.31	3.17	1.34	9.06
8	90 cm	6.11	2.88	1.24	8.86
9	90 cm	6.98	3.00	1.26	8.95
10	90 cm	5.28	2.64	1.20	8.65
12	90 cm	7.69	3.01	1.32	8.80
13	90 cm	7.10	2.85	1.26	8.93
14	90 cm	6.87	2.78	1.24	8.72
15	90 cm	7.86	3.04	1.34	8.87

Day	Location	Acetate (mM)	Cl (mM)	Br (mM)	SO_4 (mM)
16	90 cm	7.72	2.98	1.32	8.73
17	90 cm	7.90	3.03	1.33	9.07
18	90 cm	6.36	2.73	1.26	8.84
19	90 cm	7.98	3.08	1.34	9.02
20	90 cm	7.78	3.03	1.33	8.81
21	90 cm	7.58	3.00	1.32	8.99
22	90 cm	7.30	2.94	1.30	8.71
23	90 cm	8.28	3.12	1.33	9.07
24	90 cm	6.95	2.88	1.29	9.00
25	90 cm	7.97	3.06	1.26	8.65
26	90 cm	6.40	2.82	1.22	8.58
27	90 cm	5.88	2.82	1.31	8.48
28	90 cm	5.57	2.80	1.26	8.11
29	90 cm	4.96	2.71	1.20	7.83
30	90 cm	4.40	2.69	1.25	7.45
31	90 cm	4.28	2.88	1.27	7.27
32	90 cm	3.34	2.81	1.28	6.44
33	90 cm	5.35	3.04	1.31	5.79
34	90 cm	4.03	2.98	1.28	4.76
35	90 cm	3.16	3.08	1.25	4.48
36	90 cm	1.71	2.93	1.24	3.31
37	90 cm	0.59	2.99	1.27	2.19
38	90 cm	0.00	3.00	1.25	1.25
39	90 cm	0.00	3.00	1.26	0.80
40	90 cm	0.00	2.96	1.23	0.69
41	90 cm	0.00	3.08	1.28	0.49
42	90 cm	0.00	3.01	1.25	0.47
43	90 cm	0.00	3.16	1.27	0.48
1	Effluent	0.00	2.78	0.00	8.63
2	Effluent	0.00	3.06	0.50	8.79
3	Effluent	0.86	3.00	0.77	8.91
4	Effluent	4.58	3.10	1.04	8.67
5	Effluent	6.25	3.01	1.23	9.09
6	Effluent	6.13	3.12	1.33	8.62
7	Effluent	5.54	2.92	1.28	9.05
8	Effluent	7.04	3.09	1.32	8.76
9	Effluent	5.07	2.69	1.21	8.80
10	Effluent	6.73	2.88	1.26	8.75
11	Effluent	8.08	3.05	1.34	9.09
12	Effluent	7.56	3.04	1.33	8.79
13	Effluent	8.04	3.04	1.30	8.75
14	Effluent	6.85	2.84	1.26	8.83
15	Effluent	7.52	2.99	1.32	8.81
16	Effluent	7.42	2.95	1.31	8.63
17	Effluent	6.37	2.81	1.29	9.01
19	Effluent	7.80	3.05	1.33	8.97
20	Effluent	8.85	3.24	1.38	8.63

Day	Location	Acetate (mM)	Cl (mM)	Br (mM)	SO_4 (mM)
21	Effluent	7.31	2.94	1.31	8.73
22	Effluent	8.51	3.14	1.38	8.66
23	Effluent	8.13	3.07	1.34	8.97
24	Effluent	6.74	2.86	1.29	9.02
25	Effluent	6.62	2.86	1.22	8.71
26	Effluent	6.20	2.82	1.23	8.53
27	Effluent	5.74	2.79	1.30	8.26
28	Effluent	5.34	2.81	1.27	7.99
29	Effluent	4.44	2.65	1.18	7.57
30	Effluent	5.06	2.95	1.24	7.17
31	Effluent	3.74	2.90	1.27	6.96
32	Effluent	2.68	2.80	1.24	6.00
33	Effluent	4.63	3.01	1.26	5.40
34	Effluent	3.52	2.97	1.26	4.28
35	Effluent	1.88	2.96	1.24	3.59
36	Effluent	0.94	2.93	1.25	2.85
37	Effluent	0.00	2.92	1.27	1.92
38	Effluent	0.00	2.99	1.24	1.22
39	Effluent	0.00	2.97	1.25	0.78
40	Effluent	0.00	2.87	1.22	0.70
41	Effluent	0.00	3.08	1.27	0.53
42	Effluent	0.00	3.01	1.25	0.49
43	Effluent	0.00	3.05	1.26	0.47

Table A6: Cation concentrations from the mesoscale column study for all side ports and effluent as described in chapter 4 & 6.

Day	Location	Na (mM)	K (mM)	Mg (mM)	Ca (mM)	U (μM)
1	10 cm	20.62	0.63	4.64	5.54	0.0052
2	10 cm	21.84	0.94	4.38	5.30	0.0050
3	10 cm	22.34	1.27	4.35	5.25	0.0052
4	10 cm	22.31	1.40	4.33	5.21	0.0059
5	10 cm	22.39	1.41	4.25	5.16	0.0146
6	10 cm	22.13	1.40	4.24	5.08	0.0193
7	10 cm	22.24	1.45	4.28	5.19	0.0187
8	10 cm	22.37	1.46	4.28	5.21	0.0169
9	10 cm	22.20	1.47	4.26	5.20	0.0150
10	10 cm	22.55	1.50	4.29	5.22	0.0121
11	10 cm	22.00	1.50	4.23	5.10	0.0117
12	10 cm	21.76	1.50	4.21	5.15	0.0100
13	10 cm	21.79	1.51	4.22	5.12	0.0083
14	10 cm	22.69	1.55	4.33	5.30	0.0074
15	10 cm	22.74	1.54	4.37	5.26	0.0073
16	10 cm	22.61	1.52	4.33	5.19	0.0058
17	10 cm	22.78	1.53	4.34	5.17	0.0050
18	10 cm	22.89	1.52	4.40	5.15	0.0047
19	10 cm	22.83	1.52	4.38	5.04	0.0041
20	10 cm	22.86	1.50	4.38	5.00	0.0039
21	10 cm	22.16	1.58	4.24	5.34	0.0037
22	10 cm	22.27	1.58	4.26	5.31	0.0037
23	10 cm	22.09	1.55	4.22	5.20	0.0033
24	10 cm	22.22	1.56	4.26	5.20	0.0034
25	10 cm	21.79	1.53	4.16	5.08	0.0034
26	10 cm	22.21	1.58	4.25	5.23	0.0035
27	10 cm	22.04	1.54	4.23	5.12	0.0032
28	10 cm	21.96	1.55	4.22	5.14	0.0032
29	10 cm	23.43	1.52	4.28	4.79	0.0031
30	10 cm	23.50	1.50	4.32	4.74	0.0030
31	10 cm	23.81	1.50	4.32	4.76	0.0028
32	10 cm	23.33	1.49	4.22	4.68	0.0025
33	10 cm	23.74	1.51	4.30	4.73	0.0024
34	10 cm	22.38	1.53	4.25	4.80	0.0025
35	10 cm	22.40	1.51	4.25	4.78	0.0023
36	10 cm	22.30	1.51	4.24	4.72	0.0025
37	10 cm	22.40	1.50	4.21	4.67	0.0028
38	10 cm	22.38	1.51	4.17	4.62	0.0032
39	10 cm	22.25	1.50	4.16	4.59	0.0034
41	10 cm	22.04	1.45	4.16	4.52	0.0045
42	10 cm	22.22	1.44	4.16	4.78	0.0049
43	10 cm	22.10	1.44	4.16	4.74	0.0049
1	30 cm	12.27	0.47	4.50	5.36	0.0166
2	30 cm	17.52	0.53	5.12	6.16	0.0192
3	30 cm	21.86	0.59	4.68	5.62	0.0224

Day	Location	Na (mM)	K (mM)	Mg (mM)	Ca (mM)	U (μM)
4	30 cm	22.36	0.73	4.52	5.47	0.0210
5	30 cm	21.93	0.84	4.35	5.27	0.0390
6	30 cm	21.62	0.92	4.24	5.22	0.0615
7	30 cm	21.95	1.04	4.26	5.25	0.0636
8	30 cm	21.70	1.07	4.20	5.17	0.0602
9	30 cm	22.03	1.13	4.24	5.25	0.0571
10	30 cm	22.48	1.23	4.30	5.29	0.0459
11	30 cm	21.68	1.27	4.20	5.18	0.0406
12	30 cm	21.69	1.27	4.20	5.15	0.0349
13	30 cm	21.97	1.32	4.23	5.17	0.0264
14	30 cm	22.37	1.34	4.27	5.26	0.0220
15	30 cm	22.72	1.38	4.37	5.28	0.0182
16	30 cm	22.67	1.37	4.35	5.20	0.0151
17	30 cm	22.65	1.40	4.36	5.15	0.0114
18	30 cm	22.71	1.38	4.38	5.09	0.0101
19	30 cm	22.62	1.60	4.35	5.05	0.0085
20	30 cm	22.95	1.41	4.43	5.06	0.0076
21	30 cm	22.13	1.47	4.22	5.31	0.0070
22	30 cm	22.37	1.49	4.29	5.32	0.0067
23	30 cm	22.18	1.47	4.27	5.23	0.0063
24	30 cm	22.14	1.47	4.25	5.22	0.0060
25	30 cm	22.16	1.48	4.25	5.16	0.0057
26	30 cm	22.04	1.49	4.23	5.17	0.0058
27	30 cm	22.02	1.48	4.22	5.13	0.0057
28	30 cm	22.26	1.51	4.27	5.18	0.0061
29	30 cm	23.46	1.45	4.26	4.79	0.0059
30	30 cm	23.43	1.43	4.28	4.73	0.0058
31	30 cm	23.60	1.43	4.27	4.73	0.0062
32	30 cm	23.55	1.43	4.20	4.60	0.0066
33	30 cm	23.50	1.42	4.13	4.52	0.0075
34	30 cm	22.18	1.44	4.03	4.51	0.0085
35	30 cm	22.17	1.39	3.97	4.36	0.0085
36	30 cm	22.21	1.38	3.89	4.53	0.0091
37	30 cm	22.06	1.35	3.70	4.24	0.0109
38	30 cm	22.08	1.34	3.62	4.00	0.0125
39	30 cm	22.22	1.34	3.57	3.82	0.0135
40	30 cm	22.29	1.33	3.58	3.63	0.0151
41	30 cm	21.84	1.29	3.56	3.41	0.0147
42	30 cm	21.86	1.29	3.63	3.31	0.0144
43	30 cm	21.93	1.30	3.71	3.25	0.0133
1	50 cm	11.32	0.45	4.19	4.94	0.0293
2	50 cm	12.64	0.48	4.77	5.67	0.0327
3	50 cm	18.60	0.52	5.11	6.04	0.0411
4	50 cm	21.02	0.52	4.83	5.74	0.0459
5	50 cm	21.91	0.55	4.52	5.42	0.0768
6	50 cm	21.84	0.61	4.39	5.37	0.1110
7	50 cm	22.00	0.68	4.38	5.37	0.1120

Day	Location	Na (mM)	K (mM)	Mg (mM)	Ca (mM)	U (μM)
8	50 cm	22.14	0.75	4.37	5.38	0.1013
9	50 cm	22.15	0.83	4.34	5.34	0.0891
10	50 cm	22.37	0.96	4.36	5.42	0.0736
11	50 cm	21.71	0.99	4.27	5.26	0.0667
12	50 cm	21.76	1.03	4.23	5.23	0.0551
14	50 cm	22.68	1.09	4.38	5.34	0.0386
15	50 cm	22.75	1.10	4.42	5.33	0.0323
16	50 cm	22.81	1.13	4.42	5.26	0.0264
17	50 cm	22.97	1.17	4.46	5.26	0.0217
18	50 cm	22.83	1.16	4.44	5.15	0.0182
19	50 cm	22.93	1.18	4.42	5.09	0.0152
20	50 cm	22.74	1.19	4.42	5.07	0.0133
21	50 cm	22.28	1.29	4.30	5.40	0.0123
22	50 cm	22.33	1.29	4.30	5.32	0.0107
23	50 cm	21.93	1.26	4.26	5.24	0.0104
24	50 cm	22.07	1.28	4.26	5.20	0.0096
25	50 cm	21.69	1.29	4.19	5.12	0.0092
26	50 cm	21.91	1.32	4.24	5.17	0.0092
27	50 cm	22.10	1.33	4.25	5.17	0.0097
28	50 cm	22.07	1.34	4.24	5.16	0.0101
29	50 cm	23.38	1.30	4.25	4.74	0.0097
30	50 cm	23.41	1.31	4.22	4.72	0.0099
31	50 cm	23.60	1.31	4.25	4.66	0.0102
32	50 cm	23.43	1.31	4.14	4.53	0.0108
33	50 cm	23.58	1.29	4.04	4.39	0.0117
34	50 cm	21.81	1.29	3.87	4.52	0.0129
35	50 cm	22.15	1.30	3.82	4.46	0.0130
36	50 cm	21.70	1.24	3.57	4.12	0.0137
37	50 cm	21.58	1.22	3.37	3.78	0.0148
38	50 cm	21.67	1.18	3.11	3.29	0.0165
39	50 cm	21.78	1.16	2.99	3.01	0.0177
40	50 cm	21.51	1.11	2.83	2.63	0.0192
41	50 cm	21.73	1.10	2.79	2.39	0.0214
42	50 cm	21.82	1.09	2.81	2.22	0.0224
43	50 cm	21.85	1.10	2.91	2.13	0.0223
1	70 cm	11.18	0.45	4.19	4.83	0.0384
2	70 cm	11.67	0.45	4.46	5.16	0.0392
3	70 cm	15.91	0.51	5.34	6.20	0.0530
4	70 cm	19.28	0.51	5.17	6.01	0.0648
5	70 cm	21.19	0.48	4.76	5.59	0.1035
6	70 cm	21.62	0.46	4.59	5.51	0.1467
7	70 cm	21.98	0.48	4.47	5.47	0.1514
8	70 cm	21.99	0.50	4.47	5.49	0.1406
9	70 cm	22.22	0.55	4.41	5.46	0.1193
10	70 cm	21.89	0.62	4.37	5.39	0.0968
11	70 cm	21.60	0.64	4.31	5.35	0.0873
12	70 cm	21.80	0.68	4.35	5.35	0.0742

Day	Location	Na (mM)	K (mM)	Mg (mM)	Ca (mM)	U (μM)
13	70 cm	22.35	0.74	4.34	5.43	0.0594
14	70 cm	22.90	0.78	4.49	5.47	0.0502
15	70 cm	22.94	0.80	4.50	5.45	0.0428
16	70 cm	23.03	0.84	4.52	5.38	0.0356
17	70 cm	23.16	0.92	4.54	5.29	0.0275
18	70 cm	22.66	0.91	4.44	5.16	0.0244
19	70 cm	22.85	0.96	4.44	5.11	0.0198
20	70 cm	22.36	1.13	4.33	5.78	0.0186
21	70 cm	22.42	1.08	4.35	5.43	0.0165
22	70 cm	22.20	1.08	4.32	5.34	0.0146
23	70 cm	22.42	1.10	4.35	5.36	0.0141
24	70 cm	22.28	1.12	4.31	5.26	0.0129
25	70 cm	22.21	1.18	4.30	5.23	0.0122
26	70 cm	22.41	1.20	4.26	3.17	0.0116
27	70 cm	21.98	1.18	4.24	5.13	0.0136
28	70 cm	23.50	1.19	4.29	4.85	0.0134
29	70 cm	23.50	1.17	4.23	4.72	0.0140
30	70 cm	23.57	1.18	4.23	4.66	0.0143
31	70 cm	23.64	1.19	4.17	4.58	0.0149
32	70 cm	23.38	1.20	4.04	4.40	0.0153
33	70 cm	23.39	1.18	3.93	4.24	0.0179
34	70 cm	21.90	1.19	3.73	4.35	0.0206
35	70 cm	21.63	1.16	3.58	4.14	0.0206
36	70 cm	21.55	1.12	3.37	3.76	0.0207
37	70 cm	21.57	1.09	3.12	3.37	0.0215
38	70 cm	21.44	1.05	2.79	2.87	0.0230
39	70 cm	21.42	1.02	2.61	2.58	0.0236
40	70 cm	21.24	0.98	2.44	2.30	0.0258
41	70 cm	21.38	0.96	2.36	2.10	0.0291
42	70 cm	21.43	0.96	2.34	1.98	0.0319
43	70 cm	21.56	0.96	2.36	1.88	0.0334
1	90 cm	11.29	0.45	4.40	4.74	0.0520
2	90 cm	11.26	0.45	4.47	4.82	0.0525
3	90 cm	13.68	0.50	5.45	5.94	0.0691
4	90 cm	17.15	0.51	5.60	6.14	0.0817
5	90 cm	19.94	0.48	5.14	5.72	0.1233
6	90 cm	20.86	0.45	4.83	5.57	0.1982
7	90 cm	21.49	0.44	4.69	5.48	0.2084
8	90 cm	22.04	0.45	4.69	5.56	0.2011
9	90 cm	22.11	0.44	4.55	5.48	0.1655
10	90 cm	21.77	0.46	4.47	5.38	0.1313
11	90 cm	22.03	0.47	4.51	5.44	0.1184
12	90 cm	21.91	0.49	4.45	5.41	0.0974
13	90 cm	22.23	0.51	4.44	5.42	0.0752
14	90 cm	22.64	0.55	4.48	5.45	0.0619
15	90 cm	22.81	0.57	4.54	5.46	0.0528
16	90 cm	22.84	0.60	4.54	5.38	0.0430

Day	Location	Na (mM)	K (mM)	Mg (mM)	Ca (mM)	U (μM)
17	90 cm	22.91	0.65	4.54	5.35	0.0336
18	90 cm	23.21	0.68	4.59	5.31	0.0297
19	90 cm	22.99	0.71	4.53	5.21	0.0245
20	90 cm	22.42	0.83	4.37	5.62	0.0213
21	90 cm	22.14	0.83	4.32	5.40	0.0186
22	90 cm	22.42	0.85	4.38	5.38	0.0166
23	90 cm	21.65	0.85	4.22	5.20	0.0144
24	90 cm	22.48	0.91	4.37	5.36	0.0140
25	90 cm	22.05	0.92	4.28	5.22	0.0134
26	90 cm	22.42	0.95	4.32	5.25	0.0136
27	90 cm	22.00	0.97	4.23	5.11	0.0149
28	90 cm	23.48	0.96	4.25	4.79	0.0147
29	90 cm	23.49	0.97	4.22	4.69	0.0157
30	90 cm	23.35	0.98	4.19	4.60	0.0167
31	90 cm	23.42	0.98	4.07	4.47	0.0181
32	90 cm	23.27	1.00	3.94	4.27	0.0200
33	90 cm	23.13	0.99	3.80	4.36	0.0227
34	90 cm	21.84	1.01	3.58	4.11	0.0260
35	90 cm	21.78	1.02	3.45	3.97	0.0261
36	90 cm	21.66	0.98	3.21	3.54	0.0277
37	90 cm	21.09	0.94	2.87	3.09	0.0279
38	90 cm	21.29	0.92	2.61	2.69	0.0290
40	90 cm	21.05	0.88	2.33	2.28	0.0350
41	90 cm	21.01	0.86	2.24	2.12	0.0424
42	90 cm	21.22	0.86	2.19	2.02	0.0478
43	90 cm	21.51	0.87	2.17	1.96	0.0515
1	Effluent	10.62	0.43	4.44	4.25	0.0582
2	Effluent	11.24	0.44	4.73	4.62	0.0616
3	Effluent	13.95	0.53	5.69	5.75	0.0818
4	Effluent	17.62	0.55	6.09	6.29	0.0983
5	Effluent	19.52	0.50	5.64	5.91	0.1273
6	Effluent	21.42	0.46	5.31	5.78	0.2229
7	Effluent	22.33	0.45	5.12	5.71	0.2462
8	Effluent	21.68	0.42	4.80	5.45	0.2160
9	Effluent	22.86	0.42	4.86	5.59	0.1869
10	Effluent	23.14	0.42	4.82	5.61	0.1508
11	Effluent	22.79	0.41	4.68	5.49	0.1290
12	Effluent	21.78	0.43	4.51	5.55	0.1080
13	Effluent	22.36	0.46	4.58	5.65	0.0870
14	Effluent	22.52	0.48	4.56	5.61	0.0727
15	Effluent	22.07	0.47	4.47	5.54	0.0595
16	Effluent	21.66	0.49	4.36	5.42	0.0496
17	Effluent	22.22	0.53	4.46	5.54	0.0402
18	Effluent	21.84	0.54	4.39	5.50	0.0346
19	Effluent	21.66	0.58	4.39	5.53	0.0297
20	Effluent	21.52	0.61	4.32	5.45	0.0248
21	Effluent	21.86	0.65	4.38	5.48	0.0214

Day	Location	Na (mM)	K (mM)	Mg (mM)	Ca (mM)	U (μM)
22	Effluent	21.43	0.66	4.30	5.37	0.0188
23	Effluent	22.16	0.70	4.41	5.50	0.0172
24	Effluent	21.97	0.71	4.34	5.41	0.0163
25	Effluent	21.86	0.74	4.29	5.35	0.0154
26	Effluent	21.85	0.76	4.28	5.35	0.0161
27	Effluent	21.73	0.79	4.23	5.24	0.0163
28	Effluent	21.87	0.82	4.22	5.19	0.0171
29	Effluent	21.72	0.83	4.13	5.07	0.0175
30	Effluent	21.71	0.84	4.05	4.94	0.0177
31	Effluent	22.00	0.85	3.99	4.81	0.0189
32	Effluent	21.42	0.88	3.76	4.53	0.0211
33	Effluent	22.17	0.90	3.73	4.38	0.0237
34	Effluent	21.69	0.87	3.47	4.02	0.0261
35	Effluent	21.35	0.83	3.23	3.69	0.0269
36	Effluent	21.46	0.83	3.07	3.41	0.0292
37	Effluent	21.00	0.82	2.78	3.02	0.0322
38	Effluent	20.73	0.80	2.54	2.69	0.0361
39	Effluent	20.93	0.78	2.40	2.50	0.0397
40	Effluent	20.78	0.78	2.29	2.33	0.0486
41	Effluent	20.71	0.78	2.20	2.18	0.0599
42	Effluent	20.93	0.79	2.13	2.10	0.0685
43	Effluent	21.14	0.80	2.11	2.04	0.0719

Table A7: Aqueous ferrous iron, sulfide and pH in mesoscale column effluent, discussed in chapter 4.

Day	Fe^{++} (μM)	HS^- (μM)	pH
1	3.22	0.69	7.21
2	4.30	0.28	7.23
3	2.51	0.12	7.25
4	2.51	0.03	7.24
5	9.31	0.16	7.24
6	22.38	0.22	7.27
7	33.49	0.34	7.21
8	37.25	0.28	7.25
9	46.02	0.00	7.14
10	46.92	0.06	7.3
11	51.57	0.00	7.31
12	53.36	0.09	7.27
13	57.84	0.00	7.3
14	61.60	0.12	7.32
15	66.61	0.16	7.3
16	74.49	0.12	7.32
17	75.21	0.28	7.27
18	81.65	0.31	7.3
19	82.37	0.78	7.32
20	83.45	1.09	7.39
21			7.31
22	84.88	2.31	7.39
23	92.94	3.80	7.41
24	93.83	4.86	7.38
25	93.11	6.05	7.41
26	91.32	10.10	7.42
27	71.63	8.76	7.44
28	79.51	10.16	7.45
29	79.15	9.60	7.47
30	69.48	12.22	7.57
31	56.59	3.40	7.53
32	47.09	6.89	
33	34.38	8.67	7.57
34	24.17	14.03	7.63
35	16.83	26.49	7.67
36	10.92	29.46	7.7
37	12.00	35.43	7.74
38	9.85	24.47	7.75
39	10.21	25.09	7.76
40	13.25	6.55	7.85
41	20.41	1.46	7.8
42	22.92	0.56	7.84
43	18.09	1.37	7.86

Table A8: Total dissolved organic and inorganic carbon and corresponding $\delta^{13}C$ values in the mesoscale column effluent, discussed in chapter 4.

Day	TOC (mM)	TIC (mM)	$\delta^{13}C$ TOC (‰)	$\delta^{13}C$ TIC (‰)
1	0.18	8.54	1.7	-26.2
2	0.90	8.60	185.2	-19.9
3	8.71	8.47	907.7	14.3
4	16.89	9.22	960.5	37.5
5	17.26	10.51	922.5	151.8
6	16.03	11.72	910.8	241.9
7	16.71	11.73	914.3	233.6
8	17.77	10.62	933.1	208.8
9	18.67	10.33	935.5	169.8
10	19.16	10.12	934.4	139.8
11	19.01	10.33	946.9	134.8
12	18.74	10.38	941.9	123.9
13		10.31	953.8	118.5
14	19.38	10.23	950.5	117.1
15	19.34	10.30	945.3	121.4
16	19.28	10.43	974.8	108.1
17	19.56	10.36	926.7	103.9
18	19.57	10.20	941.0	106.1
19	19.81	10.49	962.4	99.3
20	19.59	10.61	946.5	94.9
21	19.75	10.59	943.3	95.1
22	19.30	10.79	937.8	96.5
23	19.60	10.33	939.1	101.7
24	18.59	11.02	932.3	118.9
25	19.14	11.26	914.4	136.7
26	18.04	11.69	902.7	166.3
27	18.28	12.36	890.4	186.7
28	16.90	13.13	904.4	225.0
29	16.23	13.50	821.6	259.2
30	15.68	14.84	860.1	310.3
31	13.63	14.22	824.1	353.8
32	12.19	15.68	805.9	403.8
33	9.77	17.56	773.9	455.0
34	9.02	18.74	722.8	502.0
35	7.33	20.43	665.3	540.6
36	4.54	22.17	662.5	563.5
37	2.97	23.72	599.1	615.7
38	1.39	24.22	543.6	636.7
39	0.45	25.28	443.4	648.0
40	0.00	24.02	515.9	656.6
41		25.13	513.9	660.7
42	0.82	24.81	425.2	664.9
43	0.00	24.66	426.8	666.4

Table A9: $\delta^{34}S$ of SO_4^{2-} and HS^-, $\delta^{44}Ca$ in fluid phase mesoscale column experiment, discussed in chapters 5 & 6.

Day	Location	$\delta^{34}S$ SO4 (‰)	$\delta^{34}S$ HS- (‰)	$\delta^{44}Ca$ (‰)
1	10 cm	6.38		
2	10 cm			
3	10 cm	6.27		
4	10 cm	6.23		0.32
5	10 cm	6.23		
6	10 cm			
7	10 cm	6.36		
8	10 cm	6.35		
9	10 cm	6.42		
10	10 cm	6.29		
11	10 cm	6.34		
12	10 cm	6.40		
13	10 cm	6.40		
14	10 cm	6.40		
15	10 cm			
16	10 cm	6.33		
17	10 cm	6.33		
18	10 cm			
19	10 cm	6.36		
20	10 cm	6.50		
21	10 cm	6.34		0.385
22	10 cm	6.53		
23	10 cm	6.38		
24	10 cm	6.55		
25	10 cm	6.66		
26	10 cm	6.78		
27	10 cm	6.69		
28	10 cm	6.81		0.2
29	10 cm	6.62		
30	10 cm	6.85		
31	10 cm	7.04		
32	10 cm	7.08		
33	10 cm	7.46		0.215
34	10 cm	7.62		
35	10 cm	7.76		
36	10 cm	8.03		
37	10 cm	8.76		0.24
38	10 cm	8.84		
39	10 cm	9.36		
41	10 cm	9.64		
42	10 cm	9.93		
43	10 cm	10.31		0.315
1	30 cm	6.28		
2	30 cm			
3	30 cm	6.32		

Day	Location	δ^{34}S SO4 (‰)	δ^{34}S HS- (‰)	δ^{44}Ca (‰)
4	30 cm	6.30		
5	30 cm	6.31		
6	30 cm	6.42		
7	30 cm	6.39		
8	30 cm	6.40		
9	30 cm	6.49		
10	30 cm	6.24		
11	30 cm	6.34		
12	30 cm	6.41		
13	30 cm	6.42		
14	30 cm	6.44		
15	30 cm			
16	30 cm	6.34		
17	30 cm	6.37		
18	30 cm			
19	30 cm	6.34		
20	30 cm	6.38		
21	30 cm	6.44		0.315
22	30 cm	6.72		
23	30 cm	6.60		
24	30 cm	6.70		
25	30 cm	6.69		
26	30 cm	6.81		
27	30 cm	6.80		
28	30 cm	6.98		0.3
29	30 cm	6.98		
30	30 cm	7.13		
31	30 cm	7.49		
32	30 cm	7.84		
33	30 cm	8.46		0.26
34	30 cm	9.23		
35	30 cm	9.65		
36	30 cm	10.55		
37	30 cm	11.68		0.455
38	30 cm	13.31		
39	30 cm	14.18		
40	30 cm	15.46		0.47
41	30 cm	15.72		
42	30 cm	16.69		
43	30 cm	17.18		0.6
1	50 cm	6.34		
2	50 cm			
3	50 cm	6.35		
4	50 cm	6.29		
5	50 cm	6.35		
6	50 cm	6.31		
7	50 cm	6.27		

Day	Location	δ^{34}S SO4 (‰)	δ^{34}S HS- (‰)	δ^{44}Ca (‰)
8	50 cm	6.31		
9	50 cm	6.35		
10	50 cm	6.43		
11	50 cm	6.31		
12	50 cm	6.29		
14	50 cm	6.33		
15	50 cm			
16	50 cm	6.32		
17	50 cm	6.39		
18	50 cm	6.36		
19	50 cm	6.40		
20	50 cm	6.41		
21	50 cm	6.67		0.295
22	50 cm	6.72		
23	50 cm	6.75		
24	50 cm	6.68		
25	50 cm	6.67		
26	50 cm	6.94		
27	50 cm	6.94		
28	50 cm	7.18		0.12
29	50 cm	7.27		
30	50 cm	7.59		
31	50 cm	7.84		
32	50 cm	8.36		
33	50 cm	9.26		0.265
34	50 cm	10.36		
35	50 cm	11.03		
36	50 cm	12.64		
37	50 cm	14.79		0.28
38	50 cm	18.00		
39	50 cm	19.75		
40	50 cm	22.59		0.6
41	50 cm	24.73		
42	50 cm	25.49		
43	50 cm	27.42		0.875
1	70 cm	6.24		
2	70 cm			
3	70 cm	6.33		
4	70 cm	6.24		
5	70 cm	6.29		
6	70 cm	6.38		
7	70 cm	6.33		
8	70 cm	6.32		
9	70 cm	6.41		
10	70 cm	6.36		
11	70 cm	6.33		
12	70 cm	6.39		

Day	Location	δ^{34}S SO4 (‰)	δ^{34}S HS- (‰)	δ^{44}Ca (‰)
13	70 cm	6.26		
14	70 cm	6.24		
15	70 cm			
16	70 cm	6.26		
17	70 cm	6.38		
18	70 cm			
19	70 cm			
20	70 cm	6.36		
21	70 cm	6.56		
22	70 cm	6.60		
23	70 cm	6.61		
24	70 cm	6.68		
25	70 cm	6.82		
26	70 cm	6.98		
27	70 cm	7.04		
28	70 cm	7.35		
29	70 cm	7.46		
30	70 cm	7.75		
31	70 cm	8.31		
32	70 cm	8.93		
33	70 cm	10.20		
34	70 cm	11.64		
35	70 cm	12.64		
36	70 cm	14.97		
37	70 cm	18.16		
38	70 cm	23.47		
39	70 cm	26.82		
40	70 cm	31.43		
41	70 cm	37.39		
42	70 cm	37.44		
43	70 cm	39.59		
1	90 cm	6.25		
2	90 cm			
3	90 cm	6.21		
4	90 cm	6.32		
5	90 cm	6.46		
6	90 cm	6.24		
7	90 cm	6.47		
8	90 cm	6.32		
9	90 cm	6.33		
10	90 cm	6.40		
11	90 cm	6.26		
12	90 cm	6.39		
13	90 cm	6.35		
14	90 cm	6.46		
15	90 cm			
16	90 cm	6.38		

Day	Location	δ^{34}S SO4 (‰)	δ^{34}S HS- (‰)	δ^{44}Ca (‰)
17	90 cm	6.37		
18	90 cm			
19	90 cm			
20	90 cm	6.48		
21	90 cm	6.66		
22	90 cm	6.87		
23	90 cm	6.68		
24	90 cm	6.84		
25	90 cm	6.90		
26	90 cm	7.10		
27	90 cm	7.34		
28	90 cm	7.63		
29	90 cm	7.90		
30	90 cm	8.14		
31	90 cm	8.96		
32	90 cm	9.96		
33	90 cm	10.84		
34	90 cm	12.87		
35	90 cm	13.82		
36	90 cm	16.60		
37	90 cm	20.27		
38	90 cm	26.89		
39	91 cm	30.82		
40	90 cm	35.71		
41	90 cm	38.90		
42	90 cm	39.59		
43	90 cm	42.32		
1	Effluent	6.33		
2	Effluent			
3	Effluent			
4	Effluent	6.36		0.385
5	Effluent	6.29		
6	Effluent	6.37		
7	Effluent	6.38		
8	Effluent	6.44		
9	Effluent			
10	Effluent			
11	Effluent			
12	Effluent			
13	Effluent			
14	Effluent			
15	Effluent			
16	Effluent	6.23		
17	Effluent	6.42		
18	Effluent	6.35		
19	Effluent			
20	Effluent	6.42		

Day	Location	δ^{34}S SO4 (‰)	δ^{34}S HS- (‰)	δ^{44}Ca (‰)
21	Effluent	6.56		0.35
22	Effluent	6.53		
23	Effluent	6.53	-3.42	
24	Effluent	6.78		
25	Effluent	6.97		
26	Effluent	7.19	-4.28	
27	Effluent	7.33	-4.26	
28	Effluent	7.62	-4.23	0.21
29	Effluent			
30	Effluent	8.69		
31	Effluent	9.24	-2.22	
32	Effluent	10.24		
33	Effluent	11.29	-0.88	0.315
34	Effluent	12.91	-0.58	
35	Effluent	14.91	1.59	
36	Effluent	17.14	4.23	
37	Effluent	21.37	6.67	0.365
38	Effluent	26.40	10.24	
39	Effluent	29.76	11.44	
40	Effluent	32.56	8.94	0.33
41	Effluent	35.91		
42	Effluent	35.32		
43	Effluent	36.32		0.465

Appendix B

DNA extraction and sequencing methods

Courtesy of Eoin Brodie, Lawrence Berkeley National Laboratory

DNA extraction

Total nucleic acids were extracted from 0.5 g of the triplicate pore water/effluent samples according to the protocol described in Ivanov et al (2009). Briefly, samples were resuspended in a modified CTAB buffer (10 % CTAB, 250 mM potassium phosphate, 300 mM NaCl), transferred to a lysing matrix E tube (MP biomedicals) and an equal volume of phenol:chloroform:isoamylalcohol (25:24:1) added. Samples were agitated using a FastPrep instrument (MP biomedicals: 2 x 20 seconds, 5.5. m/s) and centrifuged (16,000 x g, 5 min, 4 °C). The aqueous phase was removed to a new tube and an equivalent volume of chlorform:isoamylalcohol (24:1) added to yield a crude nucleic acid extract and the solution centrifuged again. The aqueous phase was removed to a new tube containing polyethylene glycol (30 % wt/vol), and incubated for 2 hours before being centrifuged. The supernatant was discarded and the crude nucleic acid pellet washed in 70 % ethanol. The pellet was dissolved in nuclease-free (DEPC-treated) water and purified using the DNA/RNA AllPrep kit (Qiagen, Valencia, CA) following the manufacturers protocol. Purified DNA was eluted in buffer EB (2 x 30 μl) and quantified in triplicate using the Quant-iT Picogreen assay (Invitrogen, Carlsbad, CA).

Bar-coded pyrosequencing

Pore water/effluent DNA samples were normalized to 10 ng μl^{-1} prior to PCR. Samples were amplified using a universal primer pair targeting the SSU V9 region. The forward primer was 515F (‘5-GTGCCAGCMGCCGCGGTAA-‘3, Turner et al., 1999) and the reverse primer was 907R (‘5-CCGTCAATTCCTTTRAGTTT-‘3, Lane et al., 1991). The forward and reverse primers were downstream of the FLX-454 primer adapters and the reverse primer also contained a 12-bp barcode unique to a specific sample (Hamady et al., 2008). PCR reactions were performed using Takara Ex Taq polymerase (Takara, Madison, WI), with the following thermocycling parameters: initial denaturation at 95 °C for 1 minute followed by 25 cycles of 95 °C for 20 seconds, 30 seconds of annealing at 66 °C and extension at 72 °C for 1 minute. Final product extension was at 72 °C for 10 minutes. Reaction primer dimers were removed from the PCR products via SPRI bead purification according to the manufacturers protocol (AMPure XP, Beckman Coulter Genomics, Danvers, MA) before being checked for quality and quantity on a Bioanalyzer 2100 using a DNA 7500 chip (Agilent Technologies, Santa Clara, CA). Each PCR sample was normalized to 30 ng and combined together for multiplex sequencing. Sequencing libraries were created using the SV emu-PCR kit (Lib-A, Roche, Indianapolis, IN) and sequencing on a GS-FLX sequencer (Roche, Indianapolis, IN) at the Veterans Medical Research Foundation, La Jolla, CA.

Pyrosequencing data processing and statistical analysis

Raw 454 sequences were denoised and processed using the Quantitative Insights Into Microbial Ecology (QIIME) pipeline (Caporaso et al., 2010a). Low quality reads were filtered out and the sequences assigned back to the original samples via the 12 bp barcodes. Default QIIME parameters were used for processing the pyrosequencing data. OTUs were defined at 97 % via uclust (Edgar, 2010), and a representative sequence of each OTU used for alignment via PyNAST (Caporaso et al., 2010b) and for taxonomy assignment through the RDP database (Cole et al., 2009). Phylogenetic trees were created

using FastTree under default parameters (Price et al., 2009). The trees were used for the derivation of alpha and beta diversity metrics, including weighted and unweighted unifrac distance matrices that calculate phylogenetic distances between communities through the degree of overlap between branch lengths in a phylogenetic tree.